

---

# Investigation of magnetic anomalies in archaeological prospection

Sandra Elisabeth Hahn

---



München 2022



---

# Investigation of magnetic anomalies in archaeological prospection

Sandra Elisabeth Hahn

---

Dissertation  
zur Erlangung des Doktorgrades  
an der Fakultät für Geowissenschaften  
der Ludwig-Maximilians-Universität  
München

vorgelegt von  
Sandra Elisabeth Hahn geb. Ostner  
aus Landshut

München, den 29.11.2022

Erstgutachter: Prof. Dr. Jörg W. E. Faßbinder

Zweitgutachter: PD Dr. Florian Lhuillier

Tag der mündlichen Prüfung: 03.05.2023

# Summary

Magnetometer prospecting refers to mapping the magnetic field and is an essential method in archaeological prospecting and archaeogeophysics for investigating large surface areas. Permanent and induced magnetic fields of potential features, as well as the Earth's magnetic field, are registered, but the identification of the archaeological features relies fundamentally on the magnetisation contrast to the surroundings. The devices used are categorised as scalar and vector magnetometers, which provide different elements of the superimposed fields, resulting after data processing in different visual outputs. A new approach is presented to merge vector gradiometer with high-pass filtered total field magnetometer data to obtain visually uniform magnetograms for better interpretation. The registered anomaly of a feature depends on several source-specific parameters, among them the direction of its magnetisation. Inspired by the fieldwork at Artanish, synthetic magnetograms were generated to investigate the effect of the total magnetisation variation on a spherical object's anomaly pattern. The results are discussed in terms of the impact of the remanence and their significance for the survey interpretation. The anomaly pattern also depends on the direction of the Earth's magnetic field. From synthetic magnetograms and profiles, it was determined that the effect of the declination is avoidable for prospecting. The effect of the inclination is not compensable as anomaly patterns and peak ratios vary significantly with the inclination of the Earth's magnetic field. For the case of an inclination of  $15^\circ$ , modelling results are compared to data collected at an isocline of  $15^\circ$  and the effect of the inclination discussed for spherical and linear features. Three case studies show the applicability of magnetometer prospecting under different conditions and for different research questions. Prospecting at the Sumerian site of Šuruppak, the modern Fara, brought new insights into the excavation of 1902/1903 and answered opened questions about the existence of a city wall and harbour, canal routing and settlement structure of the ancient site. The case study of Yeha and Melazo portrays how complex magnetograms appear at sites still inhabited today. Archaeological features can only be reliably identified if geological and surface anomalies of recent buildings or agricultural use are recognised. The original idea of magnetometer prospecting in Gumbati was to re-locate the mid-1990s excavation or to find related features to the Achaemenid complex discovered back then. The resulting magnetograms show prominent rectangular features that were targeted in a subsequent excavation, but the source of the magnetic anomalies was not uncovered. Chemical analyses and susceptibility measurements indicate that fertiliser residues could be the reasons for these anomalies.



# Preface

My research work in the field of archaeological prospection was initially a challenge, as there was too little overarching concept for the dissertation. This is understandable, as the work in the research group often requires extensive fieldwork in different places around the world. A structural approach to an overarching research question is difficult when the case studies have little or no archaeological, geological or other connection. However, it was clear to me from the start that this thesis should not just be a compilation of field reports but should follow a geophysical narrative and explain, explore and present interrelationships between individual factors in magnetic prospection. However, the framework of the individual field studies sets the direction in which the individual works will develop. The work on the individual field studies involves so much time in the background research of the archaeological and geological conditions, in the preparation of the data, and in their detailed interpretation that there is actually little time left for an additional topic. How can the individual works be brought together to form a common thread? Where else can we start but with the essential consideration of what exactly is measured in the magnetometer survey? A simple answer could be the vector sum of the object's and the Earth's magnetic field. Nevertheless, other factors also play a role, which will be explored and presented in this thesis with synthetic data and results from fieldwork.

Finally, this work is based on published articles, aspects of which are discussed in detail in the respective chapters. Articles included in this thesis are:

- CHAPTER 2: An excerpt of Hahn, S. E., Fassbinder, J. W. E., Otto, A., Einwag, B., & Al-Hussainy, A. A. (2022). **Revisiting Fara: Comparison of merged prospection results of diverse magnetometers with the earliest excavations in ancient Šuruppak from 120 years ago** and Hahn, S., & Fassbinder, J. W. E. (2022). **Merging Total Field Magnetometer and Vector Gradiometer Data - an Alternative Method.**
- CHAPTER 3: Hahn, S., Parsi, M., Fassbinder, J. W. E., Bobokhyan, A., & Kunze, R. (2021). **The Ecstasy of Gold: Magnetometer Prospection for the Ushkiani Project in Armenia.** and Hahn, S., & Fassbinder, J. W. E. (2021). **The Effect of Remanence in Magnetometer Prospection.**
- CHAPTER 4: Hahn, S. E. & Fassbinder, J.W.E. (in submission) **Shallow Earth's magnetic field inclination in magnetometry: A discussion in magnetograms from Ethiopia at an isocline of 15°.**

- CHAPTER 5: Hahn, S. E., Fassbinder, J. W. E., Otto, A., Einwag, B., & Al-Hussainy, A. A. (2022). **Revisiting Fara: Comparison of merged prospection results of diverse magnetometers with the earliest excavations in ancient Šuruppak from 120 years ago.** *Archaeological Prospection*, 1– 13. <https://doi.org/10.1002/arp.1878>
- CHAPTER 6: Hahn, S. E., Parsi M., Fassbinder, J. W. E., Japp S., Gerlach I. (2022). **Yeha and Melazo (Ethiopia): Magnetometry in a palimpsest of archaeological, geological and modern remains.**
- CHAPTER 7: the article is still in preparation, but the contribution was presented in a conference as Hahn, S. E., Schauer M., Fassbinder J. W. E. (2022). **Searching for a lost Achaemenid Palace – Magnetometer prospection, soil magnetism and pXRF analysis in Gumbati (Georgia) to decode a magnetic “ghost feature”** at the 17th Castle Meeting.

My contributions to the publications were: Conceptualisation, Investigation, Methodology, Formal analysis, Visualisation, Writing - Original Draft (following the CRediT author contribution statements) and editing and handling the articles during the publishing processes. Unless otherwise stated in the thesis, all illustrations are made by me. The last chapter contains sections written or conceived by Michaela Schauer and labelled accordingly.

The next page of the thesis contains a complete list of the publications published during the doctoral studies.

# List of Publications

## Full-length articles

- Hahn, S. E., Fassbinder, J. W. E., Otto, A., Einwag, B., & Al-Hussainy, A. A. (2022). **Revisiting Fara: Comparison of merged prospection results of diverse magnetometers with the earliest excavations in ancient Šuruppak from 120 years ago.** *Archaeological Prospection*, 1–13. <https://doi.org/10.1002/arp.1878>
- Hahn, S. E., Parsi M., Fassbinder, J. W. E., Japp S., Gerlach I. (2022). **Yeha and Melazo (Ethiopia): Magnetometry in a palimpsest of archaeological, geological and modern remains.** Submitted to *Taylor and Francis - Journal of Field Archaeology*.
- Hahn, S. E. & Fassbinder, J.W.E. **Shallow Earth's magnetic field inclination in magnetometry: A discussion in magnetograms from Ethiopia at an isocline of 15°.** In submission to *Elsevier - Journal of Archaeological Sciences*.
- Hahn, S. E., Schauer, M., et al. *untitled*. In preparation.

## Peer-reviewed conference proceedings

- Ostner, S., Fassbinder, J.W.E., Parsi, M., Gerlach, I. & Japp, S. (2019). **Magnetic prospection close to the magnetic equator: Case studies in the Tigray plateau of Aksum and Yeha, Ethiopia.** In *New Global Perspectives on Archaeological Prospection*, 180-183, Archaeopress Publishing Ltd. doi: 10.32028/9781789693072.
- Hahn, S., Parsi, M., Fassbinder, J. W. E., Bobokhyan, A., & Kunze, R. (2021). **The Ecstasy of Gold: Magnetometer Prospection for the Ushkiani Project in Armenia.** *Revue d'archéométrie*, 45, 67-70. doi: 10.4000/archeosciences.8544.
- Hahn, S., & Fassbinder, J. W. E. (2021). **The Effect of Remanence in Magnetometer Prospection.** *Revue d'archéométrie*, 45, 71-74. doi:10.4000/archeosciences.8580.
- Hahn, S., Fassbinder, J. W. E., Otto, A. & Einwag, B. (2022). **After the biblical flood: Magnetomer prospecting at Fara (Iraq) to assess the excavations at ancient Šuruppak from 120 years ago.** *accepted*

- Hahn, S., & Fassbinder, J. W. E. (2023). **Merging Total Field Magnetometer and Vector Gradiometer Data - an Alternative Method**. In *Advances in On- and Offshore Archaeological Prospection: Proceedings of the 15th International Conference on Archaeological Prospection*, 407-409.

## Co-authored Publications

- Thiesson, J., et al. (2019). **Magnetic signal prospecting in a former Achaemenid ‘palace’: the example of Gumbati**. *New Global Perspectives on Archaeological Prospection*, 13, 193-196, doi: 10.32028/9781789693072.
- Parsi, M. and Fassbinder, J.W.E. and Papadopoulos, N. and Scheiblecker, M. and Ostner, S. (2019). **Revealing the Hidden Structure of the Ancient City Ur (Iraq) with Electrical Resistivity Tomography**. *New Global Perspectives on Archaeological Prospection*, 13, 206-208, doi: 10.32028/9781789693072.
- Fassbinder, J.W.E. and Ostner, S. and Scheiblecker, M and Parsi, M. and v. Ess, M. (2019). **Venice in the desert: Archaeological geophysics on the world’s oldest metropolis Uruk-Warka, the city of King Gilgamesh (Iraq)**. In *New Global Perspectives on Archaeological Prospection*, 13, 197-200. doi: 10.32028/9781789693072.
- Mieth, A., Bork, H. R., Khamnueva-Wendt, S., Dreibrodt, S., Fassbinder, J. W., Ostner, S., Madella, M., Pla-Rabes, S. & Out, W. (2019). **Prehistoric production of reddish ferrous pigments by burning processes – a new finding on Rapa Nui (Easter Island)**. In *Easter Island and the Pacific. Cultural and Environmental Dynamics*. Rapanui Press, Rapa Nui, 129-150.
- Fassbinder, J.W.E. , Hahn, S.E., Parsi, M. , Becker, F. , Wolf, M. , Gagosidze, I. & Kaniuth, K. (2021). **Persian Residences in the Southern Caucasus: Latest Discoveries in the Periphery of the Achaemenid Empire**. *Revue d’archéométrie*, 45, 117-127. doi: 10.4000/archeosciences.8404.
- Fassbinder, J.W.E. , Becker, F. , Hahn, S.E. & Parsi, M. (2021). **Archaeological Geophysics: Case Studies from Bronze Age/Iron Age Sites in the Alazani and Shiraki Plain, Kakheti, Georgia**. *Schriften des Archäologischen Museums Frankfurt am Main*, vol. 34, pp. 333-340, Schnell & Steiner, ISBN: 978-3-7954-3439-7, Editors: Liane Giemsch, Svend Hansen.
- Bondar, K. M. , Fassbinder, J.W.E. , Didenko, S.V. & Hahn, S.E. (2021). **Rock magnetic study of grave infill as a key to understanding magnetic anomalies on burial ground**. *Archaeological Prospection* 28, 1-18, doi: 10.1002/arp.1843.

## Abstracts

- Ostner, S., Fassbinder J. W. E., Parsi M. & Scheiblecker M. (2019). „**More than walking on a field and producing greyscale pictures**” – **Magnetometer Prospection in Archaeology**. In *79. Jahrestagung Deutsche Geophysikalische Gesellschaft Abstracts*.
- Ostner, S., Fassbinder J. W. E., Schauer M. & Gondet S. (2020). **Magnetic studies on PARADISE soils - searching for traces of the Achaemenids** In *80. Jahrestagung Deutsche Geophysikalische Gesellschaft Abstracts*.
- Hahn, S., Parsi, M., & Fassbinder, J. W. E. (2021, December). **Shallow Inclination in Archaeological Magnetometer Prospection-Theory and Case Examples of the two Ethio-Sabaeen Sites Yeha and Melazo (Ethiopia) at an inclination of 15°**. In *AGU Fall Meeting Abstracts* (Vol. 2021, pp. GP45F-05).
- Hahn, S. E., Schauer M., Fassbinder J. W. E. (2022). **Searching for a lost Achaemenid Palace – Magnetometer prospection, soil magnetism and pXRF analysis in Gumbati (Georgia) to decode a magnetic “ghost feature”**. In *17th Castle Meeting - New Trends on Paleo, Rock and Environmental Magnetism Book of Abstracts*.

## Attended Conference, Meetings, Training Schools

- Archaeological Geophysics Environmental & Criminal Forensics 2018
- 79. Jahrestagung Deutsche Geophysikalische Gesellschaft (2019) (oral participation)
- International Conference of Archaeological Prospection 2019 (oral participation)
- 80. Jahrestagung Deutsche Geophysikalische Gesellschaft (2020)
- Virtual Event: Recent Advances in Archaeological Geophysics 2021
- International Conference of Archaeological Prospection 2021(oral participation and poster presentation)
- AGU Fall Meeting 2022 (oral poster presentation)
- 3rd COST ACTION SAGA Training School: Magnetic Laboratory Methods in support of archaeo-geophysical research (2022)
- 17th Castle Meeting (2022) (poster presentation)
- Recent Advances in Archaeological Geophysics & Forensic Geoscience 2022 (oral participation)
- International Conference of Archaeological Prospection 2023 (poster presentation)



# Contents

<b>Preface</b>	<b>vii</b>
<b>List of Publications</b>	<b>ix</b>
<b>1 Introduction</b>	<b>1</b>
1.1 The anomalous anomaly . . . . .	2
1.2 The Earth's magnetic field . . . . .	3
1.2.1 Description of the Earth's magnetic field . . . . .	3
1.2.2 Sources and changes of the global field . . . . .	4
1.2.2.1 Internal field and secular variation . . . . .	4
1.2.2.2 External field and diurnal variation . . . . .	5
1.2.3 Implications for surveying . . . . .	6
1.3 The magnetic field of a body . . . . .	6
1.3.1 Magnetic Moment and Magnetisation . . . . .	7
1.3.2 Induced magnetisation . . . . .	7
1.3.3 Remanent magnetisation . . . . .	9
1.3.4 Königsberger Ratio . . . . .	10
1.3.5 Significance for prospecting . . . . .	10
1.4 Anomaly of a buried sphere . . . . .	11
1.5 The magnetogram . . . . .	13
1.5.1 Negative and positive anomalies . . . . .	13
1.5.2 Burial depth . . . . .	13
1.5.3 Monopole and dipole character . . . . .	14
1.6 Motivation and outline of the thesis . . . . .	14
<b>2 The methodology of magnetometer prospecting</b>	<b>17</b>
2.1 Survey Magnetometers . . . . .	17
2.1.1 Alkali-vapour optical pumped magnetometers . . . . .	17
2.1.2 Fluxgate gradiometers . . . . .	20
2.1.3 Further Instruments . . . . .	21
2.2 Survey method . . . . .	21
2.2.1 Instrument set-up . . . . .	21

2.2.2	Survey procedure . . . . .	22
2.3	Data processing . . . . .	24
2.3.1	Pre-processing . . . . .	24
2.3.2	Further processing . . . . .	24
2.4	Interpretation . . . . .	25
2.5	Comparison of total-field and gradiometer measurements . . . . .	26
2.5.1	Physical background . . . . .	26
2.5.1.1	Scalar magnetometer . . . . .	26
2.5.1.2	Vector magnetometer . . . . .	29
2.5.2	Advantages and disadvantages of the different devices . . . . .	29
2.6	Merging total-field magnetometer and gradiometer data . . . . .	30
<b>3</b>	<b>The Effect of Remanence</b>	<b>33</b>
3.1	Archaeological background of the area around Artanish . . . . .	34
3.2	Investigation methods . . . . .	35
3.3	Results of the magnetometer and susceptibility survey . . . . .	36
3.4	Comparison of magnetometry and DEM results . . . . .	36
3.5	Considerations regarding the direction of magnetisation . . . . .	40
3.6	Modelling the effect of the magnetisation direction . . . . .	41
3.7	Results of the modelling . . . . .	42
3.8	Conclusion for survey results . . . . .	43
3.9	The effect of remanence . . . . .	43
3.10	Deducing the remanence from a magnetogram . . . . .	45
<b>4</b>	<b>The Effect of the Earth's magnetic field</b>	<b>47</b>
4.1	Approach for modelling the effect of the direction of the geomagnetic field . . . . .	47
4.2	Effect of declination . . . . .	49
4.3	Effect of inclination . . . . .	51
4.4	Effect of shallow inclination . . . . .	53
4.4.1	Generating synthetic data . . . . .	53
4.4.2	Theoretical Results . . . . .	54
4.4.2.1	Inclination dependency . . . . .	54
4.4.2.2	Remanence effect . . . . .	54
4.4.2.3	Registered dipole anomaly for different instrument setups . . . . .	55
4.4.3	Prospecting method and data processing . . . . .	56
4.4.4	Results for the prospecting in Yeha and Melazo . . . . .	56
4.4.4.1	Comparison of measurement setups . . . . .	56
4.4.4.2	Spherical Features . . . . .	56
4.4.4.3	Linear Features . . . . .	58
4.4.5	Discussion . . . . .	60
4.4.6	Conclusion . . . . .	62

---

<b>5</b>	<b>The Case Study of Fara</b>	<b>63</b>
5.1	Introduction . . . . .	64
5.2	Method . . . . .	67
5.2.1	Selection of survey areas . . . . .	67
5.2.2	Instruments . . . . .	68
5.2.3	Data processing . . . . .	68
5.3	Results and Interpretation . . . . .	70
5.3.1	Area A . . . . .	70
5.3.2	Area B . . . . .	72
5.3.3	Area C . . . . .	73
5.3.4	Area D . . . . .	74
5.4	Discussion . . . . .	75
5.5	Conclusion . . . . .	79
<b>6</b>	<b>The case study of Yeha</b>	<b>81</b>
6.1	Introduction . . . . .	81
6.2	Methods . . . . .	84
6.2.1	Selection of the survey area . . . . .	84
6.2.2	Magnetometer survey . . . . .	86
6.2.3	Data processing . . . . .	87
6.3	Results and Interpretation . . . . .	87
6.3.1	Susceptibility measurements . . . . .	87
6.3.2	Yeha . . . . .	87
6.3.2.1	North the Great Temple . . . . .	87
6.3.2.2	West of the Great Temple . . . . .	91
6.3.2.3	Southwest of the Great Temple . . . . .	92
6.3.2.4	Southeast of the Great Temple . . . . .	94
6.3.3	Melazo . . . . .	95
6.4	Discussion . . . . .	98
6.5	Conclusion . . . . .	101
<b>7</b>	<b>The case study of Gumbati</b>	<b>103</b>
7.1	Introduction . . . . .	103
7.2	Geographical, geological and archaeological context . . . . .	104
7.2.1	Location and geologic background . . . . .	104
7.2.2	Archaeological background . . . . .	105
7.3	Magnetometry . . . . .	106
7.3.1	Method for magnetometer survey . . . . .	106
7.3.2	Interpretation of the survey areas . . . . .	106
7.3.2.1	Results of Gmb18A . . . . .	106
7.3.2.2	Results of Gmb18B . . . . .	108

---

7.3.2.3	Results of Gmb19 . . . . .	108
7.3.2.4	Results of Gmb21 . . . . .	108
7.4	Excavation results and sample selection . . . . .	110
7.4.1	Excavation results . . . . .	110
7.4.2	Soil profiles . . . . .	110
7.4.3	Sample collection and preparation . . . . .	111
7.5	pXRF and susceptibility analysis . . . . .	114
7.5.1	Portable X-ray fluorescence (p-XRF) analysis . . . . .	114
7.5.2	Soil chemistry of trench A and B . . . . .	114
7.5.3	Susceptibility measurements . . . . .	118
7.5.4	Susceptibility . . . . .	118
7.6	First attempts on Forward Modelling . . . . .	120
7.6.1	Source and field calculation . . . . .	120
7.6.2	Results of the modelling so far . . . . .	121
7.7	Summary and Discussion . . . . .	122
7.8	Conclusion . . . . .	125
<b>8</b>	<b>Conclusion and Perspectives</b>	<b>131</b>
	<b>Acknowledgements</b>	<b>138</b>
	<b>References</b>	<b>139</b>

# Chapter 1

## Introduction

Magnetic methods have become indispensable research tools for investigating archaeological sites. However, their potential has not yet been fully uncovered in the analysis of archaeological material and the characterisation of archaeological objects. Probably the first archaeologist to point out the potential capability of geophysics in locating archaeological structures was Robert du Mesnil du Buisson (Du Mesnil du Buisson, 1934) in a 1934 textbook which includes a note on magnetic methods (Hesse, 2000). The earliest works on the application of magnetic prospecting in an archaeological context are attributed to Belshé (1957) for the in-situ identification of kilns and to Aitken (1958) and Eduard Hall for the development and application of a device specifically for detection of archaeological features by their magnetic contrast (e.g. Asăndulesei et al., 2011)<sup>1</sup>.

Magnetometer prospecting is the mapping of the magnetic field at a survey area at a fixed height relative to the Earth's surface in a high spatial resolution. It is regarded as one of the most effective methods in archaeogeophysics or archaeological prospection, often referred to as its backbone (Wynn, 1986), for investigating large surface areas in relatively short periods of time due to the rapid data acquisition. Magnetometer prospecting is considered a passive method as it does not actively induce or introduce any artificial signal into the ground but instead resorts to the registration of the induced and remanent magnetic fields of the potential features (e.g. Kvamme et al., 2006). It fundamentally relies on the magnetic contrast between archaeological features and the surrounding environment. In addition, the size of the archaeological features to the measurement density, burial depth, magnetic noise, equipment sensitivity, and quality of the resulting data all influence the detection of archaeological features. Initially applied for geology and resource exploration, the technology was adapted and methodologies have been adjusted to investigate archaeological sites. Magnetometer prospecting in archaeology faces different challenges and questions than in geology and resource research, some of which I address in this thesis. However, before I go into more detail about this method, I would like to give an overview of some basic terms, relationships and properties of magnetism.

---

<sup>1</sup>An overview of the further history and developments of geophysical methods in archaeological prospection is given by Herbich (2015).

## 1.1 The anomalous anomaly<sup>2</sup>

During a magnetometer measurement in archaeological prospecting, the magnetometer device provides a value for the magnetic field  $\mathbf{B}$ , also called the magnetic flux density, measured in teslas. In the simplest case, one measures the superposition  $\mathbf{B}_m$  of the Earth's magnetic flux density  $\mathbf{B}_E$  and the magnetic flux density  $\mathbf{B}_O$  generated by an anomalous body (e.g. Militzer & Weber, 2013):

$$\mathbf{B}_m = \mathbf{B}_O + \mathbf{B}_E. \quad (1.1)$$

Scalar magnetometer or total-field magnetometer, which will be discussed in more detail in Chapter 2, measures the intensity or magnitude  $B_m$  of this vector sum, such that

$$B_m = |\mathbf{B}_O + \mathbf{B}_E|. \quad (1.2)$$

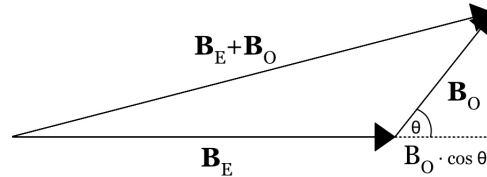


**Figure 1.1:** Vector sum of the magnetic field of the Earth and an anomalous body.

Generally in archaeological magnetometer prospecting, the results of mapping the magnetic flux density are given as the difference to a reference value. Subtracting a reference value from Eq. 1.2, one obtains the total-field anomaly:

$$B_A = |\mathbf{B}_O + \mathbf{B}_E| - B_{\text{ref}}. \quad (1.3)$$

The reference value corresponds to the intensity of the background magnetic field, also called normal field, which is primarily dominated by the Earth's magnetic flux density. As the contribution of the object's magnetic flux is several orders of magnitude lower than the Earth's magnetic field ( $|\mathbf{B}_O| \ll |\mathbf{B}_E|$ ), the sum of both values can be approximated by

$$|\mathbf{B}_O + \mathbf{B}_E| = |\mathbf{B}_E| + |\mathbf{B}_O| \cos \theta, \quad (1.4)$$

where  $\theta$  is the angle between  $\mathbf{B}_E$  and  $\mathbf{B}_O$  (see Fig. 1.1). If the reference value is the intensity of the Earth's magnetic field, the total-field anomaly is:

$$B_A = |\mathbf{B}_O + \mathbf{B}_E| - |\mathbf{B}_E| = |\mathbf{B}_O| \cos \theta. \quad (1.5)$$

That expression can be expressed with the help of the vector dot product:

$$B_A = |\mathbf{B}_O| \cos \theta = \mathbf{B}_O \cdot \frac{\mathbf{B}_E}{|\mathbf{B}_E|}. \quad (1.6)$$

Therefore, this approximation can be regarded as a projection of  $\mathbf{B}_O$  in the direction of the Earth's magnetic field  $\mathbf{B}_E$ .

<sup>2</sup>Based on teaching material of Francis Jones (F. Jones, 2007) who taught at the Department of Earth, Ocean and Atmospheric Sciences at the University of British Columbia. Unfortunately, his lecture material is no longer available online.

## 1.2 The Earth's magnetic field

It is William Gilbert who first introduced the idea of a magnetic field emanating from the Earth itself in his work "De Magnetite". The directional force of the geomagnetic field was used for navigation as early as 1000 AD (e.g. Hummel, 1963). If a magnetic needle, which was made of lodestone in ancient times, can swing freely in all directions without the influence of gravity, it aligns itself along the direction of the Earth's magnetic field. In any other direction, it experiences a torque that forces it to align precisely along this direction.

### 1.2.1 Description of the Earth's magnetic field

The Earth's magnetic flux density can be expressed as a field vector at any point in space by stating direction and intensity. Seven characteristic values, also called magnetic elements, are used to define and describe the Earth's local magnetic field (see Tab. 1.1 and Fig. 1.2.1). The individual elements can be converted into each other (see for example Butler, 1992).

**Table 1.1:** *Magnetic elements: characteristic values of the Earth's local magnetic field.*

parameter	symbol
total intensity of the field	$F$
component in geographic north direction	$X$
component in geographic east direction	$Y$
vertical component (positive downwards)	$Z$
horizontal component	$H$
inclination	$I$
declination	$D$
latitude	$\Phi$

The Earth's magnetic field can be expressed with its Cartesian components along geographic north ( $X$ ) and east directions ( $Y$ ) as well as the vertical ( $Z$ ):

$$\mathbf{B}_E = \begin{pmatrix} X \\ Y \\ Z \end{pmatrix}. \quad (1.7)$$

The vector can also be expressed by the total field intensity ( $F$ ), the declination ( $D$ ) and the inclination ( $I$ ). The two angles  $D$  and  $I$  are defined by the horizontal projection  $H$  of the vector  $\mathbf{B}_E$  onto the  $X - Y$ -plane (see Fig. 1.2.1 a). The declination  $D$ , or variation, is the angle of the horizontal  $H$  relative to the geographic north direction. The inclination  $I$ , also known as the magnetic dip, describes the deflection of the vector from the horizontal. With these magnetic elements, the local magnetic field can be expressed by

$$\mathbf{B}_E = F \begin{pmatrix} \cos I \cos D \\ \cos I \sin D \\ \sin I \end{pmatrix}. \quad (1.8)$$

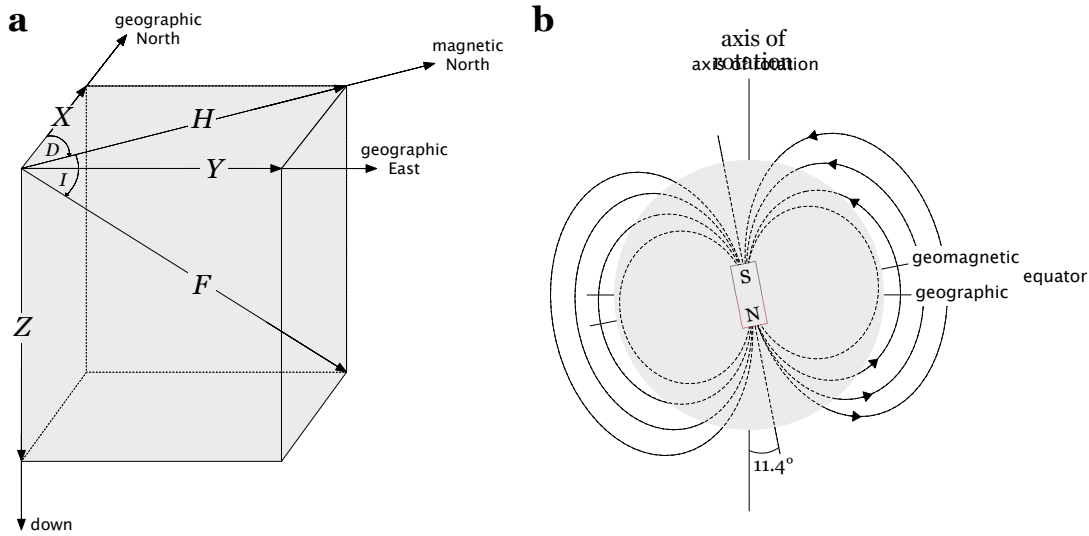


**Figure 1.2:** a) *Magnetic elements (after Soffel, 1991) in the common frame of reference, which is used to describe the Earth's local magnetic field.* b) *Earth's magnetic field as an approximation of a dipole field generated by a rotating, uniformly magnetised sphere whose magnetic properties can be represented by a bar magnet resting inside the Earth.*

From this expression, the normalised vector can be obtained by the relationship

$$\frac{\mathbf{B}_E}{|\mathbf{B}_E|} = \begin{pmatrix} \cos I \cos D \\ \cos I \sin D \\ \sin I \end{pmatrix} \quad (1.9)$$

where  $|\mathbf{B}_E| = F$ .

## 1.2.2 Sources and changes of the global field

The Earth's magnetic field is a superposition of fields from different sources. These are divided into internal and external sources, which generate the internal and external parts of the Earth's magnetic field. At the Earth's surface, the internal field is the dominant contribution of the global field.

### 1.2.2.1 Internal field and secular variation

The internal field is primarily the result of the movement of the electrically conducting iron and nickel alloy composing the Earth's liquid outer core. The heat flow from the inner core causes the outer core to convect. At the same time, the liquid metal is forced into helical rotation by the Coriolis force, which acts on the moving material due to the rotation of the Earth. The magnetic field generated by these electrical currents is known as the main field and accounts for around 95% of the global field. Its strength is between 20000 nT and 60000 nT, increasing towards the poles. An almost negligible part (up to 200 nT) of the internal field is due to the quasi-stable crust field generated by the magnetisation of the surface rock.

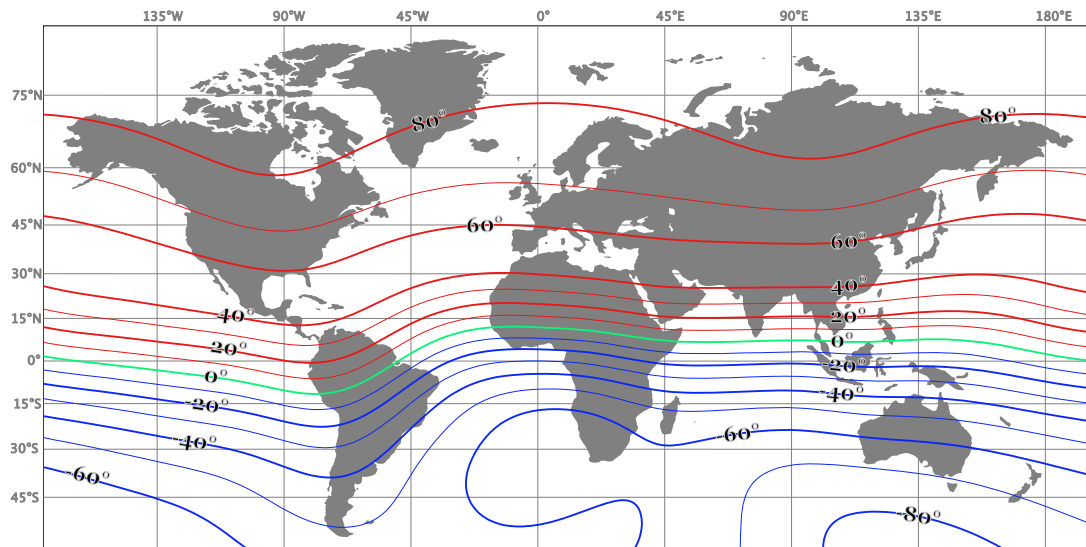


**Figure 1.3:** Miller projection of the main field's inclination. Edited map from Chulliat et al. (2020). For further maps, also see <https://www.ngdc.noaa.gov/geomag/WMM/image.shtml>.

Near the surface, the Earth's magnetic field can be simplified and closely approximated by a dipole field generated by a rotating, uniformly magnetised sphere whose magnetic properties can be represented by a bar magnet resting inside the Earth (see Fig. 1.2.1 b). If this bar magnet's axis coincides with the rotation axis, one speaks of a geocentric axial dipole. In this case,  $D = 0$  and the inclination is linked to the geographic latitude by:

$$\tan I = 2 \tan \Phi. \quad (1.10)$$

At the moment, this fictitious dipole is not located at the centre of the Earth, but about 500 km off-centre in the direction of New Guinea and its axis is misaligned by almost  $12^\circ$  to the Earth's axis (Lanza & Meloni, 2006). The dipolar field accounts for around 85 % of the global field at most locations. To get a more accurate picture, one must also consider the non-dipole contributions of the internal field. A map of the inclination illustrates the resulting more complex spatial variation of the components (see Fig. 1.3). Changes in the global field occur on time scales ranging from milliseconds to millions of years, called the secular variation. Changes of one year or more are seen as proxies for the core field and, thus, for changes in the geodynamo.

### 1.2.2.2 External field and diurnal variation

The external part of the total field is generated by currents in the ionosphere and magnetosphere. The causes are, on the one hand, the interaction of the magnetosphere with the magnetised plasma of the solar wind; on the other hand, induced currents in the ionosphere or wind moving its ionised particles. Collectively, these are the main contributors to the diurnal variations in the Earth's magnetic field. How strong these daily fluctuations are depends mainly on the latitude, which ranges around 100 nT from the baseline on quiet days without a magnetic storm.

### 1.2.3 Implications for surveying

In summary, the global field is subject to temporal and spatial changes, which applies to the magnetic field measured at the Earth's surface. Therefore, these changes can play a role in areal magnetometer prospection, and in particular, the variation of the intensity of magnetic flux density must be considered when choosing a reference value. The intensity of the background field is the sum of all global sources. Changes in the internal and external fields that exceed the measurements' time frame can be considered constant. The decisive factor is the correction of the diurnal variation. Various survey magnetometer set-ups intrinsically compensate for these fluctuations, but non-referenced total-field magnetometers do register these variations. In archaeological prospecting, it is usually sufficient to assume discrete changes of the reference value in small measuring sections (e.g. areas of 40 m by 40 m, or one 40 m line which takes around 40 s). Exceptions are high variations in the external field caused by solar storms. The periods of these fluctuations can be less than 40 s, the time required for the smallest measuring section and cannot be removed by assuming discrete changes. The rapid variations in the intensity of the external field can exceed the range of archaeological anomalies. In the worst case, the measurements must be repeated on a quieter day. Directional fluctuations in the Earth's magnetic field are generally not considered and have not caused any problems, as this has not yet been recorded in the literature. However, the direction of the internal field at the survey location significantly influences the anomalous anomaly, which I will discuss further in Chapter 4.

## 1.3 The magnetic field of a body<sup>3</sup>

An expression for the vector potential  $\mathbf{A}(\mathbf{r})$  for a magnetic dipole can be derived from classical electrodynamics:

$$\mathbf{A}(\mathbf{r}) = \frac{\mu_0}{4\pi r} \left( \frac{\mathbf{m} \times \mathbf{r}}{r^2} \right). \quad (1.11)$$

Therefore, the magnetic flux density  $\mathbf{B}(\mathbf{r})$  is:

$$\mathbf{B}(\mathbf{r}) = \nabla \times \mathbf{A} = \frac{\mu_0}{4\pi} \left( \frac{3\mathbf{r}(\mathbf{m} \cdot \mathbf{r})}{r^5} - \frac{\mathbf{m}}{r^3} \right), \quad (1.12)$$

with  $\mathbf{m}$  the magnetic moment of the object which generates the magnetic field and  $\mathbf{r}$  the position vector, which expressed in Cartesian coordinates, is:

$$\mathbf{r} = \begin{pmatrix} x \\ y \\ z \end{pmatrix}. \quad (1.13)$$

---

<sup>3</sup>For introductory reading on rock magnetism I recommend Butler (1992) or Tauxe (2010). For a more advanced reading O'Reilly (2012) or Dunlop and Özdemir (2001). For an introduction to environmental magnetism I suggest Evans and Heller (2003). For advanced reading on soil magnetism I recommend Jordanova (2016).

### 1.3.1 Magnetic Moment and Magnetisation

The magnetic moment  $\mathbf{m}$  in  $\text{Am}^2$  is defined, such that:

$$\mathbf{m} = \iiint \mathbf{M} dV. \quad (1.14)$$

Thus, the magnetic moment is determined by the volume  $V$  in  $\text{m}^3$  of a body and its magnetisation  $\mathbf{M}$  measured in  $\text{A/m}$ . For uniform magnetised bodies, this simplifies to

$$\mathbf{m} = \mathbf{M}V \quad (1.15)$$

with

$$\mathbf{M} = M \cdot \begin{pmatrix} \cos \alpha \cos \delta \\ \cos \alpha \sin \delta \\ \sin \alpha \end{pmatrix} \quad (1.16)$$

where  $\alpha$  is the angle between the horizontal and the magnetisation and  $\delta$  is the angle between magnetic North and the magnetisation.

The magnetisation can be regarded as a vector field that reflects the sum of permanent and induced magnetic dipole moments  $\mathbf{p}_m$  per volume unit (see e.g. Demtröder, 2004). The source of these magnetic dipole moments is either the movement of electrons in atoms or the spin of the nuclei or electrons. Therefore, the magnetisation can also be expressed with

$$\mathbf{M} = \frac{1}{V} \sum_V \mathbf{p}_m \quad (1.17)$$

if individual dipole moments are regarded. The total magnetisation  $\mathbf{M}$  of a body is the vector sum

$$\mathbf{M} = \mathbf{M}_r + \mathbf{M}_i \quad (1.18)$$

of the induced  $\mathbf{M}_i$  and remanent magnetisation  $\mathbf{M}_r$ .

While magnetic susceptibility surveys are only relying on a difference in susceptibility, magnetometer prospecting is based on a difference in total magnetisation (see e.g. Schmidt, 2007). That is why the magnetic contrast should be correctly termed magnetisation contrast in magnetometer prospecting. The contrast in total magnetisation results from a difference in either the induced magnetisation, remanence or both.

### 1.3.2 Induced magnetisation<sup>4</sup>

The induced magnetisation  $\mathbf{M}_i$  is the magnetisation of an object induced by an ambient magnetic field. Without the presence of an ambient magnetic field, the induced magnetisation is zero.

---

<sup>4</sup>This section and the following one are deliberately kept short, as a detailed introduction to rock magnetism, mineralogy and magnetisation processes for magnetometric prospecting has already been written and summarised by numerous authors. This introduction is only intended to briefly introduce the most important terminology. For a more detailed description of these terms and how they relate to magnetometer prospecting, please refer to N. T. Linford (2003) Chapter 1 and 2 and Górká (2009) Chapter 4, among others.

For sufficiently small magnetisation fields, the magnetisation is proportional to the magnetising field  $\mathbf{H}_i$  such that

$$\mathbf{M}_i = \chi \cdot \mathbf{H}_i \quad (1.19)$$

where  $\chi$  is the magnetic susceptibility. For most rocks and minerals, an isotropic susceptibility can be presumed, which is postulated in equation 1.19. In this case, the direction of the induced magnetisation is (anti-)parallel to the inducing field  $\mathbf{H}_i$ . In the more general case (i.e. anisotropic material),  $\chi$  is to be regarded as a tensor, which means that the induced magnetisation is in general not (anti-)parallel to the inducing field.

The property of acquiring a magnetisation when a material is exposed to an ambient magnetic field is inherent to all matter. Materials are categorised according to the sign and value of their magnetic susceptibility, which reflects their dominant form of magnetism (e.g. Demtröder, 2004):

$$\left. \begin{array}{l} \text{diamagnetic materials: } \chi < 0 \\ \text{paramagnetic materials: } \chi > 0 \end{array} \right\} |\chi| \ll 1$$

$$\left. \begin{array}{l} \text{ferromagnetic materials: } \\ \text{ferrimagnetic materials: } \end{array} \right\} \chi > 0 \left. \vphantom{\begin{array}{l} \text{ferromagnetic materials: } \\ \text{ferrimagnetic materials: } \end{array}} \right\} |\chi| \gg 1$$

In details this depends on the behaviour of the magnetic dipoles present in a material (e.g. Bender, 1985; Demtröder, 2004):

- **diamagnetism** Diamagnetic materials do not have a permanent magnetic dipole moment. When such materials are placed in a magnetic field, the moving electrons orbiting the nucleus generate a magnetic field that is opposite to the inducing field (Lenz's law). Although this effect occurs in all materials, as it only contributes very weakly to magnetism, only materials that do not exhibit any other form of magnetism are described as diamagnetic. Their susceptibility is also independent of temperature. The majority of non-iron bearing minerals, water and most plastics are diamagnetic.
- **paramagnetism** Atoms or ions of paramagnetic materials have unpaired electrons that generate atomic magnetic moments that do not interact, and their orientations are distributed over all spatial directions without an external magnetic field due to thermal (Brownian) motion.
- **ferromagnetism** Ferromagnetic minerals are those in which there is an exchange reciprocal interaction between ions with a magnetic moment that can align adjacent moments in parallel.
- **antiferromagnetism** For these materials, except that adjacent moments are antiparallel. In an ideal case, their net magnetisation is zero. In minerals, these moments are often canted to each other, allowing a small net magnetisation.
- **ferrimagnetism** Here, the dipole moments are also anti-parallel, but their strength differs, resulting in a net magnetisation.

A difference in induced magnetisation can often be the reason for a magnetisation contrast. It plays a significant role, especially when the material in question has little or no remanence magnetisation. The enrichment of the topsoils magnetisation is commonly

known (e.g. Tite & Mullins, 2007), but this effect is insofar essentially for detecting fill ditches, pits of various kinds, palisades or postholes (Fassbinder, 2015). The topsoil with the enhanced susceptibility fills these surface regularities, which reach into layers with a lower susceptibility. Hence, the area of their previous location has more magnetic material and has, therefore, a magnetisation contrast to the surrounding undisturbed soil. Also, residual ash layers of fire pits and hearths exhibit a higher susceptibility than the surrounding soil (McClellan & Kean, 1993). A variation in magnetic susceptibility in building material, which has not acquired any remanence, can influence contrast to the background field. Becker and Fassbinder (1999) give an illuminating example that mud brick walls, which have a very low remanent magnetisation, can show either a positive or negative magnetisation contrast to the ambient sediment depending on their susceptibility. In some cases, these variations are so specific that the susceptibility can determine the province of origin of these materials, e.g., the quarry of granite columns of ancient Rome buildings (Williams-Thorpe, Jones, Tindle, & Thorpe, 1996).

### 1.3.3 Remanent magnetisation

The remanent magnetisation is the part of the total magnetisation which can still be immanent in a material without the presence of an ambient field. This property is not present in dia- and paramagnetic materials and only limitedly to ferro-, ferri- and antiferromagnetic materials. Natural materials hold a remanence which is called natural remanent magnetisation (NRM) which can be acquired through different processes and combination of them. There are various mechanism how a material can acquire a remanent magnetisation, the most important ones for archaeological prospecting are (e.g. Fassbinder, 2015; Schmidt, 2007):

- **Thermoremanent magnetisation (TRM)** A material acquires a thermoremanent magnetisation if it is cooled in an ambient magnetic field and crosses the interval of the Curie temperature to the blocking temperature. Normally, the direction of the thermoremanence is parallel to the ambient field present during the acquisition. In a magnetic field in the range of the intensity of the Earth's magnetic field, the acquired intensity of the magnetisation is proportional to the magnetising field.
- **Detrital remanent magnetisation (DRM)** occurs when sufficiently small magnetic mineral grains are deposited in calm water. Their magnetic moments acquire a preferred direction parallel to the Earth's magnetic field as they subside, and this direction is maintained to a certain extent even when the sediment consolidates.
- **Chemical remanent magnetisation (CRM)** occurs when magnetic grains grow, or when magnetic material is produced by chemical processes or phase changes below their Curie temperature in an ambient field.
- **Isothermal remanent magnetisation (IRM)** is the magnetisation that a material acquires without the aid of temperature changes but solely through changes in the ambient field.
- **Lightning-induced remanent magnetisation (LiRM)** is a special case of the IRM. Lightning strikes introduced high currents and, therefore, high magnetic fields in the impacted rocks, sediments or soils, producing an anomalously high remanence (Burks, Viberg, & Bevan, 2015; Maki, 2005).

The greatest contribution to a magnetisation contrast is the acquisition of thermal remanence. When firing kilns and furnaces, the firing temperature exceeds the Curie temperature of the magnetite and maghemite present in the clay material of the walls and floors (Aitken, 1974). When cooled below the Curie temperature (or blocking temperature), they acquire a (partial) thermoremanence that aligns with the current geomagnetic field. The same applies to fired bricks and pottery, which is why the latter in particular are used for archaeomagnetism, but also for any other material that - intentionally or unintentionally - has been excessively heated. The in-situ remanence acquisition and continuance in place is why kilns and furnaces are so distinct in magnetograms. Pottery sherds and brick walls show weaker anomalies as their individual vectors of magnetisation point in any direction, resulting in an overall smaller intensity (Bevan, 1994). Additionally, weakly magnetic minerals such as haematite or goethite may transform into stronger magnetic iron oxides. Strictly speaking, if this process happens below the Curie temperature of the newly formed minerals, it would be a case of chemical remanence. Detrital remanence is considered to have a rather weak effect compared to other magnetisation contrast contributors. It can cause detectable anomalies if there is a lack of DRM after excavating a site. The DRM inherited in the sediment is destroyed by mixing the sediment layers and their original layering. Mud bricks are suspected of acquiring a remanence similar to a DRM when the wet clay is pushed into moulds during production (Herbich & Zych, 2003). What is known is that mud bricks and baked bricks have a magnetic fabric (Hus, Ech-Chakrouni, & Jordanova, 2002; Hus, Ech-Chakrouni, Jordanova, & Geeraerts, 2003; Tema, 2009). Anomalies generated by a lightning-induced remanence show exceedingly high intensities and are also often recognisable by their star-shaped form (G. Jones & Maki, 2005; Bevan, 1995).

### 1.3.4 Königsberger Ratio

The Königsberger ratio (Koenigsberger, 1932)  $Q$  describes the ratio

$$Q = \frac{|\text{NRM}|}{|M_i|} \quad (1.20)$$

of natural remanent magnetisation to the induced magnetisation. It provides an idea to which degree both magnetisations affect the total magnetisation. This accounts for its intensity as well as the direction of the magnetisation. For  $Q \ll 1$ , the total magnetisation is dominated by the induced magnetisation, and therefore, it is sub-parallel or anti-parallel to the geomagnetic field. For  $Q \gg 1$ , the total directions are dominated by the remanence and is, therefore, sub-parallel to the remanence.

### 1.3.5 Significance for prospecting

As stated in the previous section, the magnetisation of rocks, sediments, soils and objects made of these materials, e.g. archaeological artefacts, is the sum of induced and remanent magnetisation. It is clear from the discussion of the Königsberger ratio that the direction of the total magnetisation is not necessarily parallel to the geomagnetic field. However, it must be assumed that it points in any direction. The bodies encountered in magnetometer prospecting are usually not homogeneously magnetised but show considerable inhomogeneities in their magnetisation and are irregularly shaped; therefore, the shape anisotropy of the magnetisation and its magnetic field are not neglectable. With increasing prospecting distance to the body, the amplitudes contributed by the inhomogeneities and

irregularities with small-scale features decrease quicker than the ones of the more broad-scale features (Breiner et al., 1973). Since in archaeological magnetometer prospection, the distance to the bodies of interest is rather small, this attenuation of the small-scale features does not happen, which can complicate the interpretation, but the effect is also unavoidable as archaeological features are rather small-scale. That is why one has to be aware that the magnetic field emitted by archaeological features can only limitedly be compared to model bodies. In the interpretation of magnetograms in archaeological prospection, the focus is the variation of the strength in magnetisation to the reference value and the shape of the anomaly. I will discuss in chapter 3 how the magnetisation direction impacts the anomaly of bodies.

## 1.4 Anomaly of a buried sphere

Starting with the expression found in section 1.1,

$$B_A = |\mathbf{B}_O| \cos \theta = \mathbf{B}_O \cdot \frac{\mathbf{B}_E}{|\mathbf{B}_E|}$$

the magnetic flux density of a buried sphere with its own field generated by the remanent and the induced magnetisation in an ambient field can be calculated. With the equation 1.9 the direction of the Earth's magnetic field can be expressed by its declination and inclination. The magnetic flux density of a dipole can be calculated with 1.12. In case of a uniform magnetised sphere with radius  $a$  the magnetic moment is given by

$$\mathbf{m} = \mathbf{M} \frac{4\pi a^3}{3}. \quad (1.21)$$

With the direction of magnetisation (see equation 1.3.1) one obtains for the anomaly of a buried sphere:

$$B_A = \frac{\mu_0}{4\pi} M \frac{4\pi a^3}{3} \left( \frac{3}{r^5} \begin{pmatrix} x \\ y \\ z \end{pmatrix} \left[ \begin{pmatrix} \cos \alpha \cos \delta \\ \cos \alpha \sin \delta \\ \sin \alpha \end{pmatrix} \cdot \begin{pmatrix} x \\ y \\ z \end{pmatrix} \right] - \frac{1}{r^3} \begin{pmatrix} \cos \alpha \cos \delta \\ \cos \alpha \sin \delta \\ \sin \alpha \end{pmatrix} \right) \cdot \begin{pmatrix} \cos I \cos D \\ \cos I \sin D \\ \sin I \end{pmatrix} \quad (1.22)$$

with  $r^2 = x^2 + y^2 + z^2$ . This can be rewritten to:

$$B_A = -\frac{\mu_0}{4\pi} M \frac{4\pi a^3}{3} \frac{Ax^2 + By^2 + Cx + Dy + E + F}{(x^2 + y^2 + z^2)^{5/2}} \quad (1.23)$$

with

$$\begin{aligned} A &= \sin \alpha \sin I - 2 \cos \alpha \cos \delta \cos I \cos D + \cos \alpha \sin \delta \cos I \sin D \\ B &= \sin \alpha \sin I + \cos \alpha \cos \delta \cos I \cos D - 2 \cos \alpha \sin \delta \cos I \sin D \\ C &= -3z(\sin \alpha \cos I \cos D + \cos \alpha \cos \delta \sin I) \\ D &= -3z(\sin \alpha \cos I \sin D + \cos \alpha \sin \delta \sin I) \\ E &= z^2(\cos \alpha \cos \delta \cos I \cos D + \cos \alpha \sin \delta \cos I \sin D - 2 \sin \alpha \sin I) \\ F &= -3xy \cos \alpha \cos I (\sin \delta \cos D + \cos \delta \sin D) \end{aligned}$$

with considering a coordinate system transformation with  $z = -z$ . Note  $F = 0$  because

of the symmetry of the magnetic field.

Considering  $D = 0$  thus yields the expression noted by Murthy (1974):

$$B_A = -\frac{\mu_0}{4\pi} M \frac{4\pi a^3}{3} \frac{Ax^2 + By^2 + Cx + Dy + E}{(x^2 + y^2 + z^2)^{5/2}} \quad (1.24)$$

with

$$\begin{aligned} A &= \sin \alpha \sin I - 2 \cos \alpha \cos \delta \cos I \\ B &= \sin \alpha \sin I + \cos \alpha \cos \delta \cos I \\ C &= 3z(\cos \alpha \cos \delta \sin I + \sin \alpha \cos I) \\ D &= 3z(\cos \alpha \sin \delta \sin I) \\ E &= z^2(\cos \alpha \cos \delta \cos I - 2 \sin \alpha \sin I) \end{aligned}$$

If the direction of magnetisation of the body is parallel to the geomagnetic field one derives the formula stated by Tite (1966). For that

$$\alpha = I \quad (1.25)$$

and

$$\delta = 0. \quad (1.26)$$

That simplifies equation 1.24 to:

$$B_A = -\frac{\mu_0}{4\pi} M \frac{4\pi a^3}{3} \frac{Ax^2 + By^2 + Cx + Dy + E}{(x^2 + y^2 + z^2)^{5/2}} \quad (1.27)$$

with

$$\begin{aligned} A &= \sin^2 I - 2 \cos^2 I \\ B &= \sin^2 I + \cos^2 I \\ C &= 6z \cos I \sin I \\ D &= 0 \\ E &= z^2(\cos^2 I - 2 \sin^2 I) \end{aligned}$$

with

$$\begin{aligned} \sin^2 I - 2 \cos^2 I &= 1 - 3 \sin^2 I \\ \cos^2 I - 2 \sin^2 I &= 1 - 3 \cos^2 I. \end{aligned}$$

With giving  $x$  and  $y$  in units of the burial depth  $z$

$$\begin{aligned} x &= x/z \\ y &= y/z \end{aligned}$$

one obtains:

$$B_A = -\frac{\mu_0}{4\pi} \frac{4\pi a^3}{3} \frac{M}{d^3} \frac{(1 - 3 \sin^2 I)x^2 + y^2 + 6x \cos I \sin I + (1 - 3 \cos^2 I)}{(x^2 + y^2 + 1)^{5/2}}. \quad (1.28)$$

These formulas are used for generating synthetic magnetograms in the following chapters.

## 1.5 The magnetogram

The magnetogram provides an image map of the intensity deviation from the background field at a defined height over a certain area. Also, a deviation from the direction is indirectly measurable in the intensity distribution (which I will discuss in Chapter 3). In other words, an anomaly represents a local disturbance from the reference value. The reference value reflects the background field. It is dominated by the Earth's magnetic field, but large-scale magnetic features like a broad uniform magnetic surface are also contributing. If a feature and its surroundings are equally magnetised, it will not exhibit any magnetic anomaly as there is no local change in magnetisation. A variation in magnetisation, however, will be perceptible as a positive or negative anomaly depending on the geomagnetic latitude as well as the degree of distortion the total magnetic field of the object experiences from the geomagnetic field (further details in Chapter 3 and 4).

### 1.5.1 Negative and positive anomalies

It is crucial to understand what negative and positive anomalies mean in the context of a magnetogram. For the northern hemisphere, a positive anomaly means an intensity higher than the reference value, while a negative value means an intensity lower than the reference value. I listed multiple reasons above for an enhancement in magnetisation contrast, which is usually the cause of a positive anomaly. In archaeological prospecting, these can be the refill of postholes, palisade holes, pits and ditches which enriched topsoil, ash layers or any increase in susceptibility so that the induced magnetisation generates a field of higher intensity above the background field. Every structure with a strong remanence is usually detectable, above all fired features, and shows partly positive anomalies. Geomagnetic latitude and whether the feature has a dipole character dictates if it also shows a related negative anomaly. A negative anomaly does not necessarily mean that the material in question is diamagnetic. Though it is true that limestone and sandstone are often weaker in magnetic susceptibility than their surroundings, their often diamagnetic nature is not predominantly the reason for their negative anomaly but their negative contrast to the surroundings. Excavation pits and trenches refilled with the same material also usually show a negative anomaly as their DRM is demagnetised during the excavation and refilling processes. Chemical processes can partially dissolve ferrimagnetic particles, for example, in water-logged soil so that the affected area contains magnetic minerals with a lower total magnetisation. The complexity of an anomaly is also attributable to its magnetisation intensity, direction of magnetisation, shape and dimension. Some of these factors also decide if the feature shows an anomaly with a monopole, dipole character or a variation of these two.

### 1.5.2 Burial depth

The burial depth, or better, the distance between the magnetometer and the body, plays a significant role in the characteristics of its anomaly. The deeper the burial depth, the broader the anomaly, but also a considerable decrease in signal intensity. The width of the anomaly is also important when someone looks at the wavelength in a magnetogram, which impacts whether the features are detectable with vector gradiometers.

### 1.5.3 Monopole and dipole character

Though magnetic monopoles do not exist in the classic macroscopic nature, magnetograms show anomalies which cannot be associated with a true dipole character. Hence, not all assemblies of induced or permanent dipoles in a body can be approximated as magnetic dipoles. Shape, dimension, burial depth of the anomalous body, and the geomagnetic latitude define the applicability of an approximation (e.g. Breiner et al., 1973). A point dipole approximation is valid for a body whose shape is close to a sphere. If the body's width is small compared to its extent into depth and with an elongation along its magnetisation, its anomaly will instead have a monopole character. A vertical sheet can be approximated as a line of monopoles for high magnetic latitudes, while it shows more dipole character for low magnetic latitudes. Usually, while a dipole approximation works for bodies with a limited extent of depth, a line of dipoles needs to be considered for horizontal cylinders. Smellie (1956) provides expressions for total magnetic intensity anomalies and some profiles for these approximations.

## 1.6 Motivation and outline of the thesis

The primary motivation to conduct magnetometer prospecting in archaeology is the large-scale investigation of archaeological sites and gaining new insights into their outline, organisation and structure. Various parameters and factors contribute to a successful and reliable interpretation. Three of them are the main protagonists in the following chapters. The thesis concludes with three detailed case studies that show the interplay of multiple factors, conditions, and challenges.

- I first introduce the functioning of various field magnetometers, the methodology of magnetometer surveys, and the data processing as carried out in the case studies of this thesis. Starting with comparing scalar magnetometers and vector gradiometers, focusing on their different physical output values, I then present an alternative method to merge their results into a visually uniform magnetogram.
- As shown in the previous section, the anomaly of a buried body also depends on the direction of its magnetisation. Preambled by a case study of a burial site at the Artanish peninsula, I discuss the effect of the total magnetisation direction on synthetic magnetograms and address the effect of remanence on anomaly patterns.
- Another factor affecting the anomaly of a buried body is the direction of the geomagnetic field at the survey site. The effect of declination and inclination is discussed on synthetic magnetograms. The focus is on prospecting at an isocline of  $15^\circ$ . I show and discuss how such a shallow inclination influences the anomaly patterns, what this means for the characterisation and detectability of features, and which magnetometer setup and image processing step are best suitable using synthetic magnetograms and data collected in Ethiopia.
- Ancient Šuruppak, today Fara in Iraq, was first explored by the Deutsche Orient-Gesellschaft in the years 1902 and 1903 and became again a target for research in the FARSUP project, which was accompanied by a magnetometer survey in 2018, the results of which I present here. Challenged by thousands of deep looting pits covering the majority of the mound, which not only destroyed its upper metres but also made the application of geophysical prospecting methods and their interpretation more difficult, the case study is nevertheless a unique example of how large-scale

prospection techniques can provide answers to a hundred-year-old question and new insights into an already investigated excavation site, even though the survey only lasted a couple of days. I interpret the magnetograms obtained and compare my results in detail to the descriptions and drawings of the 1902/1903 investigations.

- The magnetometer survey at the settlement Yeha and the hamlet Melazo, two cultural sites with an Ethio-Sabaeen background located in the Tigray high plateau in the north of Ethiopia, had the primary objective to gain new insights into the Ethio-Sabaeen architecture and the extent of both sites at this period. It turned out that the results are a superposition and combination of anomalies of a highly magnetic geology, magnetic rocks on the surface of the survey areas, field boundaries and other agricultural features, modern buildings and installations and anthropological traces. In the interpretation of the collected magnetic data over two campaigns, I try to name and associate all anomalies in the magnetogram to factor out all non-anthropogenic traces to allow conclusions about the buried and yet uncovered archaeology. I have deliberately chosen to make the interpretation comprehensive and detailed so that the case study can be an example of how to decipher the amalgamation of different anomalies.
- The original aim of the magnetometer survey in Gumbati (Georgia) was to rediscover the old excavation trenches and search for structures and features associated with the "palace" discovered during the campaigns in the mid-1990s. Although the results were inconclusive, excavation began at the locations that showed suspicious anomalies in the magnetogram. The excavation results were similarly disillusioning, and, above all, no cause for the anomalies detected by magnetometry was found. Therefore, I expanded the case study by initiating a subsequent pXRF analysis and carried out magnetic susceptibilities measurements of soil samples from vertical profiles of the excavation trenches, which might give an explanation for the „ghost feature“.



## Chapter 2

# The methodology of magnetometer prospecting

For mapping the magnetic flux density of buried objects, whether they are of geological, environmental, archaeological or modern origin, an exciting magnetising field is advantageous. In archaeological prospecting, the local geomagnetic field takes over this role. The superposition of the magnetic flux density due to the induced and remanent magnetisation of buried objects and the geomagnetic field is measured during magnetometer prospecting. As this approach does not require any further magnetic excitation, it is called a passive detection method. In the following, I will expand on the functioning of the magnetometers we use in our group, explain the surveying method, give a brief introduction to the steps of data-processing and interpretation, elaborate on the differences between total-field magnetometer and vector gradiometer and show how data sets of these two devices can be merged.

### 2.1 Survey Magnetometers

Broadly speaking, instruments for magnetometer prospecting are divided into scalar and vector instruments. In the following, alkali vapour magnetometers are presented as an example of a scalar instrument and fluxgate gradiometers as an example of vector instruments.

#### 2.1.1 Alkali-vapour optical pumped magnetometers<sup>1</sup>

The principle of operation of alkali-vapour instruments, including the Geometrics and Scintrex magnetometers used in our group, is based on quantum-mechanical properties of atoms, various electromagnetic phenomena and characteristic values of alkali group elements, whose members each have one valence electron per atom. Their valence electron orbits the nucleus on a specific subshell on the outer electron shell, depending on its energy. Generally, it can be elevated from a ground state  $E_i$  to a specific excited state  $E_j$  with a discrete excitation energy (see Fig. 2.1).

---

<sup>1</sup>This section is based on Aspinall, Gaffney, & Schmidt, 2009 and Gröger, 2005.

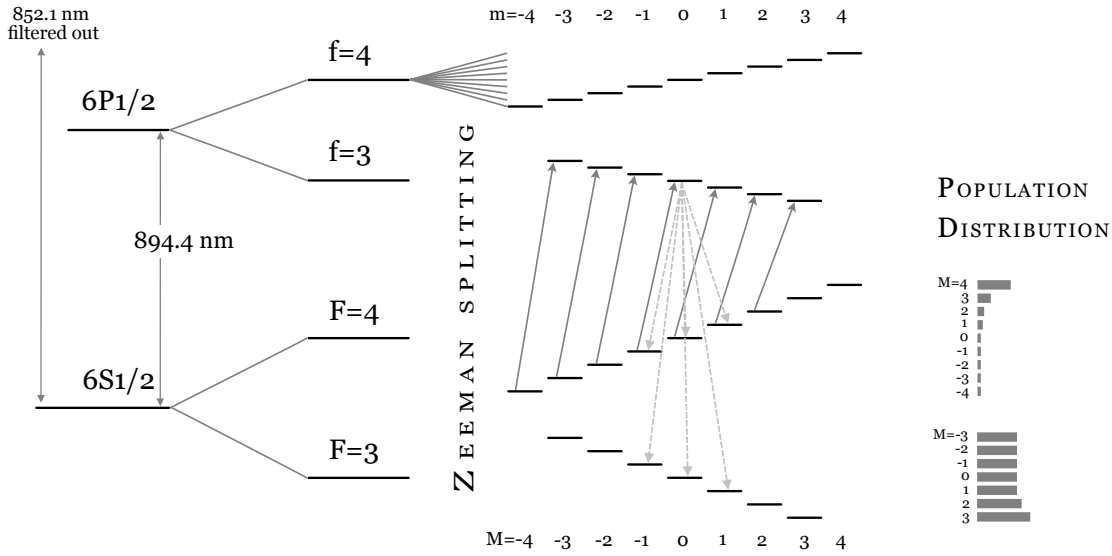


**Figure 2.1:** Schematic representation of optical pumping in a Caesium vapour magnetometer. Filtered and right circularly polarised light induces transitions of electrons between the Zeeman levels of the hyperfine structure. This is shown in solid lines, while the dashed lines represent the decay channels. The electron distribution of two ground-state hyperfine multiplets is shown on the right.

When returning to the ground state, the same amount of energy is subsequently emitted as electromagnetic radiation with a frequency  $\nu$ , such that

$$h \cdot \nu = E_j - E_i, \quad (2.1)$$

with  $h$  being the Planck's constant.

The different energy levels of the ground and excited states can additionally be split into fine and hyperfine structures (see Fig. 2.1) due to electromagnetic interaction of nucleus and electrons. However, the splitting of the energy levels in the presence of an external magnetic field is decisive for the functioning of a magnetometer. The magnetic moment of the individual electron can be either parallel or antiparallel to the external magnetic field. The energy of the precession of the magnetic moment at the Larmor precession frequency interacts with the energy state of the electron. Consequently, it splits the original energy level into two. This phenomenon is known as the Zeeman effect.

Thereby, the energy difference ( $\Delta E$ ) of these two energy levels or spectral lines is exactly proportional to  $B$ . By returning to a less excited state, the precession direction of the electron magnetic field also leads to the emission of circularly polarised radiation. Depending on the Zeeman line, the rotation of the radiation is either clockwise or counter-clockwise. Again, the energy level transitions that emit energy with a specific frequency and polarisation have the same excitation properties. If the electron returns to a less excited state, it can assume all the different ground states because its precession direction is random.

An alkali-vapour magnetometer, e.g. a caesium vapour magnetometer, comprises a glass cell filled with the alkali vapour. The only stable isotope  $^{133}\text{Cs}$  is used for this, which has the electron configuration  $[\text{Xe}]6s^1$ . The cell is operated at elevated temperatures to maintain the vapour state. A caesium lamp, which incandescences by high-frequency induction heating, emits a beam which passes through a lens, a filter and a polariser to produce a parallel beam of circularly polarised light of a specific frequency. In the case of a caesium magnetometer, the filter removes the 852.1 nm line, so that only the 894.4 nm spectral line is transmitted, the energy at which the valence electron is excited from the ground state  $6S_{1/2}$  to the lowest excited state  $6P_{1/2}$ . The hyperfine interaction of the total electronic angular momentum  $J = 1/2$  and the nuclear spin  $I = 7/2$  of the Cs atoms split the  $6S_{1/2}$  ground state into two hyperfine levels  $F = |I \pm J| = 3, 4$  and the  $6P_{1/2}$  excited state into the levels  $f = 3, 4$ . In an ambient magnetic field, the hyperfine levels  $F$  and  $f$  split into  $2F + 1$  and  $2f + 1$  magnetic sublevels, the so-called Zeeman levels.

Initially, all 16 sublevels are evenly populated. For efficient optical pumping, the filtered light from the Cs discharge lamp not only triggers the  $D_1$  transition, but the right-hand circularly polarised light resonates with the  $F = 4$  to  $f = 3$  hyperfine transition after polarisation. When an atom absorbs a photon of this radiation, it triggers precisely a  $|4, M\rangle$  to  $|3, M + 1\rangle$  transition (see Fig. 2.1). As long as the light from the lamp is absorbed and electrons are pumped into the higher energy state, a lower light intensity hits the detector. The light intensity of the lamp is low enough so that the excited atom spontaneously decays to a ground level. With further radiation of the lamp, all atoms are pumped into  $M=3,4$  stages. This creates a population imbalance in the ground state. This process is called Zeeman pumping, a variant of optical pumping, and is used in magnetometry. Eventually, a ground state is depleted, no more light can be absorbed and the lamp's light hits the detector unhindered in full intensity. To repopulate all sublevels equally again, the transition between adjacent Zeeman levels can be triggered by absorbing photons from an additionally applied resonant radio-frequency field. A coil around the vapour cell is operated with an alternating current until the varying frequency reaches the precession frequency and all electrons are equally distributed in the lower ground state again. Radiation from the discharge lamp can be absorbed again and the intensity of the transmitted light decreases again.

When all effects are combined, there is a flickering signal that falls on the photocell and corresponds to the precession frequency  $\nu_L$ :

$$2\pi\nu_L = \gamma B_0 \quad (2.2)$$

with the gyromagnetic ratio  $\gamma = 2\pi \cdot 3.5 \text{ Hz/nT}$  for the caesium ground state. A small oscillating signal is returned to the coil to amplify the coil signal and maintain a frequency around the resonance. The measured frequency of the light modulation is directly related to the total intensity of the ambient magnetic flux density  $B_0$ . Elizabeth Ralph (1964) conducted the first documented use of an alkali-vapour device for archaeological prospecting.

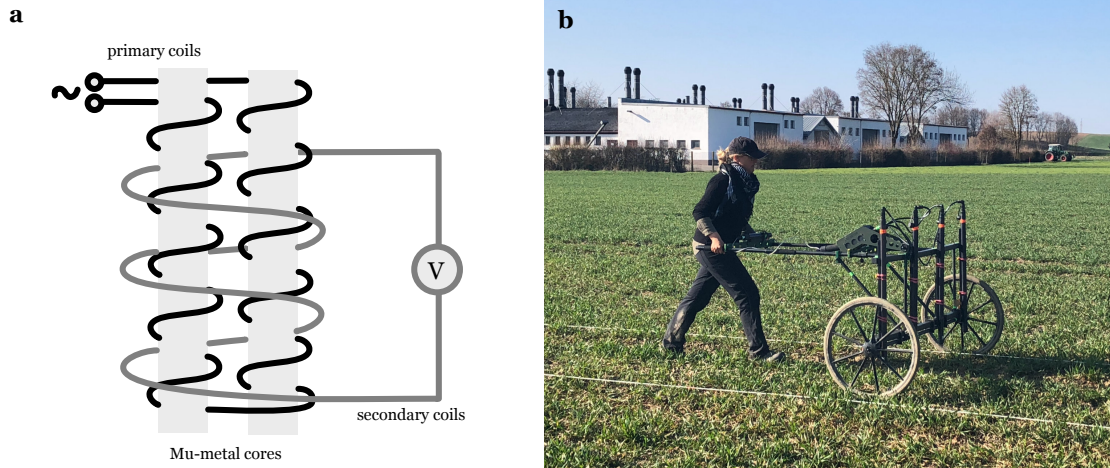


**Figure 2.2:** a) The design of the Vacquier fluxgate sensor. Two wires, acting as primary and secondary coils, are wound around mu-metal cores. The primary coils induce a small alternating current. The presence of an external field induces a proportional voltage in the secondary coil. b) Prospecting with the Foerster Ferex 4.032, a vertical axial gradiometer. It has four sensors mounted vertically in a distance of 0.5m on a frame. This enables the measurement of four survey lines at the same time.

### 2.1.2 Fluxgate gradiometers<sup>2</sup>

There are various fluxgate sensors (Primdahl, 1979), but the principle of operation is explained using the Vacquier fluxgate sensor (see Fig. 2.2 a). The dual-core fluxgate sensor in Vacquier configuration consists of two wires that act as primary coils and are wound tightly around two mu-metal cores. The windings of the primary coils are connected in series but are wound in opposite directions. A small alternating current flows through the wires, periodically saturating the soft magnetic coil cores. The two generated alternating magnetic flux densities  $B_{sat}$  are equal but constantly opposite and cancel each other out in the absence of an external field. In the presence of an external field  $B_E$ , the alternating fields of the coils overlap with the component of the external field along the core axis. With a sensor oriented at an angle  $\theta$  to the total flux direction of the external field, this component is:

$$B_{\theta} = B_E \cdot \cos \theta \quad (2.3)$$

This results in a decrease of the magnetic flux density of  $2B_{\theta}$  in one coil and an increase in the other coil. The superposition of both alternating core fields results in an oscillating net field  $B_s$  with the amplitude  $2B_{\theta}$ . The alternating net magnetic flux density induces a voltage in a secondary coil wound around the primary coils and their cores. The voltage signal is proportional to  $dB_s/dt$  and pulses at twice the input frequency, with its amplitude proportional to the surrounding magnetic field.

The sensor is sensitive to changes in angle, which can be estimated by the following formula:

$$dB_{\theta}/d\theta = (-)B_E \cdot \sin \theta \quad (2.4)$$

<sup>2</sup>This section is based on Aspinall et al., 2009.

In order to compensate for this sensitivity to sensor tilting, survey fluxgate instruments are constructed as a gradiometer: Two identical fluxgate sensors are mounted opposite each other at a fixed distance on a rigid rod (see Fig. 2.2 b). The output voltage is proportional to the difference of the magnetic flux density of the lower and upper sensor ( $B_{bottom} - B_{top}$ ). Therefore, a vertical axial fluxgate gradiometer like the Ferex only measures variations in the  $z$  component of the magnetic flux density. This approach also eliminates the influence of the surrounding geomagnetic field, including its diurnal variations and other large-scale features such as geological features, and ultimately registers only small-scale anomalies. The first development of a fluxgate gradiometer for archaeological prospecting is attributed to John Alldred (1964).

### 2.1.3 Further Instruments

As already mentioned, the devices are divided into vector and scalar magnetometers. As the names suggest, scalar magnetometers measure the total intensity of the ambient magnetic flux density; therefore, they are also often called total-field magnetometers. In contrast, vector magnetometers measure only one of the components or, more correctly, the component, which is the projection on the sensor axis. Vector magnetometers can also compromise multiple vector sensors so that more than one component can be measured. In archaeological prospecting, scalar measuring devices that are used are proton, Overhauser, and the above-presented alkali-vapour magnetometers. Vector measuring devices that are used are the SQUID magnetometers and fluxgate gradiometers.

## 2.2 Survey method

### 2.2.1 Instrument set-up

Since I have mainly operated our group's Geometric's instrument in campaigns, I will only describe this instrument's setup. The Geometrics G-858 MagMapper Magnetometer is supplied with one Caesium probe and an accompanying readout unit. The instrument's specifications are listed on the company's website: <https://www.geometrics.com/product/g-858/>.

We use two probes in combination with one readout unit to operate them in the duo-sensor configuration based on Helmut Becker's idea (Becker, 1999) to use both probes to measure the total-field anomaly and not operate the probes in vertical or horizontal gradiometer mode as was standard at the time. This has three advantages: higher sensitivity, higher spatial resolution, and speed of measurement. For this purpose, the sensors are mounted horizontally parallel on a wooden frame at a distance of 50 cm (see Fig. 2.3) like the setup for the horizontal gradiometer mode. With the plastic plate mounted vertically on the wooden frame, the probes can be carried at the desired distance of 30 cm above the ground. The sensors are connected to the readout unit with the integrated sensor cable. The readout unit is hooked into the belly strap of a small hiking backpack. Additional straps prevent the readout unit from being wildly jerked around. Two batteries that are stored in the backpack serve as a counterweight. These provide the power for the readout unit and the sensors via the readout unit. We use a hand-held trigger to execute simple commands on the readout unit. We use water bottles on the opposite side of the frame to balance the weight of the probes on the frame.



**Figure 2.3:** *Prospecting of the Geometric's instrument. The Caesium probes are fixed on a wooden frame to move the whole setup around 30 cm above the ground. The probes are connected to the read-out unit, powered by the batteries carried in the backpack. A water bottle is used as a counterweight.*

### 2.2.2 Survey procedure

The selection of survey areas is based upon the interest of the directing archaeologist or the surveyor, the accessibility and walkability of the survey area and the presence of modern features that could contaminate or disturb the survey.

An area of interest is segmented into a grid of squares with an ideal edge length of 40 m by 40 m (see Fig. 2.4). If necessary, the size of individual squares can be adjusted to fit the local conditions. The edge points of the squares are determined either via GPS, tachymeter or simply with measuring tape and angle prism. In the latter case, these edge points are georeferenced later.

The grid is preferably orientated along north-south and east-west magnetic axes. Two sets of two ropes are used to set up a finer grid within the grid square: Base lines, marked every meter, and walking lines, marked every 5 meters (see Fig. 2.4). Base lines are placed along the north-south axis, two parallel to each other, and form the eastern and western boundaries of the square. One walking line is laid perpendicular to the base lines at the southern edge, the other two meters further north. The starting point of the measurement is the southeast corner of the square. The surveyor walks along the walking line towards the western base line. Once there, they switch to the next measurement line, the line between the ropes, one metre further north and walks along that one back towards the eastern base line. Thereby, the instrument switches constantly the direction of operation. This measurement pattern is called „zig-zag“. If the instrument's orientation doesn't change, this pattern is called „parallel“.

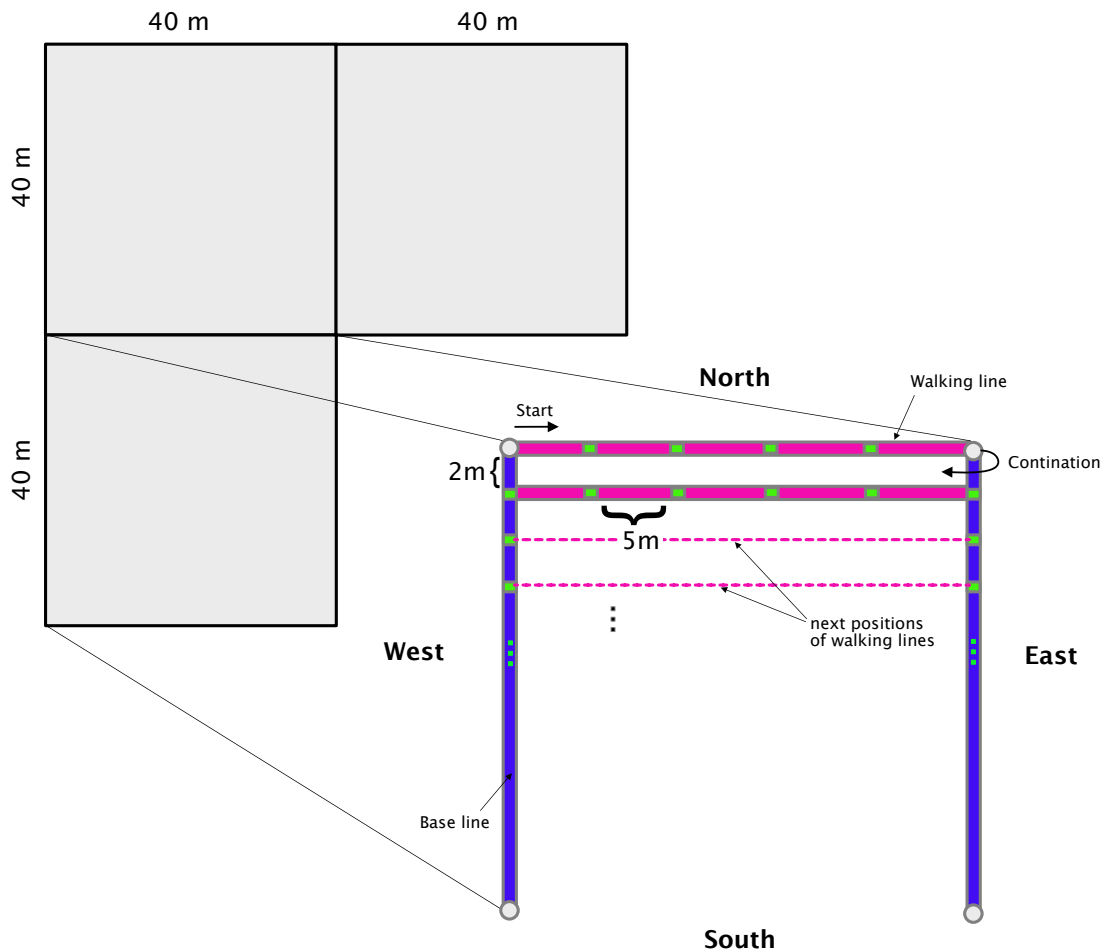


**Figure 2.4:** Sketch of the survey procedure. The survey area is divided in a 40 m by 40 m grid. Base lines with 2 metre marks are placed at the western and eastern boundary. The walking lines are placed perpendicular to the base lines and have marks every 5 metres. Starting point of the survey is the north-western edge point. Walking direction is towards the east. At the eastern boundary, the surveyor returns between both walking lines using them as guidelines towards the western boundary. With a sampling frequency of 10 Hz this results in data resolution of 1 m by approximately 15 centimetres.

The walking lines are constantly repositioned to provide always a guideline for the surveyor. Consequently, the walking direction is preferably east-west so that the instrument itself, the battery, and the readout unit do not or only minimally influence the measurements. The measurement progresses from south to north.

With a sensor distance of 0.5 m and a line separation of 1 m, the data point coverage along north-south axis is 0.5 m. The measurement frequency for the Geometrics instruments is 10 Hz, and with a constant average walking speed, this results in a data point coverage along the east-west axis of at least 12.5 cm. The orientation of the grid can be rotated to accommodate the orientation of plough furrows or weirdly shaped survey areas.

## 2.3 Data processing

In the following, I exemplarily depict the processing of data acquired with the Geometrics magnetometer.

### 2.3.1 Pre-processing

The data from the readout unit is downloaded to a computer with the Geometrics proprietary software "MagMap2000". The mark and end positions, as well as the survey direction, are displayed graphically after downloading. The software allows for corrections of the mark and end positions and the survey direction of each measurement line.

During the survey, a certain amount of distortion occurs when setting the position marks, which depends primarily on the height as well as on the skill of the surveyor. The position markers are usually set too early, as the surveyor looks at the carried probes and markings of the ropes at an angle. The result is that parallel and anti-parallel lines are shifted in relation to each other. This shift is small and constant for skilled surveyors and can be easily removed with a re-shift of the lines ("MagMap2000" - Destaggering). This proceeding is called „destaggering“ of a data set and should preferably be the first step in pre-processing. If the shift constant is unknown or non-constant, it is advisable to carry out this step later in the processing.

This is followed by removing the coherent offsets ("MagMap2000" - Destriping). In addition to the constant offset introduced by the readout unit, cables, and ferromagnetic objects on the frame and potentially on the operator, this also includes the heading error of the probes. The heading error is a measurement error which occurs if the probes are not inclined in a  $45^\circ$  to the ambient field direction. The manual describes the application as a technique of comparing magnetic offsets on a line-to-line basis, taking into account the orientation of the measurement lines. Since the offsets also change orientation depending on the direction of the measurement, these offsets are either added to or subtracted from the value measured for the ambient magnetic field for parallel or anti-parallel lines. The technique compares the values of lines perpendicular to the survey lines. It identifies the local minima and maxima for every perpendicular line and determines the total number of minimums and maximums for each survey line. By adding small values, the occurrence of maximums and minimums can be equally distributed, consequently destripes the data.

The pre-processing of the data continues with the "MagPick" software. Since the data distribution along the survey lines is arbitrary up to this step, resulting from the time-based measurements, it is interpolated to an appointed spatial resolution of  $0.25\text{ m} \times 0.5\text{ m}$  using the Spline method („Magpick“ - Spline Interpolation). The data is finally exported as .xyz-file, which can be read with the "Geoplot" software, among others.

### 2.3.2 Further processing

The data sets are further processed using the "Geoplot" software. The individual grids are combined to produce a graphical output of the survey areas. When visualising the data, the magnetic field values are preferably displayed on a grey scale with white as the minimum and black as the maximum. A pixel represents a data point on a scale of 256 grey levels with 0 (black) and 255 (white). The reference value is, by definition, equal to zero when representing the variation, i.e. the value 127 on the grey scale. With this grey

scale, there is a linear relationship between colour and anomaly value (von der Osten-Woldenburg, 1992). The idea is that structures with similar values can be traced better than on colour scales and more intuitively than on isoline maps, representations in point density, symbolic form or profiles.

If this has not already been done (see 2.3.1.), the data sets are now destaggered ("Destagger" command).

A discrete variation is initially assumed for the compensation of the daily fluctuations of the earth's magnetic field. The mean grid value is determined for each grid and subtracted from the data values of the grid (command "Mean grid value", Threshold 0.25 SD). Of course, a stable geomagnetic field is assumed for the measurement time of a grid (usually approx. 40 min for a 40 m x 40 m grid). Adjustments to the mean value are made to match the edges of two adjacent grids and to eliminate edge deviations ("Edge match" or "Add" command). Linear changes in the geomagnetic field during the measurement time of a grid are compensated for by multiplying the data of individual profile lines by a gradually increasing or decreasing multiplication factor ("Deslope" command). Non-linear changes can be compensated for by adding different values to sections or entire profile lines ("Add" command). The correction is purely visual and is not based on predefined values for the diurnal fluctuations in the date and time of the measurement.

If required, further steps such as the removal of random spikes in the data sets ("Despike" command, possible for different X and Y radii and threshold values (from 0.5 to 3 SD), spikes are replaced by the mean value) and single value adjustments to eliminate artefacts which were introduced when processing the data can be carried out.

Finally, the data is interpolated to an appointed resolution of 0.25 m  $\times$  0.25 m ("Interpolate" command, Expand with Linear Method). An image high-pass filter (R=10, in X and Y radius, weighting: uniform) is applied to a copy of the total field data set. Both data sets and their visual representation with different colour scales and palettes are used for the interpretation. The data is displayed in figures using either Surfer or Matlab software with the traditional greyscale palette with appropriate scaling, which allows the majority of the archaeological features to be recognised. The total-field data is usually overlaid with the high-pass filtered data with a transparency of 30 %.

## 2.4 Interpretation

While one can follow instruction manuals, books and guidelines to obtain, process and present the raw physical data, the interpretation requires experience combining principles of magnetism with knowledge of a site's archaeology, geology, geomorphology and condition and history.

For interpretation, the magnetogram is viewed in different scale ranges and colour scales with active hill shading and compared to the high-pass filtered data. The main aim of the interpretation is primarily to characterise geological, archaeological and modern anomalies or structures. With good data, this interpretation can be more detailed and comprehensive. Various factors should be considered to identify anomalies and structures, including the bedrock and drift geology, soil types, geomorphology, topography, surface features, weather history, landscape history, agricultural practices and modern interventions on the site, known and suspected archaeological features, survey disturbance and data processing (Schmidt et al., 2015), susceptibility and remanent magnetisation of the

soil, rock and archaeological features. And this list could be extended. Most importantly, one should be aware of all these factors' role in the site's „magnetic image“of the site. Magnetic contrasts, shape, inhomogeneous magnetisation, remanence orientation, and geomagnetic field direction should not be ignored.

How the interpretation is presented is entirely the choice of the author or interpreter. Different variants are in use, ranging from just the reproduction of the magnetogram to outlining the structures based on their character, classification and colour coding based on an intensity range or directly based on tesla values. The presentation of the interpretation should form the basis for a discussion and demonstration of the results. It should include all relevant findings and be adapted according to the requirements of the presentation.

## 2.5 Comparison of total-field and gradiometer measurements

Sometimes, the circumstances of a campaign or fieldwork require the use of a total field magnetometer and fluxgate gradiometer in the same survey area. For example, a large survey area should be magnetically measured in a short time, as it was the case with our prospecting at the site of Fara (see chapter 5). In order to keep the survey team together and not spread out over the tell, these different magnetometers were applied in different but neighbouring segments of the same survey area. However, the different designs of the magnetometers mean that different elements of the magnetic flux density are measured and, therefore, the optical output of the data is also different. This can have a disturbing or distracting effect on the archaeo-geophysical interpretation. In the following, I want to elaborate on the mathematical details of total-field magnetometers and vector gradiometers and discuss ways to combine their output into a visually uniform magnetogram.

### 2.5.1 Physical background

#### 2.5.1.1 Scalar magnetometer

From a physical point of view, a scalar magnetometer measures to a fair approximation the projection of the magnetic field of the anomalous field onto the direction of the Earth's magnetic field at the survey area:

$$B_{AT} = \mathbf{B}_a \cdot \hat{\mathbf{B}}_E \quad (2.5)$$

as demonstrated in Chapter 1 when the intensity of the Earth's magnetic field is subtracted. Commercial alkali-vapour magnetometers are often sold with two sensors. Different configurations (see Fig. 2.5) can be chosen for the prospecting:

- duo-sensor configuration
- horizontal or vertical gradient or gradiometer mode
- variometer mode.

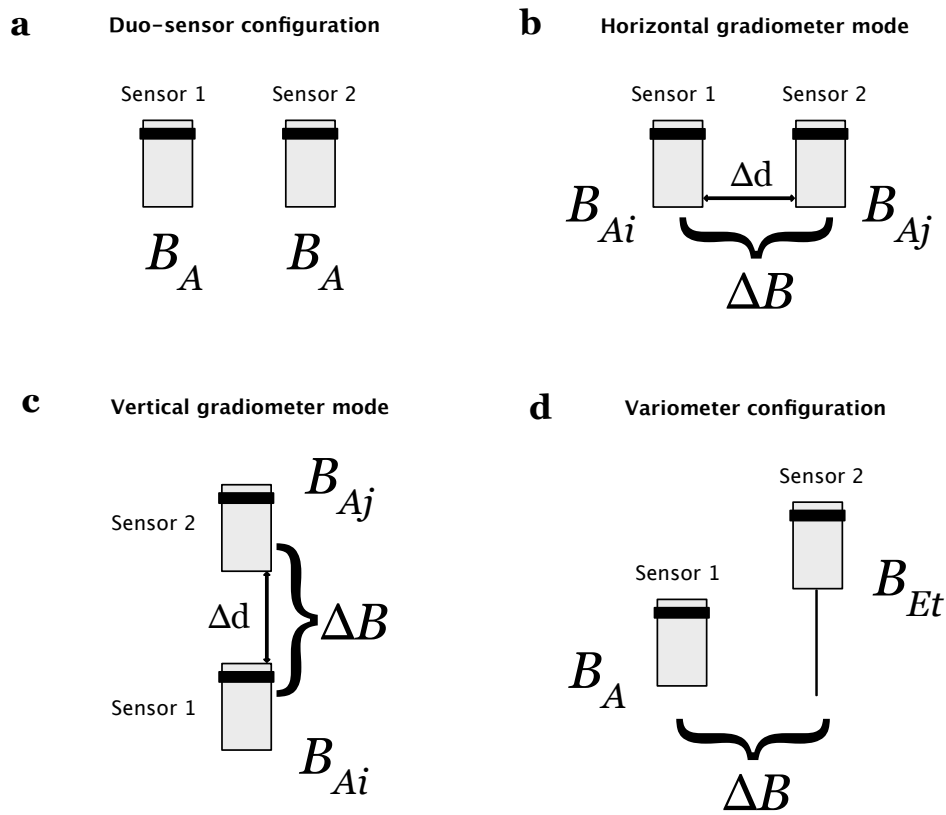


**Figure 2.5:** Different configurations of two sensors of alkali-vapour magnetometer: a) Duo-sensor configuration. b) Horizontal gradiometer mode. c) Vertical gradiometer mode. d) Variometer mode.



**Figure 2.6:** a) Measurement with the Geometrics magnetometer. The sensors are mounted at a horizontal distance of 0.5 m on the frame. Both sensors are moved parallel to the survey direction. This setup is called duo-sensor configuration or horizontal gradiometer mode. The processing of the data determines which of the two it is. b) Survey in vertical gradiometer mode with both sensors mounted on top of each other.

**Duo-sensor configuration** In a duo-sensor configuration (Becker, 1997), the sensors are carried at a fixed horizontal distance from each other, which in our practice is 0.5 m (see Fig. 2.5 a and Fig. 2.6 a). This horizontal axis is perpendicular to the measurement direction. In this way, the measurement of one survey line provides two readings so that one sensor scans the left and the other right of the survey line. Each probe measures independently the vector sum of the earth's magnetic field and the anomaly. The reference value is only determined and subtracted later in the data processing so that the output conforms to equation 2.5..

**Gradiometer or gradient mode** In gradiometer mode, the probes are mounted at a fixed distance from each other and moved along the survey line. The arrangement of the sensors determines the type of gradiometer mode. The arrangement described above corresponds to the horizontal gradiometer mode (see Fig. 2.5 b). In a vertical gradiometer mode, the sensors are arranged one above the other (see Fig. 2.5 c and Fig. 2.6 b). The two data sets are then subtracted from each other, and the result is divided by the sensor distance:

$$\frac{\Delta B}{\Delta d} = \frac{|B_{a_i} + B_{E_i}| - |B_{a_j} + B_{E_j}|}{d_i - d_j} \quad (2.6)$$

where  $d$  is the distance between the sensors positions  $d_i$  and  $d_j$ . Accordingly, this method corresponds to a linear derivative, which is also referred to as the calculation of a pseudo-gradient. A real gradient  $\nabla B$  would be the vector of partial derivatives in each direction. This is not calculated here, hence the prefix „pseudo “. The unit of this quantity is T/m.

The sensors can be arranged in any order. For a vertical gradiometer mode, the sensor  $j$  is positioned in the distance  $d$  above sensor  $i$ , or vice versa. Both sensors are arranged at a distance of  $d$  for a horizontal gradiometer mode. Traditionally, in archaeological prospecting, the vertical gradient is calculated via the bottom minus the upper sensor. The application horizontal gradiometer mode is rarely recorded, and the subtraction order of the sensor data is not defined, only that the results of one sensor are subtracted from the other and not a "running" subtraction of the data recorded by one sensor data in a horizontal offset.

Alternatively, the subtraction of the results of the sensors is not divided by sensor distance, resulting in the difference in magnetic flux density at the two sensors. This result has the unit T.

**Variometer mode** Another possibility is to apply the two sensors as a variometer. For this, one sensor is at a fixed base position and records the geomagnetic field, while the other sensor is used for the actual magnetometer survey (see Fig. 2.5 d). In this configuration, the base sensor constantly provides the correct reference value. The output is according to equation 2.5.

### 2.5.1.2 Vector magnetometer

Compared with that, one fluxgate sensor measures the projection of the superposition of the anomalous field  $\mathbf{B}_a$  and the Earth's magnetic field  $\mathbf{B}_E$  on the sensor axis:

$$B_\theta = |\mathbf{B}_a + \mathbf{B}_E| \cdot \cos \theta. \quad (2.7)$$

A vertical gradiometer, the combination of two fluxgate sensors mounted on one staff, measures the difference in  $\hat{\mathbf{z}}$  component, which can be expressed as:

$$B_{Az} = (\mathbf{B}_{a_{\text{bottom}}} + \mathbf{B}_{E_{\text{bottom}}}) \cdot \hat{\mathbf{z}} - (\mathbf{B}_{a_{\text{top}}} + \mathbf{B}_{E_{\text{top}}}) \cdot \hat{\mathbf{z}} \quad (2.8)$$

where  $\mathbf{B}_{E_{\text{bottom}}} = \mathbf{B}_{E_{\text{top}}}$  for small sensor distances which simplifies the equation to

$$B_{Az} = (\mathbf{B}_{a_{\text{bottom}}} - \mathbf{B}_{a_{\text{top}}}) \cdot \hat{\mathbf{z}} = \Delta \mathbf{B}_a \cdot \hat{\mathbf{z}}. \quad (2.9)$$

A horizontal gradiometer measures correspondingly either

$$B_{Ax} = \Delta \mathbf{B}_a \cdot \hat{\mathbf{x}} \quad (2.10)$$

or

$$B_{Ay} = \Delta \mathbf{B}_a \cdot \hat{\mathbf{y}}. \quad (2.11)$$

Therefore, the orientation of the gradiometer dictates which element of the anomaly's flux density is measured. If several fluxgate sensors are combined, more ambient magnetic flux density components can also be measured. A triaxial instrument, for example, covers all three spatial directions.

## 2.5.2 Advantages and disadvantages of the different devices

As mentioned in Section 2.1.2, the design of the fluxgate gradiometer eliminates the need to correct for diurnal variations, saving time during data processing. One disadvantage is that the distance between the two sensors affects the possible detection depth. E.g. the distance between the sensors of our group's fluxgate gradiometer (Foerster Forex 4.032) is reported to be 65 cm, and its detection depth is assumed to be 1 m (Fassbinder, 2017). At the same time, the vector gradiometer acts as a spatial high-pass filter whose cut-off wavelength is related to the sensor distance. This allows deep and broad features to be filtered out, such as geological effects, but can also cause archaeological signals to be lost. For this reason, gradiometers are also referred to as intrinsic high-pass filters (Schmidt, 2008).

With these factors, the gradiometer is considered less sensitive than the total-field magnetometer. Different instruments' sensitivities are listed e.g. by Fassbinder (2015). The noise level of the Geometrics probes is also lower than that of the fluxgate gradiometer (Schmidt, Dabas, & Sarris, 2020). This might affect the detection of certain features like clay bricks (N. Linford, Linford, Martin, & Payne, 2007) and postholes of palisades. The detection depth of total-field measurement is estimated to be about three metres (Fassbinder, 2017). The missing intrinsic high-pass filter allows the detection of geological features but also traces of harbour basins and (palaeo-)channels (e.g. Fassbinder, 2009). However, the measurement technique is sensitive to road traffic, steel structures, solar storms or magnetically noisy days.

The comparison is intentionally brief here as it is not the focus of the thesis. Various reasons speak for and against an instrument. However, the most important factor is that the surveyor knows how to use the instrument, read and interpret the data correctly.

## 2.6 Merging total field magnetometer and gradiometer data<sup>3</sup>

As Section 2.5.1. shows, total-field magnetometers and vector gradiometers measure or provide different information about the magnetic flux density. If these are now displayed in a combined magnetogram, these physical differences also become apparent visually. The difference is evident when combining the segments measured by the instruments directly after data processing, as shown in Fig. 2.7 a. The magnetometer survey of the Fara campaign 2018, the results of which I show here, was conducted with two total-field magnetometers, a Scintrex Smartmag SM4G-special magnetometer and a Geometrics G-858 magnetometer, as well as a vertical vector gradiometer, a Foerster Ferex instrument.

The traditional physically procedure to obtain comparable readings of both instruments involves:

1. A transformation of the scalar magnetometer data from the total-field anomaly to the vertical component of the anomaly.
2. Adjusting this data to one fluxgate gradiometer sensor height and computing a signal for a fictional second sensor through upwards or downward continuation.
3. Calculating the difference of these two data sets.

In the following, I discuss a more accessible way to combine scalar magnetometer and fluxgate gradiometer output to a visually uniform magnetogram.

With the knowledge that a vector gradiometer measurement is also called an intrinsic high-pass filter (Schmidt, 2008) and the results of Stella Manoli's master's thesis (2014), inspired the approach to merge the high-pass filtered total-field magnetometer data with the fluxgate data. Our group already uses a high-pass filter for total-field magnetometer data to remove larger spatial wavelengths and thus suppress the contribution of geological sources, among others. Theoretically, this and the correction for diurnal variations are akin to the principle of gradiometer measurements. The mean value of the individual data sets of the segments is shifted to zero before the combination. Empirically tested, a visual match works best when an image high-pass filter with a radius 10 ("Geoplot" software) is applied to the total-field data. This visual result is shown in Fig. 2.7 b. Comparing the standard deviation for all three magnetometer data sets, the high-pass filtered total-field magnetometers' data sets have the same value.

In contrast, the Fluxgate gradiometer data sets show only half of the high-pass filtered total-field magnetometers' data sets for all magnetograms of the case study. Therefore, I multiplied the gradiometer data set to achieve a better match of the data sets in terms of their data values as well as their optical output. The result is a visually uniform appearing magnetogram (Fig. 2.7 c).

---

<sup>3</sup>This section is an excerpt of the article:

Hahn, S. E., Fassbinder, J. W. E., Otto, A., Einwag, B., & Al-Hussainy, A. A. (2022). **Revisiting Fara: Comparison of merged prospecting results of diverse magnetometers with the earliest excavations in ancient Šuruppak from 120 years ago.** *Archaeological Prospection*, 1–13. <https://doi.org/10.1002/arp.1878>

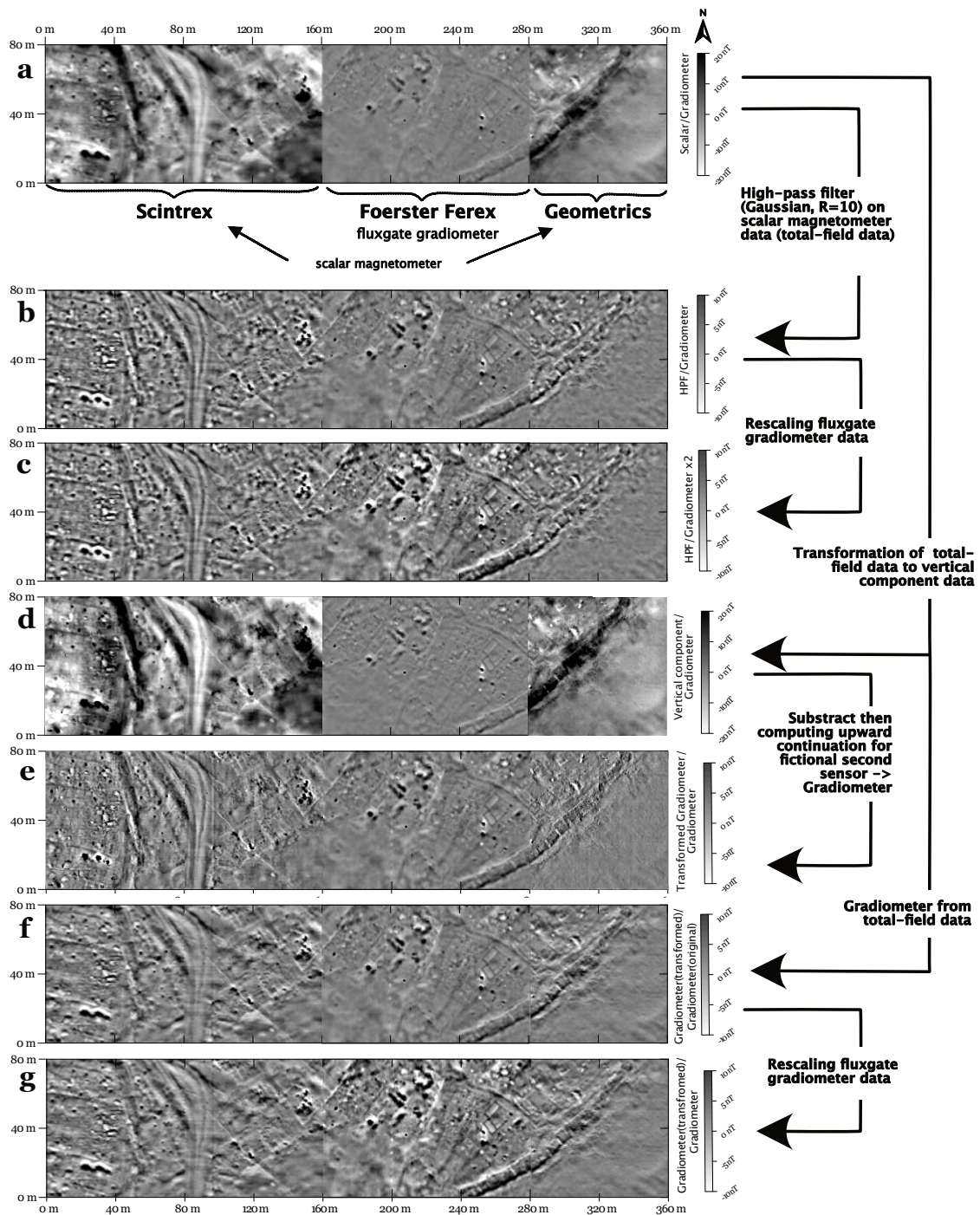


**Figure 2.7:** Comparison of various combination of total-field and vertical gradiometer data and their additional processed output: a) Combination of the total-field data sets and the vertical gradiometer data sets. b) Combination of the high-pass filtered total-field data sets and the gradiometer data sets. c) Combination of the high-pass filtered total-field data sets and the gradiometer data sets multiplied by 2. d) Combination of the vertical component computed from the scalar magnetometer data sets and gradiometer data sets from the Ferex vertical gradiometer. e) Combination of vertical upwards continuation (0.65 m) of the vertical component of the total-field data set minus the original data set (transformed gradiometer data) and gradiometer data sets from the Ferex vertical gradiometer. f) Combination of vertical upwards continuation (0.65 m) of the total-field data set minus the original data set (transformed gradiometer data) and gradiometer data sets from the Ferex vertical gradiometer. g) Combination of vertical upwards continuation (0.65 m) of the total-field data set minus the original data set (transformed gradiometer data) and gradiometer data sets from the Ferex vertical gradiometer multiplied by 2.

The interpretation of the magnetometer survey in the case study of Fara highlights the benefit of combining both data sets into one magnetogram. The application of a high-pass filter on the segments of total-field data, corrected for diurnal variations, effectively filters out larger spatial wavelengths as theoretically proposed by Scollar (1969). This successfully resembles the visual appearance of the gradiometer data set of the adjacent segments. By multiplying the data set of the gradiometer by a factor of two, the lack of signal strength compared to the total field data is at least visually compensated. Naturally, the total-field data can be divided by the reciprocal of the factor. The lack of signal strength results from measuring only one component of the magnetic flux density and, to a smaller extent, the subtraction of the two readings of the upper and lower fluxgate sensors. This factor is expected to mostly depend on the inclination of Earth's magnetic field in the survey area. For the site of Fara, this is around  $50^\circ$  (NCEI Geomagnetic Modeling Team and British Geological Survey, 2019). Most observed anomalies hold a total magnetisation parallel or sub-parallel to the Earth's magnetic field direction. Therefore, the vertical component's ratio to the anomaly's absolute strength decreases with decreasing inclination. Consequently, the multiplication factor will be higher for lower inclinations. How the inclination affects the required settings of the image high-pass filter is yet unknown.

To compare my method with the physically correct way, I transformed the total-field anomaly data with a self-written Matlab script based on Gerovska and Araúzo-Bravo (2006), see Fig. 2.7 d, and used the programme „MagPick“ (Geometrics) to obtain the upward continuation (Blakely, 1996) for a second sensor at height of 0.65 m and subtracted these values from each other. The result can be seen in Fig. 2.7 e. The high-pass filtered and the transformed gradiometer data of the scalar magnetometer data show good visual agreement (see Fig. 2.7 c and e).

Additionally, to compare my method with a more established method of combining total-field and gradiometer data, I transformed the total field data into gradiometer data, as it has been done similarly by N. Linford et al. (2007). I used the programme "MagPick" (Geometrics) to obtain the upward continuation (e.g. Blakely, 1996) of the entire field data set up to a height of 0.65 m and subtracted these values from the original data set. The result can be seen in Fig. 2.7 f. To calculate the pseudo-gradient, one would divide these values by the sensor separation, or in this case, more accurately, the vertical height difference between the original data set and upward continuation. I deliberately refrain from doing this to better compare with the Ferex instrument's gradiometer data. For further comparison, I also show the Ferex gradiometer data multiplied by 2 in Fig. 2.7 g. The high-pass filtered and the transformed gradiometer data of the total field data show good visual agreement (see Fig. 2.7 c and g). The transformed gradiometer output still shows a certain „depth impression“ like the total-field output, which is completely absent in the high-pass filtered output. At least in this example, the latter visually resembles the Ferex gradiometer output more closely. A comparison of the Figs. 2.7 f and 2.7 g shows that the gradiometer data of the Ferex instruments should also be multiplied by the factor of two because of the above-mentioned reasons.

The introduced method successfully provides a uniformly appearing magnetogram regardless of the instruments used. Visually, the interpretation of our magnetograms was made significantly simpler since features were easier to trace and compare over the different segments. In our group's case, using a high-pass filter is more favourable since all visual data processing is then carried out by one software and is, therefore, more convenient and time-saving.

## Chapter 3

# The Effect of Remanence

The graphical representation of the magnetometer prospection results often shows spatial small-scale dipole anomalies with seemingly random orientations of the positive and negative parts of the signal. The magnetogram of the case study of two Bronze Age burial grounds near Artanish (see 3.1), north of Lake Sevan in Armenia (Fig. 3.1 a) at a geomagnetic inclination of  $58^\circ$  exemplified these different signal sequences. Some burials feature single rectangular rock chambers (Fig.3.2 a and b), and others are enclosed by a ring of stones. The surrounding sediment consists of pebble gravel, which is mainly composed of weakly magnetic dolomite or limestone. The topsoil is poorly developed and only a few centimetres thick. The rocks used for the burial circles are of volcanic origin and parautochthone, meaning they are only marginally transported from the location of their formation. Almost all detected anomalies are related to the burials or megalithic stone circles, also called cromlechs. The high intensities of the anomalies and their sharp contours link the randomly appearing dipole anomalies to surficial volcanic rocks on lake sediments, which is confirmed by comparison with orthophotos, vertical drone images of the investigated terrain. With certainty, one can assume that the volcanic rocks originate from the same provenance, which is why their magnetic properties should also be similar. Nevertheless, they show different orientations of the dipole anomalies. Inspired by the results of this fieldwork, I like to investigate this behaviour in more detail. I show in

Chapter 1 that the magnetic flux density of an object plays a key role in the calculation of the magnetic flux density of an anomalous body. Equation 1.22 shows that this magnetic flux density depends on the distance between observation point and the centre of the object's magnetisation  $\mathbf{r}$  as well as the magnetic moment  $\mathbf{m}$  of the object. The latter can be expressed by integrating the magnetisation  $\mathbf{M}$  over its volume  $V$ :

$$\mathbf{m} = \iiint \mathbf{M} \, dV.$$

The (total) magnetisation  $\mathbf{M}$  is the vector sum of the remanence  $\mathbf{M}_r$  and the induced magnetisation  $\mathbf{M}_i$

$$\mathbf{M} = \mathbf{M}_r + \mathbf{M}_i.$$

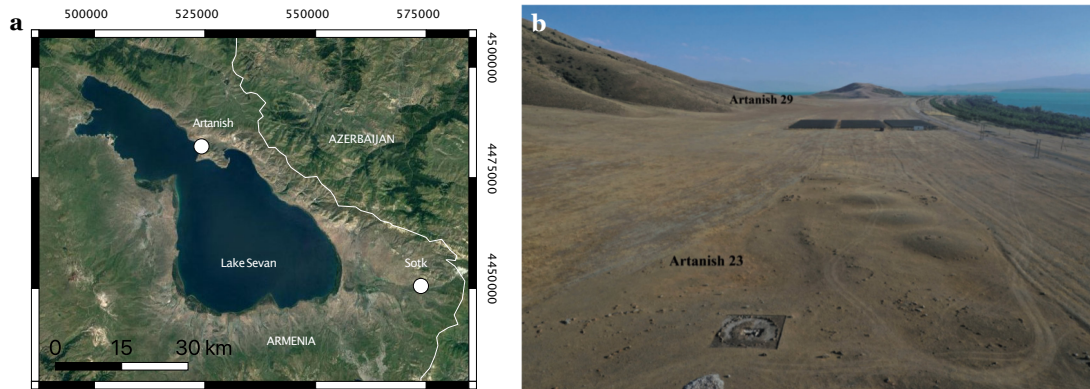


**Figure 3.1:** a) The location of the survey area is the Artanish peninsula in Armenia, and the gold mine is in Sotk. Satellite image: Google, ©1002, TerraMetrics. b) The area of and around the cemeteries Artanish 23 and Artanish 29. View to the south (from Bobokhyan & Kunze, 2021, Fig. 5).

For a uniformly homogeneously magnetised body, the magnetisation can be expressed with the intensity of magnetisation  $M$  and the angles  $\alpha$  and  $\delta^1$ .

$$\mathbf{M} = M \cdot \begin{pmatrix} \cos \alpha \cos \delta \\ \cos \alpha \sin \delta \\ \sin \alpha \end{pmatrix}$$

In the following, I elaborate on the case study of Artanish and discuss whether the different dipole anomalies' orientations are explainable by the direction of magnetisation of their source.

### 3.1 Archaeological background of the Artanish area<sup>2</sup>

Gold mining near the village of Sotk—southeast of Lake Sevan in the Gegharkunik province, Armenia (Fig. 3.1 a)—has a long history of exploitation, and the Sotk mine is still in operation today (Kunze, Bobokhyan, Meliksetian, Pernicka, & Wolf, 2011). It is the largest gold deposit in the Caucasus and was probably exploited as early as the 2<sup>nd</sup> millennium BC. The mine remained active intermittently until the 14th century AD and was rediscovered in the 20th century AD. Early traces of the mining are evidenced by wooden parts of working tools, stone mortars for ore extraction and underground workings, among others (Wolf & Kunze, 2013). The occupation in the Bronze Age left behind settlements, cemeteries and further findings, like weapons and cult objects around the mine. The investigation of archaeological sites around the Sotk mine and in the Gegharkunik province confirmed the possibility of prehistoric mining and trading of gold in that region. Archaeological excavations have shown that the region was inhabited already during the Early, Middle, and Late Bronze/Early Iron Ages (Kunze et al., 2013). How gold mining and trading influenced the prehistoric settlement structures is being investigated. The landscape around the Artanish

<sup>1</sup>Chapter 1 provides a general introduction to the formulae and quantities.

<sup>2</sup>This section, as well as the next three sections, are a reproduction of the article Hahn, S., Parsi, M., Fassbinder, J. W. E., Bobokhyan, A., & Kunze, R. (2021). **The Ecstasy of Gold: Magnetometer Prospection for the Ushkiani Project in Armenia.** *Revue d'archéométrie*, 45, 1. The text has been slightly altered to fit the narrative flow of the chapter. Supplemental figures are added for clarity.



**Figure 3.2:** *a) DEM of the excavated burial mound of Arthanish 23 (©Jonas Abele). b) Limestone burial chamber with Ruben Davtyan mimicking the buried body. c) Magnetometer prospecting at Arthanish 23 with the Geometrics G-585. In the background is the open excavation visible and Jörg Fassbinder prospecting with the SM4G-special magnetometer (©René Kunze).*

Peninsula on the north side of Lake Sevan lacks detailed archaeological investigation up to date. Different scientific approaches revealed possible outlines of settlement structures which can indicate a relation to regional gold mining. The geographical position of the peninsula suggests a natural pathway of super-regional communication and trade routes. In this framework, we conducted magnetometer surveys near Artanish at the seaside of Lake Sevan in 2019. Among other sites, we surveyed two necropolises (Fig. 3.1 b), the results of which I present here. My analysis and interpretation of the magnetograms is the first step to a subsequent excavation of the burial grounds to extend the knowledge of the prehistoric past of the northern part of Lake Sevan. The archaeological and archaeometallurgical analyses of the found metals will decode if there is a connection with gold mining in Sotk.

## 3.2 Investigation methods<sup>3</sup>

The magnetometer prospecting was conducted with the Scintrex Smartmag SM4G-special magnetometer and a Geometrics G-585 magnetometer (see Fig. 3.2 c). Details on the survey method and data processing can be found in Chapter 2. The final data has a spatial resolution of  $0.25\text{ m} \times 0.25\text{ m}$ . Our measurements were accompanied by high-resolution drone orthophotos (Fig. 3.4 a) and, derived from these photos, a Digital Elevation Model (DEM) of the survey area (Fig. 3.4 b). Additionally, we collected volume susceptibility data of the soil and rocks at the archaeological site using a SM-30 susceptibility meter (ZH instruments).

<sup>3</sup>The geophysical prospecting in 2019 was funded by the Gerda-Henkel Foundation. The State Office for Heritage Management and Archaeology of Saxony-Anhalt initiated the preliminary Sotk project from 2010 to 2014, and the State of Saxony-Anhalt, Germany, founded it. Thanks to René Kunze and his team for the support of our measurements. Also, thanks to Jonas Abele for the drone images.

### 3.3 Results of the magnetometer and susceptibility survey

What is striking in the resulting magnetograms of the two burial grounds (Fig. 3.4 c and 3.5 b) is the relatively high magnetic contrast of magnetic susceptibility as well as the natural remanent magnetisation (NRM) between the soil and the rocks used for the cromlechs. According to the soil map, the Artanish peninsula is dominated by the lake sediments of Lake Sevan (Antrosols and Regosols) as well as mountain-forest brown soils (Acrisols) at higher altitudes (Ghazaryan, 2013). The soil at the prospecting locations shows a magnetic volume susceptibility of around  $0.750 - 1.32 \cdot 10^{-3}$  (in SI units, see Fig. 3.3 a). The cromlechs were built with different gabbros or other ophiolite complexes, probably of locally occurring Jurassic-Cretaceous rocks (Kharazyan, Sargsyan, & Hayastan, 2005). The values of the magnetic susceptibility of the ophiolite complexes range from around  $1.37 \cdot 10^{-3}$  over  $13.4 \cdot 10^{-3}$  to  $25.4 \cdot 10^{-3}$  to even  $41.1 \cdot 10^{-3}$  (see Fig. 3.3 b-d). A variation in the rocks can also be seen in slight colour deviations. The chambers of the burials are constructed with limestones, probably also local late Cretaceous sedimentary rocks (Kharazyan et al., 2005), with an expectable negligible remanence and small magnetic susceptibility of around  $(0.0245 - 0.0505) \cdot 10^{-3}$ .

At the site of Artanish 23 (see Fig. 3.4), the survey area is around 1.5 ha. We recognise clearly four large burials, marked with solid yellow lines in Fig. 3.4 c, with cromlechs with diameters up to 20 m. Otherwise, at least 32 smaller burial sites (marked with dashed lines) with varying diameters are visible in the magnetogram. For the four larger ones, marked with solid circles in Fig. 3.4 c, it can be assumed that these are burial mounds — kurgans — since their grave chambers are visible in the magnetograms (shaded yellow in Fig. 3.4 c). The positive anomalies suggest that the burial chambers are sealed at the top with stronger magnetic rocks, probably ophiolite, rather than only with low magnetic limestones.

In 1 km distance to Artanish 23, we prospected the site Artanish 29 (see Fig. 3.5). Here, the survey covered around 1 ha. The radii of the burials are noticeably smaller (less than 10 m) than at the previously mentioned site, and the cromlechs are less clearly traceable. The clearer traceable are marked with dashed circles in Fig. 3.5 b. Some rocks seem to be misplaced, especially in the top left grid.

### 3.4 Comparison of magnetometry and DEM results

The burial chambers of the kurgans are clearly visible in the magnetogram, but not recognisable in the orthophotos (Fig. 3.4 a) or in the DEM analysis (Fig. 3.4 b). Additionally, the magnetometer survey also detects stones buried beneath sediment. The reason for this is the high magnetic contrast between the rocks used at the archaeological site and the surrounding soil. However, the variation in the magnetic properties of the used rocks biases the perception of the actual stone sizes of the cromlechs. In other words, the ratio of stone size to anomaly size need not be proportional. The aerial images give here a better indication of the actual stone sizes. In addition, the magnetic contrast between rock and soil can sometimes be marginal. Here, the aerial images can help to reconstruct the enclosures. In conclusion, the enclosures and burial chambers cannot be solely reconstructed by magnetometry or aerial images. Compared to orthophotos and DEM analysis, the stone circles of the burial are more pronounced in the magnetograms. The dipole anomalies of the stones of the cromlechs appear as different patterns, even though most are caused by volcanic rocks. The results show anomalies with one positive or negative signal and two

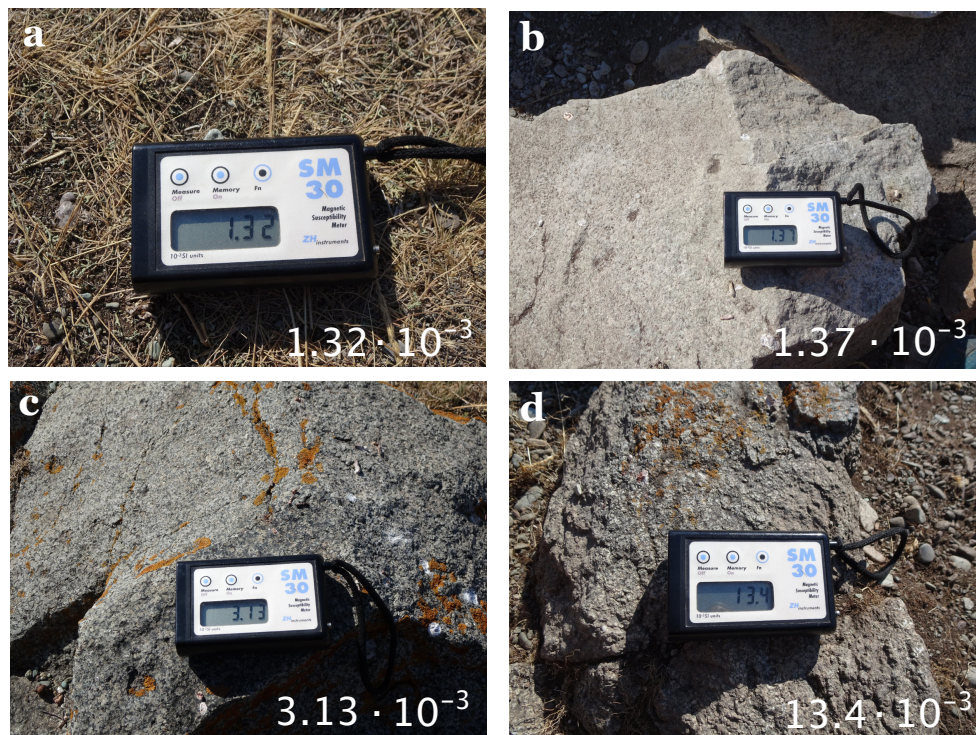


**Figure 3.3:** *Examples of susceptibility measurements: a) Soil at the burial sites. b) - d) Different gabbros or ophiolite complexes.*

signals in any succession or orientation, but still belonging to a ferrimagnetic source. This might be explained by a dominating remanent magnetisation over the induced magnetisation. While the induced magnetisation is parallel to the ambient Earth's magnetic field, the remanence can point in any direction if the stone is randomly orientated. Even though this hypothesis is reasonable, in the following section, I conduct an analytical approach, ascertained with a visual demonstration to confirm the hypothesis.

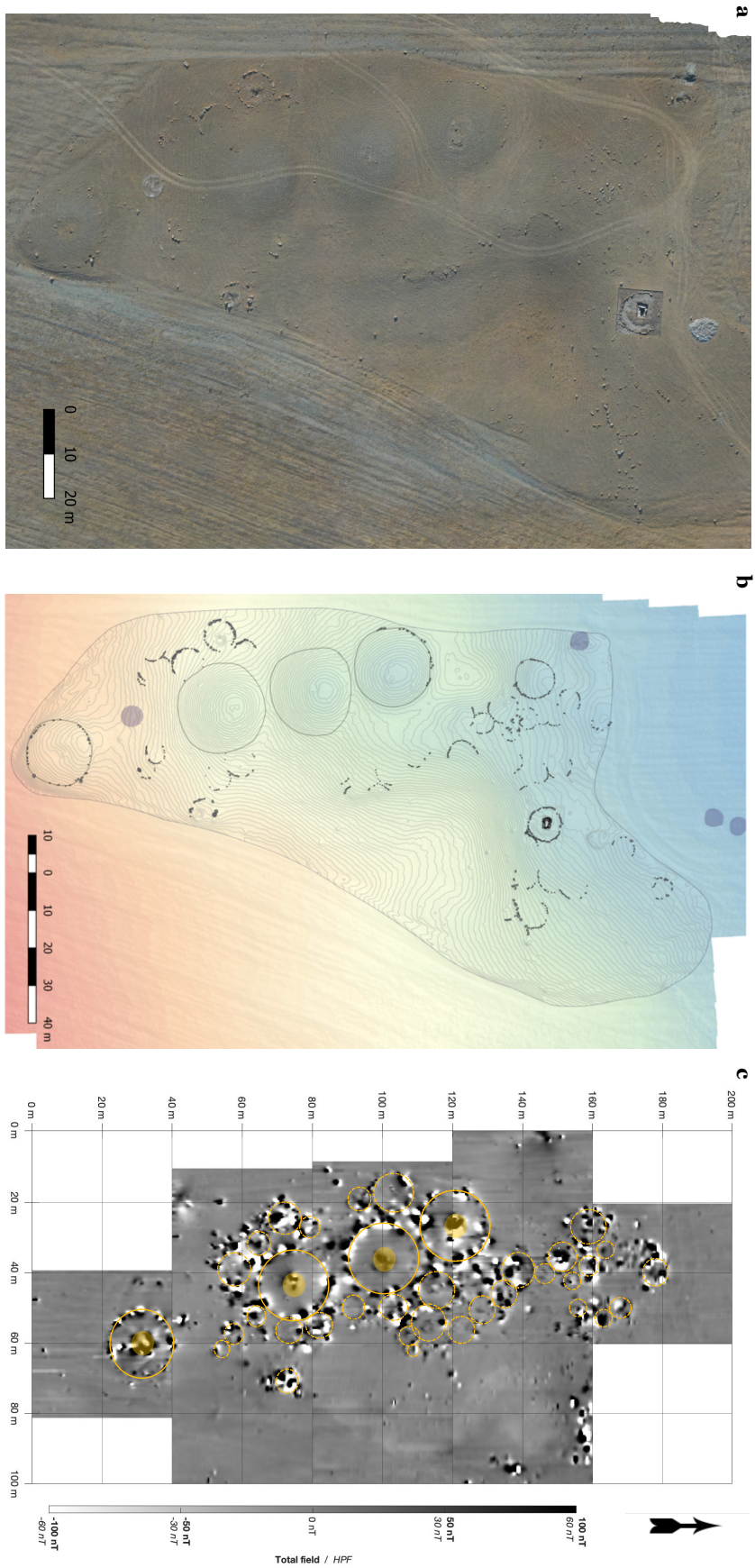


**Figure 3.4:** a) Ortho image of the necropolis Arthamish 23 (@Jonas Abele). b) Digital elevation model (DEM) of Arthamish 23 (@Jonas Abele). c) Magnetogram of Arthamish 23.

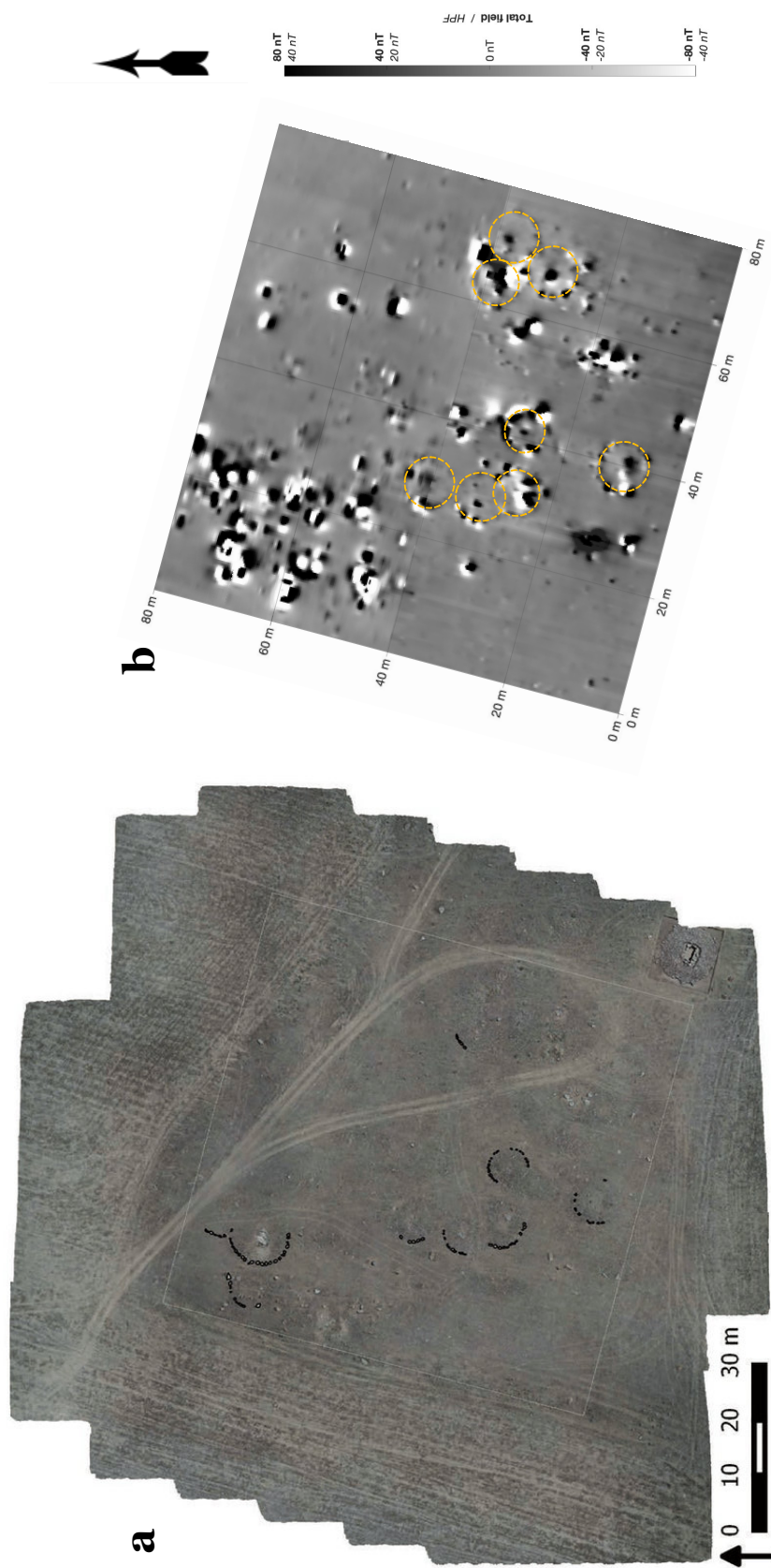


**Figure 3.5:** a) Ortho image on Arthanish 29 (from Bobokhyan & Kunze, 2021, Fig. 5)  
b) Magnetogram of Arthanish 29.

### 3.5 Considerations regarding the magnetisation's direction<sup>4</sup>

During magnetometer prospecting, one measures the superposition of the Earth's magnetic flux density  $B_E$  and the magnetic flux density  $B_O$  of an object (see chapter 1), such that:

$$B_A = B_O \cdot \frac{B_E}{|B_E|}$$

Even though the intensity of the Earth's magnetic field does not directly affect the result, the inclination of the Earth's magnetic field affects the dipole anomaly (see Chapter 4 or Ostner, Fassbinder, Parsi, Gerlach, and Japp (2019)). However, this does not explain different anomaly patterns for sites with the same inclination. The answer is the object's own magnetic field, which is generated by the object's magnetisation. For ferri- and ferromagnetic objects, the total magnetisation  $M$  is a superposition of remanent magnetisation  $M_r$  and induced magnetisation  $M_i$  (see Fig. 3.6 a):

$$M = M_r + M_i.$$

In the simplest case, the induced magnetisation is assumed to be parallel as well as proportional to the ambient field  $H$  by the magnetic volume susceptibility  $\chi$ :

$$M_i = \kappa \cdot H = \kappa \cdot \frac{B_E}{\mu_0} \quad (3.1)$$

The remanent magnetisation is also present without an ambient field and can be obtained by different mechanisms (e.g. TRM, DRM, CRM). If the remanence is not acquired in situ, it can point in any direction. The ratio of natural remanent (NRM) to induced magnetisation is given by the Koenigsberger ratio  $Q$ :

$$Q = \frac{|NRM|}{|M_i|}$$

For  $Q$  values larger than one, the ratio is dominated by the remanence and, consequently, also the direction of the total magnetisation. Withal, the absolute value of the total magnetisation is maximal for parallel induced and remanent magnetisation and is minimal when the vectors are antiparallel. For basaltic rocks,  $Q$  values can vary between 1 and 20 (Clark & Emerson, 1991); for archaeological samples,  $Q$  values range from 0.1 to over 100 (Schnepp et al., 2004). That high  $Q$  values and thus the remanence influences the anomaly patterns was already stated by different authors (e.g. Hesse, Barba, Link, & Ortiz, 1997). However, I want to prove this hypothesis with an analytical approach and show on synthetic magnetograms how the total magnetisation influences the signal sequence of a dipole anomaly.

---

<sup>4</sup>This section, as well as the next three sections, are a reproduction of the article Hahn, S., & Fassbinder, J. W. E. (2021). **The Effect of Remanence in Magnetometer Prospection**. *Revue d'archéométrie*, 45, 1. The text has been slightly altered to fit the narrative flow of the chapter.

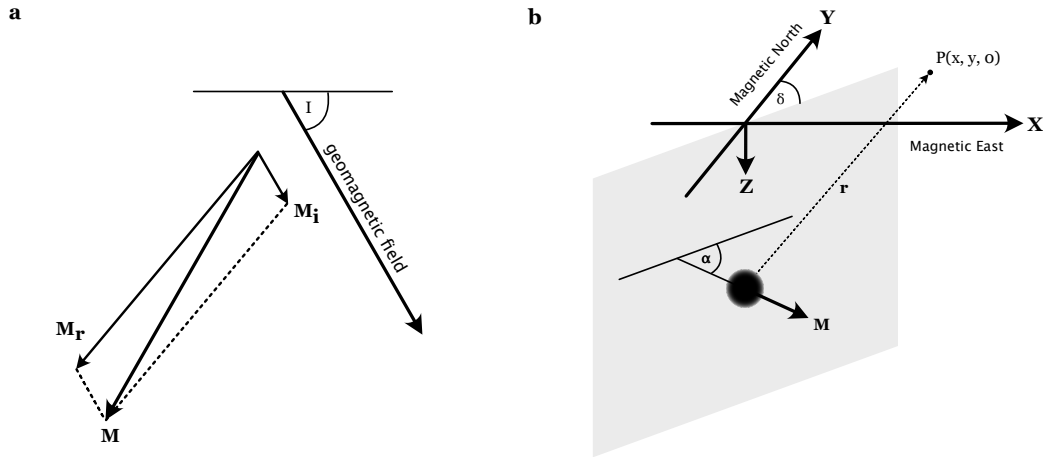


**Figure 3.6:** a) The total magnetisation is a superposition of remanent and induced magnetisation. The induced magnetisation is parallel to the geomagnetic field. b) Sketch of a uniformly magnetised sphere with the magnetisation  $M$ . The direction of  $M$  is given by  $\delta$ , the angle towards magnetic north, and  $\alpha$ , the angle towards the horizontal. The sphere is located at the origin at a depth of  $z$ . The observing point is  $P(x, y, 0)$ .

### 3.6 Modelling the effect of the magnetisation direction

The magnetic flux density generated by a dipole is given by

$$\mathbf{B}(\mathbf{r}) = \frac{\mu_0}{4\pi r^5} (3\mathbf{r}(\mathbf{m} \cdot \mathbf{r}) - \mathbf{m}r^2)$$

with  $\mathbf{r}$  being the distance between the position of the magnetometer and the uniformly magnetised sphere (see Fig. 2b),  $\mathbf{m}$  the magnetic moment of the uniformly magnetised sphere and  $\mu_0$  the magnetic vacuum permeability. The magnetic moment for this sphere is

$$\mathbf{m} = \frac{4}{3}\pi a^3 \mathbf{M}$$

with the magnetisation

$$\mathbf{M} = M \cdot \begin{pmatrix} \cos \alpha \cdot \cos \delta \\ \cos \alpha \cdot \sin \delta \\ \sin \alpha \end{pmatrix},$$

representing a sphere with radius  $a$  and a total magnetisation with the absolute value  $M$  and  $\delta$ , the angle towards magnetic North in the horizontal plane, and  $\alpha$ , the angle towards the horizontal plane. With the sphere located at the origin, a magnetometer position at  $P(x, y, 0)$ , and an approximation of the superposition of the Earth's magnetic flux density and sphere's flux density, one obtains the magnetic flux density depending on the Earth's magnetic field as well as the direction of the total magnetisation of a dipole spheric object similar as shown in Murthy (1974).

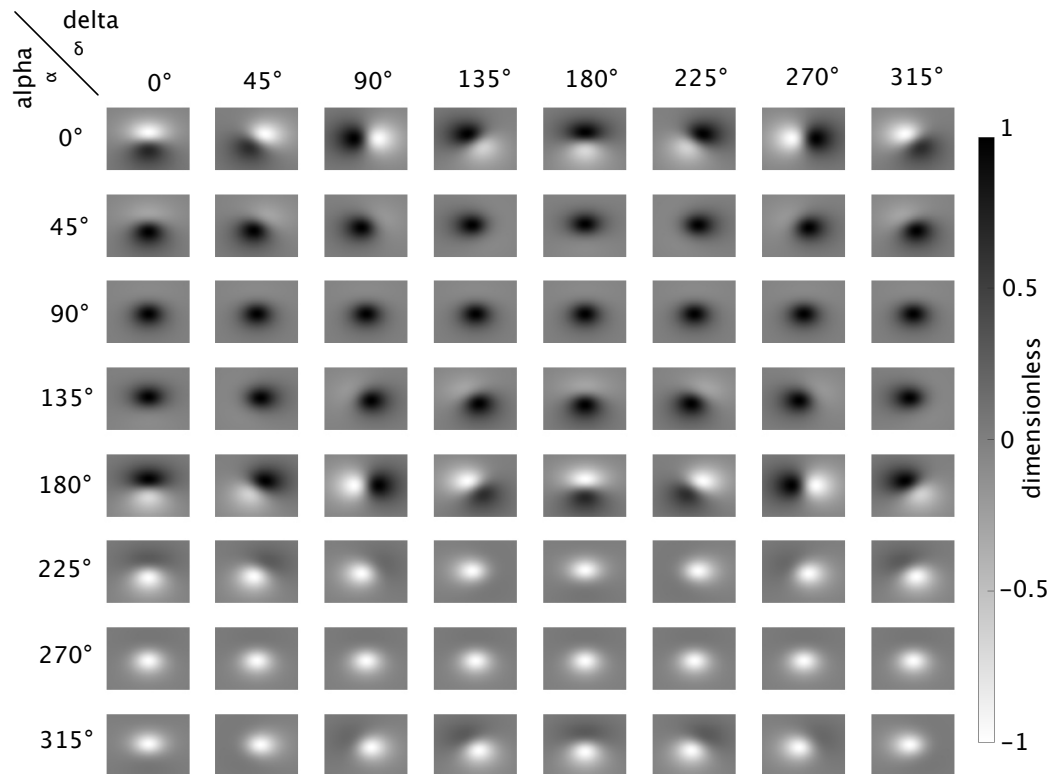


**Figure 3.7:** Synthetic magnetograms of a uniform magnetic sphere with varying directions of total magnetisation at an inclination of  $60^\circ$ . Each subplot shows a range of  $0.5\text{ m} \times 0.5\text{ m}$  around the centre of the anomaly. The flux density values are normalised by the maximum absolute value, making the scale dimensionless. The grey scale ranges symmetrically from -1 (white) to 1 (black).

### 3.7 Results of the modelling

For an inclination of  $60^\circ$  (which accounts for most European latitudes), I generated synthetic magnetograms (see Fig. 3.7) with progressively increasing values of alpha and delta in increments of  $45^\circ$ . Each magnetogram is normalised by the maximum absolute value of the magnetic flux density, removing any influence of the magnetic moment strength on the flux density. Therefore, the results are independent of  $a$  and  $M$ , but still depend on the orientation of the magnetisation. This neglects changes in the anomaly intensities with varying angles; in this work, however, I focus on an explanation for different signal sequences of strong remanent spheric objects. The depth of the sphere also has an influence on the results. Here, I assume a depth of  $(-)30\text{ cm}$ , which is comparable to a magnetometer carrying position at  $30\text{ cm}$  above the ground and an object placed on the surface. I set the grey scale of my results from -1 (white) to 1 (black) for a symmetric grey shade coding, which is normally used in displaying magnetograms in archaeological prospection. The synthetic magnetograms show an area of  $0.5\text{ m} \times 0.5\text{ m}$  around the origin, where the sphere is located.

For a fixed  $\alpha$  (rows), the progressive increase of delta describes a clockwise rotation of the total magnetisation vector towards magnetic north. The same rotation can be seen in the synthetic magnetograms. For an  $\alpha = \delta = 0$ , the signal sequence is a negative signal joined by a positive in the south. With increasing values of delta, one sees the rotation of this sequence around the origin. The distribution of the negative to positive signal is independent of delta (for fixed  $\alpha$ ).

Analogously, for a fixed  $\delta$  (columns), the progressive increase of alpha describes the rotation of the total magnetisation towards the horizontal plane. First, it submerges, pointing towards the Earth's centre and then emerges again on the other side. Again, one sees the same rotation in the results. The negative signal of the anomaly sequence is less and less pronounced and seems to vanish for  $90^\circ$ , then emerges on the south side of the positive signal. With increasing rotation, the positive signal decreases, resulting in a single negative signal.

### 3.8 Conclusion for survey results

My results show that even with positive magnetic contrast to the surrounding material, the anomaly of the sphere can assume distinctively different signal sequences, including only one positive or negative signal anomaly (see  $\delta = 90^\circ/270^\circ$ ) and also an inversion of the signal sequence (see  $\alpha = 0^\circ$  and  $180^\circ$ ). If the person who conducts the interpretation of a magnetogram is not aware of this phenomenon, wrong conclusions could be drawn. In that case, e.g. the surrounding material carries more magnetisation than the buried object or the material of the buried material is diamagnetic and, therefore, limestone or sandstone. Evidently, dipole anomalies originating from the same sphere can indeed show various signal sequences. The different remanence directions can explain their variations. Obviously, it is not sufficient to assume only total magnetisations parallel to the ambient field, as it is usually the case in current literature. My work demonstrates and emphasises the consideration of the remanence of an object on dipole anomaly patterns.

### 3.9 The effect of remanence

So far, I have shown that the direction of the total magnetisation and, thus, indirectly, the remanence affects the signal patterns and sequences. I focused with intention on the change in direction of the total magnetisation and not on the remanence directly, mainly because in a magnetogram, only the resulting effect of the total magnetisation is apparent. The question of how exactly the remanence influences the signal patterns and sequences remains open.

The total magnetisation is the vector sum of induced and remanent magnetisation (see formula 3.5). If  $\mathbf{M}_i$  is approximated with the expression found in formula 3.1 and  $\mathbf{M}_r$  with the expression

$$\mathbf{M}_r = M_r \cdot \begin{pmatrix} \cos \alpha_r \cdot \cos \delta_r \\ \cos \alpha_r \cdot \sin \delta_r \\ \sin \alpha_r \end{pmatrix}. \quad (3.2)$$

With  $M_r$  being the intensity of the remanence and  $\alpha_r$  and  $\delta_r$  defining the direction of the remanence vector analogous to the convention established in 3.6, one derives for the total magnetisation:

$$\mathbf{M} = \mathbf{M}_r + \mathbf{M}_i = M_R \cdot \begin{pmatrix} \cos \alpha_r \cdot \cos \delta_r \\ \cos \alpha_r \cdot \sin \delta_r \\ \sin \alpha_r \end{pmatrix} + \kappa \cdot \frac{\mathbf{B}}{\mu_0} \quad (3.3)$$

Replacing  $\mathbf{B}$  with the expression 1.8, one derives:

$$\mathbf{M} = M_R \cdot \begin{pmatrix} \cos \alpha_r \cdot \cos \delta_r \\ \cos \alpha_r \cdot \sin \delta_r \\ \sin \alpha_r \end{pmatrix} + \kappa \cdot \frac{F}{\mu_0} \cdot \begin{pmatrix} \cos I \cdot \cos D \\ \cos I \cdot \sin D \\ \sin I \end{pmatrix}. \quad (3.4)$$

In case of a parallel remanent magnetisation to the Earth's magnetic field, this simplifies to:

$$\mathbf{M} = (M_R + \kappa \cdot \frac{B}{\mu_0}) \cdot \begin{pmatrix} \cos I \cdot \cos D \\ \cos I \cdot \sin D \\ \sin I \end{pmatrix}. \quad (3.5)$$

In this case, the direction of the total magnetisation is evidently parallel to the Earth's magnetic field. However, the intensity of the total magnetisation and, therefore, the intensity of the anomalous anomaly depends on the intensity of the remanence of the object. In order to correctly assess the intensity of the resulting anomaly, either the latter or the Königsberger ratio must be known.

Suppose the remanence is non-parallel to the ambient Earth's magnetic field. In that case, it complicates the issue as the resulting anomaly depends on an interplay of the remanence's direction and intensity. The induced magnetisation pulls the total magnetisation towards the direction of the geomagnetic field. How effectively that works reflects the Königsberger ratio (see Fig. 3.8). For  $Q \ll 1$ , the total magnetisation is dominated by the induced magnetisation, and therefore, it is sub-parallel to the geomagnetic field. For  $Q \gg 1$ , the remanence dominates the total direction and is, therefore, sub-parallel to the remanence.

Obtaining actual values of the Königsberger ratio of soil, rocks and archaeological material on-site is not simple. Determining the NRM during a campaign is difficult because it requires special instruments and sample sizes, meaning archaeological samples must be drilled or cut. Facilities enabling these are not available during excavations. Wunderlich et al. (2022) suggest a method using two caesium probes, usually used for fieldwork, to determine the remanent magnetisation. The setup is sophisticated and requires some additional equipment. However, the measurement of the susceptibility is considerably easier, which is usually done with the ZH-instrument's Kappameter in my campaigns.

If the direction and intensity of the remanence are known, the total magnetisation can be easily calculated, and the signal sequences and patterns can be read from figure 3.7 for an inclination of  $60^\circ$ . Naturally, the signal patterns and signal sequences also depend on the direction of the Earth's magnetic field.

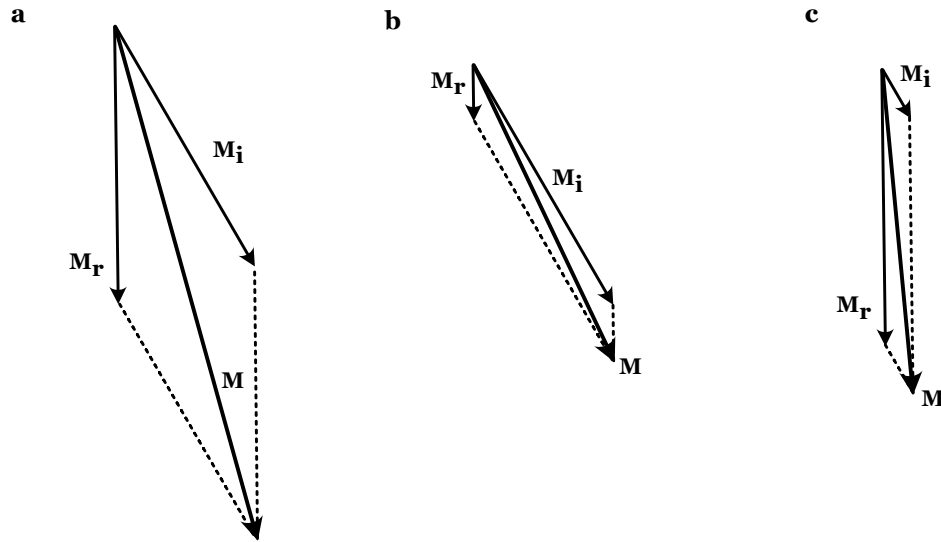


**Figure 3.8:** The total magnetisation ( $M$ ) is the vector sum of remanent ( $M_r$ ) and induced magnetisation ( $M_i$ ). The Königsberger ratio is  $M_r/M_i$ . The figure shows vector sums for different Königsberger ratios a)  $Q = 1$ . b)  $Q \ll 1$ . c)  $Q \gg 1$ . (after Lowrie and Fichtner (2020)[fig. 5.40] )

### 3.10 Deducing the remanence from a magnetogram

Assuming that the object is uniformly magnetised, has no shape anisotropy, and is a singular dipole source, among others, it can be said that the anomaly in the magnetogram reflects the direction of the total magnetisation. The 2-D greyscale magnetogram will provide a good estimation for the angle  $\delta$  of the total magnetisation if one considers an axis through the maximum and minimum of a signal sequence and determines its deflection from magnetic north. A comparison of the anomaly pattern with Fig. 3.7 provides a rough estimation of the angle  $\alpha$ . One has to be careful to give the position of the object's centre of magnetisation. Only if  $\delta = 0$  the axis of minimum and maximum provides its true location (Murthy, 1974). If the Königsberger ratio is high, this direction estimation will reflect the direction of the remanent magnetisation.

The analysis and a more accurate estimation of the remanence are decidedly more complex. There are multiple methods to estimate the total magnetisation from the magnetogram. Clark (2014) provides a good overview of the different methods. The separation of induced and remanent magnetisation can be conducted in several ways but often requires additional information on the anomaly source. One possibility is the forward modelling of the susceptibility and remanent magnetisation and obtained results equal to the original anomaly. Baniamerian et al. (2020) propose another method using a transformation in the Fourier domain, separating both magnetisations with filters and then a re-transformation in the space domain. However, this requires information on the Königsberger ratio a priori to the procedure. These methods are usually applied in aeromagnetism and seldom in archaeological prospection.

Estimating the total magnetisation from archaeological prospecting results is not as simple but has potential, e.g. dating iron slags, furnaces or kilns, shows and discusses Bruce Bevan in a few of his works (e.g. Bevan, 2009; Bevan & Smekalova, 1996). He concludes that the remanence can be estimated, but with not negligible error, primarily due to shape anisotropies (Bevan, 2010) and non-homogenous magnetisation or the interaction with other magnetic features (Bevan, Smekalova, Cucarzi, & Conti, 2001), which I agree upon.

Mastering the understanding of remanence in magnetometry and managing to determine its direction from the magnetogram opens new windows and possibilities for analysing magnetic data. For example, Scheiblecker (2021) uses the direction of magnetisation of hearths to separate different occupation phases in a multiphase magnetogram along with ceramic data. Alternatively, just an adequate method of fireplaces or hearth from magnetic rocks, as I will do in the next chapter.

## Chapter 4

# The Effect of the Earth's magnetic field

As shown in Chapter 1 Equation 1.2, the anomalous magnetic field of an anomaly at any given point also depends on the Earth's local magnetic field. Suppose a reference value equal to the intensity of the Earth's magnetic field is chosen. In that case, the approximation of the total intensity of the anomaly's magnetic field depends just on the direction of the Earth's magnetic field, which can be expressed with:

$$\mathbf{B}_E = \begin{pmatrix} \cos I \cos D \\ \cos I \sin D \\ \sin I \end{pmatrix}. \quad (4.1)$$

Consequently, the recorded anomaly of a feature depends on the declination  $D$  and the inclination  $I$  of the Earth's magnetic field to which the survey site is exposed. In the following, I will discuss the effect of the declination and the inclination, focusing on how they affect the anomaly pattern, firstly, on synthetic magnetograms and later on prospecting results for an inclination of  $15^\circ$ .

### 4.1 Approach for modelling the effect of the direction of the geomagnetic field

For the theoretical considerations, synthetic magnetograms were generated for a buried sphere with a uniform homogeneous magnetisation whose direction of magnetisation is parallel to the direction of the present ambient geomagnetic field (see Chapter 1). Therefore, the directional angles of the magnetisation of the buried sphere must be chosen so that  $\alpha = I$  and  $\delta = D$ .

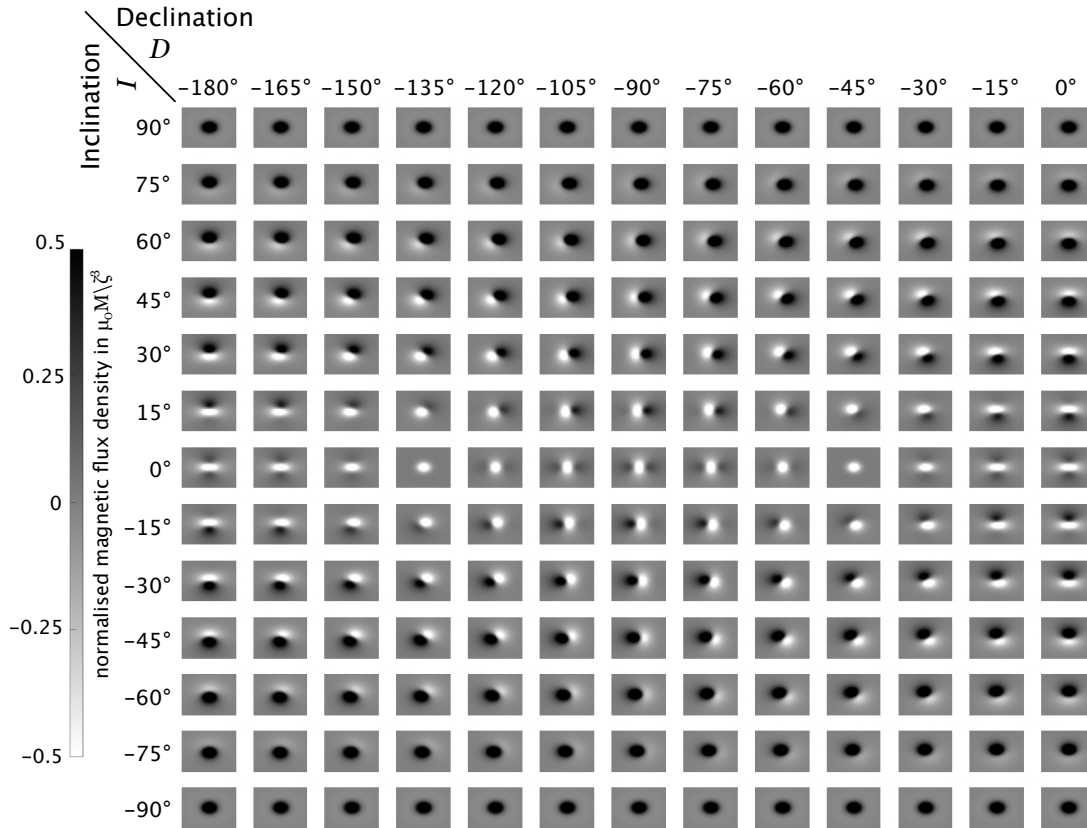


**Figure 4.1:** Synthetic magnetograms for a buried sphere with a direction of the total magnetisation parallel to the Earth's magnetic field. The units of  $x$  and  $y$  are given in burial depth.

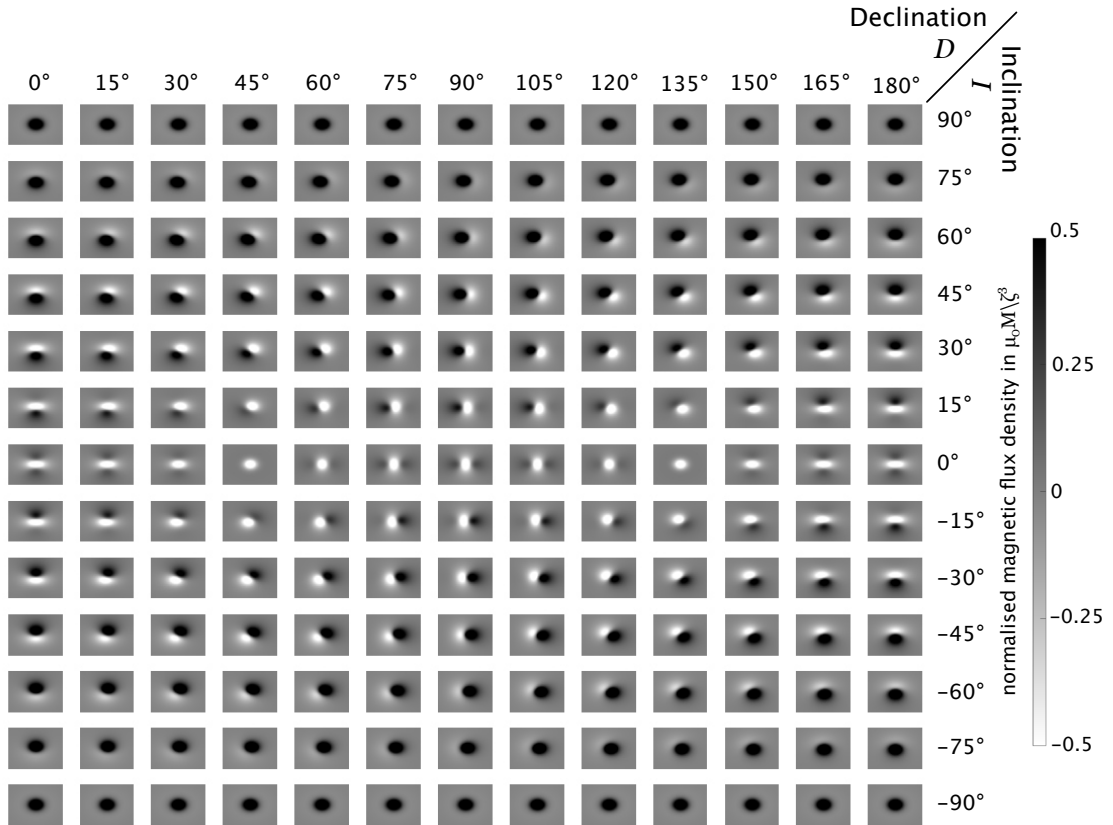
The formula

$$B_A = -\frac{\mu_0}{4\pi} M \frac{4\pi a^3}{3} \frac{Ax^2 + By^2 + Cx + Dy + E}{(x^2 + y^2 + z^2)^{5/2}}$$

with

$$\begin{aligned} A &= \sin \alpha \sin I - 2 \cos \alpha \cos \delta \cos I \cos D + \cos \alpha \sin \delta \cos I \sin D \\ B &= \sin \alpha \sin I + \cos \alpha \cos \delta \cos I \cos D - 2 \cos \alpha \sin \delta \cos I \sin D \\ C &= -3z(\sin \alpha \cos I \cos D + \cos \alpha \cos \delta \sin I) \\ D &= -3z(\sin \alpha \cos I \sin D + \cos \alpha \sin \delta \sin I) \\ E &= z^2(\cos \alpha \cos \delta \cos I \cos D + \cos \alpha \sin \delta \cos I \sin D - 2 \sin \alpha \sin I) \end{aligned}$$

is then evaluated for different  $D$  and  $I$  in increments of  $15^\circ$ . The resulting magnetograms are shown in Fig. 4.1. The peak heights of the anomaly's minima and maxima are shown in Fig. 4.2. The results will be discussed separately for the effect of the declination and the inclination.



## 4.2 Effect of declination

The declination  $D$  describes the deviation of the horizontal component of the Earth's magnetic field from the geographic north direction. With an increase in the values of  $D$ , the horizontal component describes a clockwise rotation in the horizontal plane, where  $D = 0$ , points towards the geographic North,  $D = 90^\circ$  the geographic East,  $D = \pm 180^\circ$  the geographic South,  $D = 270^\circ$  or  $D = -90^\circ$  the geographic West. The rows of Fig. 4.1 portray the changes in the anomaly pattern with increasing values of  $D$  for fixed inclinations  $I$ . For  $I$  which hold true  $|I| < 90^\circ$ , the anomaly pattern comprises two parts, or in the graphical output 'patches', a negative (white) and a positive one (black). In Fig. 4.1, these two patches are noticeable for  $I$ , which holds true  $|I| < 75^\circ$ . For these inclinations, the rotation of the anomaly pattern is recognisable. For  $I$ , which hold  $75^\circ \geq I > 0$ , the negative part (white patch) is directly north of the black patch for  $D = 0^\circ$ . With increasing values of  $D$ , this patch moves eastwards around the black patch until it is directly south to the black patch ( $D = 180^\circ$ ). For decreasing values of  $D$ , the white patch moves westwards around the black patch until it is also directly south to the black patch ( $D = -180^\circ$ ).

For  $I$  which hold true  $-75^\circ \leq I < 0^\circ$  and  $D = 0^\circ$ , the negative part (white patch) is directly south of the black patch. Analogously, for increasing values of  $D$ , the white patch moves westwards around the black patch until it is directly north of the black patch. In contrast, with decreasing values of  $D$ , the white patch moves eastwards around the black patch until it is also directly north of the black patch. Therefore, and especially if the combination of white and black patches is considered, the rotation of the anomaly pattern

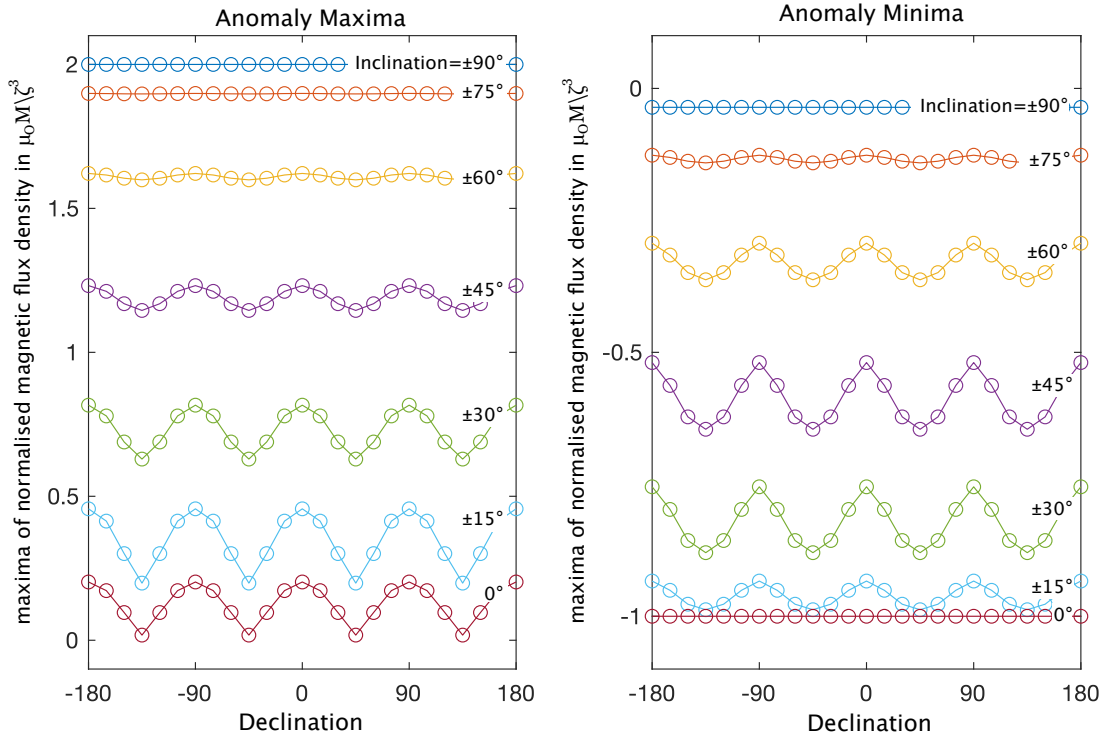


**Figure 4.2:** Maximal and minimal peak heights of the anomaly signal versus the declination for different inclinations.

corresponding with the declination is evident. The orientation of the anomaly pattern axis or the dipole anomaly axis corresponds to the declination and can thus be used to estimate the declination.

Special cases are  $I = 0^\circ$  and  $I = \pm 90^\circ$ . For  $I = 0^\circ$ , the anomaly pattern consists of up to three patches, but the rotation of the anomaly pattern axis with the declination is only limitedly recognisable. For  $I = \pm 90^\circ$ , the anomaly pattern only consists of one positive patch. As the geomagnetic field vector points directly downwards or upwards, the horizontal component is zero and, therefore, cannot show any declination. The anomaly pattern is consequently the same for every  $D$ .

To summarise, the anomaly patterns are alike for a fixed value of  $I$  (except  $I = 0$ ) but are rotated by an angle of  $D$ . Consequently, the survey direction should be chosen along the magnetic orth axis to eliminate this effect, not the geographical north axis.

However, the declination affects the peak heights of the minima and the maxima of the dipole anomaly, as shown in Fig 4.2. The curves are congruent for the positive and negative inclination, which indicates a reflection of the anomaly pattern on the axis perpendicular to the direction of declination or a rotation of  $180^\circ$ . The curves shown in both subplots oscillate with signal repetition every  $90^\circ$ . Both show their maximal inflection point at  $0^\circ$  ( $\pm 90^\circ$  and  $\pm 180^\circ$  respectively) and their minimal turning point at  $45^\circ$  ( $\pm 135^\circ$ ). The difference is that the maxima's peaks resemble  $|\cos|$ -curves while the minima's depressions resemble  $-|\sin|$ -curves with different amplitudes. Note that the minimal inflection points in the minima curves actually mean the highest negative peaks. Based on the plot, the values vary the most for an inclination of  $I = 15^\circ$  in absolute values and for  $I = 0^\circ$  in relative values (decrease of 91%) for the maxima of the dipole anomaly. For the minima,

the largest absolute and relative variation is expected for  $I = 45^\circ$ . As expected, the values stay the same for every declination for an inclination of  $\pm 90^\circ$ .

This may be interesting in theory, but it is more important to reflect what this actually means for magnetometer surveys. Regarding the world declination map (e.g. <https://www.ngdc.noaa.gov/geomag/WMM/image.shtml>), declinations up to  $\pm 90^\circ$  Chulliat et al. (2020) are observed for the Earth's magnetic field. This is true for the Arctic and Antarctic regions, but regions where magnetometer prospecting is and can be conducted are exposed to maximum declination of  $-30^\circ$  (South Africa) and  $30^\circ$  (north of Russia). The declination is usually between  $-20^\circ$  and  $20^\circ$ . For an inclination of  $\pm 15^\circ$  and a declination of  $\pm 30^\circ$ , the signal loss is 35% for the positive peak. On the other hand, a higher declination leads to a small increase in the negative part of the anomaly. For an declination of  $\pm 30^\circ$ , this increase with 11% maximal for inclinations of  $\pm 45^\circ$ . As for inclinations of Europe and Asia between  $40^\circ$  and  $80^\circ$ , the decrease in positive signal is negligible. Other effects, such as shape anisotropy, will be more significant for the detectability of the anomaly. In summary, the declination effect is avertible if the magnetometer grid is simply rotated toward magnetic north.

### 4.3 Effect of inclination

The inclination  $I$  describes the deflection of the direction of Earth's magnetic field from the horizontal plane. To explore the effect of the geomagnetic field's inclination, formula 4.1 is evaluated for the parameters  $D = 0$ ,  $\delta = 0$  and  $\alpha = I$ . This reflects a body with a total magnetisation direction parallel to the ambient Earth's magnetic field. The results are shown in Fig. 4.3 a as profile lines, also called sections, along the magnetic north-south axis, in Fig. 4.3 b along the magnetic west-east axis. Synthetic magnetograms for different inclinations are represented in the columns of Fig. 4.1.

The results shown in Fig. 4.3 a indicate that one records a two-parted signal for inclinations between the pole and equator of the northern hemisphere: a negative peak north directly followed by a positive peak south of the position of the anomalous body. The signal is reversed for the southern hemisphere. Here, the negative peak is south of the positive peak. For inclinations larger than  $30^\circ$ , the positive peak dominates signal as it can be noticed for the profile line for  $I = 60^\circ$  whose positive peak height is five times higher than the negative one. For  $I = 30^\circ$ , the ratio of both peak heights is almost equal and for decreasing inclinations, the ratio favours the negative peak until there is a dominant negative deflection at the location of the anomalies body for  $I = 0^\circ$ , the magnetic equator. The same ratios are valid for the negative inclinations. For  $I = \pm 90^\circ$ , the magnetic poles, the signal one shows a positive peak. Sections along the magnetic east-west axis, perpendicular to the magnetic north-south axis, at  $x = 0$  are shown in Fig. 4.3 b. The results show an axis symmetry of the signal for all inclinations.

In the synthetic magnetograms, see Fig. 4.3 c, the change in the peak distribution is visible through changes in the size and intensity of the two different parts/patches of the anomaly. For  $60^\circ$ , the positive patch is prevalent and sharp, with a small negative "shadow" adjacent in the north. The "shadow" becomes sharper, and its intensity increases with decreasing inclinations. For  $30^\circ$ , the intensity is similar, but the patches divert slightly: the negative is sharper while the positive one is distorted towards the south.

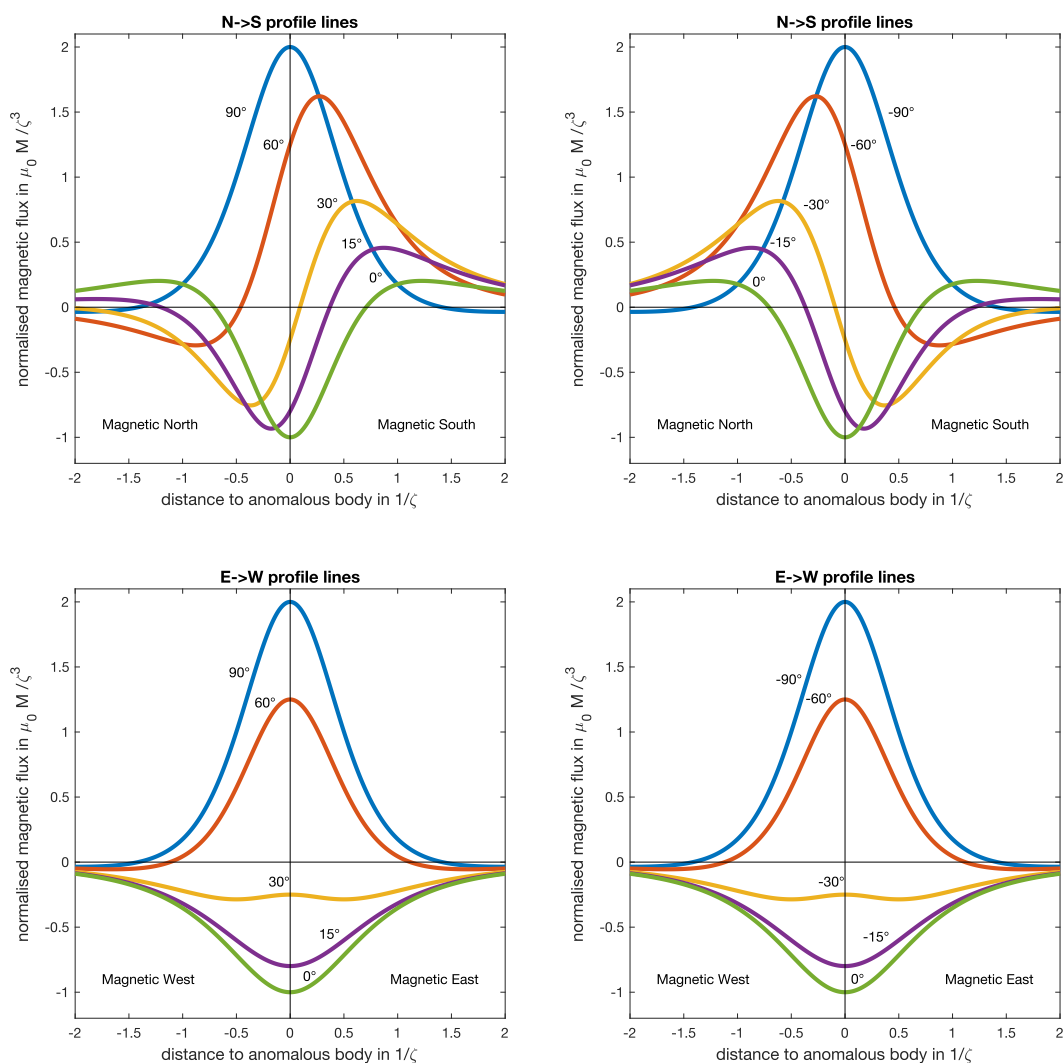


**Figure 4.3:** The recorded intensity of the magnetic flux density of a buried object in an ambient geomagnetic field with different inclinations versus the distance to the anomalous body. The magnetic flux and the distance to the anomalous body are given in units of burial depth (after Tite (1966)). The magnetic flux density is also normalised by the strength of the magnetic moment. a) North-south profile lines. b) East-West profile lines.

The effect of the declination is, to my knowledge, not discussed in the literature for archaeological prospection. The effect of the inclination is discussed in some works, (e.g. Aspinall et al., 2009). Probably the first one who discussed that the anomalies are not comparable to the commonly known European anomalies was Tite (1966) with an example at the magnetic equator and later resumed again e.g. Fassbinder and Gorka (2009). The topic is theoretically discussed in different works, but only a handful describe the effects on actual prospecting results (e.g. Fassbinder & Gorka, 2011; L ev eque, 2020). Works of different authors, Schmidt, Coningham, and Gunawardhana (2009) or Fassbinder and Gorka (2009) imply that the total field measurement can be challenging at shallow inclinations and the equator and should be accompanied by horizontal gradiometer results.

## 4.4 Effect of shallow inclination<sup>1</sup>

Fieldworks in Ethiopia in 2018 and 2020 (see Chapter 6) raised the question of how a shallow inclination ( $30^\circ < I < 0^\circ$ ) affects the magnetometer survey and its result. The Ethio-Sabaeen sites of Yeha and Melazo in the Tigray highland in northern Ethiopia, where we conducted the magnetometer survey, are exposed to an inclination of  $15^\circ$ . The results of selected magnetograms will serve as practical examples in the following comparisons. In addition, I will discuss which results can theoretically be expected for the recorded dipole anomalies with different magnetometer setups and how these results can be compared with the measurements carried out on site.

### 4.4.1 Generating synthetic data

As my study focuses on the effect of the inclination of the Earth's magnetic field, I evaluate the formula for  $D = 0$  for all the examples mentioned. To observe the effect of the inclination for buried bodies with a magnetisation parallel to the geomagnetic field, the parameters are set to  $\alpha = I$  and  $\delta = 0$  and evaluated for different  $I$ , focusing on  $I = 15^\circ$ . These are the same set of parameters as in the previous sections, so Fig. 4.1 and Fig. 4.3 are respectively the corresponding results. To study the effect of a magnetisation direction of a body unequal to the geomagnetic field at an inclination of  $15^\circ$ , I generate synthetic magnetograms for different values of  $\alpha$  and  $\delta$ . The magnetic moment normalises the magnetic flux density to obtain values of the flux density independent of the sphere's diameter and magnetisation strength. In addition, the magnetic flux density and the distance to the anomalous body are given in burial depth units, allowing a signal comparison independently of the burial depth. The theoretical results for scalar gradiometers are calculated by evaluating the signal for each individual probe, and then the values are subtracted accordingly. I assume a sensor separation of 0.5 m and 1 m for the vertical gradient. I subtract the value for the upper probe from the lower probe and divide it by the distance of the probes. For the horizontal gradiometer (separation = 0.5 m), I test for the two possible orientation directions of the device by subtracting once the east minus the west probe and once the north minus the south probe. These values are then divided analogously by the probe separation.

---

<sup>1</sup>This is a reproduction of the article Hahn, S. E. & Fassbinder, J.W.E. (in submission) **Shallow Earth's magnetic field inclination in magnetometry: A discussion in magnetograms from Ethiopia at an isocline of  $15^\circ$** . In submission to *Elsevier - Journal of Archaeological Sciences*

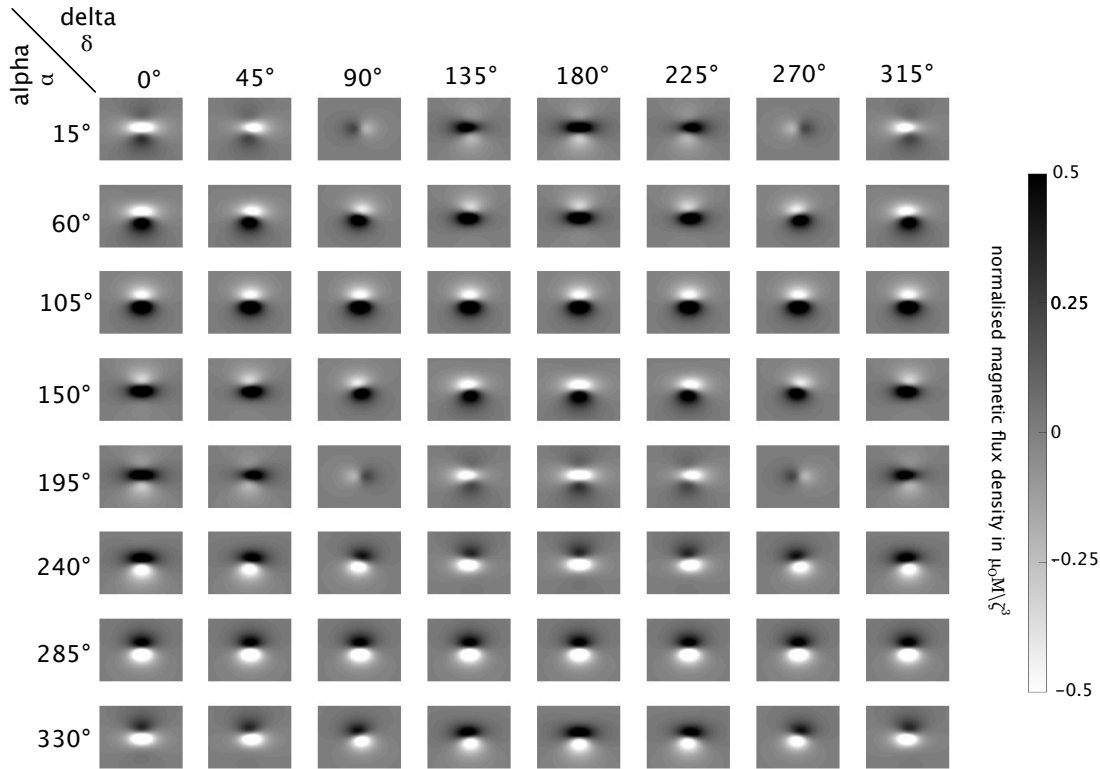


**Figure 4.4:** Synthetic magnetograms for different orientations of the total magnetisation of a buried sphere at  $I = 15^\circ$  for increasing values of  $\alpha$  and  $\delta$ . The magnetic flux is normalised by the buried object's magnetic moment and depth.  $\alpha = 15^\circ$  and  $\delta = 0^\circ$  is the anomaly pattern for a body with a total magnetisation parallel to the ambient field.

## 4.4.2 Theoretical Results

### 4.4.2.1 Inclination dependency

At an inclination of  $15^\circ$ , the negative peak of the signal is almost twice as high as the positive one (see Fig. 4.3), and the negative peak is close to the position of the anomalous body ( $x = y = 0$ ). In the magnetogram (Fig. 4.1, column  $D = 0^\circ$ , row  $I = 15^\circ$  or Fig. 4.4,  $\delta = 0^\circ$ , row  $\alpha = 15^\circ$ ), the sharp-edged negative anomaly is framed by a positive patch adjacent to the south and a positive shadow in the north. This results from values slightly higher than the reference value (see Fig. 4.1).

### 4.4.2.2 Remanence effect

Considering a remanent magnetisation that is not parallel to the induced magnetisation causes the total magnetisation of the buried object to deviate from parallelism with the direction of the geomagnetic field. The effect of varying the total magnetisation is shown for increasing values of  $\alpha$  and  $\delta$  in Fig. 4.4 in synthetic magnetograms for  $I = 15^\circ$ .

For a fixed  $\delta$  (columns in Fig. 4.4), the increase of  $\alpha$  describes the rotation of the total magnetisation from the horizontal plane over the downwards vertical towards the inverse horizontal and upwards vertical. One can see the equivalent rotation in the magnetograms. For example, for  $\delta = 0^\circ$ , the negative patch of the anomaly is less and less pronounced

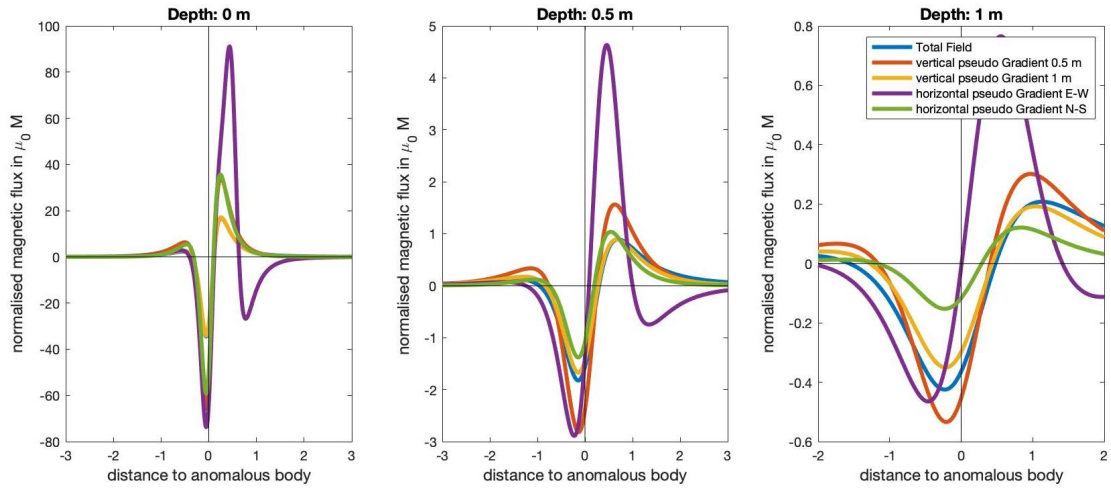


**Figure 4.5:** Comparison of different setups of scalar (or total-field) magnetometer probes for different burial depths (0 m, 0.5 m, 1 m). The setups are assumed to be carried 0.3 m above the ground. Note that the total field (blue) and the pseudo-gradient have different units. The distance to the anomalous body is given in metres.

for increasing  $\alpha$ , while the positive patch emerges more and more on the southern side till it is the middle patch of the anomaly ( $\alpha = 195^\circ$ ). For further increasing values of  $\alpha$ , the anomaly shows an inverted signal than its step  $180^\circ$  before.

The increase of  $\delta$  (rows in Fig. 4.4), the angle between magnetic North and the projection of the total magnetisation in the horizontal plane, causes a clockwise rotation of the total magnetisation vector from magnetic North. This rotation, however, is not distinctly visible in the magnetograms. The rotations cause small variations of the signal pattern but no distinct clockwise rotation, though it affects the number, size and intensity of the positive and negative patches.

#### 4.4.2.3 Registered dipole anomaly for different instrument setups

To compare the depth sensitivity of different magnetometer configurations, I evaluated the formulas for  $D = \delta = 0^\circ$  and  $I = \alpha = 15^\circ$ , but for different burial depths (see Fig. 4.5). The total-field anomaly is measured with a scalar magnetometer in duo-sensor configuration. This signal corresponds to the abovementioned one (see 4.4.2.1). The two probes can also be applied as a gradiometer or (pseudo-)gradient configuration.

Although the total-field signal and the (pseudo-)gradient do not have the same units, I present them in one graph for a better comparison. The results for a vertical gradient (bottom probe minus top probe) with 0.5 m and 1 m probe distance is shown in Fig. 4.5. The two curves resemble the total-field signal, which is described above, but the peak heights are different. Due to the multiplication factor, the 0.5 m gradient shows the highest peak maxima for all depths.

For the horizontal gradient, there are two possibilities: east probe minus west probe and north minus south probe. The north-south (pseudo-)gradient shows a sensitivity comparable to the 1 m vertical gradient and total field signal but a noticeably smaller signal strength for deeper burial depths. The east-west gradient shows a slight deviation from

the total-field signal in which the positive peak is distinctively higher than the northern negative peak. Furthermore, this setup introduces a negative "shadow" in the south. While the negative northern peak is of comparable size to the 0.5 m vertical gradient, the positive peak is remarkably high, up to three times higher than the other setups.

### 4.4.3 Prospecting method and data processing

The magnetometer surveys in Yeha and Melazo were conducted using either a Scintrex Smartmag SM4G-special magnetometer or a Geometrics G-858 magnetometer, both in a duo-sensor configuration. The data point resolution for these measurements is 0.125 m  $\times$  0.5 m. For more details on the survey technique and the data processing, see Chapter 2. Finally, I interpolated the data to a resolution of 0.25 m  $\times$  0.25 m. For a test area in Melazo, we applied the Geometrics G-585 magnetometer additionally in vertical (pseudo-)gradient configuration with 1.1 m sensor separation. With a profile line spacing of 1 m, we obtained a data point resolution of at least 0.125 m  $\times$  1 m. For the dataset of the test area, I calculated the (pseudo-)vertical gradient (bottom-top sensor) from the gradiometer measurement. I also determined the (pseudo-)horizontal gradient from the total-field data (right-left sensor). For both data sets, the heading error was removed (see Chapter 2), and they were interpolated to a data coverage of 0.25 m  $\times$  1 m and, after smaller correction of the data sets, to 0.25 m  $\times$  0.25 m. For further comparison, I also applied an image high-pass filter (HPF) to the total field data (R=10).

### 4.4.4 Results for the prospecting in Yeha and Melazo

#### 4.4.4.1 Comparison of measurement setups

The test measurement on a field in Melazo (Ethiopia), see Chapter 6, had a rough surface structure, was covered by small volcanic rocks and transected by two field boundaries. The immediate proximity to the excavation trench of an Ethio-Sabaeen monumental building suggests the existence of deeper features. Comparing the results of the different setups and processing of the data, there is a notable difference between the total field data and the two gradient magnetograms and HPF (see Fig. 4.6). The total field data shows large-scale lateral features which can be associated with deeper structures. The anomalies of the surface rocks are recognisable but not dominant. The HPF and the gradients remove the large-scale lateral features (see upper left corner) without enhancing the small-scale features, such as the rocks on the surface. The HPF enhances the contrast of the total field data, making the differences sharper and more distinctive. The vertical gradient only achieves this to some extent. The blurriness of the vertical gradient could be due to the coarse sampling resolution. The result of the horizontal gradient shows a freckled magnetogram showing high-intensity anomalies of the surface rocks, enhancing these anomalies.

#### 4.4.4.2 Spherical Features

To compare the signals of features in an approximated spherical form, I selected two magnetograms (see Fig. 4.7) measured in Yeha, whose features I could verify on-site or via orthophotos. Field boundaries transect both areas. For each magnetogram, I chose an identified surface rock and a feature not visible on the surface. Based on the anomaly pattern and intensity, it can be assumed they belong to a hearth and a shallow pit. The sections of these features are plotted versus the sections of the surface rocks. The signal of the pit and the hearth is comparable to the signal described in 4.4.2.1 and plotted in

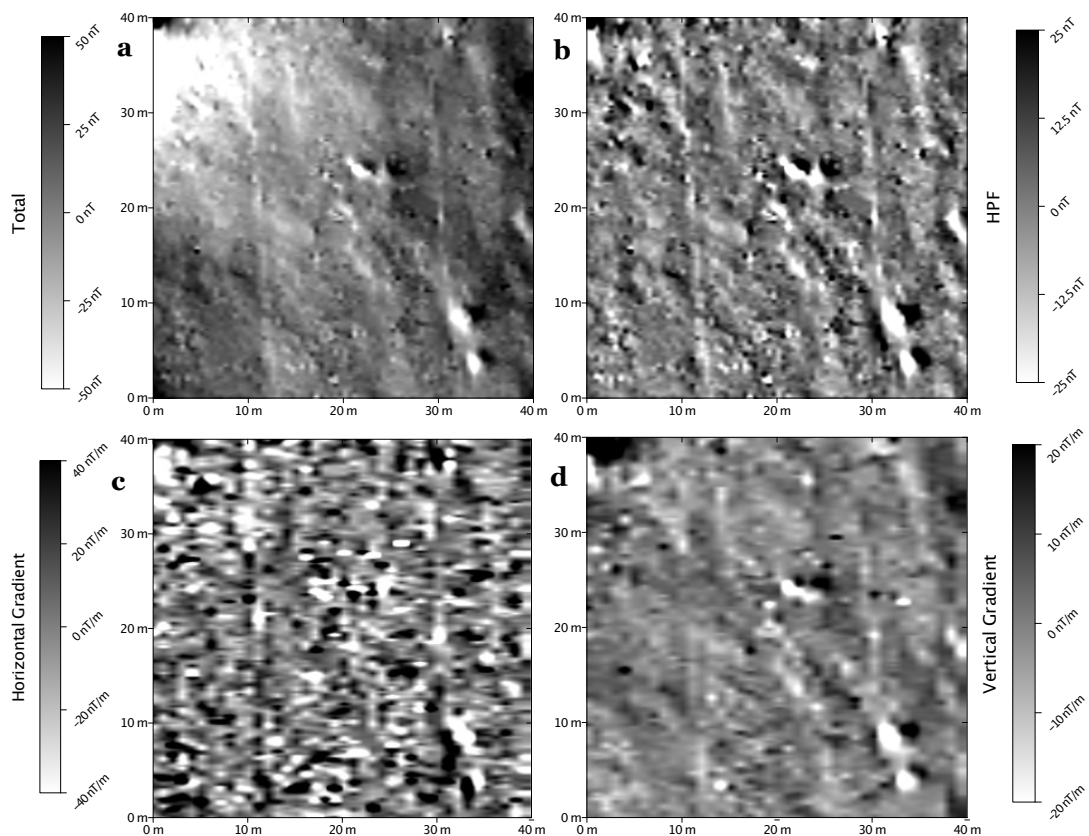


**Figure 4.6:** Comparison of different magnetometer setups and data processing of a field in Melazo. a) Results of the scalar magnetometer in duo-sensor configuration measuring the total field anomaly. b) Results of the high-pass filtered total field anomaly data. c) Results of the horizontal (pseudo-)gradient derived from the total field data. d) Results of the scalar magnetometer applied in vertical gradiometer configuration.

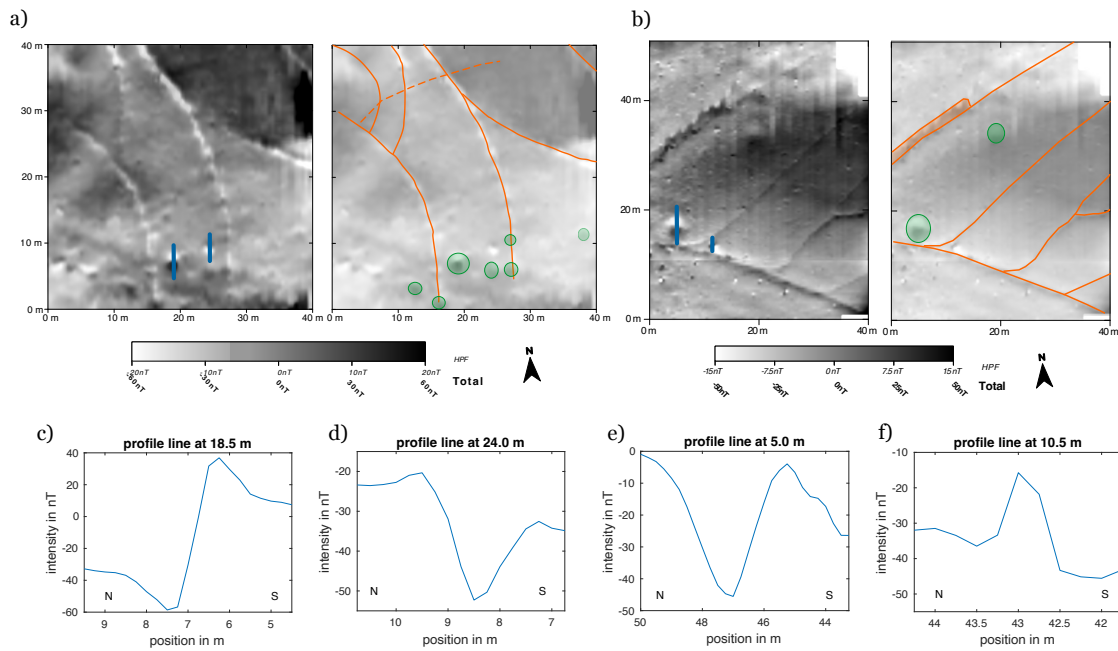


**Figure 4.7:** Magnetic anomalies of spherical features at an isocline of  $15^\circ$ . a) + b) Magnetograms and their interpretation for prospected fields in Yeha. Solid orange lines mark field boundaries visible in the aerial photos. The dashed line marks a field boundary not visible in the aerial photos, but anomalies indicate a previous field boundary. Marked in green are the fireplaces and pits. c) + d) Sections which cross features marked in a). e) + f) Sections which cross features marked in b). The sections of fireplaces and shallow pits, c) and e), resemble the signal of a dipole anomaly expected for an inclination of  $15^\circ$ . The sections of rocks, d) and f), show an arbitrary signal because their strong remanence has a direction non-parallel to the geomagnetic field.

Fig. 4.3 a for  $I = 15^\circ$  suggesting a total magnetisation of the features parallel or sub-parallel to the geomagnetic field. The signal strength values should be ignored as they vary on the chosen reference value. The signals of the surface rocks clearly deviate from the expected signal and show patterns plotted in Fig. 4.4, indicating a strong remanence non-parallel to the ambient geomagnetic field.

#### 4.4.4.3 Linear Features

Not every buried body can be approximated as spherical features; e.g. field boundaries or walls must be considered as linear features. Since we can reliably identify them, I use superficial field boundaries as an example. The two selected magnetograms of fields in Yeha with field boundaries perpendicular to each other with a north-south and east-west orientation, respectively, are shown in Fig. 4.4.4.3. Notably, the anomalies of these linear features depend on the direction in which they extend. East-west oriented field boundaries show anomalies with a positive-negative-positive sequence similar to the anomalies plotted in Fig. 4.1, column  $D = 0^\circ$ , row  $I = 15^\circ$  or Fig. 4.4,  $\delta = 0^\circ$ , row  $\alpha = 15^\circ$ , and the profile lines are comparable to Fig. 4.3 a for  $I = 15^\circ$ . North-south orientated field lines show a solely negative anomaly, whose sections are comparable to Fig. 4.3 c for  $I = 15^\circ$  or show hardly any anomaly.

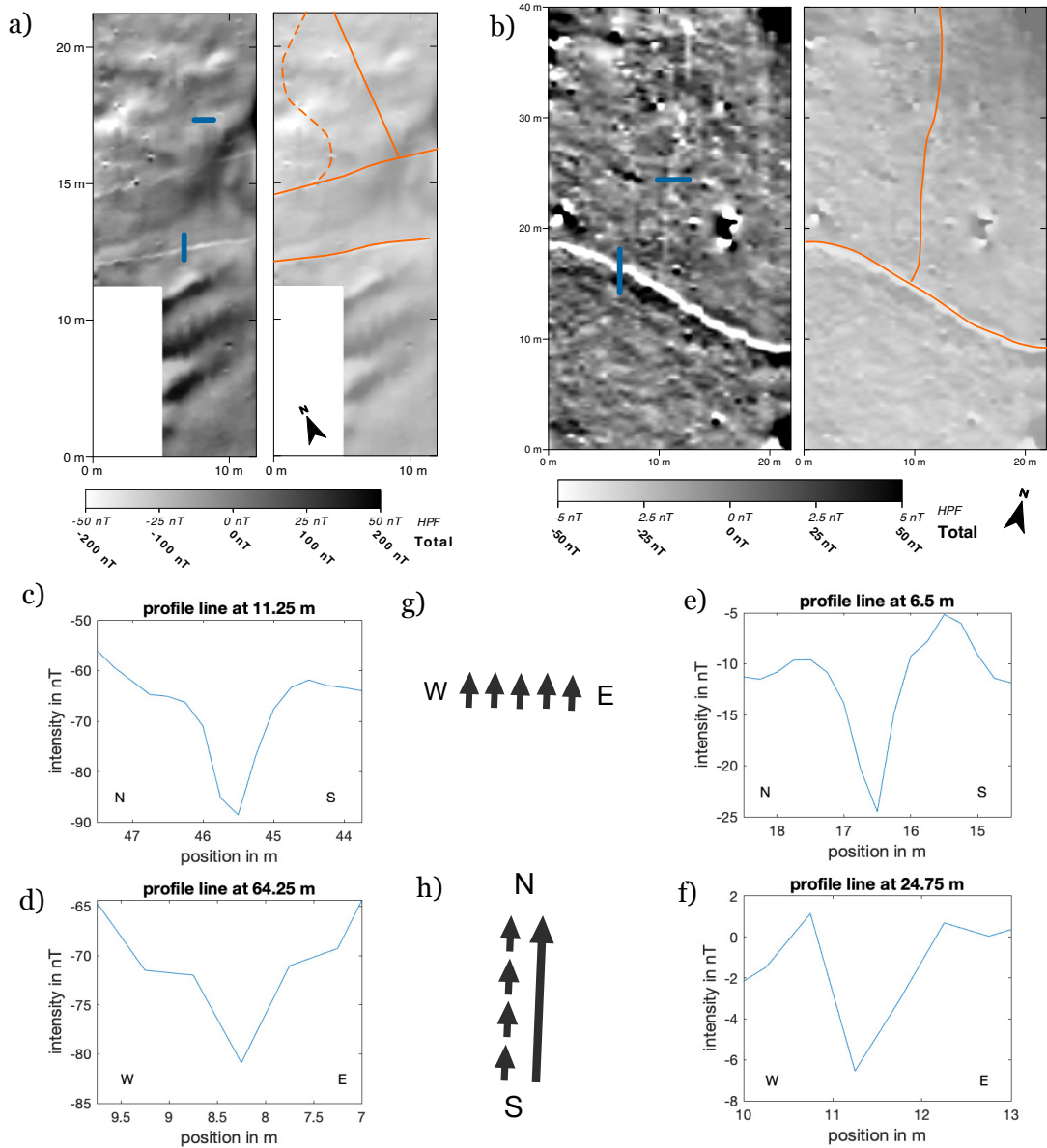


**Figure 4.8:** *Magnetic anomalies of linear features at an isocline of  $15^\circ$ . a) + b) Magnetograms and their interpretation for prospected fields in Yeha with field boundaries with a north-south and east-west orientation. Solid orange lines mark field boundaries visible in the aerial photos. The dashed line marks a field boundary not visible in the aerial photos, but anomalies indicate a previous field boundary. c) + d) Sections that cross the field boundaries are marked in a). e) + f) Sections that cross the field boundaries are marked in b). The anomalies of the field boundaries running east-west direction, c) and e), resemble the expected dipole signal for  $15^\circ$  with a negative-positive-negative pattern. The anomalies of the field boundaries running in the north-south direction, d) and f) are axisymmetrical. However, their signal is weak, which makes it hard to identify them in the magnetogram. g) The anomaly of the field boundaries running in the east-west direction can be imaged to be caused by a chain of parallel dipoles extending in the east-west direction next to each other. The direction of magnetisation is parallel to the Earth's magnetic field. h) For north-south running field boundaries, the anomaly can be imaged to be caused by dipoles' success north-south so that the south pole of one dipole is adjacent to the north pole of the next dipole. This resembles a large dipole vector along the entire field boundary.*

#### 4.4.5 Discussion

In addition to source-specific parameters, the recorded signal of a magnetic also depends on the direction of the ambient magnetic field. In the case of magnetometer prospecting for archaeology, this is the direction of Earth's magnetic field at the survey area. While the effect of the declination of Earth's magnetic field is negligible, the effect of the inclination is more severe. The effect of the declination can be easily avoided by either rotating the direction of the measurement grid during the survey or post-processing to magnetic North to avoid possible confusion during the interpretation.

The recorded anomaly signal and pattern depend strongly on the inclination of the Earth's magnetic field. The obtained results agree with earlier findings (Smellie, 1956). At European latitudes, at an inclination of around  $60^\circ$  for a body with a magnetisation direction parallel to the Earth's magnetic field, the signal is dominated by the positive part of the signal with a small negative shadow adjacent in the magnetic north. For decreasing inclinations, i.e. for survey sites closer and closer to the magnetic equator, the signal becomes more and more balanced between the positive and negative parts until the negative signal is dominant at the magnetic equator and shows two accompanying positive signals. For  $I = 15^\circ$ , the negative peak of the signal is almost twice as high as the positive one. In the southern hemisphere, the signal sequence is inverted. With larger inclinations, the positive signal again becomes more dominant, but the negative shadow is in the south. If the prospector and interpreter are unaware of this effect, it is possible to misinterpret anomalies, e.g. that the magnetisation is not acquired in situ.

A remanence of a buried object that is non-parallel to the ambient geomagnetic field causes a deviation of the anomaly signal from the above-described signal and shows different patterns. This fact is already known for different inclinations (Hahn & Fassbinder, 2021; Hesse et al., 1997). This divergence can be used to determine whether an object acquired its remanence in situ or not. Archaeological objects or related features acquire a remanence through different mechanisms, such as heating (TRM). The in-situ remanence acquired is parallel or sub-parallel to today's Earth's magnetic field, especially to the inclination. If the remanence is strong and diverts from this direction as well, it also affects the total magnetisation of the object. In the shown examples, one can distinguish volcanic rocks on the surface from fireplaces and pits, demonstrating the usefulness of knowing how to distinguish the two signals. Every feature with a roundish shape can be approximated as a sphere. As archaeological features, this applies to fireplaces, small ovens and hearths. One should keep in mind that a shape anisotropy may cause arbitrary signals, which is the case for features that cannot be approximated as spheres. For example, bigger kilns often resemble a dipole anomaly but can be more complex in pattern due to their shape anisotropy. Volcanic rocks and iron parts can be seen as spherical features. Shallow spherical pits might be approximated as spherical dipoles, but for larger and deeper pits, the assumption fails. More often, pits resemble a monopole anomaly (Von Frese & Noble, 1984; Parkinson et al., 2010).

The fact that the difference in shape influences the anomaly is shown by the anomalies of the field boundaries, which I consider as linear features. While the field boundaries running in the east-west direction show anomalies and intersections comparable to those of an induced spherical body, the field boundaries running in the north-south direction have exclusively negative, almost axisymmetrical sections of their anomalies or can hardly

be discerned. Approximately, the anomaly of the field boundaries running in the east-west direction can be imagined as being caused by a series of parallel dipoles forming a chain running side by side in the east-west direction. The direction of the magnetic moment of each of these dipoles is aligned in the north-south direction with a dip that corresponds to the inclination of the earth's magnetic field. Crossing the field line with the magnetometer, one records a dipole anomaly each time. For field boundaries running in the north-south direction, the comparison with a dipole anomaly caused by a buried sphere is not directly applicable, but they can be approximated by a chain of dipoles with the same orientation of the magnetic moment as described above. The dipoles success north-south, so that the south pole of one dipole is adjacent to the north pole of the next dipole. In approximation, this resembles a large dipole vector along the entire field boundary. The shallow inclination enhances this effect. If one crosses the field boundary, one would not really record a dipole anomaly but rather the transition between the poles. A similar effect can be imagined if one crosses the dipole anomaly always at  $x = 0$  along the entire field boundary. Nevertheless, the dipole approximation fails in this example because the north and south poles are not at an infinitesimal distance from each other but at a distance larger than the observation distance. The anomaly will still be symmetric, but the expected intensity of this anomaly will be significantly lower, even to the degree that the linear feature is no longer recognisable in the magnetogram. The intensity of these anomalies depends on the step size of the field boundary. The same can be expected for wall structures. The strength of the magnetisation of the material plays a role in the strength of the recorded intensity. In the case of field boundaries, a large step size leads to a topographical effect, which can cause an inversion of the signal sequence.

Comparing the different configurations of a total-field magnetometer, the horizontal gradient seems too sensitive to surface anomalies (e.g. small rocks), as theoretically expected, and the magnetogram tends to be too noisy to detect deeper structures. The total-field configuration is more sensitive to large-scale lateral or deep features, usually associated with geological features, whereas the vertical gradient and the HPF remove these. The latter two, therefore, show a larger sensitivity for spatial small-scale features. The blurriness of the vertical gradient could be due to the coarse sampling resolution. A combination of the total-field data and the HPF appears to resemble the vertical gradient's graphical result only in better resolution. Therefore, I conclude that the collection of total-field data is sufficient and time-saving. An interpretation based on the total-field data and its filtered version provides two insightful data sets and can replace vertical (pseudo-)gradient measurement data. A word about the rotation of the probes: when working with optically pumped magnetometers, it is generally recommended to align the probes at an angle of  $45^\circ$  to the local geomagnetic field direction. The sensibility regarding the change in the angle to the field is referred to as the heading error. For modern magnetometers, including the Sintrex and Geometrics magnetometer, the heading error is negligible at angles around  $15^\circ$  to  $75^\circ$ . Due to the setup of our Geometrics instrument, we could not tilt the probes from the vertical. In some instances during the measurement, the signal in one or both probes was lost for a few seconds. A plausible explanation: We accidentally rotate the probes into the so-called dead zones, where the optical pumping or the light modulation fail to work. The consequence is missing data for a few metres. Also, one should be careful when applying the instrument in a north-south walking direction. The magnetic field of the batteries, even when carried in a backpack, causes stripes in the magnetogram, which are barely removable in the data processing. The shallow inclination increases this effect even more. I therefore recommend an east-west walking direction.

Applying a reduction to the pole (RTP) in the post-processing of the data ideally removes the effect of the Earth's field direction on the anomaly and provides anomalies corresponding to their signal at the pole. The 3D analytical signal map is a function of the magnetic gradients. Both should theoretically provide comparable results around the globe, but experiences in geological prospection show a lack of resolution for shallow inclinations (Rajagopalan, 2003). Moreover, both remove or suppress information of the remanence, which can usually give hints on the source whether they formed their remanence in situ (e.g. fireplaces and pits) or not (e.g. rocks and lightning strikes).

#### 4.4.6 Conclusion

Magnetometer prospecting is possible around the globe, but the effect of Earth's magnetic field inclination on the results cannot be ignored. The "negative" shadow in the north of a positive anomaly at European inclinations is the more dominant part of the signal sequence at shallow inclinations (around  $15^\circ$ ). This fact can be used to distinguish between bodies which acquired their remanence in situ (e.g. fireplaces) or which show an arbitrary remanence (volcanic rocks on the surface). The shallow inclination has a detrimental effect on linear features (e.g. field boundaries and walls), as their distinctness in the magnetogram also depends on their orientation. North-south-oriented are almost impossible to spot. The shallow inclination also needs to be considered into the choice of the magnetometer configuration. We recommend a duo-sensor configuration and an east-west walking direction if prospecting with total-field magnetometer probes. Combing the data with an image high-pass filter is an easy and time-efficient alternative to a vertical gradient setup.

## Chapter 5

# The Case Study of Fara<sup>1,2</sup>

### Abstract

Ancient Šuruppak, today's Fara, was one of the major Sumerian cities in Mesopotamia. It was situated along one of the ancient watercourses of the Euphrates River. Findings date the site to the Jemdet-Nasr period (around 3000 BC), with a continuous settlement until the end of the Ur-III period (around 2000 BC). Fara was first explored and excavated in the years 1902 and 1903 by the Deutsche Orient-Gesellschaft (German Orient Society) under the direction of Walter Andrae. Multiple excavation trenches of up to 900 metres in length transecting the 1 km<sup>2</sup> wide mound are still visible to this day, enabling us to georeference the early 19th-century excavation maps. Today, the 2.2 km<sup>2</sup> archaeological area is dry and devoid of any vegetation. Thousands of deep looting pits cover most of the mound, which not only destroyed its upper metres but posed a challenge to the application of geophysical prospection methods and their interpretation. Today, the 2.2 km<sup>2</sup> wide archaeological area is dry and without any vegetation. The magnetometer prospection of selected areas on and around the mound was carried out with three devices: two total-field magnetometers and one vector gradiometer. The individual survey areas were combined in post-processing by applying a high-pass filter to the total-field datasets and multiplying the vertical gradiometer datasets by a factor of two. This approach provides visually uniform magnetograms, despite being obtained by different devices, which simplifies subsequent visual interpretation. These magnetograms allow us to review and extend the results of the old excavations. The comparison shows a good correlation in accuracy to the old drawings and positive identification of the already excavated features with magnetometry. Highlights of the survey are the discovery of the city wall confirming its existence, the layout of a unique building complex in the centre of the mound, likely a temple, traces of canals inside the city and an evaluation of magnetometer prospection over a looted area.

---

<sup>1</sup>This chapter is a reproduction of the article:

Hahn, S. E., Fassbinder, J. W. E., Otto, A., Einwag, B., & Al-Hussainy, A. A. (2022). **Revisiting Fara: Comparison of merged prospection results of diverse magnetometers with the earliest excavations in ancient Šuruppak from 120 years ago.** *Archaeological Prospection*, 1–13. <https://doi.org/10.1002/arp.1878>. The section addressing the discussion of the alternative method for merging vector gradiometer and total-field magnetometer data can be found in Chapter 1. A supplementary figure has been added for clarity.

<sup>2</sup>Funding for the project was provided by the Faculty for Cultural Studies of the LMU, by the Münchener Universitäts-Gesellschaft, and through funds attached to the appointment of A. Otto as chair of Near Eastern Archaeology. We thank the graduate students from al-Qadissiyah University who helped us in the field. Special thanks go to Marion Scheiblecker, who, as part of the geophysicist team, helped to conduct the magnetometer prospection.



**Figure 5.1:** *The region of Mesopotamia is situated within the Tigris-Euphrates river system. It occupies mainly present-day Iraq. Historical sites are marked in red. Modern Iraqi cities are provided for orientation purposes and are marked in white. Fara is located on one of the branches of the Euphrates River. Satellite data: Google, ©2022 CNES / Airbus, Landsat / Copernicus, Maxar Technologies / U. S. Geological Survey.*

## 5.1 Introduction

Prima facie, the modern site of Fara, located in the province of al-Qadissiyah in Iraq (see Fig. 5.1), around 40 km southeast of Diwaniyya, appears "unimpressive" (Heinrich & Andrae, 1931), however, it hides the remains of one of the third millennium's major Sumerian cities of Mesopotamia in plain sight: ancient Šuruppak (Koldewey, 1902b). The pear-shaped tell (see Fig. 5.2) lies in the Mesopotamian alluvial plain at 31.777222 N and 45.510833 E. The main mound's dimensions are around 1100 m in length and 600 m in width, and the site covers a total area of 220 ha (Martin, 1988). The tell is generally flat and rises only a few meters above the modern plain with a maximum elevation of 10 m. Fara was situated on the banks of one of the main branches of the Euphrates River, whose course eventually led to Uruk. River avulsions deposited metre-thick layers of water-laid silt and sand of varying ages over the last millennia (Morozova, 2005). The havoc of flood events in the Tigris-Euphrates delta finds its climax in the "Mesopotamian Flood" (Brückner & Engel, 2020), the biblical Deluge mentioned in the Sumerian King List.

Šuruppak is named as the seat of the last dynasty "before the flood"; its King Utnapištim / Ziusudra, the biblical Noah, is said to have built the ship for the evacuation of his people. The mound of Fara presents itself today as a shallow rise barren of vegetation in the otherwise flat landscape with soils of different shades of brown and red, peppered with plano-convex bricks and pottery sherds, and nowadays, it is disturbed by myriads of looting holes covering nearly the entire site (Otto et al., 2018; van Ess et al., 2006).

A team of the Deutsche Orient Gesellschaft started to excavate Fara in June 1902. Robert Koldewey, who also was in charge of the excavation in Babylon, and Walter Andrae shared the direction of the excavation of Fara as well as the smaller mound of Abu Hatab, both of which were concluded in March 1903. The published letters to the Deutsche Orient-Gesellschaft (Andrae, 1902a, 1902b, 1903; Koldewey, 1902a, 1902b; Nöldeke, 1903) from the time of the excavation are short, focusing on the ceramics or other findings and on the adventurous life during excavation. In 1931, Heinrich and Andrae published the excavation results of this campaign (Heinrich & Andrae, 1931) with a more detailed presentation of the findings and brief descriptions of the architectural discoveries. Fifty years later, the results of the German excavations in 1902/03 and the American work in 1931 were analysed by Harriet Martin and brought into the context (Martin, 1988). In combination with her survey results, Martin was able to establish the occupation history throughout the third millennium, with the foundation in the Jemdet Nasr period, an extensive occupation in the Early Dynastic I–IIIa period, and a rapid degeneration thereafter to almost total abandonment of the site at the end of the Ur III period (Martin, 1983).

The most advanced method of excavation of the early twentieth century was to lay out systematic trenches. In the case of Fara, these were 3 m wide, and usually, 2 m deep to get through all settlement layers and up to 900 m long (Koldewey, 1902b). By the end of the campaign, one search trench, heading from north-north-east to south-south-west, and twenty trenches, heading east to west, were transecting the mound (see Fig. 5.3). These excavation trenches, their debris and the Kal'a, the excavation house, are still visible today, especially in the elevation model (Otto & Einwag, 2020). The excavation uncovered dozens of so-called houses, of which only around 15 were excavated and later described in detail (Heinrich & Andrae, 1931, p. 9-17). The walls of the buildings have only 5 to 7 layers of bricks remaining. Baked and mud bricks likely alternate with the designated use of the room or the construction. Further details on the architectural findings have to be re-evaluated with the present knowledge of Sumerian architecture.

The resulting picture of the ancient city of Šuruppak is nevertheless astonishing. However, it does not fit with the supposed structure of a large Early Dynastic city, and with the information about the city which can be derived through the approximately 1000 cuneiform tablets found in the houses: Is it possible that a city of this importance did not have a city wall? Where was the palace of the ruler, which headed the centralised administration, and where was the temple of the city goddess Sud (Otto & Einwag, 2020, p. 295)? These were the reasons for the magnetometer survey at Fara in 2018, which accompanied the conventional surface survey of the site in the framework of the Fara Regional Survey Project FARSUP (Otto & Einwag, 2020). Magnetometer prospection has proven to be an adequate tool to prospect Mesopotamian sites (e.g. Becker & Fassbinder, 2001; Lambers, Fassbinder, Campbell, & Hauser, 2019; Creekmore, 2010; Fassbinder, Becker, & van Ess, 2005; Darras & Vallet, 2021).

Magnetometer prospection relies on the differences in susceptibility and remanent magnetisation between soil and archaeological features (Fassbinder, 2015). The shape of the detected anomalies depends on the shape of the feature, its orientation of the total magnetisation (Hahn & Fassbinder, 2021) and the direction of the ambient Earth's magnetic field (Ostner et al., 2019). Instruments commonly used for magnetometer surveys include total field magnetometers and vertical gradiometers. The former measures the total strength of the superposition of the flux density of buried features and the Earth's magnetic field, while the latter only provides the difference in vertical component between the

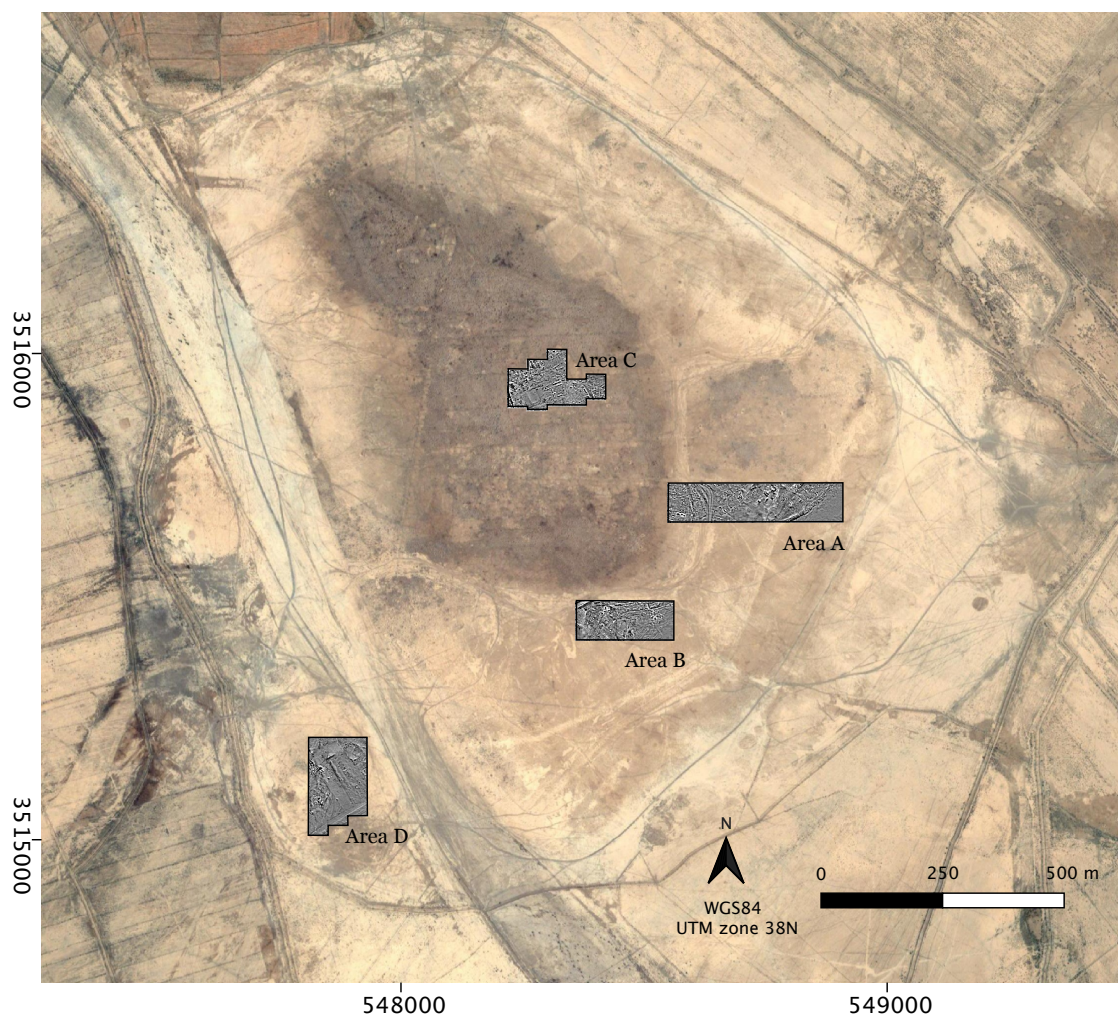


**Figure 5.2:** Overview of the tell of Fara and its situation. Fara is located in Iraq, in the province of al-Qadissiyah, around 40 km southeast of Diwaniyya. The main mound is 1 km<sup>2</sup> wide and rises only a few metres from the otherwise flat plan. The archaeological area covers around 220 ha and is today without vegetation. Satellite data: Google, ©2022 CNES / Airbus, Landsat / Copernicus, Maxar Technologies / U. S. Geological Survey.

two probes of this superposition. In the following, we present the results of this magnetometer survey and answer the posed questions: With all the recent looting, what do we still see in the magnetogram, and how does this compare to the excavations of 120 years ago? Can magnetometry help to reconstruct the settlement pattern and outline of this major Sumerian city and answer the open questions? Can the data sets of different total field magnetometers and vertical gradiometers from adjoining areas be combined into one visually uniform magnetogram?

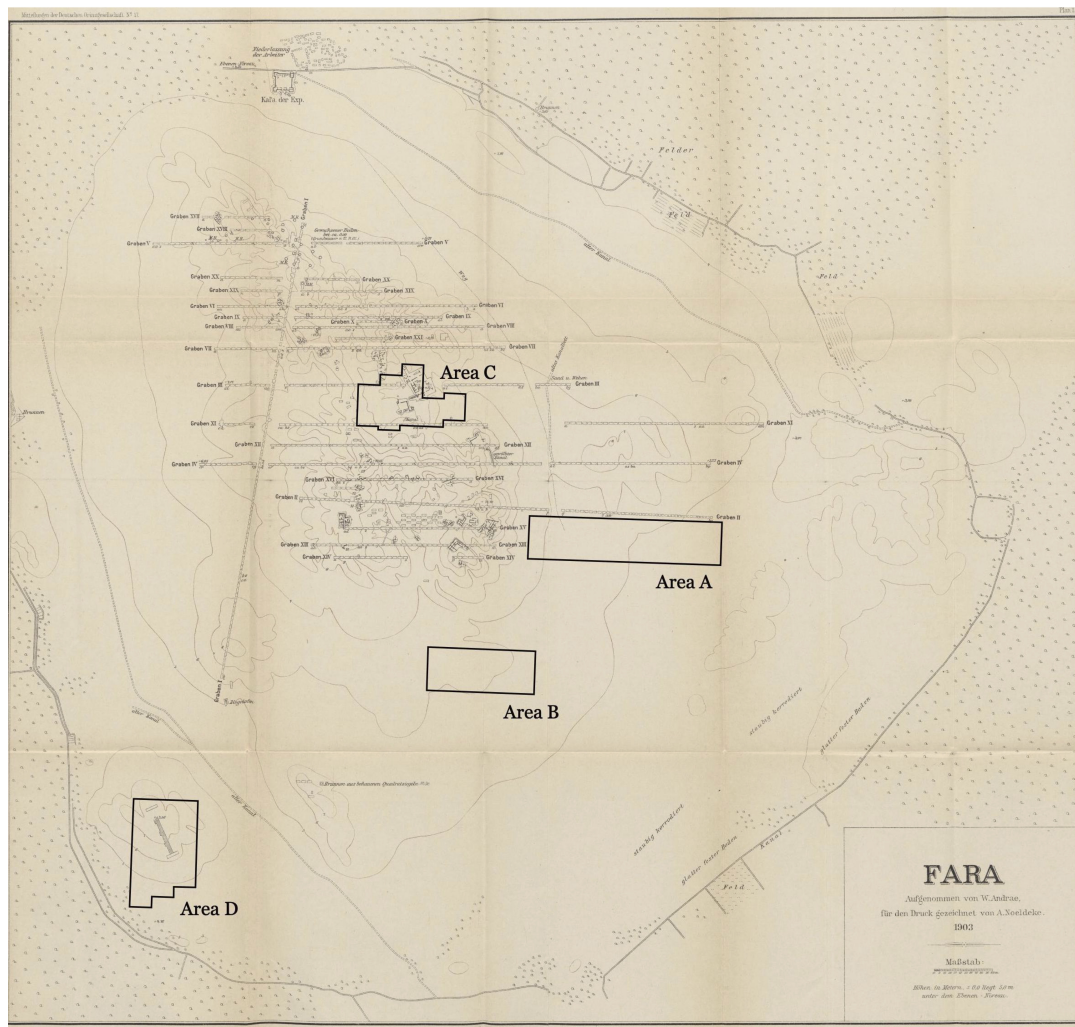


**Figure 5.3:** 1903's overview map of Fara, the excavation trenches and architectural findings, modified after (Heinrich & Andrae, 1931) with the approximate locations of our magnetograms.

## 5.2 Method

### 5.2.1 Selection of survey areas

We selected the location of the survey areas mainly based on two factors: how accessible the area was for the magnetometer survey — this depends on the number and size of the looting pits and their debris — and on their location in comparison to Andrae's overview plan (Heinrich & Andrae, 1931, Tafel 1) of 1903 (see Fig. 5.3). The old excavation plan was georeferenced using the noticeable topography caused by the old excavation trenches. Area A runs parallel and lies south of Trench II and 55 m east of Trenches XV, XIII and XIV. It covers the southern end of a smaller mound to the east of the main mound. The layout of houses had appeared in this area after rainfall, making this a promising area for magnetometry. Area B is located in the shallow lower town which surrounds the main mound. This area had not been investigated earlier by test trenches, nor had it suffered severe looting due to its flat character (see also Fig. 5.2). Area C is situated in the middle of the main mound, where the central depression separates the southern and the northern halves of the site. Andrae's Trench III a-c had brought to light a building which differed

from other houses in several respects: it was larger, and most walls were built of baked bricks; therefore, the excavators wondered whether this had been a palace or a temple (Heinrich & Andrae, 1931, p. 13). Area D lies on the separate little mound southwest of the main mound, separated by the ancient river course. Andrae's map shows a wall, which he described as a broad brick wall that terminates at both ends. Andrae wondered if this might have been a part of the fortification wall (Andrae in Heinrich & Andrae, 1931, p. 6).

### 5.2.2 Instruments

For time efficiency, we conducted the survey with three magnetometers in Fara in 2018 over a period of a few days: Two optical-pumped, self-oscillating Caesium magnetometers in duo-sensor configuration measuring the total-field, a Scintrex Smartmag SM4G-special magnetometer and a Geometrics G-858 magnetometer, as well as a vertical vector gradiometer, a Foerster Ferex instrument, with a vertical probe spacing of 65 cm as indicated by Foerster. Each survey area was divided into three adjacent segments, each of which was measured simultaneously by a different magnetometer. We opted for this procedure primarily for safety reasons. Since the magnetometer survey team stayed together in one area, it was easier to be guarded by policemen, a requirement of the German university. It also made communication easier in the case of instrument problems, as the prospectors would not be spread over the tell. The segments of the measurement areas were further divided into individual grids measuring 40 m by 40 m. The resulting data were merged during data processing. The probes were carried approximately 30 cm above the ground. Since the probe distance of each instrument is 0.5 m, the data resolution is at least 0.1 m by 0.5 m, thus fulfilling the requirements for archaeological prospection guidelines (Schmidt et al., 2015). The edge points of each grid were georeferenced by GPS measurements.

### 5.2.3 Data processing

Pre-processing of the data focuses on the removal of a constant off-set caused by the heading error of the caesium probes and interpolating the data to an appointed resolution of 0.25 m by 0.5 m. We combined the measured grids for each instrument to obtain a graphical data output of their designated survey segments using the software "Geoplot" (Geoscan Ltd. UK) and corrected measurement mistakes. The correction for the Geometric magnetometer is worth mentioning. We were not able to fully stabilise the setup against strong winds during fieldwork, which led the probe axis to rotate around the rest of the frame. This caused unintentional spikes in our data. We removed these outliers by replacing the values that were two to three times the standard deviation above the mean with the mean value. Afterwards, we first combined the Caesium magnetometers' sections. We compensated for the diurnal variation of the Earth's magnetic field by subtracting each grid's calculated mean value from the data values. Further, we adjusted visually the data for linear changes in the Earth's field by multiplying data of individual lines with an incrementally increasing or decreasing multiplication factor. For non-linear changes, we added varying values to sections or whole lines. Eventually, we interpolated the data to a resolution of 0.25 m  $\times$  0.25 m. To a copy of this dataset, we apply a high-pass filter to enhance small-scale archaeological features and suppress the contribution of geological sources by removing larger spatial wavelengths (Scollar, 1969; Aspinall et al., 2009). This effect, along with the correction for the diurnal variation, resembles the idea of gradiometer or pseudo-gradient measurements. Consequently, we were able to combine the high-pass filtered data with the data of the Ferex instrument. Empirically tested, a visual adaptation works best when an image high-pass filter with a radius of 10 is applied

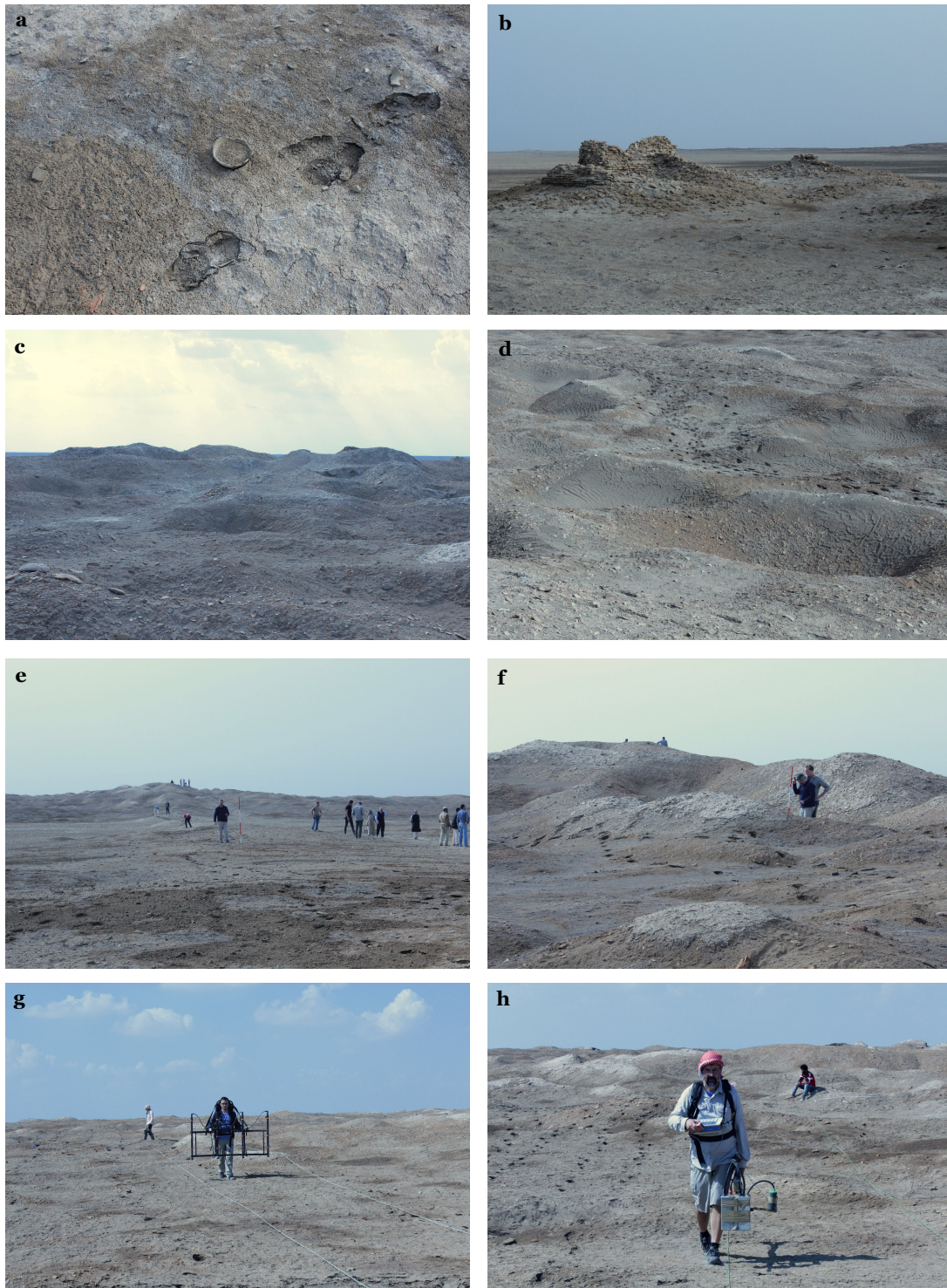


**Figure 5.4:** Site conditions at Fara and impressions of the fieldwork: a) When walking on the site, one sinks in a few centimetres and leaves footprints. b) Remains of the 1902/03 excavation house, the Kal'a. c) + d) Looting holes. e) + f) Stacking out the grid of the magnetometer survey at the east of the main mound. g) Prospecting with the Foerster fluxgate magnetometer. h) Prospecting with the Scintrex Smartmag SM4G-special magnetometer.

to the total field data. The data of the gradiometer are multiplied by a factor of two for this inclination (around  $50^\circ$ ) (NCEI Geomagnetic Modeling Team and British Geological Survey, 2019) to compensate for the only one measurement direction of the gradiometer (see Fig. 2.7c). This value is also tested empirically by comparing the standard deviation of both data sets as well as the intensity of similar features. For the interpretation, we studied the combination of total field and gradiometer data as well as the high-pass filtered data and the gradiometer data. For displaying our results, we show only the latter. Additionally, we used drone images of the area and Andrae's drawings (Heinrich & Andrae, 1931; Koldewey, 1902b) for the interpretation.

## 5.3 Results and Interpretation

### 5.3.1 Area A

Immediately adjoining the main tell to the east, we prospected Area A covering an area of 360 m by 80 m. The resulting magnetogram is shown in Fig. 5.5. In the eastern part of the magnetogram, a prominent feature is noticeable, which we interpret as the city wall. It is traceable over a length of 140 m in the magnetogram, oriented southwest to northeast and has a slightly convex curved shape. The width of the city wall's anomaly ranges between around 6 m to 11 m. The city wall seems separated into different sections by a transversal interruption in the feature, forming a pattern comparable to either a "Kastenmauer" or a casemate. Whether the compartments were originally filled or not cannot be deduced from the anomaly in the magnetogram. Transversal subdivisions can be found every 6 to 7 m, differently pronounced in the magnetogram, implying a square compartment size of 6-11 m by 6-7 m. The thickness of the internal and external walls is likely similar, but the anomaly seems wider at the external wall. Based on the anomaly of the internal wall, a thickness of around 1.5 m can be assumed. The intramural space cannot be clearly determined but can be roughly given with around 3 to 8 m. Overall, the city wall in the southern part of the magnetograms seems to be better preserved because more details are noticeable than in the northeastern part. The southern part is also more pronounced, but this can also be related to the more east-west orientation of the wall, where the direction of Earth's magnetic field enhances the structures. There is no sign of a city gate in the prospected part of the city wall. Southeast of the city wall, no houses, buildings, or streets are detectable. There are some indications for a spatial large-scale feature in the southeastern part, but the survey needed to cover more of it for an educated guess as to whether this is of architectural or geological origin. However, the lack of detected archaeological traces indicates that the magnetogram covers an eastern outer part of the ancient city. The features parallel to the city wall can be earthfills, a ditch or parts of the collapsed city wall.

The middle southern part of the magnetogram covering a half elliptic area of 40 m by 120 m seems "blurry" in the sense that features that continue in the western, northern, and eastern directions are more clearly traceable outside this part than inside. The magnetic intensity of the features reduces drastically so that we are in the instrumental noise of the Foerster Ferex magnetometer. Additionally, the anomalies appear to be broader in this part than in other parts of the magnetogram. Most features' shapes are vague; only strong magnetic features, e.g. streets, are clearly noticeable. Because this effect does continue over different grids prospected by different instruments, it must be an effect caused by the local soil conditions.

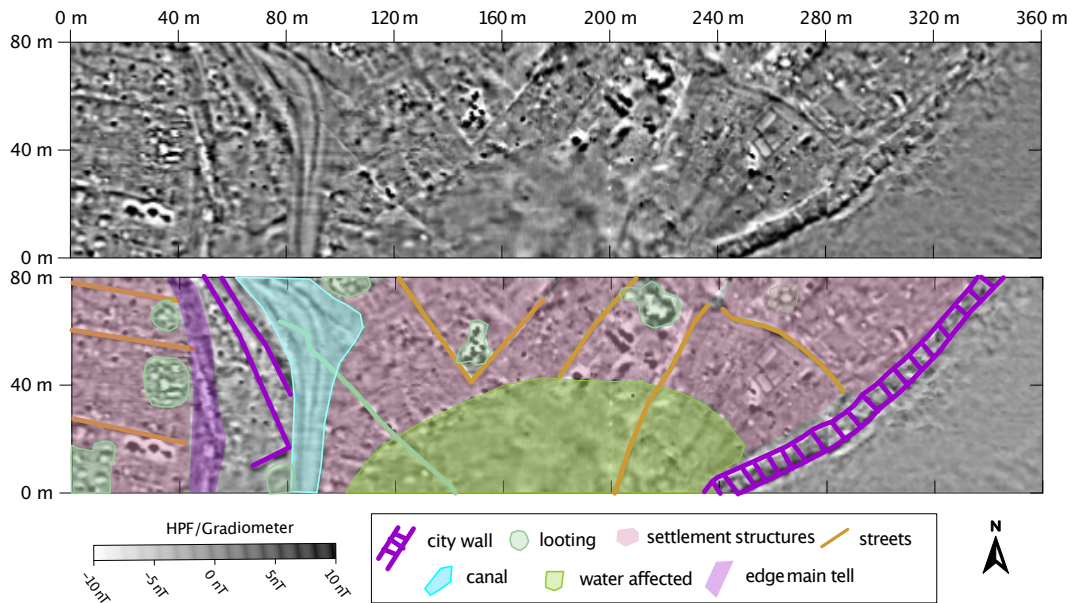


Figure 5.5: Magnetogram of Area A.

Most streets are clearly detectable in the magnetogram with a negative-positive signal sequence. This suggests that their base is supported by material with higher magnetic magnetisation, e.g. pottery sherds, or they follow brick-built vaulted drains. Similar to the city wall, the streets show a northeast-southwest orientation or are perpendicular to this direction. The majority of the magnetogram shows mostly rectangular building structures of different sizes. The anomalies of the building structures have different magnetic intensities, likely due to slight differences in the building material, which causes differences in the magnetic properties. The usage of baked bricks can explain the high intensity of some wall's anomalies. We refrain from marking the building structures in detail since the different anomalies' strengths may hide walls and door holes. Also, Early Dynastic buildings are built closely together, which complicates the assessment of rooms and space between the house and courtyards.

At 80 m, a palaeo-channel or canal is detectable with a north-south orientation with a slight bend towards the east. Its different accompanying anomalies suggest that this waterway changed its course — its deflection towards the east — over time. In the east, it seems that it cuts into pre-existing building structures. Therefore, these buildings date before this very eastern course of the canal.

Slightly more westerly, some long linear structures are noticeable. This could be an inner city wall or perhaps an earlier one before the east mound was added to the city. At 40 m, there is a large spatial anomaly recognisable over the whole width of the magnetogram, especially in the total field data. This could be the topographical transition to the main tell. West of this feature, building structures continue on the main tell. Here, streets and houses show a more east-east-south orientation, distinguishing them from the lower city. Furthermore, the features on the main tell are not as well pronounced as those in the lower city. One reason could be the rougher surface on the main tell, caused by looting holes or stronger erosion of the structures.

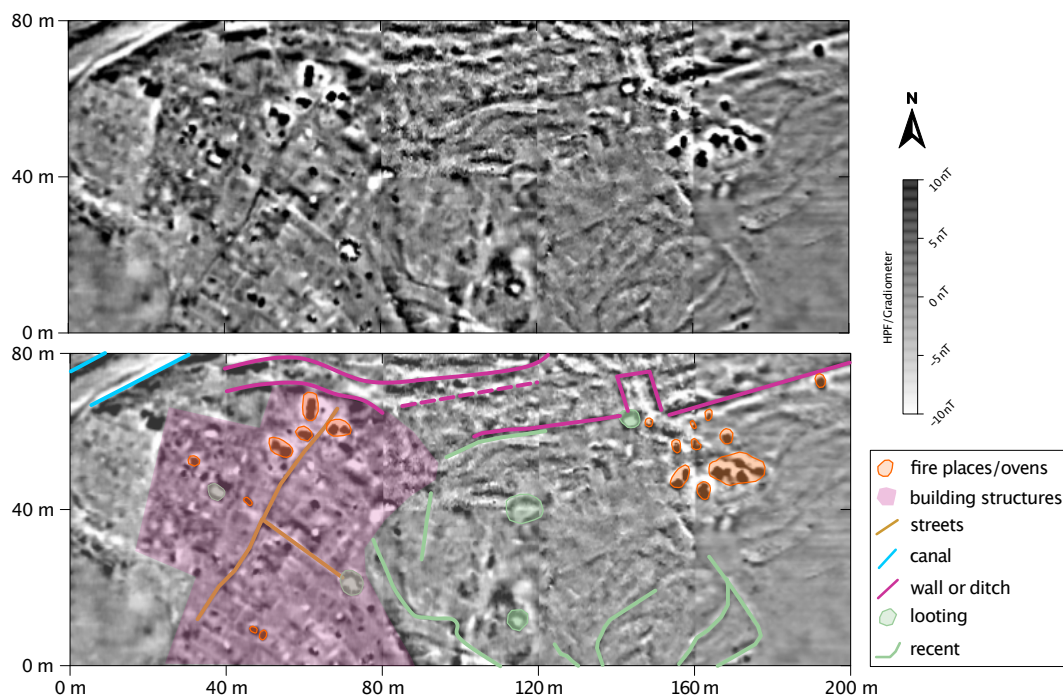


Figure 5.6: Magnetogram of Area B.

### 5.3.2 Area B

Directly south-south-east to the main tell, we prospected Area B (see Fig. 5.6), covering an area of 200 m by 80 m. The remains of a canal with a northeast orientation are visible in the very upper left corner of the magnetogram. From the digital orthophotos, it is clear that this is the continuation of the canal, which is also observable in Area A.

The majority of the western half of the magnetogram shows building structures covering an area of 60 m  $\times$  60 m. Again, we refrain from marking these in detail (see 5.3.1). Northeast-orientated streets divide the building assemblies. Very strong, round or oval anomalies are fireplaces or ovens, some of which are already visible on the surface. We only marked those with an intensity of 30 nT or higher in the merged magnetogram. This is equivalent to 15 nT in the Ferex gradiometer data set and approximately 30 nT in the total field data set. Outside of this area, a set of ovens or fireplaces is recognisable (Fig. 5.6 at 160 m and 60 m). East of the marked building structures, there are no clear traces of further houses or buildings. Only some curved features are noticeable. In comparison with the orthophotos, we identify some of these features as erosion channels or runnels, which are exemplarily marked in the magnetogram. Similar-looking anomalies could be explained by former courses of erosion channels. Another explanation for these curved features is the quarrying of mud for pottery or brick production. The possibility of this surmise is supported by the set of fireplaces in and outside of the building areal and the closeness to the canal.

Two parallel features with a separation of 6 m, possibly wall structures, oriented east-west and traceable over 80 m in the north of the magnetogram. In the middle part of the magnetogram, these two lines are accompanied by another wall structure, around 8.5 m

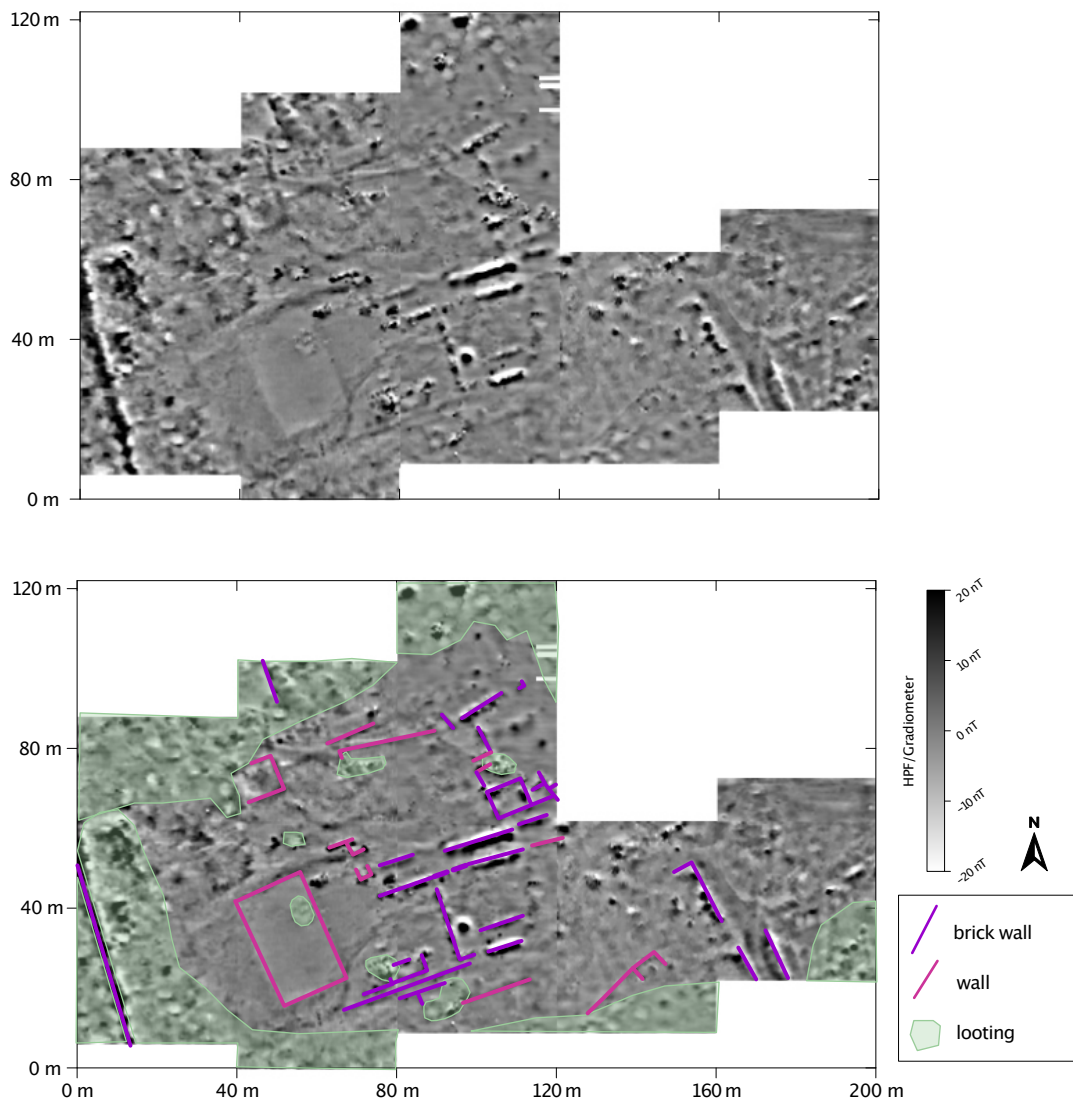


Figure 5.7: Magnetogram of Area C.

further south, with one setback. These walls could belong to a thicker wall, perhaps the inner city wall. It is difficult to deduce more from the magnetogram because this part of the magnetogram seems highly noisy.

### 5.3.3 Area C

Area C (see Fig. 5.7) covers an arbitrarily shaped area of around 16000 m<sup>2</sup> on the main tell. The extent of this area to prospect was limited by looting holes and erosion channels. The multitude of looting holes located at the outer edges of the magnetogram cause strong interferences. The northeastern corner is still covered by the debris from the 1902 excavation of this building in trench III a-c. The middle part is only "peppered" by a few looting holes, which — if also recognisable in the orthophotos — are marked in the magnetogram. A part of this area was excavated already in 1902 (see Discussion).

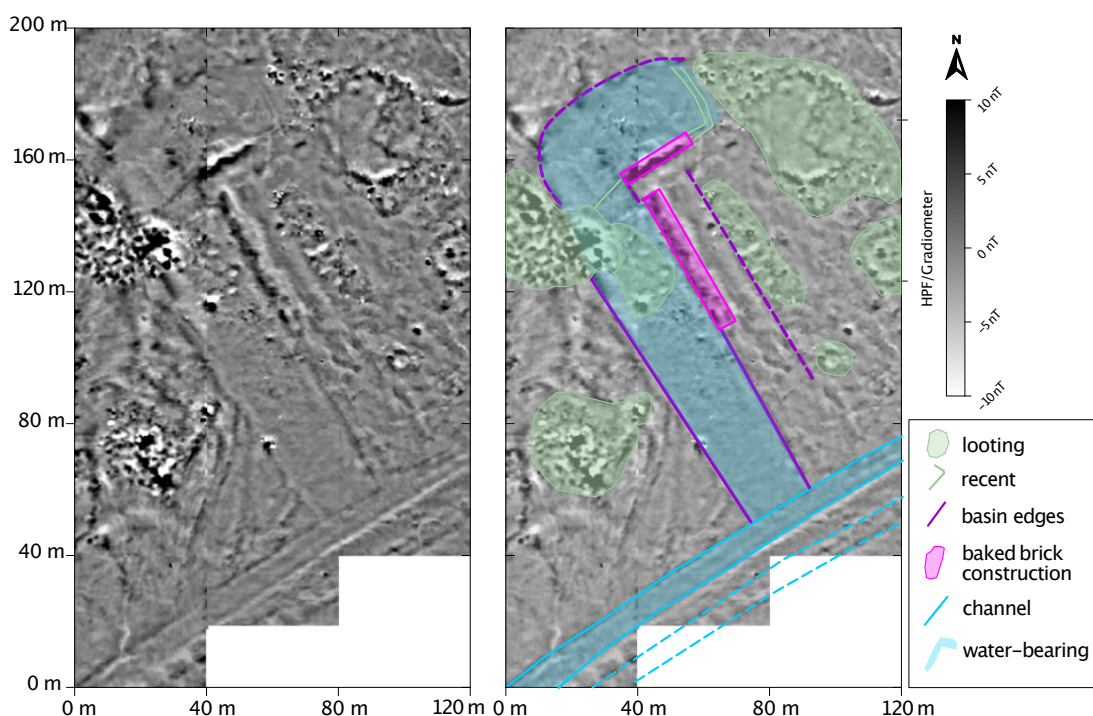


Figure 5.8: Magnetogram of Area D.

A prominent feature is a  $27\text{ m} \times 17\text{ m}$  large rectangle. The area seems magnetically very homogeneous, which indicates that uniform material was used for the whole area on a flat, smooth basis. At the western corner, a linear feature is prominent, and the magnetogram covers 53 m of its length. The anomaly width is 4 m; the true physical length might be smaller. From the strength of the anomaly, it is reasonable to assume that this is a baked brick construction. However, the anomaly shows semi-regular changes in width. This suggests a road rather than a wall. The variation in intensity also favours the idea of a road as the irregularities could be due to pavement with pottery. Baked brick walls can be seen at different places in the magnetogram. Their lengths vary from 8 m to 18 m. Other wall structures noticeable in the magnetogram show a lesser strength in intensity. They are made from a different material, e.g. mud bricks or slightly fire-damaged mud bricks. Almost all of these features, including the baked brick structures, show an east-north-east orientation or perpendicular to this direction. Some of the features' anomalies are affected by the early twentieth-century excavation, but mostly, the looting compromises the identification and, eventually, the interpretation of less distinct features. In other words, if pre-existing archaeological features are not magnetically strong and predominantly linear, their identification over the strong interference caused by the looting holes is difficult.

### 5.3.4 Area D

Approximately 450 m south-west of the main tell, we surveyed Area D (Fig. 5.8) with a size of around  $200\text{ m} \times 120\text{ m}$ . It was situated west of the main watercourse. Large parts of Area D are affected by looting, which we marked in the magnetogram. In this example, the biggest looting pit has a diameter of 28 m. In the unaffected parts, no streets or buildings are detectable. Prominent in the centre of the magnetogram is a strong

magnetic anomaly feature which forms a right angle. The high intensity (around +20 nT) implies a construction with a material with a high total magnetisation, quite likely baked bricks. Based on the shape of the feature and the surrounding anomalies, we propose that this is the quay wall of one of the city's harbours. The hook-shaped area around the quay wall seems more magnetically homogeneous than other parts of the magnetogram and can be interpreted as the basin surrounding the quay. The basin shows a width of 20 to 26 m.

In the south, a parallel running linear feature implies an adjacent channel, oriented northeast/southwest, with a width of around 8 m. A continuous linear anomaly along the harbour basis could imply that this channel was still active or at least water-bearing when the harbour was no longer supplied with water. There are some parallel features south of the channel, but whether these belong to another fortification of the channel or a separated construction is unclear because of the lack of survey in this part.

The long side of the quay adjoins orthogonally the channel. From this edge to the northern edge, the quay measures a total length of 110 m. The quay's northern part shows higher intensity anomalies, which are likely caused by baked brick construction. For the long side, a length of 71 m of this high-intensity anomaly can be confirmed. The northern edge shows a similar strong anomaly of 21 m in length. The quay seems to resemble a slight T-shape at its northern end. The true width of the quay remains unanswered if the shape is symmetric, as well as if the basin continues in the northeast long side of the quay. Anomalies of looting pits on top of the areas in question make it impossible to reconstruct these details.

The southern part of the quay and the basin wall show a lesser anomaly intensity. Since a change in building material is unlikely, one explanation could be the different stages of preservation of the baked brick construction.

## 5.4 Discussion

In what follows, we would like to compare our magnetometer prospection results to Walter Andrae's plans and Robert Koldewey's and Ernst Heinrich's notes. As mentioned above, we refrained from enhancing individual houses for all settlement areas and found by magnetometry (which applies to Area A and Area B). Looting and differences in building materials and their magnetisation make it hard to identify walls and openings in the walls correctly. Moreover, as Andrae and Heinrich noticed (Heinrich & Andrae, 1931, p. 10), baked bricks, remains of the paving, can be found inside the rooms and the courtyards, which also deludes a clear magnetic response from the walls. What certainly plays a role in the visibility of the wall structures is the usage of baked bricks as wall bases (Andrae, 1903; Heinrich & Andrae, 1931, p. 10). Surprisingly visible are the streets in the settlement areas. Since it is not undoubtedly clear where the recorded vaulted drains were running (Heinrich & Andrae, 1931, p. 10), the magnetometer results suggest that they were running below the streets.

Area A lies south, 5 to 10 m distant from trench II (see 5.2.1 and Fig. 5.3). Our identification of buildings or settlement structures visible in the magnetogram is partly confirmed and complemented by drone photos taken after rainfall (Otto & Einwag, 2020). Both the magnetogram and the drone images show streets and the ground plans of houses with several rooms and courtyards. The walls must be close to the surface to be detected with both methods. The drone photos also confirm a continuation of the settlement

towards the north (Otto & Einwag, 2020, p. 304, Fig. 7). Puzzling, therefore, is why there are no descriptions of the architectural structures found in trench II or on this eastern mound in general or why the excavation trench stopped at this eastern point. With our results, though, we have the answer to Andrae's posed question (Heinrich & Andrae, 1931, p. 7), whether the search trenches extended far enough into the periphery of the tell to trace the city wall! They missed the city wall by a few meters only. In order to trace the course of the city wall, we suggest continuing the magnetometer survey north of area A in future campaigns.

Area B has never been investigated before. Our findings of multiple fireplaces complement the survey results that this area of the lower town was used for pottery production (Otto & Einwag, 2020). In the magnetogram, we see settlement structures. It is unclear if the upper part of the magnetograms shows a continuation of the inner city wall. The visibility of features of this area is clearly more affected by differences in topsoil conditions. One explanation for the "washed out" sections in the magnetograms could be the soil's and archaeological features' interaction with water. Though Fara is relatively dry today, until the twentieth century, the mound of Fara was still close to the marshes (Andrae, 1902b; Martin, 1988), and it seems, therefore reasonable, that the tell or at least the lower parts of it were prone to flooding events and/or their soils were saturated with water. Either the "blurry" areas are covered with more alluvial sediments than the other parts, or water-logging is dissolved partly by the iron oxide minerals of the soil and the buried archaeological features. The dissolution of iron oxide minerals decreases the magnetic susceptibility of the soil (Thompson & Oldfield, 1986; Dearing, Lees, & White, 1995; Hanesch & Scholger, 2005) which also applies to the iron oxides present in the archaeological features, which consequently makes them less detectable with magnetometry.

For Area C, we compare our results with the details of the building excavated in trench III a-c (Heinrich & Andrae, 1931, p. 10, 12-13) and its drawing (Heinrich & Andrae, 1931, Tafel 5). The approximate location of the building is provided by Andrae's (5.3) overview plan, and with the help of the anomalies featured in the magnetogram, we were able to georeference the drawing. To compare the drawing with the relevant part of the magnetogram (Fig. 5.9), we copied the contour of the excavation section and the room numbers given by Andrae onto the magnetogram. Regrettably, we were only able to cover the identical area since the northeastern part is inaccessible for magnetometer prospecting because of the debris of the 1902 excavation.

Heinrich refers to it as the largest building excavated at Fara (Heinrich & Andrae, 1931, p. 12). Andrae already mentioned the uniqueness of the building, as all its walls were built with baked bricks (Andrae, 1903), thus explaining their good visibility in the magnetogram. Apparently, though, the visibility of features also depends on the state of preservation of the walls. For example, the southern wall of Room 1 (see Fig. 5.9) is traceable in the magnetogram in its entire length. The small wall segment in line with this longer wall is also recognisable in the magnetogram. Andrae sketched these two walls in his drawing with throughout with small bricks. This implies a good preservation upon excavation and, based on the magnetogram, a good conservation until today. The western wall of the room was only hinted at by Andrae with a few bricks. Its traces are barely visible in the magnetogram. Even more pronounced is the difference in the visibility of the walls for Room 2: the eastern and southern walls are identifiable in the magnetogram, again sketched throughout with bricks, while the western wall, sketched with only a few bricks, is magnetically not traceable at all. The more remains are intact, the clearer and

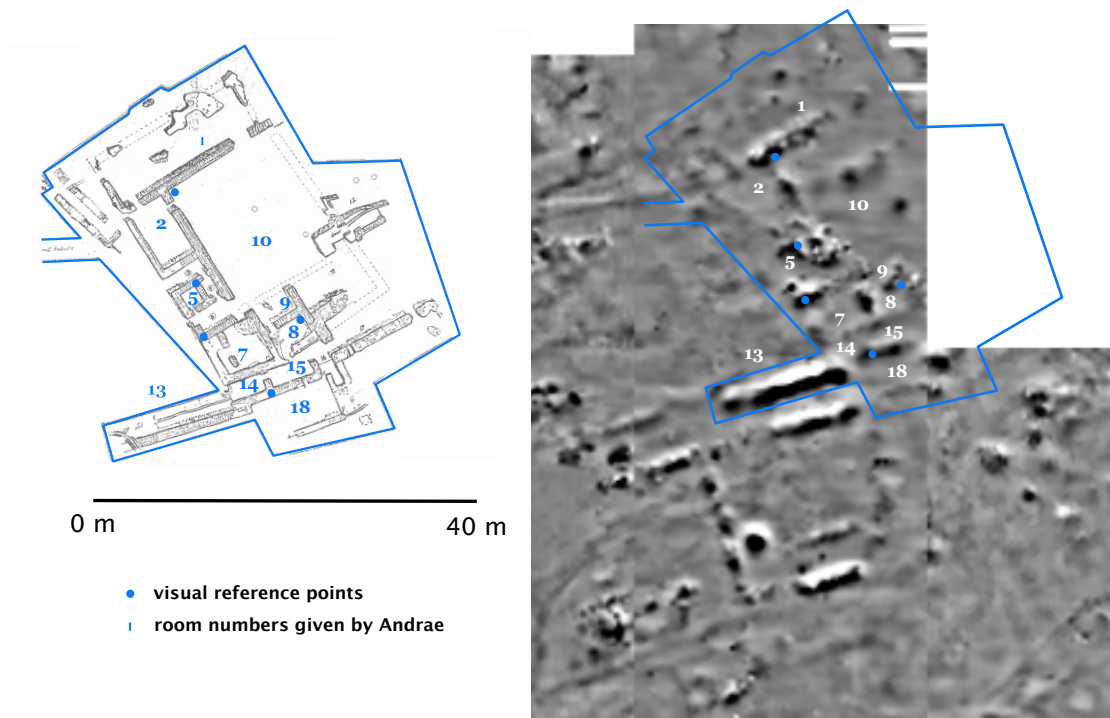


**Figure 5.9:** Comparison Area C of the map of the building in trench III a-c (Heinrich & Andrae, 1931, Tafel 5) with the magnetometry. The numbers refer to the room numbers given by Andrae and are displayed here in colour and enlarged. The blue dots serve as visual reference points which have the same geographic coordinates.

more pronounced their anomalies are in the magnetogram. In other words, if there is no change in building material, in the case of baked bricks, no change in source material and the firing process, the strength of the magnetic anomaly of a wall relates dominantly to the number of bricks preserved on that wall. Similar relationships can be found for all other walls as well. The high correspondence of drawing and magnetogram testimonies Andrae's attention to detail and the good conservation of the remains after excavation. It also shows that the width of magnetic anomalies does not necessarily reflect the true physical width. In our example, east/west orientated walls show an anomaly width three times higher than the width recorded by Andrae. For the width of magnetic anomalies, the object's magnetisation strength (high for baked bricks), burial depth and physical dimension play a role. The object's orientation towards the Earth's magnetic field direction also impacts the recorded anomaly. In this example, walls orientated east/west are more enhanced than north/south-oriented ones. The northeast corner of room 5 seems to be an exception to this conservation statement. However, the magnetic anomaly caused by the remains of this corner is veiled by the magnetic anomaly caused by the looting at this very spot.

Looting disturbs the natural remanent magnetisation of the soil that it acquires during pedogenesis or deposition. In the magnetogram, this is usually noticeable as "freckled" areas with a lot of small dipole anomalies with very small radius. Furthermore, the natural distribution of the magnetic susceptibility is mixed and causes differences in the induced magnetisation and, consequently, in the anomalies. Larger dipole anomalies with higher intensities could be due to iron particles and pieces introduced to the soil during the

looting, whose strong and spacious anomalies can hide potential archaeological features. Additionally, the edge of the looting holes causes noticeable anomalies since they vary topographically from the surrounding area. At the edge, more soil and, therefore, more magnetic material is gathered, explaining the circular character of the anomalies of the looting pits. Comparable features have been recorded by e.g. Fazeli Nashli and Schmidt (2006) or Millaire and Eastaugh (2011).

In the magnetogram, we also see features west of the area covered by Andrae's map of the building in trench III a-c. These anomalies are not distinct enough to provide detailed evidence of further rooms in this part of the magnetogram. The excavation plan for the whole site (Fig. 5.3) shows walls south of the building plan whose anomalies we also detect in the magnetogram. The reason why these remains are featured in the overview excavation map but not in the excavation drawing for this building is not evident.

The usage of baked bricks, as well as the larger dimensions of the rooms and the courtyard, might imply that the building had a special function. Earlier suggestions were a palace or a temple, while the niches in the southern wall (Andrae, 1903, p.9-11) could speak in favour of the latter. Dimensions and layout are comparable to the large Early Dynastic temple at Umm al-Aqarib (Almamori, 2014).

As mentioned above, Andrae's excavation plan shows a uniform feature at the location of Area D. The way it is sketched differs notably from the other features. Andrae was apparently aware of its unique character since he tentatively interpreted this massive built wall, with strong reservations and doubts, as a part of the fortifications (Heinrich & Andrae, 1931, p. 6-7). We interpret this as a massive construction of baked bricks. The width of the feature is 6.8 m with 6.5 to 7 m long and 2 m strong projections, maybe buttresses, on the southeast side every approximately 22 m (measurements from the georeferenced map). The sketched feature is traceable over a length of 71 m. Directly adjacent to the south, the map quite likely shows an excavation trench as well as one towards the north, about 15 m from the top of the sketched feature, but no features are visible within these trenches. In comparison to our magnetometer results, the sketched feature could be, indeed, the quay wall constructed from baked brick, as we detected. At most places, the anomaly's width is around 7 m, coinciding with Andrae's map. This implies that the feature lies very close to the surface. Otherwise, the deeper burial depth would broaden the detected anomaly. At some places, the feature's anomaly is 9 m wide, likely resembling the width of the buttresses. The buttresses are not very distinctive in the magnetogram, but irregularities and an asymmetry implicate the presence of buttresses. We are able to trace the brick construction for 45 m only, but we are able to detect the basin wall over a length of another 57 m. As already stated, we are not able to say whether the building material changes or not. Andrae's map lets us assume it doesn't. Also, with its help, it can be assumed that the quay does not continue towards the East. According to our georeferenced map, they just missed the head of the quay by meters.

[...<sup>3</sup>]

---

<sup>3</sup>The discussion on the method how to merge total-field magnetometer and vector gradiometer data sets can be found in Chapter 2.

For the survey at Fara, the method introduced in Chapter 2 successfully provides a magnetogram that appears uniform regardless of the instruments used. Visually, the interpretation of our magnetograms was made significantly simpler since features were easier to trace and compare over the different segments. In our case, the use of a high-pass filter is more favourable since all visual data processing is then carried out by one software and is, therefore, more convenient and time-saving.

## 5.5 Conclusion

The case study in Fara shows that magnetometer prospection can offer new insights into already partly excavated sites. The magnetometer survey was conducted with one vertical vector gradiometer and two total field magnetometers on adjoining segments of the measurement areas. The method of applying an image high-pass filter ( $R=10$ ) on the total field data sets and multiplying the gradiometer data sets by a factor of two successfully provided a combined magnetogram of all three segments in which the change in the instrument is imperceptible. The comparison to the old excavation reports and maps shows a good correlation with our magnetometry results, especially regarding intact baked brick walls and vice versa. The results of the magnetometer survey bear testimony to the accuracy and richness of details of the excavation maps drawn by Walter Andrae. Heavy looting of the tell affects not only the accessibility of the site but also challenges the further interpretation of magnetograms or even renders parts of them interpretable. Looting pit anomalies provide strong background interference, which makes the identification of weak magnetic features difficult or impossible. If the magnetic contrast is good and the features are linear, they can be detected even despite heavy looting. This is the case for Area C, where we were able to detect an unknown road in trench III. One further detail which can imply that this building is indeed a temple. One of the major findings is traces of the city wall on the east side of the town, which confirms its existence and proves that the search trenches of 1902 to 1903 were not heading far east enough. We see an intact part of the city wall, which seems to be a casemate wall. Former flooding events might play a role in the sharpness of features in the magnetograms by adding sediments or dissolving magnetic minerals. Nevertheless, the continuation of the magnetometer survey at Fara has the potential to add further and more detailed insights into the settlement structure, which future excavations will hopefully complement.



## Chapter 6

# The case study of Yeha<sup>1</sup>

### Abstract

The settlement Yeha and the hamlet Melazo, both located in the Tigray high plateau in the north of Ethiopia, are two ancient sites of the Ethio-Sabaeen culture. A Magnetometer survey was conducted to gain new insights into the Ethio-Sabaeen settlement structure and the extent of both sites during this period. The results are a superposition and combination of anomalies of a highly magnetic geology, magnetic rocks on the surface of the survey areas, field boundaries and other agricultural features, modern buildings and installations and anthropological traces. In the interpretation of our magnetograms, we try to name and associate all anomalies in the magnetogram to factor out all non-anthropogenic traces. What remains are fireplaces, pits, and rests of the walls, but their ascription to a period is only possible for the continuation of a monumental building. In this amalgamation of different features, we show the capability and the limit of magnetometry.

### 6.1 Introduction

The fortunate location as a focal point for crossroads of various cultures, the Tigray high plateau in the north of Ethiopia (see Fig. 6.1 a+b) spawned and flourished two wealthy, influential, powerful and widespread realms in historic times, the polity of Di'amat during the first half of the first millennium BC and later the Aksumite kingdom during the first millennium AD (Michels, 2005; Phillipson, 2012; Gerlach, 2017b). The Ethio-Sabaeen polity is to be understood as a kind of union of Ethio-Sabaeen sites rather than a defined ruler's territory.

The Ethiopian-German Archaeological Mission to Hawelti, Yeha and their surroundings is a cooperation project of the Ethiopian Antiquities Authorities (ARCCH and TCTB), the Sanaa Branch of the Orient Department of the German Archaeological Institute (DAI) and the Seminar for Oriental Studies of the Friedrich Schiller University in Jena. Since 2009, the mission has comprised archaeological and geological surveys, archaeological excavations and surveys, consolidation and restoration work, and site management and capacity-building measures. The key point of the project is the exploration of the Ethio-Sabaeen culture in the first half of the 1st millennium BC, its development and its termination.

---

<sup>1</sup>This chapter is a reproduction of the article:

Hahn, S. E., Parsi M., Fassbinder, J. W. E., Japp S., Gerlach I. (2022). **Yeha and Melazo (Ethiopia): Magnetometry in a palimpsest of archaeological, geological and modern remains**. Submitted to the *Taylor & Francis - Journal of Field Archaeology*. A supplementary figure has been added for clarity.

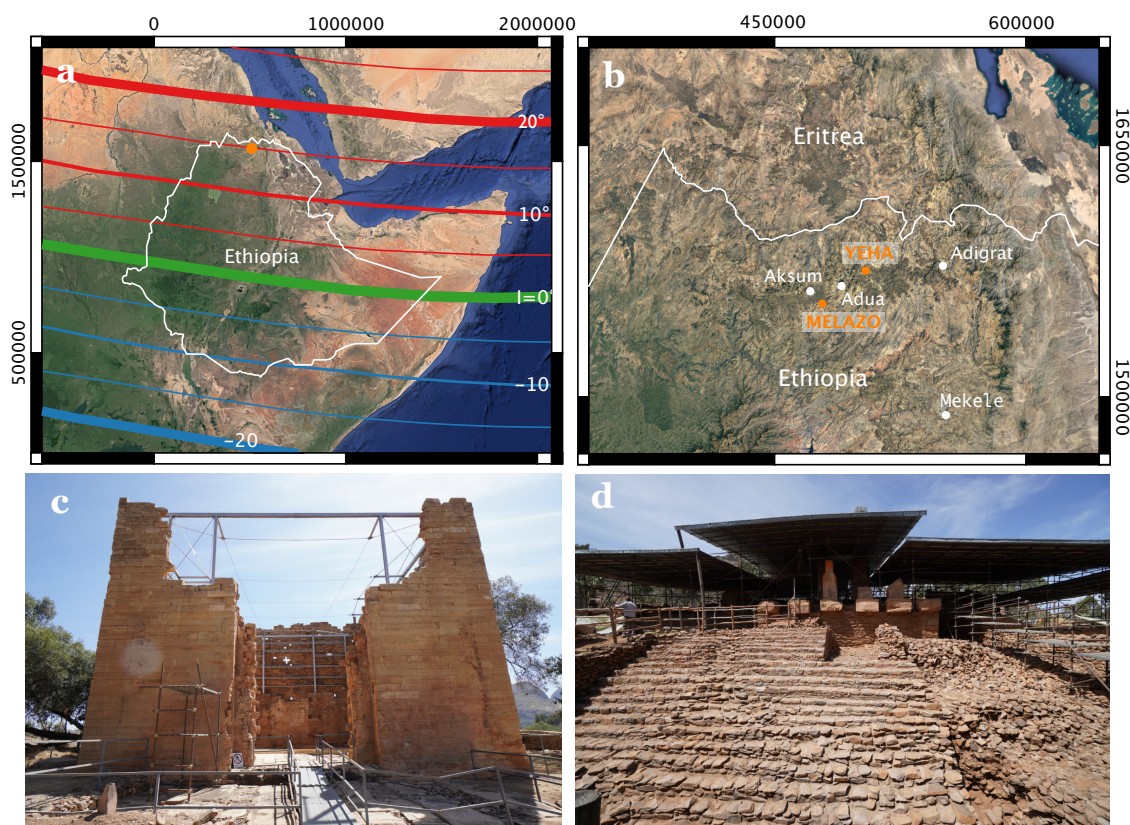


**Figure 6.1:** a) Map of Ethiopia at the Horn of Africa with Earth's magnetic field inclination isoclines. Yeha and Melazo are exposed to a shallow inclination of the Earth's magnetic field of  $15^\circ$ . b) Location of Yeha and Melazo in the north of Ethiopia in the Tigray Highlands. (Satellite image: Google, ©2021 TerraMetrics.) c) The Great Temple of Yeha. d) The palatial building Grat Be'al Gibri.

Yeha in the Ethiopian Highlands of Tigray seems to be the political and religious centre of the Ethio-Sabaeen polity. It is located 35 km northeast of the UNESCO World Heritage site Aksum, the capital of the Aksumite kingdom (see Fig. 6.1 b) and 30 km north of Adua. Today, the site is known for the Ethio-Sabaeen ruins of the monumental structure Grat Be'al Gibri and the Great Temple right in the centre of the modern settlement.

The Great Temple (see Fig. 6.1 c), dating back to the 7th century BC, resembles a rectangular outline, 18.5 m long and 15 m wide, with a maximum height of 14 m (Robin & de Maigret, 1998; Schnelle, 2011). Its cut stone blocks of snow-white limestone are so well-crafted that they fit tightly together without using mortar. Comparable masonry and architecture were found at South Arabian sites such as the Almaqah Temple at Sirwah and the Bar'an Temple in Ma'rib (Japp, Gerlach, Hitgen, & Schnelle, 2011; Schnelle, 2014).

The Grat Be'al Gibri (see Fig. 6.1 d) was erected around 800 BC and is located almost 200 m northwest of the Great Temple. It is the oldest preserved timber-frame structure in Eastern Africa (Schnelle, 2017). The multi-storied building (Japp et al., 2011; Schnelle, 2019) has a squared ground plan of about 65 m  $\times$  65 m. The facade has projections at the corners, and each side is segmented with risalites. The architecture of Yeha's monumental buildings recalls a Sabaeen influence (Schnelle, 2019, 2021). Cultural influences can also be seen, e.g. in the writing, language, social structures, and in religion (Gerlach, 2017a).

A stratigraphic 9.5 m deep sounding at the square in front of Yeha's church compound within close proximity of the Great Temple and the Grāt Be'al Gibri revealed a detailed chronological sequence of the Yeha's settlement (Japp, 2019). Bones and ceramics hint at a settlement in this area before the Ethio-Sabaeen period (late second millennium BC), followed by stratigraphic layers of the Ethio-Sabaeen period (first half of the first millennium BC). A hiatus in findings in the second half of the first millennium BC might be linked to the depopulation of the area or a shift in the settlement coverage of Yeha. Findings and walls from the first century BC to the fourth century AD suggest a restart of settlement in the early Aksumite period. The Aksumite Period lasts at least from the first millennium AD approximately until the 10th century (Michels, 2005). The appearance of one architectural structure indicates representative buildings in the 3rd/4th century AD. These layers are covered by a planar 60 cm thick layer, which is dated back to the late Aksumite period. The superjacent 1 m contained an installation dating back to the early Post-Aksumite period. Remains of modern homesteads were found in the first 1 to 1.5 m.

The Ethio-Sabaeen site of Melazo, 10 km southeast of Aksum, is located in sight of the stelae field of Hawelti and was researched in the 1960s by French archaeologists (Leclant, 1959). Ongoing excavation by the Ethiopian German project revealed an Ethio-Sabaeen monumental building. However, the true dimensions and the organisation of Yeha's ancient settlement are unknown, as well as major insights into the architecture of non-monumental Ethio-Sabaeen buildings. Therefore, one relied upon geophysical surveys, particularly magnetometry in this study, to obtain further information on these questions. In Melazo, the magnetometer survey was supposed to offer further information on the architectural structures currently being excavated and the surrounding areas.

Geophysical prospection uses the difference in physical properties to map the sub-surface and to distinguish individual features. Magnetometry (Fassbinder, 2015) relies fundamentally on the differences in total magnetisation between archaeological traces and remains, soil and geology. The total magnetisation is the vector sum of remanent and induced magnetisation. The latter's direction is parallel to the ambient magnetic field for ferri-, ferro- and paramagnetic materials and proportional to the magnetic susceptibility. The variations in susceptibility result from differences in composition and amount of magnetic minerals, which are, in nature, mostly iron oxides or iron hydroxides. The remanent magnetisation is the magnetisation a material still holds without the presence of an ambient field. It can be acquired through different processes, e.g. firing, chemical alteration or lightning strikes (Fassbinder & Gorka, 2009; G. Jones & Maki, 2005). If the magnetic properties of soil or geology and anthropological traces are indifferent, in other words, identifying the latter is nearly impossible if there is no contrast. The same applies if the contrast is dominated by geological factors, e.g. if the underlying bedrock and surface rocks are highly magnetic.

Trachytes, phonolites, alkali olivine basalts, tuffs and rhyolites (Kazmin, 1972) on either Cabisols or Leptosols (Eshetae, Hailu, & Demissew, 2021) are forming the geology of the Tigray region around Yeha and Melazo. Volcanic bumps are almost everywhere in Yeha, peeking out of the surrounding soil. This indicates that the bedrock may lie just below the surface in some places. These volcanic bumps have the shape of "noses" with several metres in length and a few metres in width, often dipping towards one side. Volcanic rocks have high magnetic properties, especially a high thermoremanent magnetisation. A high thermoremanent magnetisation is the reason why anthropological traces like fireplaces or baked bricks are usually easily detectable by field magnetometers (Fassbinder, 2017).

The detected magnetic signal of an anomaly depends not only on the magnetic properties but also on the depth of an object and the local Earth's magnetic field inclination (Lowrie & Fichtner, 2020; Aspinall et al., 2009).

The detected magnetic signal of an anomaly depends on the magnetic properties of an object's depth and the local Earth's magnetic field inclination. Although Ethiopia is in its entirety located around 1500 km north of the geographic equator, the magnetic equator divides the country (Alken et al., 2021) (see Fig. 6.1 a) and the geomagnetic field exposes the Tigray region to an inclination of  $17^\circ$  (according to NCEI Geomagnetic Modeling Team and British Geological Survey (2019) at  $14^\circ 16' 60''$ N,  $39^\circ 00' 60''$  W, 2144 m over Mean Sea Level).

Complicating the initial situation of a highly magnetic, near-surface geology is the fact that Melazo and especially Yeha are still habituated today, which brings into play also anomalies of modern occupation, e.g. buildings, metal construction, pipelines. What information can we still obtain from the magnetograms in this palimpsest of archaeological, geological, and modern features? In what follows, we show how magnetometry can be useful for such sites and if we can provide new insights into the history of the two sites of Melazo and Yeha.

## 6.2 Methods

### 6.2.1 Selection of the survey area

In the 2018 and 2020 campaigns, we covered a total survey area of around 36,000 m<sup>2</sup>. In Yeha, 15 individual areas are scattered all over the modern settlement. At the site of Melazo, we prospected 11 individual areas, and since some overlapped, we combined them into eight magnetograms. The individual magnetograms are named after the site, Yeh for Yeha and Mel for Melazo, and the year of the campaign, 18 for 2018 and 20 for 2020. The location of survey areas can be found in Fig. 6.2 for Yeha. Modern houses or recent facilities covering major parts of the areas around the Great Temple and the Grät Be'al Gibri in the settlement of Yeha are reducing the accessible area for magnetometer prospecting. For a better overview, we grouped the areas of Yeha around the Great Temple into four sections whose results and interpretations we show and discuss separately.

We prospected five areas north of the Great Temple (see Fig. 6.5). Starting in the north, clockwise around the present-day hospital, these are Yeh18D, Yeh20D, Yeh20B, Yeh20A and Yeh18C at a distance of 250 to 400 m from the temple. The western part of the settlement features three survey areas: Yeh18B, Yeh18E and Yeh20J (see Fig. 6.6). Yeh18B is the closest survey area to the temple, only 125 m from the temple, right in front of the church gate. Area Yeh20J is the most western of the prospected areas, around 500 m from the temple. In the southwest of the temple, we prospected three areas: Yeh20G, Yeh20C and Yeh18A (see Fig. 6.7). Yeh18A is located about 250 m from the temple. We enlarged this survey area in 2020 towards the north with area Yeh20C. The southern corner of the magnetogram borders on the north corner of area Yeh18A. In the south-east of the Great Temple, we were able to prospect four areas in close proximity to each other (see Fig. 6.8): Yeh20I and Yeh20H are only 50 m apart, Yeh20H borders via the northeast corner on Yeh20E and Yeh20F is around 80 m south to Yeh20E across an erosion channel.

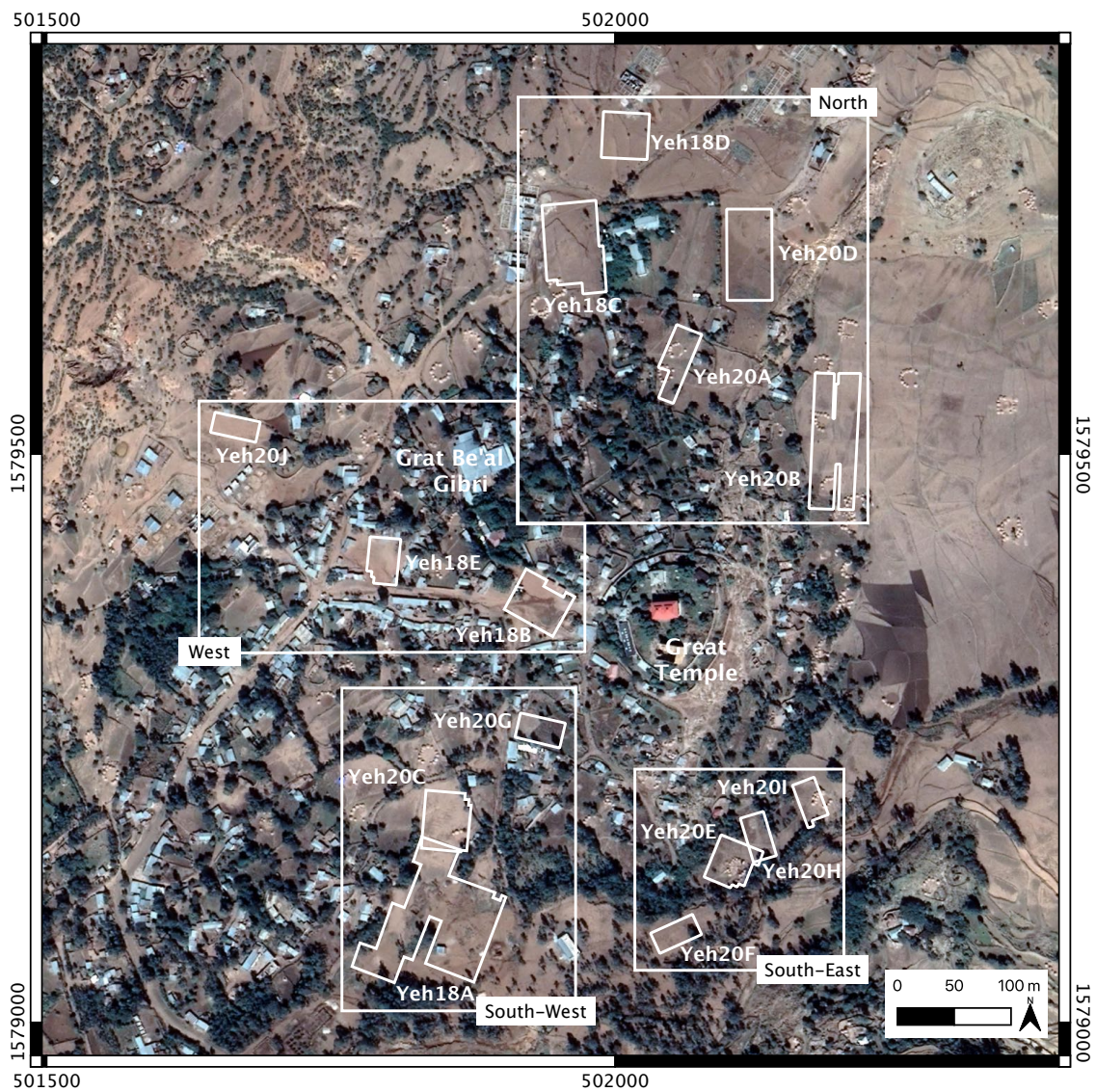


**Figure 6.2:** *The location of the magnetograms in Yeha. Yeha is deemed to be the religious and economic centre of the Di'amat polity. Prospection areas are around the monumental buildings Grat Be'al Gibri and the Great Temple. (Satellite image: Google, ©2021 CNES /Airbus, Maxar Technologies)*

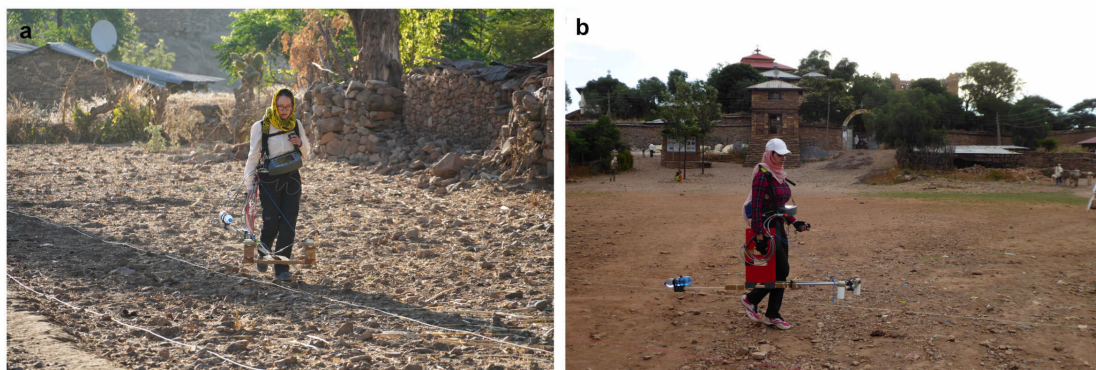


**Figure 6.3:** *a+b) Impressions survey with the Geometrics G-858 magnetometer in duo-sensor configuration. a) Survey of a small field inside the settlement of Yeha. A fence limited the survey area. A lot of small rocks were found on the surface. b) Prospecting in on the square in front of the church and Great Temple. Metal signs or other metal construction disturbed the data.*

For Melazo, the location of the survey areas can be found in Fig.6.9. The areas Mel20A, Mel18B, Mel18C and Mel18E (see also Fig. 6.10) adjoin the excavation area to the east. In 2018, we were not able to cover the whole area, as only some small parts of the fields were harvested. We closed the gap in 2020. For all areas, we kept field notes containing detailed drawings of the survey areas with trees, large rocks, field boundaries, and modern installations in the survey area or close by.

### 6.2.2 Magnetometer survey

We conducted the magnetometer survey in the 2018 campaign with both a Scintrex Smartmag SM4G-special magnetometer and a Geometrics G-858 magnetometer (see Fig.6.3); in the 2020 campaign solely with the Geometrics magnetometer. We applied both magnetometers in the so-called duo-sensor configuration. In this configuration, the Caesium magnetometers measure the total intensity of the ambient magnetic flux density. We fixed the probes on custom-built frames, and the setup is carried around 30 cm above the ground. We divided the survey areas into 40 m × 40 m grids, whose corner points are georeferenced with theodolite measurements. The probe distance is 0.5 m, and the spacing of the traverse survey lines is 1 m. We used a measurement frequency of 10 Hz to attain a data point every 10 cm with a constant walking speed. Marks are set every 5 m to compensate for variations in the walking speed. This results in a data point resolution of around 0.1 m × 0.5 m, which fulfils the requirements for archaeological prospection guidelines. Additionally, we conducted measurements with the magnetic susceptibility meter SM-30 (ZH Instruments) to determine the volume susceptibility values at the site for the soil and different rocks at the survey sites. The susceptibility meter is operated in 'interpolation mode' to correct for surrounding magnetic noise and thermal drift.

### 6.2.3 Data processing

The first step is the removal of the heading error of the probes. We interpolated the data point distribution to an appointed spatial resolution of  $0.25\text{ m} \times 0.5\text{ m}$ . We combined the grids with the "Geoplot" software to obtain a graphical data output of the survey areas. We compensated for the diurnal variation of the Earth's magnetic field by subtracting the calculated mean grid value of each grid from the data values, by multiplying data of single profile lines with an incrementally increasing or decreasing multiplying factor and by adding varying values to sections or the whole profile lines. Finally, we interpolated the data to a resolution of  $0.25\text{ m} \times 0.25\text{ m}$ . We applied an image high-pass filter on a copy of the total field data set ( $R=10$ ). Although we use both data sets for interpretation, we chose to overlay the total-field (Total) with the high-pass-filtered data with a transparency of 50 %<sup>2</sup>.

## 6.3 Results and Interpretation

### 6.3.1 Susceptibility measurements

The topsoil shows a magnetic volume susceptibility (see Fig. 6.4) of around  $6.38 \cdot 10^{-3}$  SI. The susceptibility of rocks found on the surface ranges from  $0.203 - 0.351 \cdot 10^{-3}$  to  $87.0 \cdot 10^{-3}$ . Measurements of phonolites forming ancient walls, unearthed in an excavation close to Yeh20A, gave values of different orders of magnitude:  $(0.0416 - 0.0619, 0.102 - 0.266, 6.71) \cdot 10^{-3}$ .

### 6.3.2 Yeha

#### 6.3.2.1 North the Great Temple

The metal fence and gate of the hospital generate induced magnetic anomalies (see Fig. 6.5), see Yeh18D (1) Yeh18C (2), which were still recorded even if a distance of several metres was maintained during the prospecting. In the southern part of area Yeh20A (3), three almost identical-looking anomalies are visible, which can be associated with small buried autochthonous volcanic bumps. In this example, even the dip of the bumps towards the horizontal is recognisable insofar that the anomalies fade more and more and appear less and less distinctive towards the east. Similar subsurface volcanic bumps (4) are recognisable in Yeh20B. Their less pronounced anomalies indicate that the bumps are more deeply buried and presumably wider and longer but not less rectilinear in shape than those from the previous example. The southern part features a similar set of anomalies (5) but with a more complex assembly.

Topography affects the results of Yeh20D (6). Current (7-22) and former field boundaries (23-28) can be identified. East-west running field boundaries, e.g. (22), show a significantly more pronounced anomaly than north-south running ones, e.g. (21), which appear only slightly more magnetic than the surrounding area. The anomaly pattern is also different: east-west field boundaries show a negative-positive-negative pattern, while north-south boundaries show only a positive anomaly.

---

<sup>2</sup>See Chapter 4.4 for details on the magnetometer prospecting at shallow inclinations of the geomagnetic field.



**Figure 6.4:** Examples for measured susceptibilities: a) topsoil susceptibility, b)-e) surface rocks, f)-h) phonolites unearthed in an excavation at area Yeh20A.

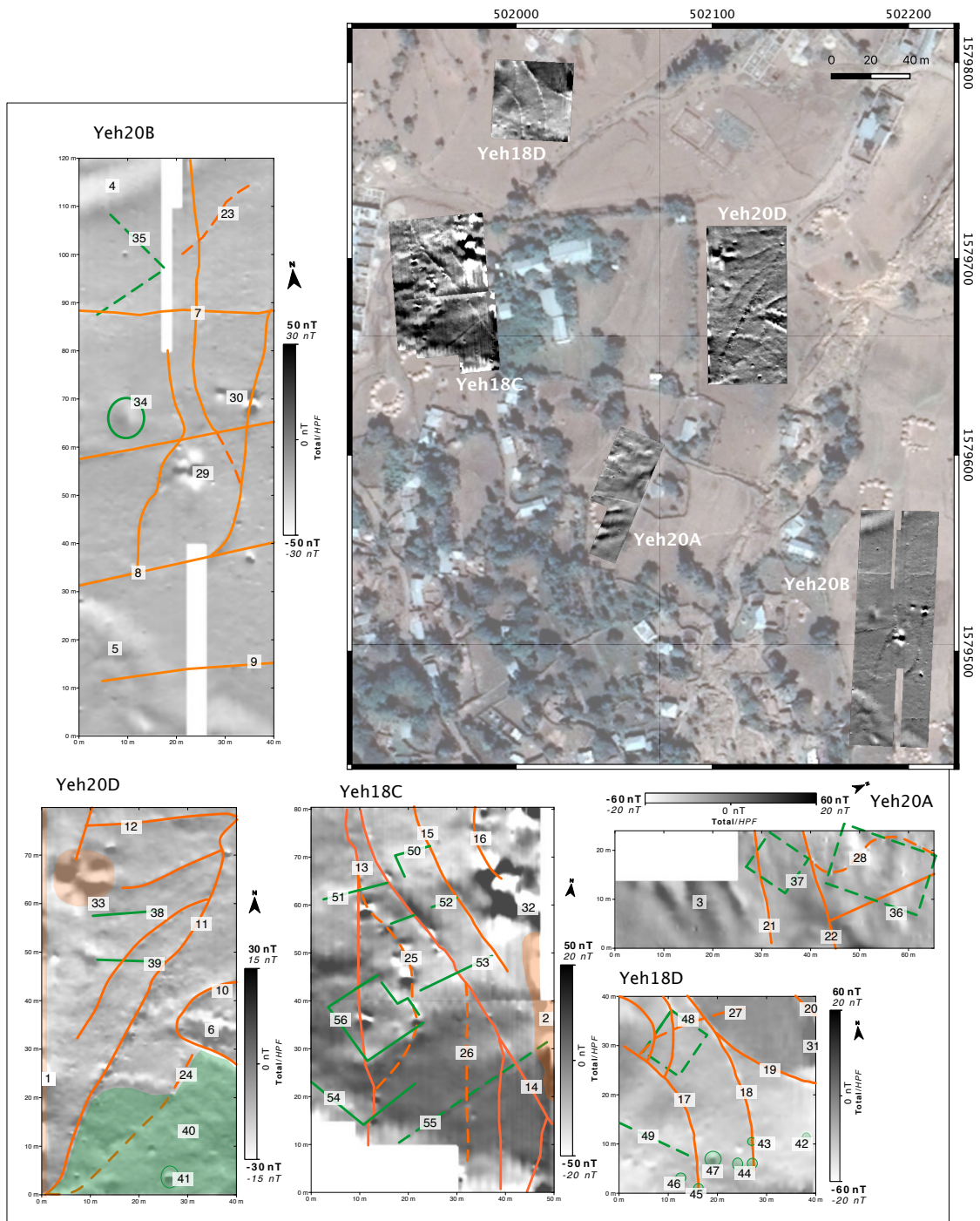


**Figure 6.5:** The northern part of the settlement of Yeha includes the magnetograms of Yeh20B, Yeh20D, Yeh18C, Yeh18D, and Yeh18A. Orange refers to modern or geological features; green to potential archaeological remains. Dashed lines are used if a feature is only vaguely recognisable. (Satellite image: Google, ©2021 CNES /Airbus, Maxar Technologies)

Sharp and high-intensity anomalies (29-31) can be undoubtedly associated with volcanic rocks on the surface. Their random but strong magnetic remanence can explain their different anomaly patterns. It dictates the direction of their total magnetisation, whose variation causes the different anomaly patterns. Highly magnetic rocks can cause large-scale anomalies (32). Volcanic rocks are also found to reinforce along field boundaries, e.g. 16. The anomaly marked 33 was caused by a lightning strike, which is commonly recognisable by the radial branches showing different orientations of the lightning-induced remanence.

In Yeh20B, the roundish anomaly (34) might either be a rather shallow pit or, more likely, of geological origin, as structures comparable to those of volcanic bumps can be seen immediately adjacent to the west. The linearity and uniformity of the kinked anomaly (35) in the north-western part of Yeh20B could potentially indicate wall remains. However, it could also be the continuation of an adjacent former field boundary (23). In the northern part of Yeh20A, two almost rectangular anomalies (36+37) are vaguely recognisable. Since we did not detect any other archaeological features within the magnetogram, we are cautious to call these anomalies of archaeological origin; they may also be modern or geologic in origin.

In Yeh20D, two straight lines (38+39) are visible. They have similar lengths, but they are inclined to each other. There are no recognisable connections between these lines that could resemble the layout of a building. However, these lines show an anomaly deviating from the recent field boundaries, but the possibility of an agricultural origin cannot be excluded. Former field boundaries may be topographically more subtle, making their anomalies less pronounced. Towards the south, Yeh20D shows a magnetically disturbed section (40) featuring a quite distinctive fireplace (41), some smaller ones and some small pits, implying an area that was heavily used in the past. We cannot distinguish these features chronologically.

Yeh18D features numerous pits (42-46) whose differences in intensity are caused by variations in depth or filling material. The strong anomaly (47) could also indicate a fireplace. A perpendicular-shaped anomaly is noticeable at 48, whose traces can be extended to form a rectangular building layout. These features may be covered by more soil and, therefore, appear less prominent. Another linear line is visible (59), which could be caused by underlying geology, but the length of the straight feature seems rather atypical. In addition, the proximity to the pits and fireplace could indicate an anthropological origin.

In Yeh18C, linear features are noticeable (50-54), which are mostly perpendicular to recent field boundaries and do not follow any recognisable outline. The presumably perpendicular connections could coincide with today's field boundaries and complement the features to an almost rectangular layout. If these features are indeed wall remains, it is reasonable to assume that they serve as reinforcement of today's field boundaries. The origin of the distinctive long line (55) is unclear, but it seems likely to be the supply pipe for the hospital's facilities. Another feature (56) with complementary anomalies is recognisable, which may resemble the layout of a rectangular building with a projection.

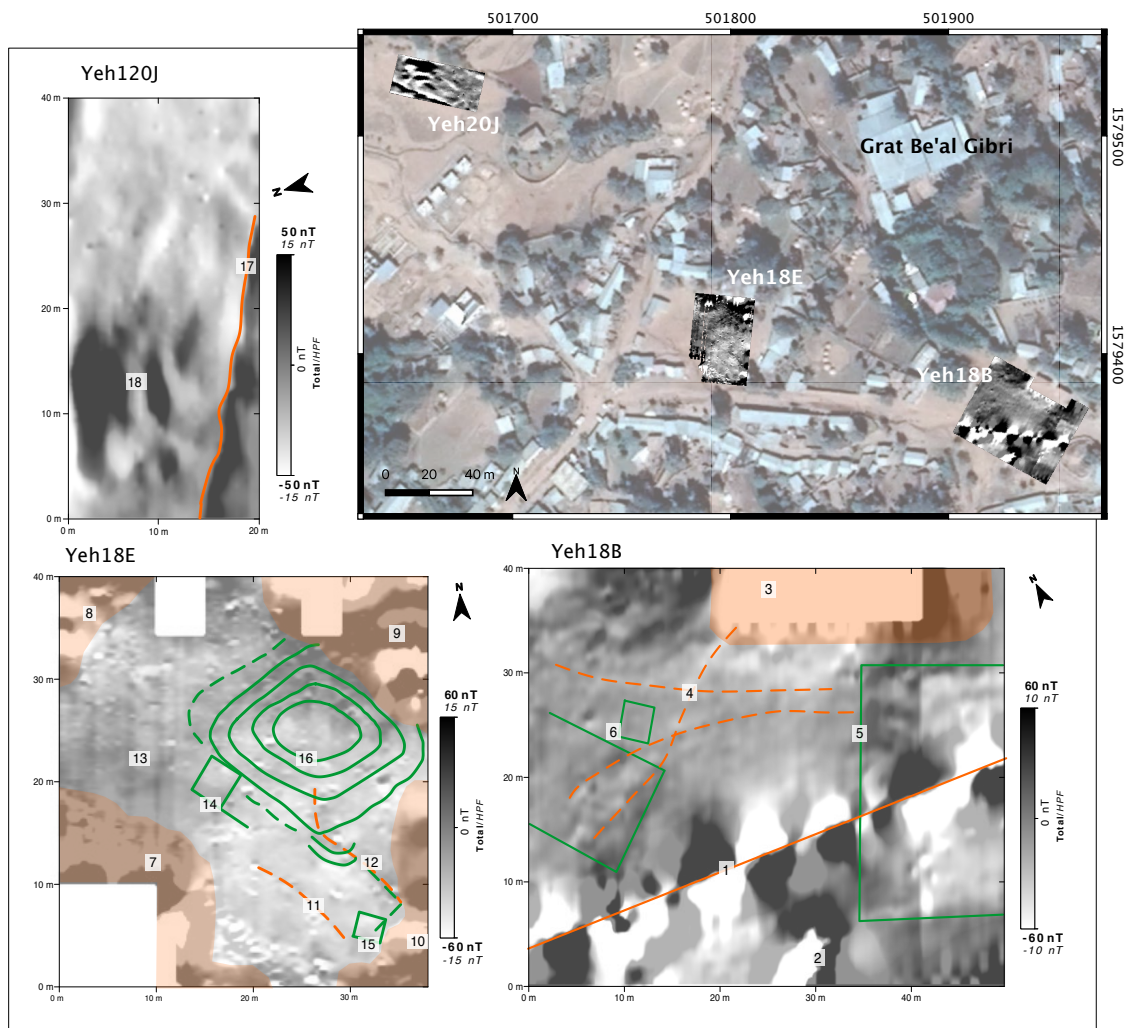


**Figure 6.6:** The western part of the settlement of Yeha includes the magnetograms of Yeh18B, Yeh18E, and Yeh20J. Orange refers to modern or geological features; green to potential archaeological remains. Dashed lines are used if a feature is only vaguely recognisable. (Satellite image: Google, ©2021 CNES /Airbus, Maxar Technologies)

### 6.3.2.2 West of the Great Temple

The result of the square (see Fig. 6.6) in front of the church compound is heavily contaminated with anomalies of modern infrastructure: an underground cable (1), an erected sign (2), and a shipping container close by (3) generate strong and large anomalies. The small-width curvy structures (4) could be runnels, small, mall channels a few centimetres wide through which water cuts its way into the soil to drain the square. The rectangular linear anomalies (5+6) could be remains of houses from more recent times. Yeh18E is the measurement on the marketplace. Modern constructions, nearby buildings, mainly metal roofs and doors, and other metal constructions cause large and strong magnetic anomalies (7-10) for Yeh18E. Small amounts of iron waste, leftovers from the weekly market, contaminate the area with small-scale but strong anomalies. Rocks on the surface cause comparable anomalies.

The steadily varying runnels (11+12) are still detectable with magnetometer prospecting even though they are not discernible on the surface because the rocks and iron waste accumulating in the draining runnels cause beads-on-a-string anomalies. Black and white lines (e.g. 13) are the accompaniments of instrument failures. Although they have been corrected, the application of filters enhanced the lack of accurate data and cause these lines.

We recognise two rectangular contours (14+15) with extending straight structures. The extension of 14 is in line with the rectangular structure, suggesting that this extension was originally part of the feature. The extension of 15 intersects with the rectangular contour, suggesting they belong to different structures or times. One runnel lies alongside this extension; this artificial obstacle probably prevents the runnel from changing direction. Therefore, it should be quite close to the surface, indicating that the extension lies on top of the rectangular outline. The angular elliptical formation (16) has at least four ellipses with increasing diameters close to each other. The outer ellipses could be closer to the surface since they are better recognisable than the inner ones. Maybe these lines mark the edges of different levels, possibly steps in a depth of around 0.5 to 1 metre, with an increment of no more than 10 cm. Their purpose or origin, though, is unclear. Topographic (17) and geological effects dominate heavily, especially at 18, Yeh20J. We do not detect any other features for this area with magnetometry.

### 6.3.2.3 Southwest of the Great Temple

In Yeh18A (see Fig. 6.7), field boundaries or surface features such as terrain steps (1-9) or deeply cutting wheel ruts (10+11) traverse this area. An underground pipe or cable causes the multipole anomaly (12). A linear anomaly (13) with projections and corners and a length of around 100 m is recognisable. The size and shape might point to an ancient monumental building. However, the walls of the known monumental buildings in Yeha and other Ethio-Sabaeans are quite thick. In that case, we would expect two parallel-running linear structures for its wall, which we do not find here. Nevertheless, the linearity of the structure would strongly suggest wall remains. The superimposition of wall remains of different periods could explain the chequered structures in 14 and 15. The pattern is too repetitive and parallel to result from underlying geology. With respect to the findings of the nearby excavations, an archaeological-related cause is more likely. We do not see a continuation of the building outline of Yeh18A within Yeh20C.

Modern field lines (16) and terrain steps (17) are noticeable. Two distinct fireplaces (18 + 19) are discernible. The first fireplace (18) is close to a part of the area (20), which shows further remains of an ancient occupation, like pits and further disturbances caused by multiphase ancient remains. The other fireplace (19) seems to be deeper than the other one, as its signal appears less sharp in the magnetogram. It is located in an area where we also detect remains of ancient occupation (21), but they are less distinctive than at (20). The Yeh20G area is contaminated with iron waste, especially the spot around (22). Pits (23-25) are recognisable. Their close proximity to the buried waste indicates a more modern origin. Strong magnetic anomalies are field boundaries (26) or result from an adjacent building (27). The ring-shaped structure (28), about 4.3 m in diameter, was probably built of rocks.

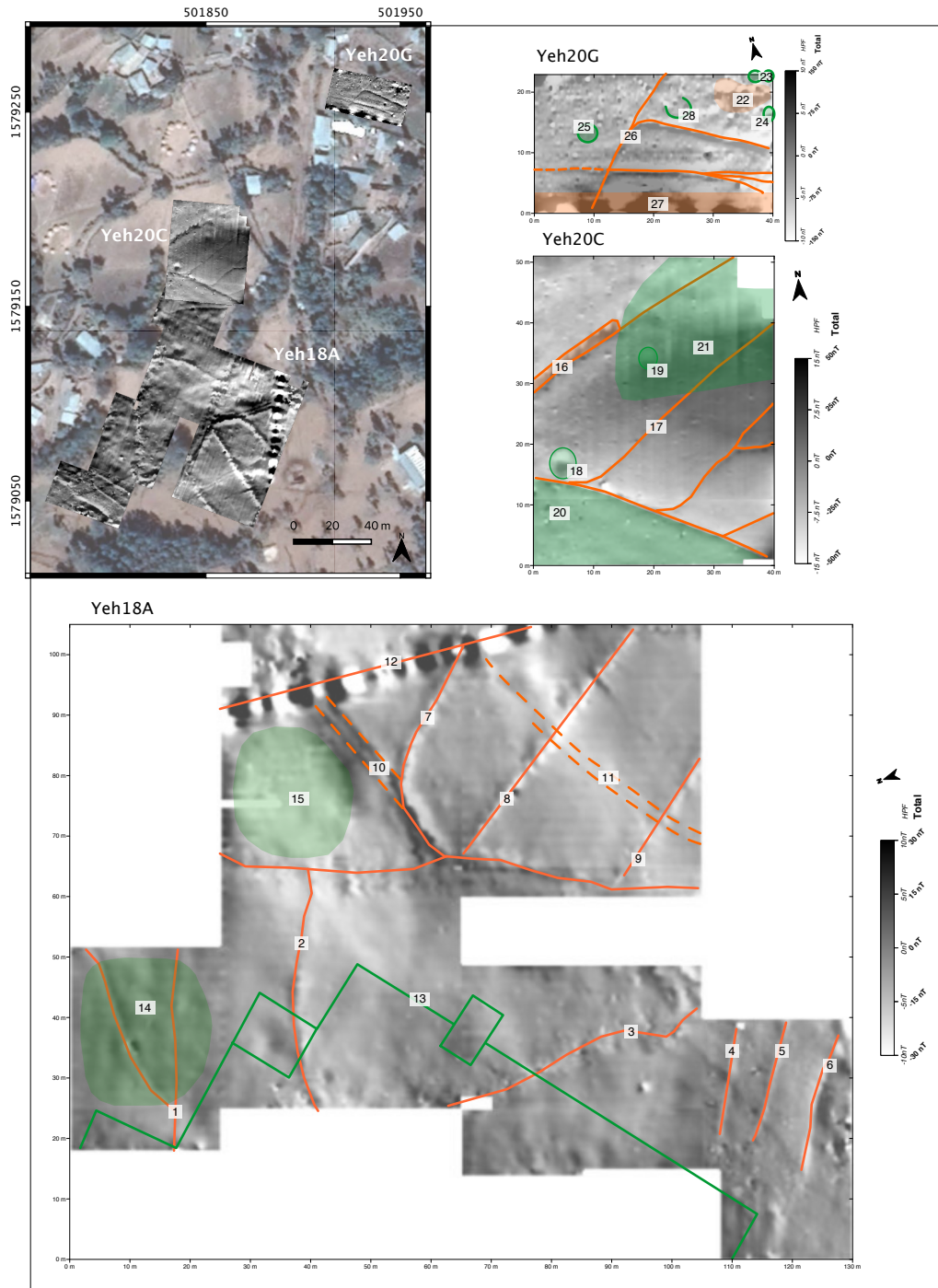


**Figure 6.7:** The southwestern part of the settlement of Yeha includes the magnetograms of Yeh20G, Yeh20C, and Yeh18A. Orange refers to modern or geological features; green to potential archaeological remains. Dashed lines are used if a feature is only vaguely recognisable. (Satellite image: Google, ©2021 CNES /Airbus, Maxar Technologies)

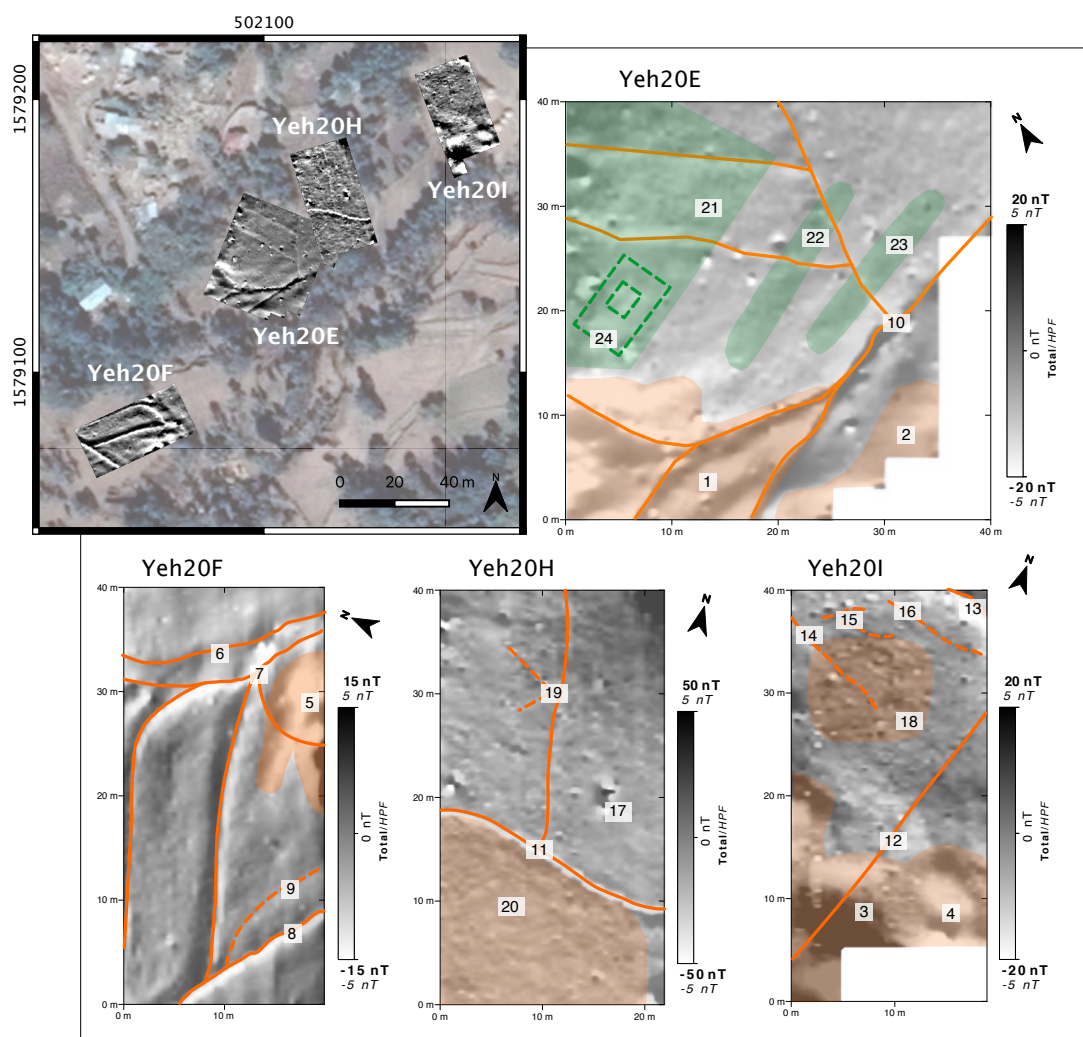


**Figure 6.8:** The southeastern part of the settlement of Yeha includes the magnetograms of Yeh20I, Yeh20H, Yeh20E, and Yeh20F. Orange refers to modern or geological features; green to potential archaeological remains. Dashed lines are used if a feature is only vaguely recognisable. (Satellite image: Google, ©2021 CNES /Airbus, Maxar Technologies.)

### 6.3.2.4 Southeast of the Great Temple

In the east-south part of Yeh20E (see Fig. 6.8), the adjacent erosion channel causes magnetic anomalies (1+2). In Yeh20I, the underlying volcanic bulges generate strong anomalies (3+4). In Yeh20F, the subjacent geology causes such large anomalies (5) that we detect any other structures. Recent (6-13) and former field boundaries (14-16) are recognisable in every survey area. In Yeh20H, the anomaly (17) could be caused by two volcanic rocks lying side by side. The northern part (18) of Yeh20I shows an area with many small-scale features. Since we identified a few old field boundaries (14-16) in and around this area, we assume these small-scale features result from deep ploughing. The same anomalies can be seen in Yeh20E. Ploughing can also be noticed in Yeh20H but is less pronounced than in Yeh20I and Yeh20E. The kinked anomaly (19) proves to result from a change in ploughing direction, as seen in the orthophotos. Ploughing in at least two directions might also explain the closely spaced and kinked anomalies (20).

In Yeh20E, two 20 m long, straight, broad, almost parallel linear anomalies (22+23) are noticeable. Their anomalies are dissimilar to the anomalies of subsurface geological features, e.g. (3). These linear anomalies (22+23) could be compacted soil steps in the subsurface. Area 21 might belong to a podium or platform. This area also shows different anomalies caused by small pits, fireplaces, and possible wall remains. Some of these potential wall remains (24) resemble a rectangular layout with a smaller rectangular layout inside. These are surrounded by strong anomalies caused either by small-scale geology or, more likely, by remains of highly magnetic rocks used as building material for a possible ancient structure. Another explanation is old fireplaces.

### 6.3.3 Melazo

In the magnetogram Mel18A (see Fig. 6.10), a one-metre-high wall at the surface causes a large negative anomaly (1). Highly magnetic rocks cause high-intensity anomalies (2-4). The pebble-sized volcanic rocks on the field surface cause speckles in the magnetogram. Rectangular structures (5-7) can be noticed, which could be wall remains. They coincide partially with modern field lines (6+7). The closeness to the excavated area lets us suggest that these are indeed remains in the underground. We interpret the dipole anomaly (8) as a fireplace.

In Mel18D, the field boundaries (9)+(10) are barely noticeable. We ascribe the long linear but curved anomaly (11) to the subsurface geology. Interpreting the linear and kinked structures (12-14) is only vaguely possible. Since the anomalies (12+14) seem to be more blurred, the feature is deeper embedded in the subsurface, so we characterise them of geological origin. The other set of structures (13) seems to be more pronounced; therefore, they are shallower. That is why we ascribe them to modern or archaeological features.

In Mel18F, current field boundaries (15+16) are identifiable. Strong large prism-shaped anomalies (17+18), up to 20 m in length, are most likely generated by an underground metal construction, perhaps some containers. An underground pipe could cause the multipole anomaly (19). The freckled impression in the magnetogram is due to ploughing and rocks scattered over the surface. The dashed lines are older field boundaries or pathways. The rectangular structure 20 is dissimilar to any other features detected in Mel18F. Since we are only detecting modern features in the magnetogram of this area, we assume that this structure is also modern.

In Mel18G, the linear anomalies are either a field boundary (21) or a crossing pathway (22). Highly magnetic rocks which mark the pathway (23) or secure a sand hill (24) cause small dipole anomalies. The circular anomaly (25) is a well that is still in use. The rock circle (26) might be outcropping bedrock or a pile of stored rocks. A pathway (27) crosses the fields, and a small wall (28) divides the fields of Mel18H. The anomalies 29+30 are the remaining parts of a former wall. The interpretation of the linear structures 31 is tricky. The outcropping rocks surrounding the hamlet show rectangular karst-like blocks. The linear structures in the magnetogram can be simply the linear and rectangular gaps or formations in the bedrock. The anomalies in the northern part show higher intensities, which could be explained by less topsoil coverage. Although the anomalies 31 are linear and rectangular, we assign them to subsurface geology because of their close proximity to the outcropping bedrock.

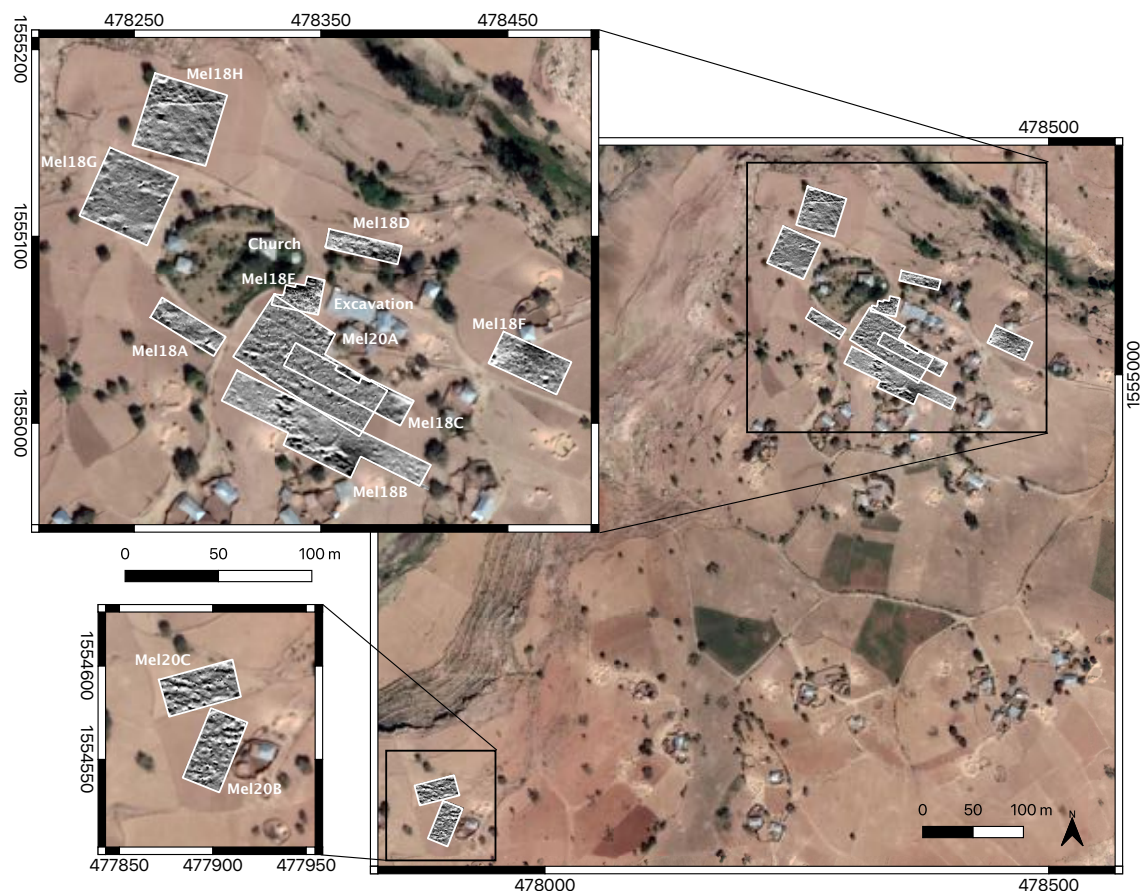


**Figure 6.9:** Overview of the locations of the magnetograms in the hamlet Melazo. (Satellite image: Google, ©2021 CNES /Airbus, Maxar Technologies)

Heavy ploughing and strong magnetic rocks cause a speckled magnetogram, which complicates the interpretation of the compilation of the areas Mel20A, Mel18B, Mel18C and Mel18E. Further modern influences seem to be moderate: some crossing field lines (32+33) and anomalies of the adjacent drystone wall (34+35). Linear kinked structures (36) with lengths of 20 m, 27 m, and 18 m and angles of  $80^\circ$  and  $110^\circ$ , are conspicuous.

The two parallel lines could be the anomalies of one thicker wall with a width of 2 to 3 m. The thickness of the wall is comparable to the building, which is currently excavated. Inclined to this structure, we detect another rectangular structure (37) with around  $4 \text{ m} \times 10 \text{ m}$ . How this is connected to the monumental building currently being investigated requires further consideration, as both are also inclined to the outline of the currently excavated building. Some other rectangular structures are hardly distinguishable and can be anomalies caused by the underlying geology. Anomalies in the south (38) with strong values could indicate fire debris, and the combination of linear structures might indicate a burned feature, possibly of archaeological origin, in the underground. The large-scale strong and linear anomalies in Mel20B and Mel20C can be attributed to the underlying bedrock. These effects are so dominant in Mel20C that we cannot identify any further structures in the magnetogram. In Mel20B, some linear and rectangular structures are recognisable. The outline of structure 39 is very vague, while the one of structures 41 and 42 is more pronounced. We are still determining if these have a geological origin or are wall remains.

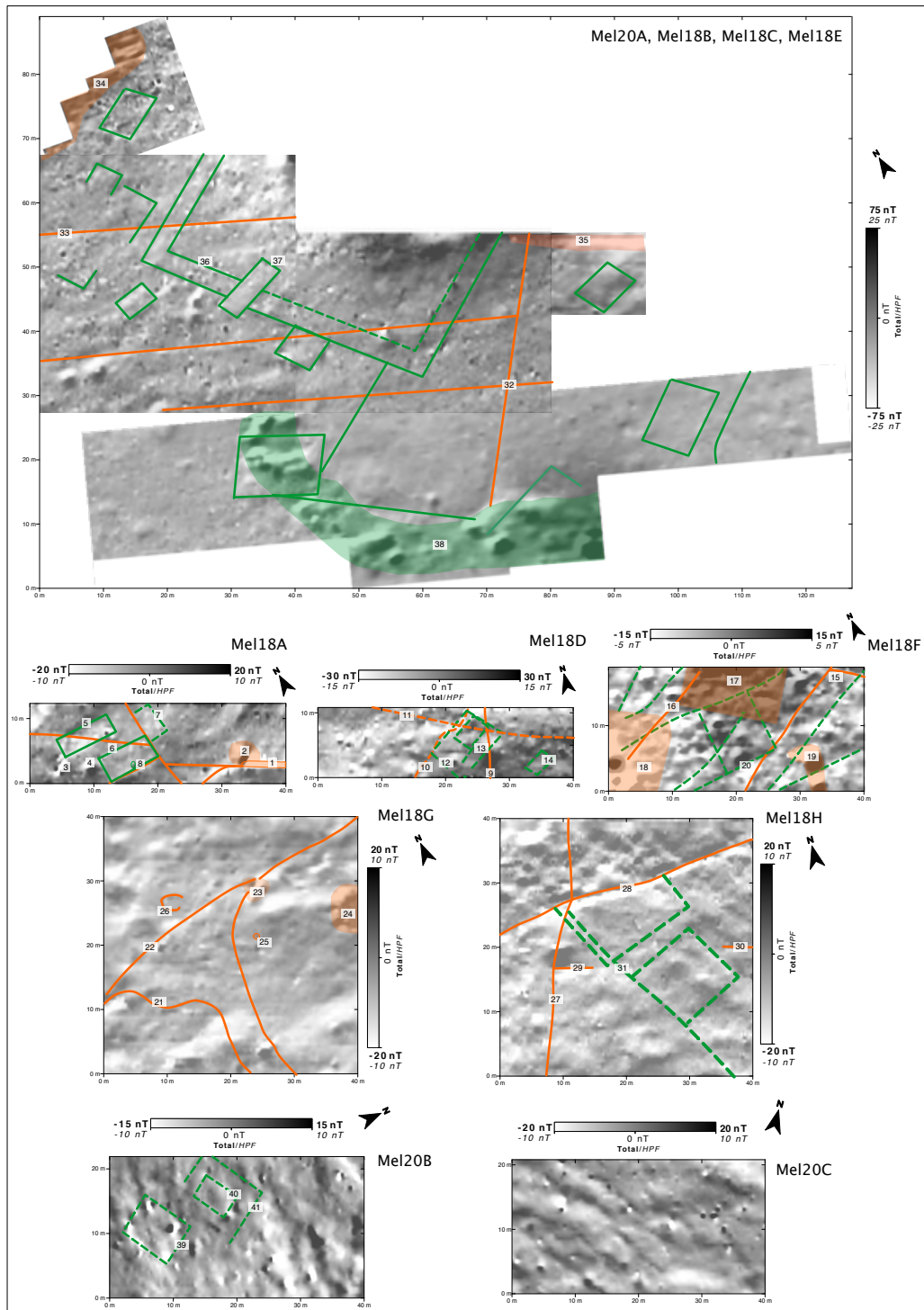


**Figure 6.10:** The resulting magnetograms for prospection in Melazo. Orange refers to modern or geological features; green to potential archaeological remains. Dashed lines are used if a feature is only vaguely recognisable.

## 6.4 Discussion

Already during the first campaign in 2018, we realised that the previously set goals for the magnetometer survey, which was to provide new insights in the Ethio-Sabaeen settlement, including the estimation of the extent of the settlement and its organisation at Ethio-Sabaeen times, were a little too ambitious, considering the encountered challenges are manifold.

Already during the first campaign in 2018, we realised that the previously set goals for the magnetometer survey, which was to provide new insights into the Ethio-Sabaeen settlement, including the estimation of the extent of the settlement and its organisation at Ethio-Sabaeen times, were a little too ambitious, considering the encountered challenges are manifold.

The volcanic bedrock generates strong large-scale anomalies whose high intensities and large dimensions can render big parts of magnetograms valueless for further interpretation (see Yeh20I, Yeh20J). In Yeha, it is often present as volcanic bumps several meters in length and a few meters in width (see Yeh20A). In Melazo, the bedrock appears as rectangular karst rocks of different lengths (see Mel18H). Applying a high-pass filter on the data does not remove these anomalies, which implies that even a survey with a gradiometer may not solve this problem. Moreover, these geological anomalies can appear quite linear (see Yeh18C, Yeh18D), which bears the particular risk of identifying geological features as archaeological ones when unaware of the local geology and its morphology.

Linked to the local geology is another factor: A large quantity of palm- to head-sized volcanic rocks are found on the surface of every one of our survey areas. Their susceptibility ranges over different orders of magnitude, also up to one order of magnitude higher than the susceptibility of the soil (see 3.1). The Königsberger ratios for basaltic rocks generally vary between 1 to 20 (Clark & Emerson, 1991)). Ethiopian flood basalts show mean values between 2.1 and 4.7 (Lhuillier & Gilder, 2019) in recent studies. Soil values usually range from around 1 to 3 (Pickartz et al., 2020). Both the higher susceptibility and Königsberger ratio thus result in a significantly higher total magnetisation of the volcanic rocks than that of the surrounding soil. The consequence is that the magnetograms are plastered with small dipole anomalies with high intensities. Their anomalies complicate the identification of anomalies in the magnetogram, which are caused by archaeological remains. On the one hand, they can mask potential archaeological remains; on the other hand, they can align to form a fallacious linear structure in the magnetogram. Comparable-looking magnetometer results were recorded by a French Ethiopian Archaeological Mission in Eastern Tigray in the Area of Wolwalo (Benoist et al., 2020) and led to a similar conclusion regarding the further interpretation, which is that archaeological features may remain hidden. Magnetometer prospecting in Aksum (Getaneh, Haile, & Sernicola, 2018) and Wakarida (Dugast & Gajda, 2011) show similar small-scale high-intensity anomalies. One can presume that the measurement with a gradiometer enhances these small-scale surficial anomalies, especially in a horizontal set-up (see Chapter 4).

Field boundaries cause other unwanted surface anomalies and are present in almost every area we surveyed. We marked their location in our field notes and additionally matched their course with orthoimages to exclude them from our further analysis. The intensity of these anomalies depends on the field boundary's step size. These vary from 5 to 20 cm but can also reach a step size of 1 m. We will call the latter terrain steps. Larger steps have anomalies whose intensities reach high values (few 10 nT, see Yeh18A), and they

cause large-scale spatial anomalies (see, e.g. Yeh20F), which again can obscure potential archaeological remains. Rocks reinforce the field boundaries, which cause small-spatial anomalies like “pearls on a string” (Yeh20B). Based on this pattern, we can identify former field lines that are not visible in the orthophotos (see Yeh20B, Yeh20A, and Mel18D). Field lines can change over time, and an inexperienced surveyor could mistake them for archaeological structures, as they also often occur as straight lines (see, e.g. Yeh20I). Field boundaries, terrain steps, rocks on top of the survey areas and the generally rougher surface complicate or prevent the application of other prospecting techniques, such as GPR.

Modern metal structures of the settlement cause large-scale high-intensity anomalies in the magnetograms, e.g. signs (Yeh18B), buildings (Yeh20B) and pipes (Yeh18). In Melazo, the drystone walls of local people’s houses and fences cause large-scale anomalies (see Mel20A and Mel18F). Today’s occupation of both sites limits the areas for magnetic prospecting, as only a few areas are accessible. In Yeha, modern houses or newer facilities cover major parts adjacent to the Great Temple and the Grat Be’al Gibri. A certain distance must also be kept from modern metal facilities so that they do not affect the data, which yet again limits the area for magnetic prospecting. We refrained from accessing fields in Yeha and Melazo, which had not yet been harvested.

The terrain steps and huge field boundaries also limit the already small number of accessible areas. Our prospection of both sites thus resembles a proverbial patchwork quilt: The individual grids are scattered across the sites, and the areas are small in comparison to the extent of present-day settlement. The smallest area is 18 m x 20 m, and the largest is 110 m x 130 m. Usually, the measurement direction should be along the magnetic east-west axis, which we also adjusted for each survey area to cover as large an area as possible. These reorientations of the measurement direction can have the disadvantage of also registering magnetic disturbances generated by the electrical currents of the instrument itself, e.g. its readout unit and battery alike, which causes a striping effect in the resulting magnetograms which is barely removable in the post-processing of the data. Connecting the puzzle pieces and deriving an overall picture for Yeha and Melazo is a challenge that is quite difficult to deal with. Small prospection areas also prohibit tracing building outlines and gaining an idea about the general connection of structures. The inhabitation of Yeha throughout the last 3300 years has left multi-layered features’ traces buried beneath the surface. Excavations in Yeha often reveal a stratigraphy containing building remains of both cultures, Ethio-Sabaeen and Aksumite, overlaying each other. However, magnetic prospection is only a two-dimensional mapping technique. Consequently, the different structures’ anomalies of the different layers will overlap, as we suspect for Yeh18A, making identifying individual ones tricky or impossible.

There is also some variability regarding the building material. Excavations revealed mostly phonolites as a building material, but other materials may also have been used for buildings in Yeha and Melazo. Even the magnetic properties of the excavated phonolites vary greatly - over two magnitudes (see 6.3.1). The magnetisation of the soil lies somewhere in between. Therefore, it is hardly possible to predict the magnetic contrast of phonolite walls to the soil and, accordingly, their anomalies in the magnetogram. In addition, the depths of possible ancient remains vary from location to location. For example, in Yeha, ongoing excavations show a depth variation for the same epoch at different places. Assigning a date based on the stratigraphy of the magnetic features is an almost pointless endeavour since there is only limited information on the architecture of non-monumental

Sabean and Aksumite buildings. Another point to consider is that anthropogenic features of both periods are often found in depths of more than 2 m, making them generally harder to detect with magnetometers.

Prospecting at a shallow Earth's magnetic field inclination complicates the interpretation since comparable studies or detailed feature analyses for archaeological magnetometer prospecting for these latitudes or Earth's field inclinations are limited. Nevertheless, we use the comparison between recorded and expected signal (Ostner et al., 2019) for this inclination to distinguish between rocks on the surface and fireplace or pits (see e.g. Yeh20C and Yeh18D). Due to their strong ambient remanence, scattered volcanic rocks show anomaly patterns that strongly deviate from the expected signal of bodies with a total magnetisation parallel to the ambient geomagnetic field. Now, if we exclude all modern, surficial and geological anomalies, what is left to be further interpreted?

As mentioned, we can detect some fireplaces and pits (Yeh20C and Yeh18D). We see rectangular outlines (Yeh20A) and potential wall remains (Yeh20B and Yeh20D) or other linear features (Yeh18C and Yeh18D) which do not coincide with field boundaries or bear resemblance to geological features. Though this feature cannot yet be linked to modern or geological anomalies, their origin is debatable. We presume they are anthropological, but a time period for their origin cannot be provided.

Obviously, there is a great need to compare the prospection results we have obtained with the results of future excavation to gain information about the potential of magnetometer prospection at the site. Plans are being made to carry out these excavations, but the civil war in this region, which has been ongoing since November 2020, has so far made it impossible to continue the work.

A detailed magnetic analysis of the unearthed building material and soil properties, followed by modelling, would help to identify still hidden features (as it has been done by Benoist et al. (2020)) and to assign these and others correctly. Field notes and ortho imagery provide a reliable source for the correct identification of surface features. From the geophysical side, a combination with ERT (Electrical Resistance Tomography), for example, is highly advisable. On the one hand, the method exploits an additional set of physical properties to gain new information about the subsurface. At the same time, one obtains a depth information on the features which might help to identify the period of the features.

Given the complications with the magnetometer prospection and the ambiguity of its results in Yeha, there are still reasons to continue the magnetometer survey there. Results from Melazo demonstrably prove that we are able to track remains if they are shallow. Here, the highlight of the magnetometer survey was the successful discovery of the continuation of the monumental building walls beyond the current excavation.

This, along with the discovery of other unassigned features at both sites, inspires us nevertheless to recommend magnetometer prospecting as a tool for further investigation of the sites, despite the challenges involved, but with a primary focus on demonstrating the existence of anthropogenic features in the subsurface rather than with the aim of gaining very detailed insights into the architecture or extent of the Ethio-Sabean settlements. At Yeha, in particular, magnetometer prospecting can help suggest new areas for the expansion of the modern settlement if it is known that there are no ancient buildings or other remains in the uppermost few metres that could be destroyed or damaged.

## 6.5 Conclusion

The magnetometer survey in Yeha and Melazo might not have yielded the desired results by offering more detailed insights into the Ethio-Sabaeen settlement. Highly magnetic subsurface geology, survey areas littered with highly magnetic rocks and their agricultural use and modern installations, either in the underground or close by, complicate the survey itself and the subsequent interpretation. With orthoimages and field notes, anomalies of surficial traces and geological anomalies can be factored out. We can detect wall remains, fireplaces and pits, but the attribution of these anthropological traces is difficult due to the almost continuous occupation of the settlements, especially in Yeha, where excavations show that the ancient remains are often deep and probably below the detection depth of the magnetometer. However, where ancient remains are shallow, we can detect their existence with certainty, as exemplary in Melazo, where we discovered the previously unknown continuation of a monumental building. Nevertheless, it is reasonable to continue the magnetometer surveys in Yeha to suggest areas for settlement extensions where no remains are discovered by archaeological prospection in the first few metres of soil.



## Chapter 7

# The case study of Gumbati

### 7.1 Introduction

The Achaemenid "palace" of Gumbati is considered in the literature as the first evidence excavated for an Achaemenid period (c. 550-330 BCE) mudbrick building in Georgia because of the architectural similarities of its ground plan to the complexes and finds of Sari Tepe (Azerbaijan) and Benjamin (Armenia) (Furtwängler, Knauß, & Egold, 1995), two other South Caucasian Achaemenid sites, as well as the royal palaces of Persepolis and Susa in Iran (Furtwängler & Knauß, 1996). Gumbati is situated in the far east of Georgia, in the province of Kakheti, in the Alazani Valley (see Fig. 7.1 b). The excavations, carried out by archaeologists from the Universities of Halle a. d. Saale and Münster together with colleagues from the Academy of Sciences in 1994-1996, were triggered by the discovery of fragments of limestone bell bases, a typical form of Achaemenid architectural fitting. They show parallels to the ones found at the sites mentioned above, and a petrological examination has shown that they originate from the same quarry as the column bases of the palace on Gurban Tepe at Karacamirli (Azerbaijan) (Gagoshidze, Knauß, & Babaev, 2007), a site which was discovered only ten years later. The remains of a monumental mudbrick building at Gumbati bear resemblance to the palace situated just 70 km to the south (Knauß, 2000). By the time the excavations in Gumbati ended, some questions regarding the size and complete plan of the complex remained open as well as the extent of the Persian occupation had not been established, so there was still great potential for further investigations of the site. Investigations in Gumbati resumed in July 2018 with geophysical and archaeological surveys within the framework of a joint Franco-German project "Paradise", funded by the Deutsche Forschungsgemeinschaft (DFG) and the Agence National de la Recherche (ANR) from 2017 to 2020. Finding the site proved to be a challenge as the geographical location of the mid-90s excavation was only roughly known and intensive agricultural activity had obliterated all traces of the trenches. One of the first objectives of the magnetometer surveys was to rediscover the old excavation (see Fig. 7.1 c+d) or traces of the "palaces" and the large-scale investigation of the site, which was continued in 2019 and 2021. The results of which are described first in this chapter. In the area of the old trenches no indicative magnetic anomalies were discovered, so that the attention focused on the linear anomalies to the north-west which were cautiously interpreted as walls and thought to be potentially outer walls or an enceinte of the Gumbati Achaemenid structure. Since no further features indicative for the "palace" were visible in the magnetogram, the excavation trenches were placed at the location of the "wall". Interestingly, no archaeological features could be documented in the trenches or in the profiles which could explain the magnetic anomalies. Soil samples were collected

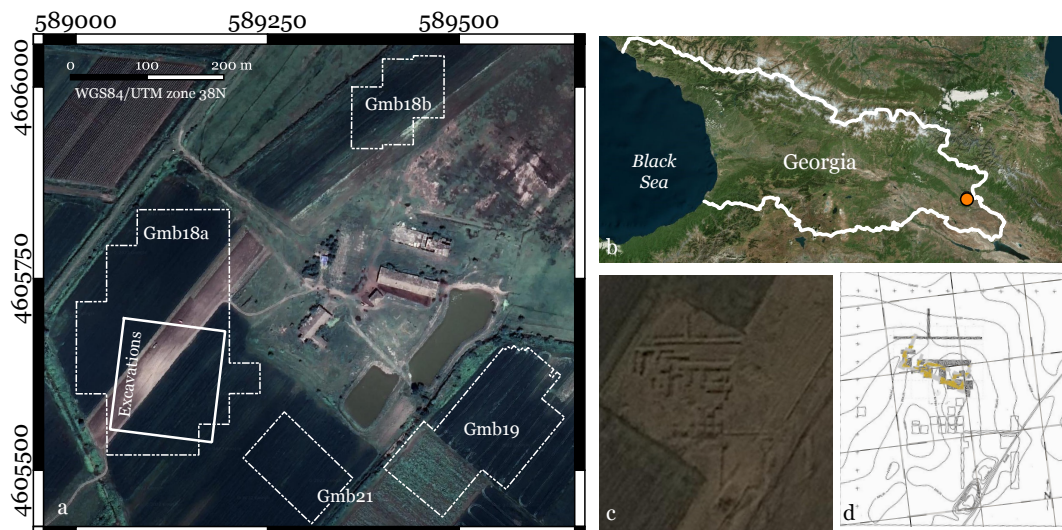


**Figure 7.1:** a) Location of the magnetograms at Gumbati with the outline of c) and d). b) Location of Gumbati in the east of Georgia. c) Excavation trenches visible in old satellite images. d) Sketch of the mid-1990s excavation trenches and outline of the Achaemenid complex.

along vertical profiles for chemical analysis and susceptibility measurements, to decode the "ghost feature" and reveal the differences in chemical and physical properties which were not visible to the naked eye.

## 7.2 Geographical, geological and archaeological context <sup>1</sup>

### 7.2.1 Location and geologic background

The site of Gumbati lies in the Kakheti region in eastern Georgia's piedmont lowland (Javakhishvili, Maruashvili, Gobejishvili, & Tielidze, 2019), more exactly in the Iberian or Kura lowland between two arms of the Greater Caucasus Mountain chain with the Kazbeg-Lagodehki zone to the north and the Mestia-Tianeti zone to the south (Gamkrelidze, Okrostsvavidze, Koiava, & Maisadze, 2021). It is situated south of the Kakheti Caucasus (Tielidze, Gobejishvili, Tsereteli, Maruashvili, & Kumladze, 2019), northeast of the Gombori Range (Tielidze, Gobejishvili, Tutberidze, et al., 2019, Fig. 1.1 or 12.1) in the Alazani river valley. The Alazani River is to the northeast, flowing in a west-east direction down from the southern slopes of the Greater Caucasus (Tielidze, Gobejishvili, Tutberidze, et al., 2019). The Alazani is one of the main tributaries to the Kura (Mtkvari) River, the waterway connecting the region with modern Azerbaijan. The geology in the vicinity of Gumbati mainly consists of quaternary terrigenous and volcanic rocks in the southeast and Jurassic terrigenous and volcanic rocks northwest of the Alazani. Further to the south, Neogene and Paleogene terrigenous, cretaceous carbonaceous and volcanic rocks make their appearance (Gamkrelidze et al., 2021). The Gombori range mainly consists of sandstone-aleurolitic covered with cluster-limestone, flysch, aleurolitic, sandstone, gravelite, turbidites, pelagic marls, flint argillites, heliotrophic limestone and marls, conglomerates and boulder breccias. Clay, loams and marine molasses can also

<sup>1</sup>This section was provided by Michaela Schauer.

be found (Tielidze, Gobejishvili, Tsereteli, et al., 2019). In the piedmont depression, the upper layer mainly consists of alluvial, alluvial marine, lacustrine and alluvial-proluvial gravels, conglomerates, sands and clays, followed by clays, sandstone, conglomerates and submarine calc-alkaline volcanic rocks. Limestone follows at further depth, as do lignites and, gypsiferous clays and sandstones (Gamkrelidze et al., 2021)[Fig. 2.7]. Other authors categorize marine and river terrace deposits as dominating the uppermost layer, followed by gritstone, spongilites, opoka, sandy argillites, claystone, and siltstones. Marls and volcanoclastic rocks lie underneath (Adamia et al., 2011, Fig. 23). In general, Pleistocene alluvial and deluvial sediments dominate in the Alazani plain (Javakhishvili et al., 2019). The geomorphological sinking and filling with alluvial sediments of the area continues today (Tielidze, Gobejishvili, Tutberidze, et al., 2019). The latter is due to the powerful mudflow of the Alazani River, which forms debris cones, especially on the lower terraces (Tielidze, Gobejishvili, Tsereteli, et al., 2019). The right side of the river, thereby, is especially influenced by Tsivi suite sediments (gravelites, cobbles) transported by mudflow from the Gombori range (Tielidze, Gobejishvili, & Javakhishvili, 2019).

A sondage documented in 1995 at the site of Gumbati shows a layer of brown earth (topsoil) followed by limestone pebbles covering artificial archaeological structures consisting of ash, mudbrick, walking horizons and burned debris on natural soil (Furtwängler & Knauß, 1996, Fig. 7) As the layer of highly eroded limestone pebbles mainly covers the area of and above the main building of Gumbati, it most possibly derives from the limestone column bases and their destruction by ploughing or other human activity (Furtwängler & Knauß, 1996).

### 7.2.2 Archaeological background

Gumbati itself is known from excavations in the mid-90th of the last century. This uncovered the mudbrick architecture of a large Achaemenid building from the 5th century BC with architectural features not in situ made of limestone in the form of column bases made of locally quarried limestone. The building was constructed of mudbrick walls with humus mortar, and its outer walls reach a thickness of up to 2.70 metres, with a possible entrance to the west. The first post-Achaemenid phase differs from these early structures in the presence of an occupation layer, limestone pebbles and hearths. Due to the lack of small finds and the possible early partial destruction of the site, it is assumed that farmers or shepherds inhabited Gumbati during this phase, which probably dates to the 3rd century BC (Furtwängler & Knauß, 1996). The area was later used as a burial ground in the 1st century BC. It is also worth mentioning that a Bronze- to Early Iron Age settlement called Naomari-Gora is nearby. Here, a burial of the 1st century BC to 1st century AD was found (Furtwängler et al., 1995). A Late Middle Bronze Age stone-covered burial mound with a diameter of around 4.40 metres was found below the Achaemenid features at Gumbati. It lay around 1.70 metres below the modern surface. The stones used for the burial mound are small to medium-sized river pebbles that could have been collected in the wadis of the Mestia-Tianeti mountain range south of the Alazani Valley (Furtwängler et al., 1995). Those kurgans are characteristic of the Trialeti culture, which is well known from the Alazani valley. The kurgans usually consist of an outer layer of earth, followed by stones and tree trunks, which form a burial chamber modelled on the burial mounds. Near Gumbati, some of the Bedeni phase kurgans at Tsnori were additionally furnished with clay-plastered tree trunks. While the inventory and burial rituals change over time, the construction of the burial mound remains pretty much the same throughout the Middle Bronze Age (Kushnareva & Kušnareva, 1997).

## 7.3 Magnetometry

### 7.3.1 Method for magnetometer survey

The magnetometer survey in 2018 was conducted with three magnetometers: two Caesium total-field magnetometers in duo-sensor configuration, the Scintrex Smartmag SM4G-special magnetometer and a Geometrics G-858 magnetometer, which measured the total ambient magnetic field as well as a vector gradiometer, a Foerster Ferex instrument. In 2019, we measured with the two Caesium magnetometers mentioned above and in 2021, we continued with two Geometrics magnetometers. The survey areas were divided into 40 m by 40 m grid squares and subdivided into adjacent segments, each scanned by a different device. The sensors of each instrument were carried circa 30 cm above the ground. With a sensor distance of 0.5 m for each instrument, a line spacing of 1 m and a continuous measurement at a frequency of 10 Hz, we obtained a data resolution of at least 0.1 m by 0.5 m, thus meeting the requirements for archaeological prospection guidelines (Schmidt et al., 2015). GPS measurements georeferenced the edge points of the grid squares. The resulting segments of the individual survey areas of the diverse instruments were merged into one magnetogram during the data processing. For this, the total-field magnetometer data were first corrected for the diurnal variation (see chapter 2) and an image high-pass filter with  $R=10$  was applied. These segments were then combined with the Ferex gradiometer data, which were multiplied by a factor determined by the difference in the standard deviation of both data sets to obtain a visual uniform output of the measured area. Although I also used the pre-filtered total-field magnetograms for the interpretation as well as the merged one. I only show the latter to present the results and interpretation.

### 7.3.2 Interpretation of the survey areas

#### 7.3.2.1 Results of Gmb18A

The results of Gmb18A, Fig. 7.2 show a heavily contaminated site. A stripe pattern with an NNE-SSW strike orientation is predominant, which can be clearly associated with the plough furrows transecting the field. Also clearly visible are the subdivisions of the field as mostly negative anomalies. There is a large number of dipole anomalies that cover most of the magnetogram in varying densities. Most of them are, in all likelihood, anomalies of iron fragments or pieces, remnants of the ongoing agricultural cultivation of the site. Their omnipresence as dipole anomalies of different sizes and structures makes it difficult to recognise underlying structures or may even obscure them.

At first glance, no obvious structures are noticeable in the magnetogram, which can be undoubtedly associated with archaeological features. Even the old excavation trenches are not recognisable in the magnetogram (see Discussion). Only by georeferencing the excavation map with old satellite photos was it possible to associate some dipole anomalies with the trenches. However, there is no clearly recognisable pattern, leading to the suspicion that these are just coincidental. Especially in the total-field data, some broad

anomalies are discernible. Their rather monopolar character hints at a variation in the magnetic properties of the soil, attributable very likely to the enrichment of iron-bearing minerals or lack thereof. Some of these areas with higher intensity show irregular forms. However, the strict linearity of some of these anomalies may lead one to believe they have an anthropogenic origin. Particularly, the kink in one of the structures may support this presumption. One of the first hypotheses was that these were wall remains or other

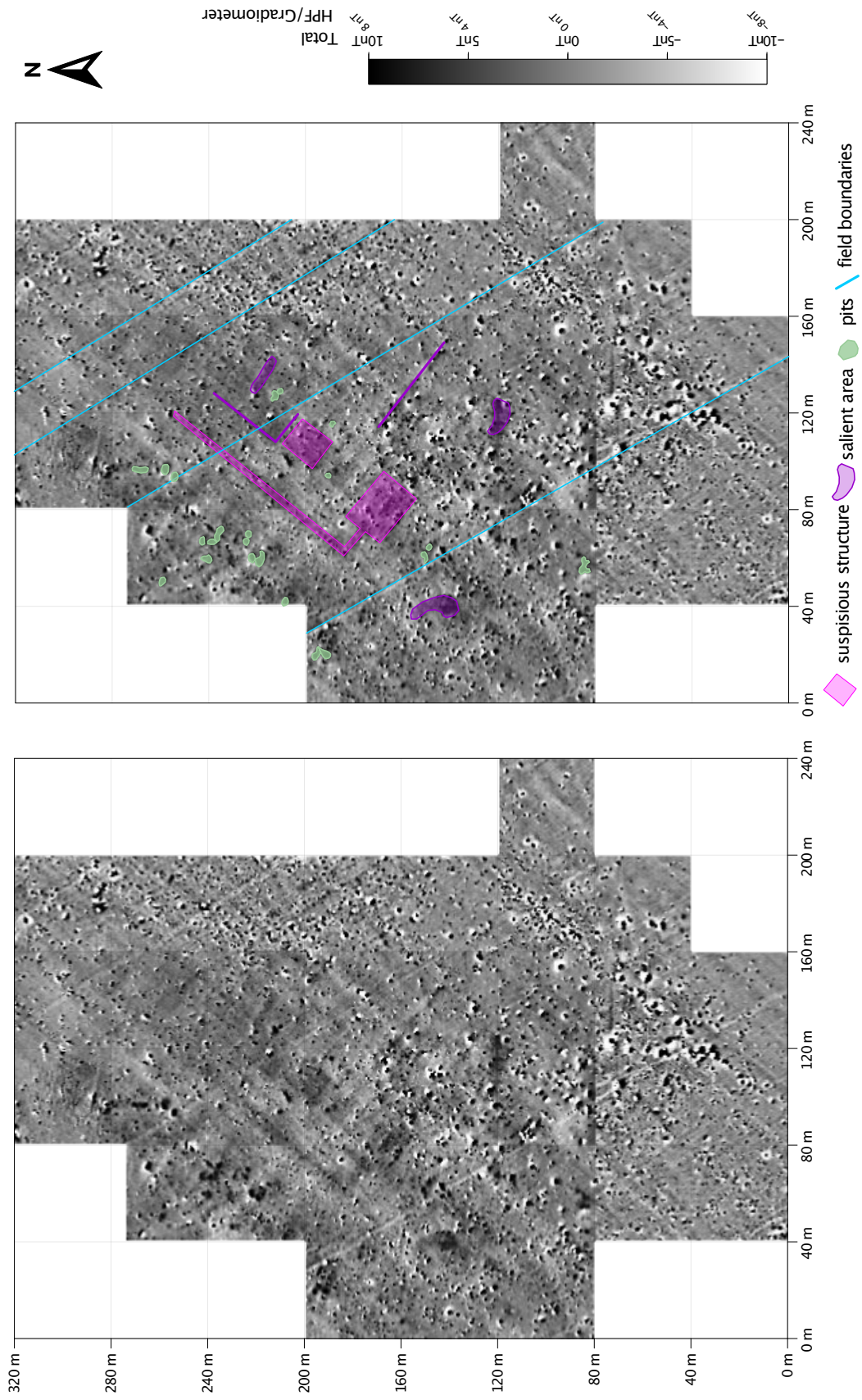
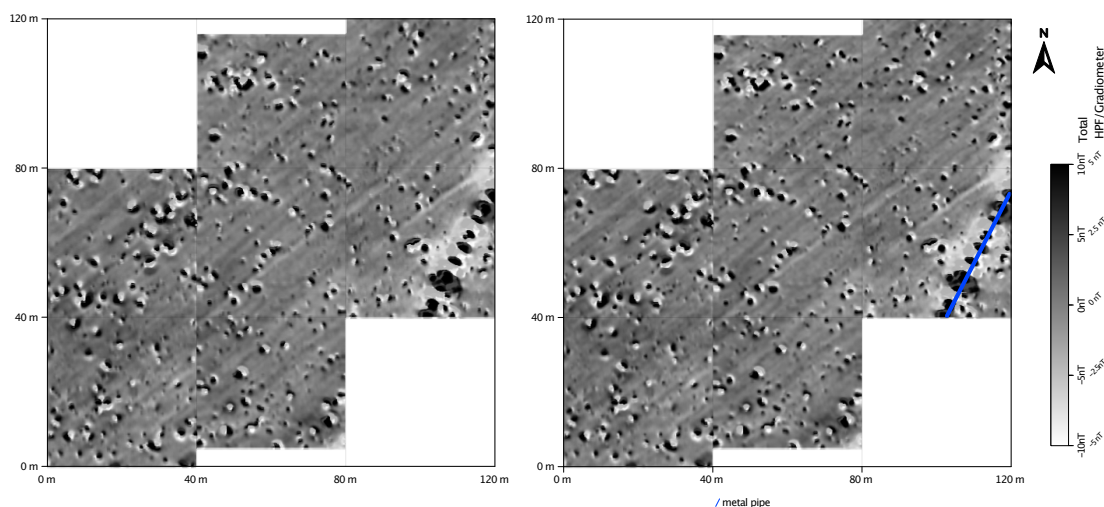


Figure 7.2: Magnetogram of Gmb18A.



**Figure 7.3:** *Magnetogram of Gmb18B.*

features connected to the palace found previously in Gumbati. However, it is somewhat contradictory that these structures are parallel or perpendicular to the modern plough lines. Sporadic pits are visible, but there is an evident accumulation in the northeast part of the magnetogram.

### 7.3.2.2 Results of Gmb18B

Like Gmb18A, the area Gmb18B (Fig. 7.3) is dominated by plough lines running NNE-SSW and is heavily contaminated with iron pieces or iron-bearing waste. A subsurface metal pipe is visible in the eastern corner of the magnetogram. The heavy contamination and the disturbances caused by the ploughing do not reveal any other features.

### 7.3.2.3 Results of Gmb19

Area Gmb19 (Fig. 7.4) is also contaminated with iron waste, presumably agricultural remains related to wine-growing. Ditches with different orientations and shapes can be distinguished in the magnetogram. Some of them are straight, bent or strongly curved. Their anomalies vary in intensity and can, therefore, be recognised differently well. There is no discernible pattern or relationship between the individual ditches. Pits are visible, too, clustering towards the northwest. The heavy contamination makes it difficult to distinguish pits and iron waste.

### 7.3.2.4 Results of Gmb21

The results of Gmb21 (Fig. 7.5) show the same NNE-SSW striped pattern going back to the plough furrows. There are some straight structures distinguishable. Most of them resemble the field subdivisions of Gmb18a. The westernmost feature shows similarities to the ditch structures in Gmb19. Odd rectangular enrichment or lack of soil magnetism is discernible and may show a relationship to the straight structures. A circular anomaly is recognisable.

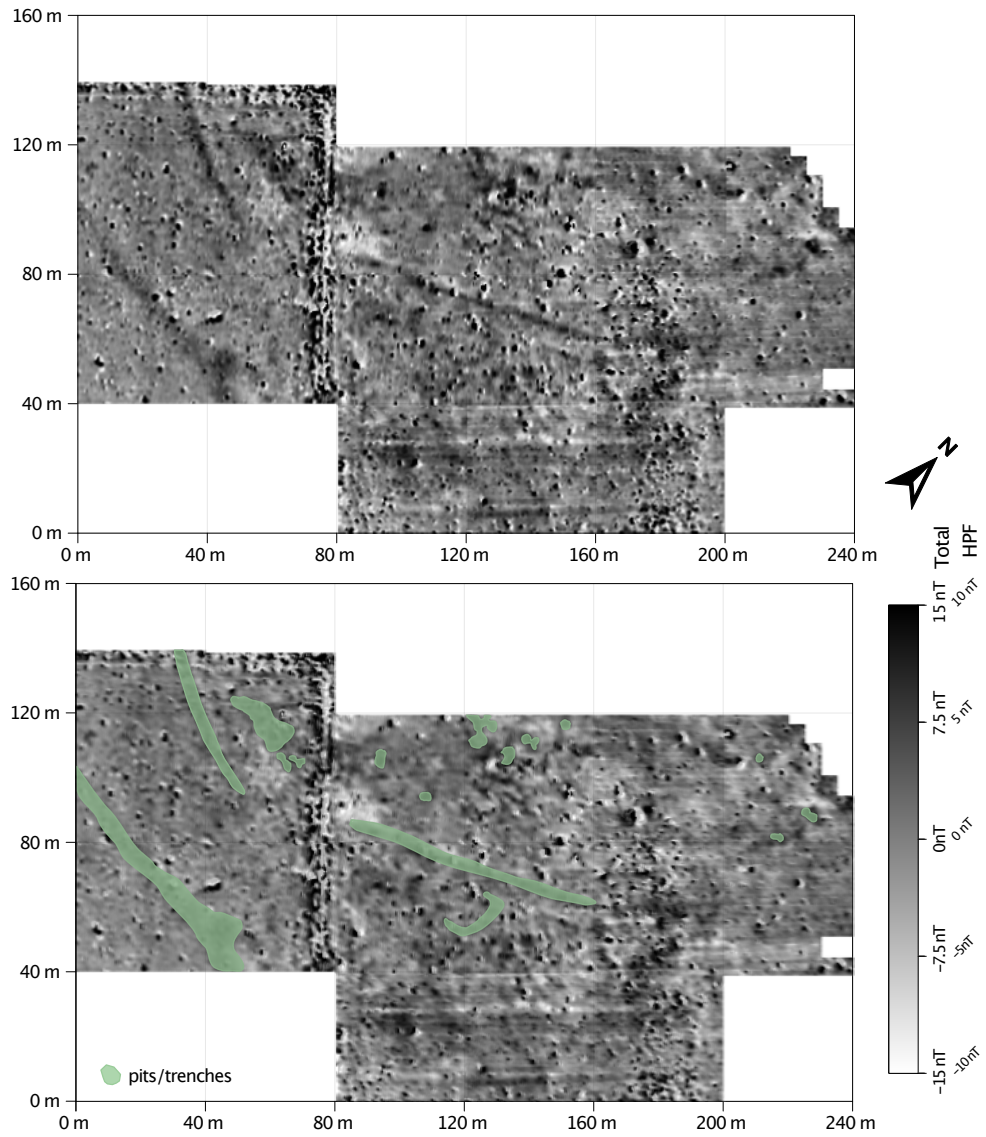


Figure 7.4: Magnetogram of Gmb19.

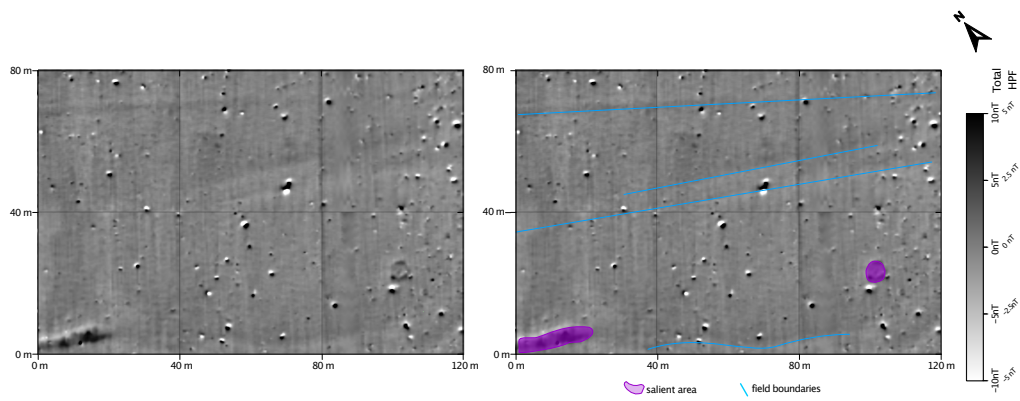
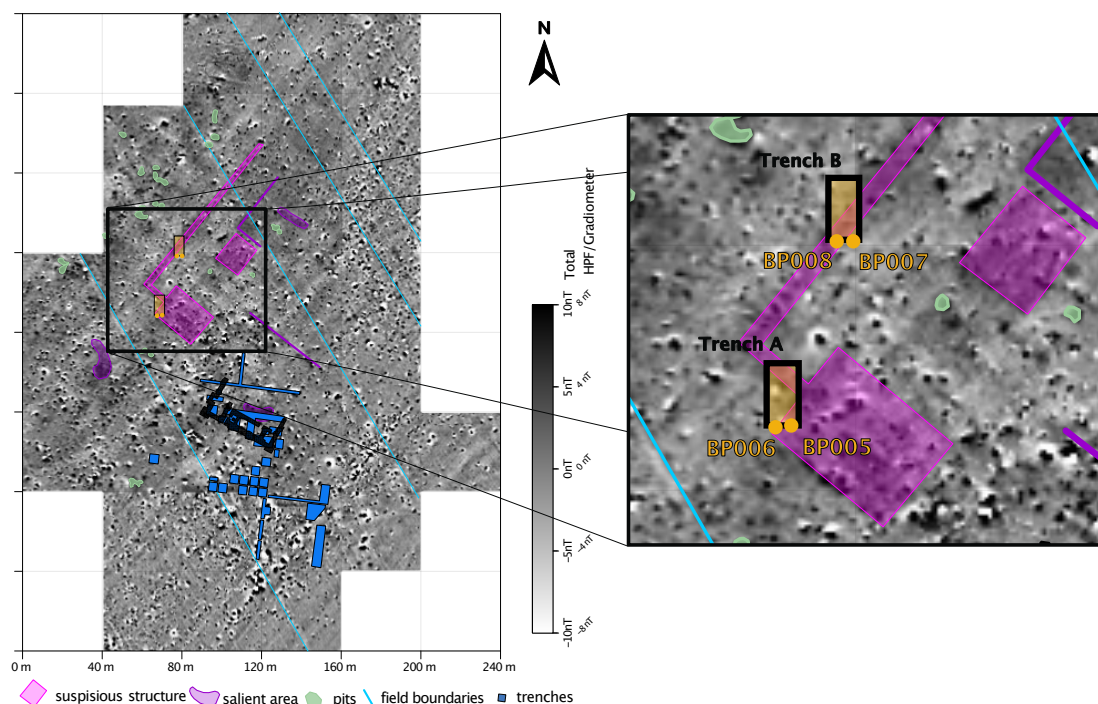


Figure 7.5: Magnetogram of Gmb21.



**Figure 7.6:** Plan of the excavation trenches and palace outline after referencing the location of the mid-1990s excavation trenches by vintage satellite images. Position of the excavation trenches A and B and the vertical profiles BP005-008.

## 7.4 Excavation results and sample selection

### 7.4.1 Excavation results

As the results of the magnetometer prospection were inconclusive regarding the re-location of the old trenches but indicated a difference in magnetisation in the form of straight, kinked and rectangular features, two excavation trenches were opened in 2019 in the area of the only larger anomaly visible ( Fig. 7.6) the feature which was suspected to be an outer wall of the Achaemenid complex. However, no features that could explain the magnetic anomalies were unearthed during the excavation. Numerous fragments of pottery and limestone were found, indicating proximity to the Achaemenid complex (Kaniuth, 2022). The excavations revealed a disturbed sequence of soil layers (see Fig. 7.7), a sign of human intervention at different periods in time. In order to explain the "ghost phenomenon" in the magnetogram, a difference in physical properties that was not visually recognisable during the excavation, the soil profiles were described in detail, and soil samples were taken from the excavation trenches to investigate the magnetic and chemical differences in the soil layers.

### 7.4.2 Soil profiles

The east-west profiles of the trenches A and B with their stratigraphy are shown in Fig. 7.7. An overview of which samples were collected from which context and a summary of its material is provided in Tab. 7.1. The different contexts (or strata) are deviated according to their colour and soil texture (on-site by means of 'Fingerprobe' after DIN 19682-2).

A layer of river pebbles marks the bottom of both trenches at a depth of around 1.50 m below the modern surface (respectively 154 cm for BP005, 135 cm for BP006, 118 cm for BP007 and 126 cm BP008, see Tab. 7.3). The stratigraphy of the two trenches is identical in the lower part of the sections, only the layering in trench B is perturbed by two pits. These layers of fist-size stone pebbles (contexts 07 & 15) are covered by a grey layer of clayey loam (contexts 06 & 14) followed by a thick yellow-beige coloured, dense clayey loam layer (contexts 05 & 11). In trench A, context 05 is covered by a sandier grey clayey loam layer (context 04). Coming from the west, a dense clayey loam layer with a high amount of salt or chalky inclusions (context 03) covers context 04. In trench B, the same dense clayey loam layer (context 10) covers directly the yellow-beige clayey loam layer (context 11). These layers can be assigned to two kurgans. Such a pebble covers had already been documented in the 1990's stratigraphic sonding of the excavation. However, the soil layers above these contexts differ. In trench A, plough horizon context 02 is characterised by oblique bands of loam (most probably deriving from context 03 or 04) and porous humus (from context 01). The topsoil here consists of porous to dense loamy humus with some bigger pebbles (context 01). In trench B, context 09, a dense loamy humus is covered by a loose humus layer (context 08). While context 09 covers context 10 in the west, in the east, it lies above pit 1 (contexts 17-22) and a sandy to loamy humus layer (context 16). Pit 1 cuts through contexts 11, 14, 13 and 16 and ends right on top of context 15. The pit itself consists of several layers ranging from brown, clayey loam (context 17), dense brown-black humus (context 19), light grey-brown loam (contexts 20 & 22), grey-orange clayey loam (context 18) to black-brown humus loam (context 21). In the west of trench B, pit 2 (context 13) undercuts mostly underneath the pebble layer (context 15). Also worth mentioning is a nearly rectangular block of yellow loam (context 12) embedded in context 11. The latter, the cover layers of the kurgan and the pit fillings, are categorised as formed through anthropogenic processes. An overview and classification of the samples of the different sections can be found in Tab. 7.3. As the thickness of each layer varies considerably in the profile, we refrain from giving the individual thicknesses and refer to figure 7.7.

### 7.4.3 Sample collection and preparation

In order to understand the reason for the "ghost feature" in the magnetogram, soil samples were taken in trenches A and B. The locations of four vertical profiles were selected (see Tab. 7.2 and Fig. 7.6) are based on the presumed location of the features according to the magnetograms and the slight variation in soil colours observed in the excavation. For Area A, two vertical sections were sampled: one in the eastern part of the trench (BP007) and one in the western part (BP008) at a distance of about five metres from each other (see also Fig. 7.7). For Area B, a vertical section in the eastern part of the trench (BP005) and one in the western part (BP006) were also sampled at a distance of about four metres. Samples were taken in 10 cm increments, starting from the bottom of the trench. Prior to the measurements, the soil samples were carefully crushed with a brass pestle and then sifted through a fine-mesh 1 mm sieve. This removes roots and coarser material, which may affect the accuracy of various measurements and subsequently distort their results. For the susceptibility measurements and the pXRF measurements, we used non-magnetic cylindrical plastic containers with one-inch diameter.



**Figure 7.7:** Photogram of the east-west profiles of trenches A and B with the position of the profiles and sample location. The red scale shows the position where the sample with the corresponding number was taken. A layer of river pebbles belonging to two kurgans (contexts 7 & 15) marks the bottom of the excavation trenches. It is covered by a grey clayey loam layer (6 & 14), which is again covered by a yellow-beige dense clayey loam layer (5 & 11) and a less sandy layer (4). Followed by a dense clayey loam layer with high salt content and chalky inclusions (3 & 10). Context 2 is characterised by bands of 3 & 4 mixed with humus from context 1. The topsoil (1) is porous to dense humus with some pebbles. Context 09 is a layer of dense, loamy humus covered by a loose humus layer (8). Two pits can be identified in Trench B: brown clayey loam (17), dense brown-black humus (19), light grey-brown loam (20 & 22 & 13), and grey-orange clayey loam (18). Context 12 is a block of yellow loam.

Context	Sample	Material
1	24-26, 52-55	porous to dense humus with bigger pebbles
2	21-23, 48-51	oblique bands of loam and porous humus
3	20	dense clayey loam with salt or chalky inclusions
4	19, 47	sandier grey clayey loam
5	17-18, 45-46	yellow-beige dense clayey loam
6	15-16, 43-44	grey clayey loam
7		river pebbles
8	12-14, 39-42	loose humus layer
9	9-11, 36-38	dense loamy humus
10	8, 34-35	dense clayey loam with salt or chalky inclusions
11	29, 31-33	yellow-beige dense clayey loam
12	30	yellow loam
13	28	light grey-brown loam
14	27	grey clayey loam
15	3	river pebbles
16		
17	6,7	brown clayey loam
18	4,5	grey-orange clayey loam
19		
20		light grey-brown loam
21	1,2	
22		light grey-brown loam

**Table 7.1:** *Overview: Context, samples and materials.*

Section	Trench	Northing	Easting	Height m.a.s.l.
BP005	B (East)	589068.910	4605689.921	227.004
BP006	B (West)	589066.076	4605689.554	226.963
BP007	A (East)	589079.090	4605720.031	226.553
BP008	A (West)	589076.237	4605720.021	226.684
BP009	D	589059.271	4605737.563	226.623

**Table 7.2:** *Position of Sections.*

## 7.5 pXRF and susceptibility analysis

### 7.5.1 Portable X-ray fluorescence (p-XRF) analysis<sup>2</sup>

A Niton XL3t device was used for the p-XRF measurements. The material to be examined in this measurement procedure is bombarded with high-energy X-rays. The electrons, thus excited from their original atomic orbital position, emit energy upon their return to their original position, hence the term X-ray fluorescence. The wavelengths of the emitted energy spectra are characteristic of each chemical element. The proprietary fundamental parameter algorithm (FP), with which the instrument is equipped, is used to convert fluorescent peaks of the energy spectra into concentration values of elements. It considers factors like emission effects, scattering, efficiency, and secondary and tertiary absorption, among others. Further, the TestAllGeo-Mode calibrated on powder samples of ancient pottery and soil samples by Analyticon and a coefficient correction for silicate matrices based on the Frankfurt ancient pottery standards is used (Helfert, 2013). Every sample was measured once with an 8 mm measurement spot under air in the main, low and high range with 60 seconds per measurement and in the light range with 120 seconds per measurement.

### 7.5.2 Soil chemistry of trench A and B

Looking at the geochemistry, we are focusing on the chemical elements significant for soil analysis. The values can be found in Tab. 7.4 as well as in Tab. 7.5 and the section profiles in Figs 7.8 and 7.9. Apparently, the values of  $\text{TiO}_2$  are constant ( $0.73 \pm 0.02\%$ ),  $\text{MnO}$  and  $\text{Al}_2\text{O}_3$  do change but not significantly or not with a recognisable pattern. As for  $\text{Sb}$ ,  $\text{U}$  and  $\text{Sn}$ , they are below the detection rate. Significant changes can be seen in  $\text{P}_2\text{O}_5$  and  $\text{CaO}$  and  $\text{MgO}$ . Based on these elements alone, the type of layer - topsoil, plough horizon, stones, pit filling and kurgan layers - can be distinguished in the vertical profiles (see Fig. 7.8 and Fig. 7.9). In scatter plots of the most influential elements for soil analysis - phosphor, calcium, iron and potassium - all the features show either a good clustering or a linear relationship. Additionally, silicate and aluminium function to separate these features (Fig. 7.11) - representing the different degrees of clayey and sandy parts of soils (Rice, 2015). Trace elements can be used to identify the source of the soils (Fig. 7.10) or supplement the comparison between types of soils.

For the topsoil and plough horizon, calcium, strontium, and phosphorus show a similar pattern in the vertical profile and linearity in the scatter plot - an indication of human activity (Save et al., 2020). Especially the content of phosphor ( $\text{P}_2\text{O}_5$ ) is significantly higher than for the topsoil layers and plough horizon (trench A  $0.84 \pm 0.07\%$ , trench B  $0.53 \pm 0.03\%$ ) which also includes the peak of the profile (BP008 1.32%, BP007 1.37%, BP005 0.59%, BP006 0.57%) than the kurgan layers. Also, topsoil and plough horizon show slightly elevated amounts of potassium ( $\text{K}_2\text{O}$ ), e.g. for BP008  $5.9 \pm 0.3$  to  $4.9 \pm 0.1$  (kurgan layers). Also, copper and zinc are slightly elevated in the layers compared to the kurgan layers, indicating human activity. To some extent, calcium, strontium, and barium show the same trend with depth and a linear relationship in the scatter plot - an indicator for natural soil. The slightly lower aluminium, magnesium, and slightly higher silicate content compared to the kurgans, and the elements' values are comparable throughout the sections. Therefore, topsoil and plough horizon can be considered as natural soil altered by human activity.

<sup>2</sup>The measurements and analyses were performed by Michaela Schauer. Text and Figures 7.11 and 7.9 were also suggested by Michaela Schauer, but reorganised or recreated for the purpose of this thesis.

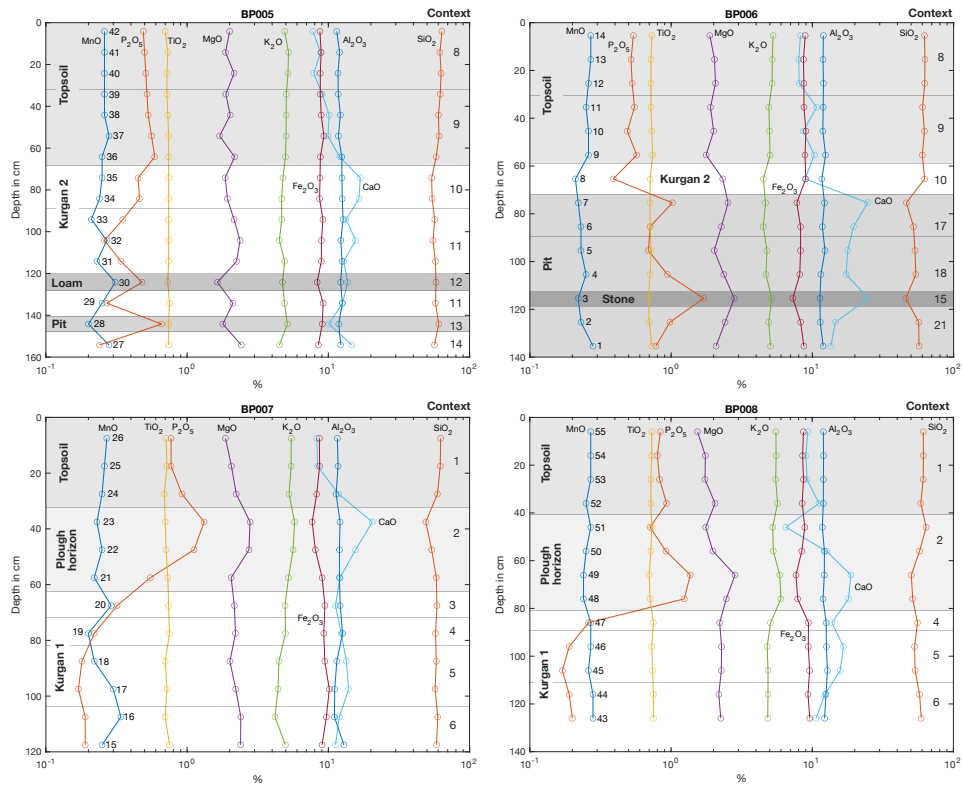


Figure 7.8: Depth versus main elements.

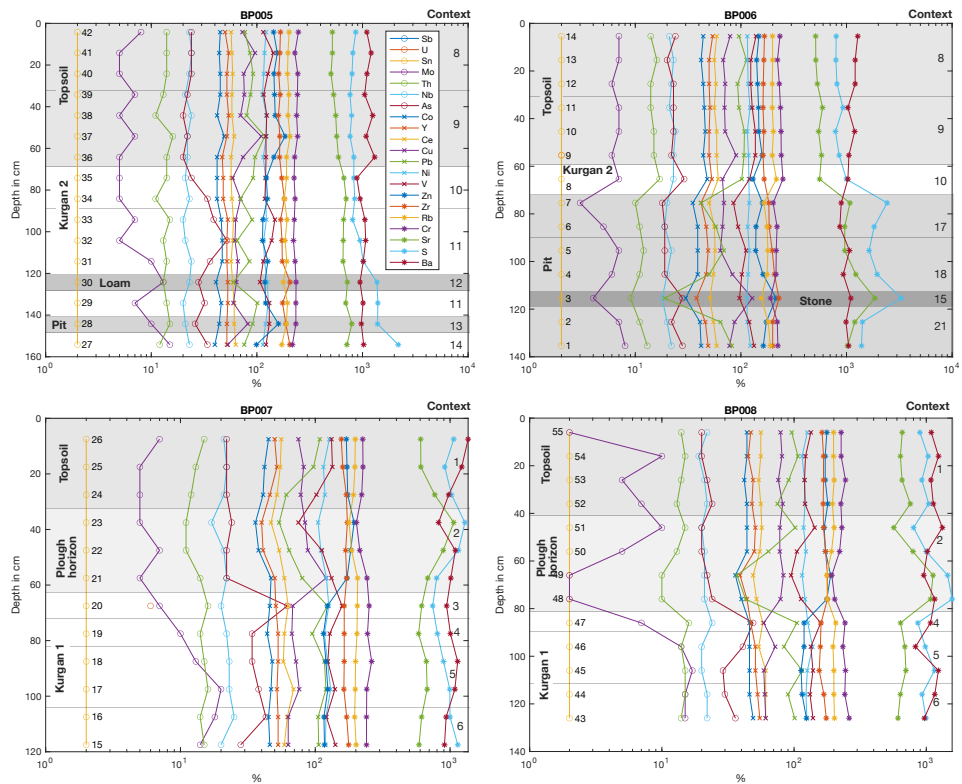


Figure 7.9: Depth versus trace elements.

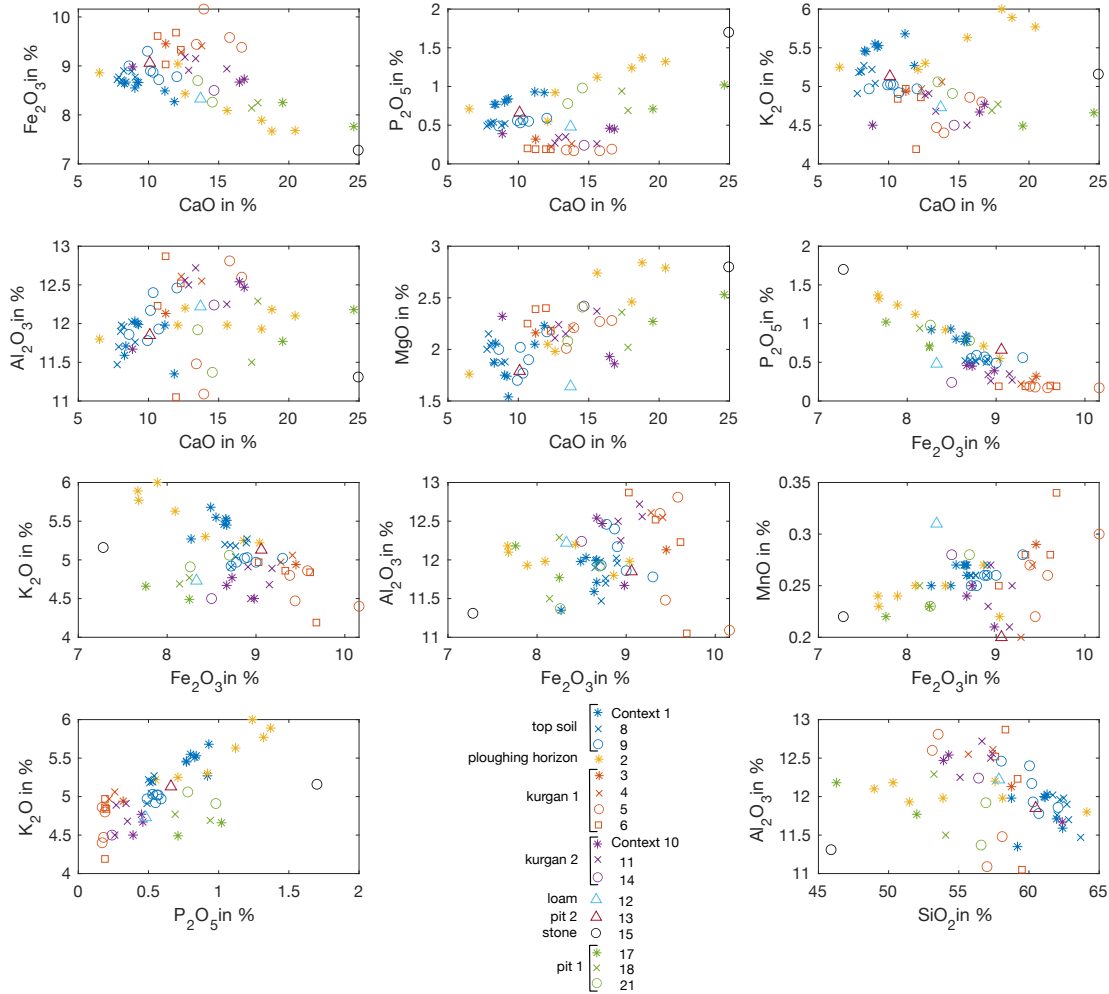


Figure 7.10: Scatter plots of the main elements.

The plough horizon has a different chemical composition depending on the layer sampled - either humus or clay - and shows good clustering either with the topsoil or the kurgan layers. The calcium content is high in the plough horizon and the lower parts of the topsoil of Trench A (samples 24/52) and behaves similarly to the phosphorus content here, while the calcium values for the topsoil are generally in the lower range with less fluctuation. Therefore, this can be interpreted as a plough horizon, and small parts of the topsoil still seem to contain residues of last years' fertiliser, with a higher concentration in the plough horizon. As this part is less disturbed by weathering, the added calcium is also better preserved in these lower layers.

The layers of the kurgans have lower phosphorus and potassium concentrations but higher aluminium and iron concentrations than the topsoil (see Tab. 7.4 and Fig. 7.8). Kurgan 1 has the highest iron, aluminium and vanadium/chromium values but the lowest phosphate values of the measured samples. The different element concentrations suggest that different soils were used to construct these two kurgans. Furthermore, the excavation did not reach the burial as the most important elements for this interpretation - phosphorus, copper, manganese, potassium and calcium levels - are comparatively low. Looking at the scatter plot of trace elements, Kurgan 1 appears to be comparable to the area's topsoil

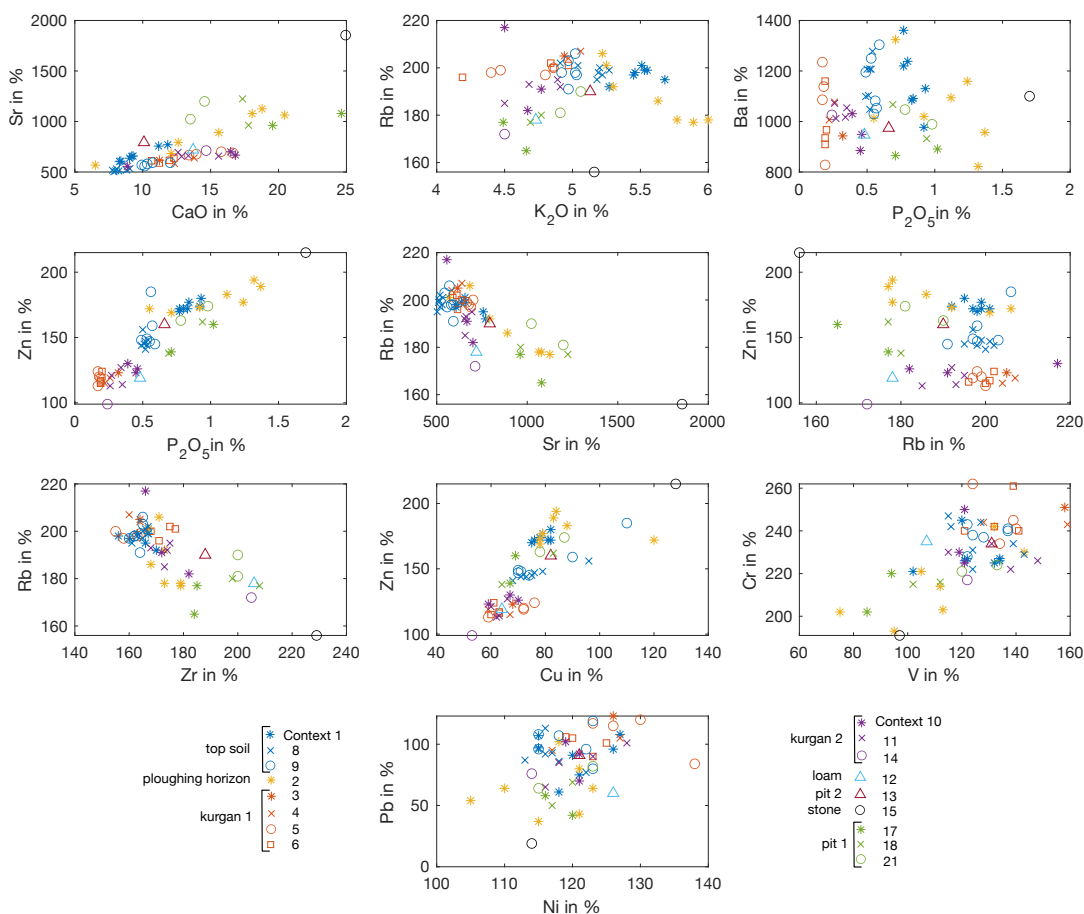


Figure 7.11: Scatter plots of the trace elements.

in some aspects, while Kurgan 2 is clearly not. Nevertheless, both are similar in their low copper and zinc values, distinguishing them from pits, arable horizons and topsoil. This suggests that the soils for Kurgan 1 may have come from the local area, while the soils of Kurgan 2 may have been transported from further afield. This is supported by the increased iron, manganese and aluminium content in the lower layers of Kurgan 1 (contexts 4 to 6), which is not the case for Kurgan 2. These chemical characteristics could be related to the use of (grass) sods in the construction of Kurgans 1 (see, e.g. Breuning-Madsen, Holst, & Rasmussen, 2001). Should this be the case, it would be unlikely that they were transported from far away.

Pit 1 shows comparable markers of human activity as the topsoil and the plough horizon. Pit 1 has low iron but high calcium, strontium, zinc and phosphate levels, which strongly indicates anthropogenic organic residues. However, as very high potassium and manganese values are missing, it does not appear to be a "real" waste pit. According to the aluminium/silicon ratio and the average zircon values, the soil is less sandy and more clayey than the other samples examined in this study. Some trace elements differ significantly from the natural soils included in this study, while some show a similarity. Interestingly, the phosphorus and manganese contents in pit 1 (trench B) are also in comparable ranges to some samples of the plough horizon (trench A). Therefore, it is possible that the natural material of the area was altered by human activity and then

deposited in Pit 1. Pit 2 clearly shows many parallels with the topsoil. Of the main elements, only manganese differs; of the trace elements, only a few - zircon, strontium and barium - differ slightly. It is, therefore, possible that Pit 2 is either a pit that has been slowly filled by natural sediments from the area and, therefore, bears a strong resemblance to the natural soil or an old topsoil layer that differs from the modern topsoil only in a few trace elements.

The chemistry of context 12 resembles - in major and trace elements - for the most part, the chemistry of Kurgan 2, only in some cases that of pit 1 (see Fig. 7.11 and Fig. 7.10). It is possible that this clay brick is either part of Kurgan 2 or reflects a phase shortly before the construction of the kurgan. The loamy rectangular object could then represent an earlier structure or phase in this area and could have been deposited here by chance. On the other hand, it could be a working clay that was deposited here unintentionally.

### 7.5.3 Susceptibility measurements

To determine the low-field susceptibility as well as the coefficient of frequency dependence of the susceptibility, I used the Bartington Instruments' Dual Frequency Sensor (0.47 and 4.7 kHz). The zero reference of the instrument is when the sensor only contains air. The instrument's calibration is confirmed by measuring a 10 ml sample of water and comparison to the textbook value. Each sample was measured a total of three times for each frequency, and an "air" measurement was taken before and after each measurement. With

$$R = \sum_{n=1}^3 R_n - (R_{air\ before} + R_{air\ after})_n / 2 - R_{container}, \quad (7.1)$$

the measurements are corrected for the instrument's thermal drift and the empty container's reading. The average is calculated from the three readings. I weighed the samples, determined their net weight by subtracting the weight of the sample holder and calculated the mass susceptibility with

$$\chi = R \cdot \frac{\text{calibration mass}}{\text{sample mass}}, \quad (7.2)$$

where the calibration mass is given with 10 g. The coefficient of frequency dependence is calculated with

$$\chi_{FD}\% = 100 \cdot (\chi_{LF} - \chi_{HF}) / \chi_{LF}. \quad (7.3)$$

Since the volume of sample holders I used is smaller than the calibration volume, I corrected the value with

$$\kappa = R \cdot \frac{\text{calibration volume}}{\text{sample volume}}, \quad (7.4)$$

where the sample's volume is calculated from the fill height of the sample holders.

### 7.5.4 Susceptibility

The uppermost topsoil layer shows for all four profiles similar volume susceptibility values (all in SI units),  $91.7 \cdot 10^{-5}$  for BP005,  $90.4 \cdot 10^{-5}$  for BP006,  $90.1 \cdot 10^{-5}$  for BP007,  $94.9 \cdot 10^{-5}$  for BP008, (see Tab. 7.7 and Fig. 7.12) and all profile show a decreasing trend in susceptibility for deeper layers. The susceptibility of the topsoil for BP005 and BP006 ranges around the same value with slight variations,  $(90.5 \pm 2.1) \cdot 10^{-5}$  for BP005 ( $88.75 \pm 2.8) \cdot 10^{-5}$  for BP006. For BP007 and BP008, there is a noticeable enhancement in

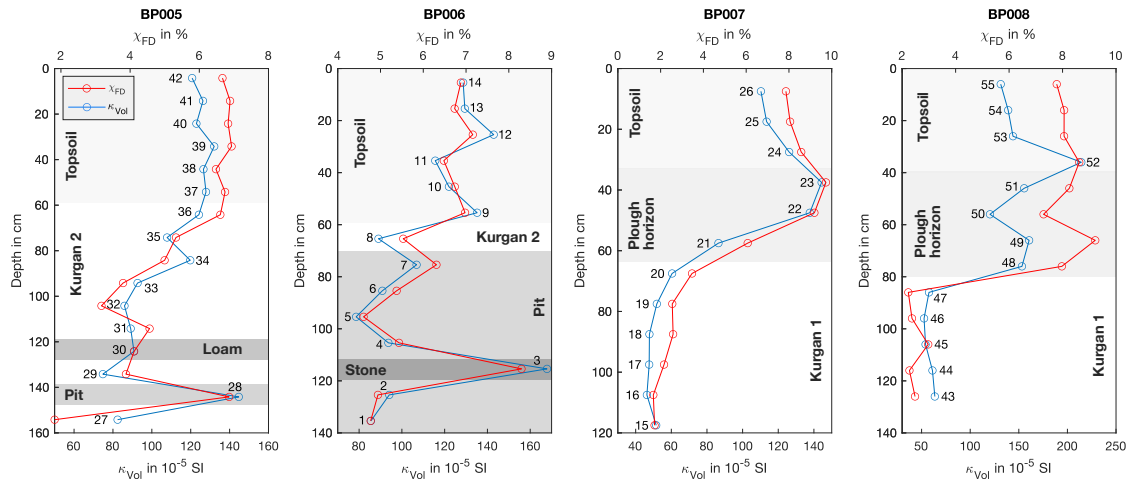


Figure 7.12: Susceptibility and  $\chi_{FD}$  with respect to depth.

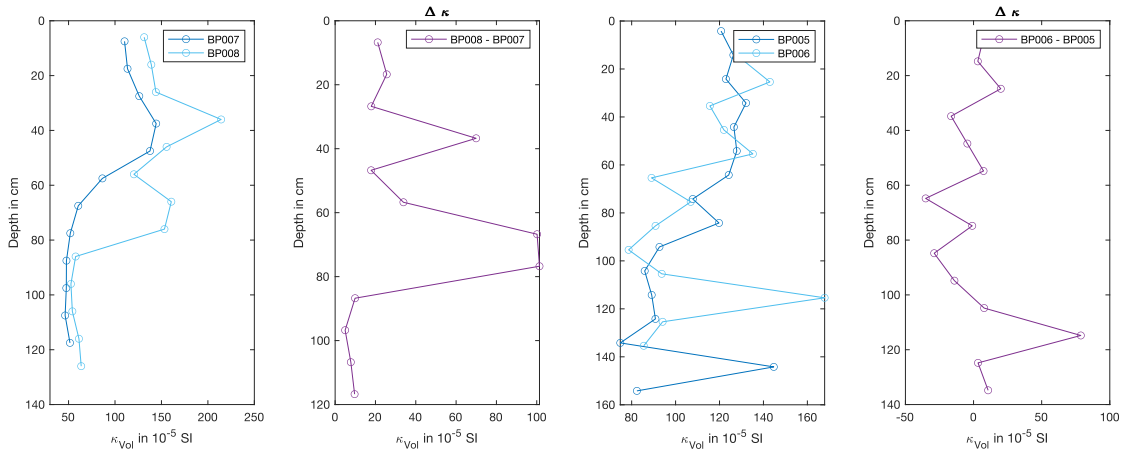


Figure 7.13: Comparison of the volume susceptibility values of BP007 and BP008 with depth and their absolute difference with depth, as well as the comparison of the volume susceptibility values of BP005 and BP006 with depth and the absolute difference with depth.

susceptibility towards the plough horizon with maximum values of  $104.2 \cdot 10^{-5}$  (BP007) and  $142.5 \cdot 10^{-5}$  (BP008). BP007 shows elevated values for two samples close to the topsoil layer; sample 21 (BP007) appears to be an intermediate sample between the enriched plough horizon and the kurgan levels. The values for the plough horizon of BP008 seem to vary more. While the values for the samples are similar to the topsoil, sample 50 with  $82.3 \cdot 10^{-5}$  is considerably lower. There is a distinct jump in the susceptibility values for kurgan 1 in profile BP008 to  $(39.5 \pm 2.8) \cdot 10^{-5}$ . BP007 shows similar values,  $(38.4 \pm 4.2) \cdot 10^{-5}$  for the kurgan 1. BP006 gives only one value of  $64.3 \cdot 10^{-5}$  for sample 8 of Kurgan 2. For BP005, the value decreases from topsoil levels (sample 36,  $87.3 \cdot 10^{-5}$ ) over intermediates, (sample 35,  $69.7 \cdot 10^{-5}$  and sample 34,  $70.5 \cdot 10^{-5}$ ) to  $(56.6 \pm 4.5) \cdot 10^{-5}$ . The loam piece shows  $60.9 \cdot 10^{-5}$ , a similar value to the surrounding kurgan. The pit filling in BP005 shows an elevated value of  $88.0 \cdot 10^{-5}$ . The filling of the pit featured in BP006 varies around  $(63.5 \pm 3.5) \cdot 10^{-5}$ . The stone shows an outline in the pit profile with a susceptibility of  $121.2 \cdot 10^{-5}$ .

If the susceptibility difference of the sections of a trench is compared with each other (see Fig. 7.13), the kurgan layer of BP007 and BP008 shows similar values with a slightly higher level for BP008 with a maximum difference of about  $10 \cdot 10^{-5}$ . The plough horizon of BP008 shows significantly higher values than BP007 up to a difference of  $101 \cdot 10^{-5}$ . The topsoil shows a higher variability in absolute difference with a drop below  $40 \cdot 10^{-5}$  but with a peak at the lower topsoil up to  $70 \cdot 10^{-5}$ . For BP005 and BP006, the topsoil variation is only between  $\pm 20 \cdot 10^{-5}$ . The lower layers are harder to compare as BP005 shows mostly kurgan layers and BP006 pit filling. The biggest peak in the absolute difference is in the stone layer with  $79 \cdot 10^{-5}$ .

The frequency-dependent magnetic susceptibility  $\chi_{fd}$  is only of limited informative value, as some susceptibility values are below  $100 \cdot 10^{-5}$ .  $\chi_{fd}$  strongly follows the profile trend of the susceptibility. It ranges for the topsoil levels and plough horizons between  $(6.76 \pm 0.16)$  % for BP005,  $(6.83 \pm 0.23)$  % for BP006,  $(8.68 \pm 0.78)$  % for BP007 and  $(8.16 \pm 0.56)$  % for BP008. The values for kurgan 1 are  $2.48 \pm 0.31$  % for BP008 and  $(2.35 \pm 0.67)$  % for BP007 and for kurgan 2  $(4.27 \pm 1.5)$  % and 5.53 % (sample 8). The loam (sample 26) has a  $\chi_{fd}$  of 4.12 %, agreeing with the values of the surrounding kurgan layers. The pit layer, sample 28, shows a strongly elevated value of 6.86 %. The values of the pit featured in BP006 vary around  $5.24 \pm 0.62$  %. The material of the stone shows a high  $\chi_{fd}$  of 8.30 %.

## 7.6 First attempts on Forward Modelling

Forward modelling was performed to verify whether the differences in magnetic susceptibility of the soil layers are strong enough to generate the ghost features. Inspired by our work (Bondar, Fassbinder, Didenko, & Hahn, 2022) with the GaMField programme, a modelling software by Pignatelli, Nicolosi, Carluccio, Chiappini, and Von Frese (2011), to model the magnetic anomalies of grave infill. However, I encountered some limitations and inconveniences with the GaMField application. I decided to develop my own code into MATLAB®. The GaMField application is based on the works of Sharma (1966), a method to compute the magnetic anomalies of bodies of arbitrary shape by dividing a body into rectangular plates and evaluating the whole body by summing the field of these plates. The idea of adding up the magnetic field of the individual prism drew my attention to the Grav\_mag\_prism programme by de Barros, Bongiolo, de Souza, Ferreira, and de Castro (2013), whose code is based on the work of Rao and Babu (1991). My code is based on the formula derived in this article as it is already evaluated for an observation point at  $z = 0$ , simplifying the equations and the computation time significantly.

### 7.6.1 Source and field calculation

As mentioned above, the locations of the excavation trenches above the suspicious anomalies in the magnetogram. As it turns out, while BP008 is at the location of the "ghost feature", BP007 is next to it, making both sections an adequate premise for forward modelling. Fig. 7.13 shows a significant increase in susceptibility in the lower topsoil and plough horizon.

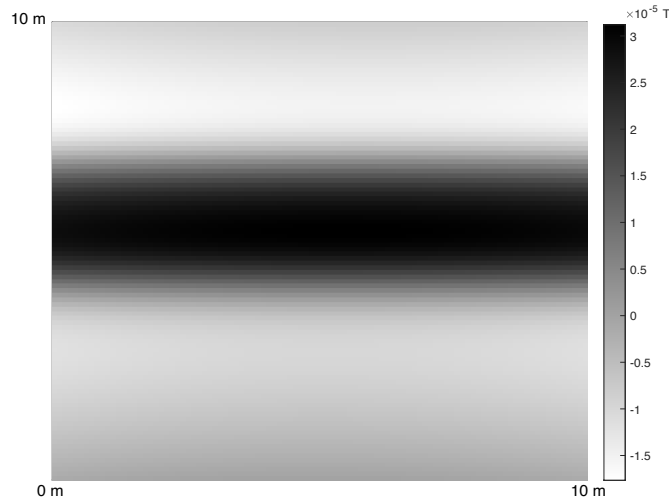


**Figure 7.14:** Simulation results: 10 m × 10 m magnetogram in a height about 30 cm above the ground of a 20 m × 20 m × 1.5 m containing prism size 0.1 m × 0.1 m × 0.1 m. The values are set to the magnetisation values obtained by the susceptibility measurements of BP007, except for a horizontal stripe whose values are set to the ones of BP008.

We decided on a prism size of 0.1 m × 0.1 m × 0.1 m to accommodate the sampling increments of our sections. The mesh size is 20 m × 20 m with 1.5 m depth. I used the values provided by Alken et al. (2021) for the Earth’s magnetic field direction. According to that, the geomagnetic field around Gumbati (as reference: 41.624967° N, 45.976148° E, 230 m, August 2018, IGRF 2020) showed a declination of 6.7020, an inclination of 60.7701 and a total field of 49,894.2 nT.

From the susceptibility values, I calculated the total magnetisation and assumed that the Königsberger ration is equal to 1 for the soils (as suggested by Bevan, 2016):

$$M = M_i + M_r = M_i + Q \cdot M_i = 2 \cdot \kappa_{vol} \cdot \frac{B}{\mu_0} = \frac{2 \cdot 46940 \cdot 10^{-9} \text{T}}{4 \cdot \pi \cdot 10^{-7}} \cdot \kappa_{Vol} \cdot 10^{-5} \text{SI} \quad (7.5)$$

I set all values to BP007 except for a stripe of 2.7 m thickness of BP008, which transects the mesh.

### 7.6.2 Results of the modelling so far

The simulation results show a large anomaly for the stripe of BP008 values compared to the BP007, but the obtained values of the simulations are unusually high for anomalies in archaeological prospection. The simulation shows values up to 31 μT. The magnetogram shows values below 5 nT for this anomaly. The applied model should be verified by other modelling software, such as GaMField. For now, I calculate the magnetic field resulting from the susceptibility contrast just from the enhancement of the topsoil layer, such that

$$B = \Delta\kappa \cdot V \cdot B_{Earth} / r^3 = 70 \cdot 10^{-5} \cdot 0.10 \cdot 2.7 \cdot 20 \text{m}^3 \cdot 49,894.2 \text{nT} / (0.37 + 0.3) \text{m}^3 = 28 \mu\text{T}. \quad (7.6)$$

The results are, therefore, comprehensible, and the choice of volume size can explain the high values. Even if just the volume dimensions are chosen to be 0.1x1x1m<sup>3</sup> the anomaly drops down to 5.2 nT, a value much closer to the values observed in the magnetogram.

## 7.7 Summary and Discussion

Interestingly, the magnetometer survey, almost 20 years after the mid-1990s excavation at Gumbati, could not locate the position of the old excavation trenches beyond doubt. Typically, excavations are traceable as local, large-scale monopole anomalies or areas dotted with many minute dipole anomalies with random orientation or a combination of both effects. An excavation disturbs the natural layering of the soil layers and, therefore, the original magnetic susceptibility profile, as well as destroys the detrital remanent magnetisation (DRM) originally inherent in the soil (e.g. Fassbinder & Becker, 2003; Fassbinder & Gorka, 2009). Both processes combined usually lead to a decrease in the total magnetisation of the refilled soil material. This should be visible in the magnetogram as a negative broad monopole anomaly. Depending on the depth of the excavation trench and its filling material, this can also increase the total magnetisation and thus lead to a broad positive monopole anomaly. The dotting with dipole anomalies results from the backfilling of the trenches with agglomerates of soil or sediments, which retained their DRM and, therefore, locally exhibit a higher total magnetisation than their surroundings. Also, iron fragments from the digging can contaminate the filling. However, none of these features are recognisable in the magnetogram as the heavy littering and deep plough prevent the slight variations in the soil magnetisation from being seen. These signs or other traces of the places are not identifiable in Gmb19A and the other magnetograms. Also, when assessing the fields visually, traces of the old excavation were indeterminable through the agricultural use of the fields over the last two decades.

Eventually, the old excavation trenches could only be relocated at the end of 2019 after the discovery of vintage satellite photos (see Fig. 7.1 c) showing the trenches of the old excavation (see also Fig. 7.1 d). We realised that the magnetometer survey area of Gmb19A indeed covered the excavation trenches (see Fig. 7.6). One larger monopole anomaly might be linked with the excavation, but it might be coincidental. The further findings, or better, the lack of findings around that area in the magnetogram, suggest that the site is badly preserved, if preserved at all, and that the deep plough of the site is the primary cause that destroyed the archaeological remains.

Until the old excavation trenches were re-located, the only indication of the possible location of the old excavation or other archaeological features was the prominent linear structures in Gmb18a. The positions of the two excavation trenches in 2019 were based on the magnetometer survey results. However, the excavation unearthed no features which might explain the structures visible in the magnetometry. These phantoms in geophysical data sets are referred to as "ghost features" (e.g. Simon, Koziol, & Thiesson, 2012). This results from a contrast in physical properties, which is why they are distinguishable in the geophysical data, here the magnetogram, but cannot be identified in the excavation primarily due to a lack of distinctive colour or texture differences. Therefore, we collected four profiles in the two excavation trenches to analyse the change in chemistry and the magnetic properties to answer the detection of the "ghost feature".

Looking at the soil profiles, trenches A and B show a similar sequence of layers. The bottom of the trenches is a layer of pebbles followed by soil layers covering the kurgans. The difference in geochemistry and the traces of grass-sods in kurgan 1 (trench B) suggest that we are, archaeologically speaking, witnessing two different types of construction of grave mounds – and therefore two different grave rituals. The use of sods is sometimes interpreted as symbols for pasture as a personal possession of the deceased, which should be available to them also in the afterlife (Parzinger, 2017). A topsoil layer follows the

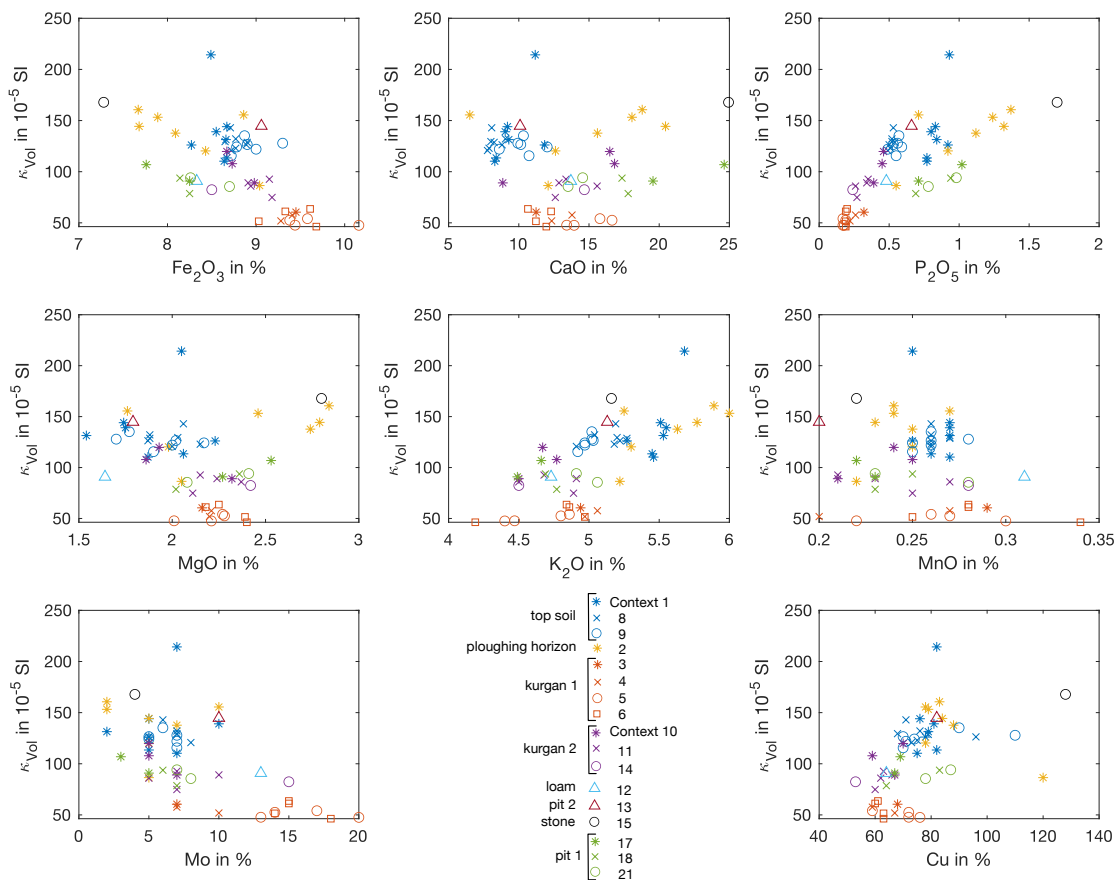


**Figure 7.15:** Scatter plots of volume susceptibility versus iron, calcium, phosphorus and other indicative elements for human activity and fertiliser. The susceptibility shows a reciprocal relationship with iron for the topsoil and plough horizon, while it shows a linear relationship with calcium and phosphorus, potassium, and others.

soil layers of the kurgans. For trench A, the plough horizon is characterised by a swirl of bands of the topsoil and upper kurgan layers, which is also reflected in the soil chemistry. For trench B, the intermediate layer between the uppermost topsoil layer and the kurgan layers seems visually more homogenous and closer to the topsoil material and texture, which can also be seen in the soil chemistry. The uppermost topsoil layer differs in texture as the topsoil in trench A is more porous to dense loamy humus with larger pebbles, and the topsoil of trench B is more of a loose humus layer.

The topsoil shows a clear indication of human activity with elevated calcium, strontium, phosphorus, potassium, copper and zinc levels. We concluded that, especially as calcium and phosphorus values behave similarly for the topsoil and plough horizon, these layers still contain residues of last year's fertiliser. One sees in Fig. 7.15 that the susceptibility shows a linear relationship with calcium, phosphorus, potassium, manganese and copper for most of the plough horizon and, to some extent, for the topsoil. Strangely, the magnetic susceptibility shows a negative linear relationship with iron. This implies a different share of iron oxides in the plough horizon, which explains this relationship. Further rock magnetic analyses of the samples will explain which magnetic minerals are present in the plough horizon and the topsoil.

So far, the increased values in the magnetic susceptibility correlate with the indicators for human activity, especially with calcium and phosphorus, which are indicators for fertilisers. It is known that fertilisers, e.g. wood ash (Petrovský et al., 2018), can increase soil susceptibility. The deep ploughing of the field might have enriched the lower topsoil and plough horizon. Magnetic methods are highly sensitive to even small changes in the magnetic properties, here namely the magnetic susceptibility. That is why susceptibility differences are so significant in the magnetometer measurements. The distribution of fertiliser is highly inhomogeneous, but it would explain why the positive and monopole features are parallel and perpendicular to the plough furrows in Gmb19a and often look like squares or rectangles. Kai Kaniuth mentioned in his habilitation speech that residuals from irrigation systems might generate the observed magnetic anomalies.<sup>3</sup> The simulation of the different susceptibility values of B007 as background and BP008 as source of the anomaly causes high but replicable values for the generated anomaly. It is probably more the choice of the volume of the source anomaly, which is the cause of the high values. Therefore, the assumed physical volume of the susceptibility contrast contributing to the anomaly in the simulation shown in this chapter is apparently overestimated. It is more likely that the regions with higher magnetic susceptibility are lenses with a thickness of a few millimetres and a horizontal extension of a few decimetres, making up the total anomaly, which is entirely plausible for the distribution of fertiliser in the soil.

The results of the susceptibility measurements and the subsequent simulation show that the susceptibility differences between the two profiles is sufficient to cause the anomalies. Similar positive and monopole anomalies parallel and perpendicular to the plough furrows can also be seen in Gmb19b and Gmb21. Further sample taking will not be possible at the site for a better understanding of the susceptibility distribution and its link to the residuals of the fertiliser. Unfortunately, we do not know which fertiliser was used by the farmer in the years before the magnetometer prospection.

Due to quarrels with the owner, the excavation site had to be cleared at short notice in 2019, and excavation could not yet be resumed. Thus, it has not yet been possible to clarify with the help of excavations how much of the palace complex is still preserved. However, the abandonment of this excavation site had the consequence that, following a clue, the investigations were continued on another field. The geophysical surveys (Fassbinder et al., 2021; Parsi, Hahn, & Fassbinder, 2021) and the subsequent excavation in 2020 discovered a large new building complex with representative architecture, which was part of an administrative compound (Kaniuth, 2022).

---

<sup>3</sup>To my knowledge, this was not confirmed during the excavation. It also does not explain why we see similar areas of increased magnetisation in the northeast and why these areas have a rectangular rather than a linear structure. Further rock magnetic measurements may shed light on what magnetic minerals are in the ground and whether they may have originated from iron-bearing pipes. However, the correlation of calcium and potassium with susceptibility is undeniable and supports the theory mentioned in the chapter.

## 7.8 Conclusion

Rediscovery of the old trenches of the mid90 excavation or the remains of the Achaemenid complex using magnetometer prospecting at the site of Gumbati was unsuccessful. Only much later discovered, old satellite images could prove that one of the prospected areas was on top of the old excavation. No features in the magnetogram correlate undoubtedly with the old excavations. However, the magnetometer prospection revealed positive rectangular features that seemed suspiciously parallel and perpendicular to the plough furrows. Excavations at the location of one of these anomalies started but unearthed no features, such as wall remains, which could explain the "ghost feature" in the magnetogram. Soil samples taken in vertical profiles at the supposed location of the feature compared to a profile next to it show a significant increase in volume susceptibility in the lower topsoil layers and plough horizon. The volume susceptibility correlates for these layers with human activity markers, elements obtained by pXRF measurements and especially with calcium and phosphorus, indicators for fertiliser residuals. The unequal distribution of fertiliser and, with that linked, the unequal distribution of the magnetic susceptibility, which, proven by stimulations, is the primary cause for these anomalies. So far, it can only be said that the elements indicating the presence of fertiliser correlate with the susceptibility, but not if this is a causal relationship. However, it would also explain why the features are parallel and perpendicular to the plough furrows. To sum up, the "ghost feature" in the magnetogram is not visible in the excavation as it does not show any colour or texture differences. However, there is a difference in susceptibility likely linked to fertilisation of the field, which explains the anomaly in the magnetogram. Pending rock magnetic measurements will reveal from which magnetic minerals the increase in susceptibility originates. For Gumbati, the lack of further anomalies in the magnetogram and the deep ploughing of the field observable in the soil profiles implies that the Achaemenid complex is not well preserved.

Section	Sample	Height	Height	Depth	Context	Process	Type
		m.a.s.l.	cm.a.e.l.	cm.b.g.l.			
BP006	1	225.609	0	135	Context 21	anthropogenic	pit 1 filling
BP006	2	225.709	10	125	Context 21	anthropogenic	pit 1 filling
BP006	3	225.809	20	115	Context 15	natural stone	kurgan 2 - stone
BP006	4	225.909	30	105	Context 18	anthropogenic	pit 1 filling
BP006	5	226.009	40	95	Context 18	anthropogenic	pit 1 filling
BP006	6	226.109	50	85	Context 17	anthropogenic	pit 1 filling
BP006	7	226.209	60	75	Context 17	anthropogenic	pit 1 filling
BP006	8	226.309	70	65	Context 10	anthropogenic	kurgan 2
BP006	9	226.409	80	55	Context 09	topsoil	topsoil
BP006	10	226.509	90	45	Context 09	topsoil	topsoil
BP006	11	226.609	100	35	Context 09	topsoil	topsoil
BP006	12	226.709	110	25	Context 08	topsoil	topsoil
BP006	13	226.809	120	15	Context 08	topsoil	topsoil
BP006	14	226.909	130	5	Context 08	topsoil	topsoil
BP007	15	225.378	0	118	Context 06	anthropogenic	kurgan 1
BP007	16	225.478	10	108	Context 06	anthropogenic	kurgan 1
BP007	17	225.578	20	98	Context 05	anthropogenic	kurgan 1
BP007	18	225.678	30	88	Context 05	anthropogenic	kurgan 1
BP007	19	225.778	40	78	Context 04	anthropogenic	kurgan 1
BP007	20	225.878	50	68	Context 03	anthropogenic	kurgan 1
BP007	21	225.978	60	58	Context 02	anthropogenic	plowing horizon
BP007	22	226.078	70	48	Context 02	anthropogenic	plowing horizon
BP007	23	226.178	80	38	Context 02	anthropogenic	plowing horizon
BP007	24	226.278	90	28	Context 01	topsoil	topsoil
BP007	25	226.378	100	18	Context 01	topsoil	topsoil
BP007	26	226.478	110	8	Context 01	topsoil	topsoil
BP005	27	225.462	0	154	Context 14	anthropogenic	kurgan 2
BP005	28	225.562	10	144	Context 13	anthropogenic	pit 2 filling
BP005	29	225.662	20	134	Context 11	anthropogenic	kurgan 2
BP005	30	225.762	30	124	Context 12	anthropogenic	loam
BP005	31	225.862	40	114	Context 11	anthropogenic	kurgan 2
BP005	32	225.962	50	104	Context 11	anthropogenic	kurgan 2
BP005	33	226.062	60	94	Context 11	anthropogenic	kurgan 2
BP005	34	226.162	70	84	Context 10	anthropogenic	kurgan 2
BP005	35	226.262	80	74	Context 10	anthropogenic	kurgan 2
BP005	36	226.362	90	64	Context 09	topsoil	topsoil
BP005	37	226.462	100	54	Context 09	topsoil	topsoil
BP005	38	226.562	110	44	Context 09	topsoil	topsoil
BP005	39	226.662	120	34	Context 08	topsoil	topsoil
BP005	40	226.762	130	24	Context 08	topsoil	topsoil
BP005	41	226.862	140	14	Context 08	topsoil	topsoil
BP005	42	226.962	150	4	Context 08	topsoil	topsoil
BP008	43	225.424	0	126	Context 06	anthropogenic	kurgan 1
BP008	44	225.524	10	116	Context 06	anthropogenic	kurgan 1
BP008	45	225.624	20	106	Context 05	anthropogenic	kurgan 1
BP008	46	225.724	30	96	Context 05	anthropogenic	kurgan 1
BP008	47	225.824	40	86	Context 04	anthropogenic	kurgan 1
BP008	48	225.924	50	76	Context 02	anthropogenic	plowing horizon
BP008	49	226.024	60	66	Context 02	anthropogenic	plowing horizon
BP008	50	226.124	70	56	Context 02	anthropogenic	plowing horizon
BP008	51	226.224	80	46	Context 02	anthropogenic	plowing horizon
BP008	52	226.324	90	36	Context 01	topsoil	topsoil
BP008	53	226.424	100	26	Context 01	topsoil	topsoil
BP008	54	226.524	110	16	Context 01	topsoil	topsoil
BP008	55	226.624	120	6	Context 01	topsoil	topsoil

Table 7.3: Sample Overview.

Section	Sample	SiO <sub>2</sub>	TiO <sub>2</sub>	Al <sub>2</sub> O <sub>3</sub>	Fe <sub>2</sub> O <sub>3</sub>	MnO	MgO	CaO	K <sub>2</sub> O	P <sub>2</sub> O <sub>5</sub>
BP006	1	56.93	0.73	11.92	8.7	0.28	2.08	13.51	5.06	0.78
BP006	2	56.59	0.7	11.37	8.26	0.23	2.41	14.55	4.91	0.98
BP006	3	45.9	0.69	11.31	7.28	0.22	2.80	24.94	5.16	1.7
BP006	4	54.07	0.71	11.5	8.14	0.25	2.36	17.35	4.69	0.94
BP006	5	53.23	0.72	12.29	8.25	0.23	2.02	17.79	4.77	0.69
BP006	6	52.01	0.71	11.77	8.25	0.23	2.27	19.56	4.49	0.71
BP006	7	46.29	0.71	12.18	7.76	0.22	2.53	24.63	4.66	1.02
BP006	8	62.37	0.71	11.67	8.98	0.21	2.32	8.86	4.5	0.39
BP006	9	60.04	0.74	12.4	8.87	0.26	1.77	10.33	5.02	0.57
BP006	10	62.07	0.73	11.86	9.00	0.26	2	8.61	4.97	0.49
BP006	11	60.29	0.72	11.93	8.72	0.25	1.9	10.73	4.92	0.55
BP006	12	62.47	0.72	11.98	8.71	0.26	2.06	8.07	5.19	0.53
BP006	13	62.7	0.72	11.9	8.65	0.27	2.03	8.01	5.2	0.52
BP006	14	62.2	0.73	11.96	8.9	0.27	1.88	8.24	5.27	0.54
BP007	15	58.32	0.75	12.87	9.03	0.25	2.39	11.22	4.97	0.19
BP007	16	59.5	0.7	11.05	9.68	0.34	2.4	11.96	4.19	0.19
BP007	17	57.01	0.72	11.09	10.16	0.3	2.21	13.94	4.4	0.17
BP007	18	58.09	0.7	11.48	9.44	0.22	2.01	13.41	4.47	0.18
BP007	19	57.43	0.75	12.61	9.28	0.2	2.2	12.34	4.97	0.22
BP007	20	58.75	0.74	12.13	9.45	0.29	2.16	11.23	4.94	0.32
BP007	21	58.12	0.73	11.98	9.04	0.22	2.05	12.09	5.22	0.55
BP007	22	53.88	0.71	11.98	8.09	0.25	2.74	15.6	5.63	1.12
BP007	23	48.97	0.7	12.1	7.68	0.23	2.79	20.45	5.77	1.32
BP007	24	59.18	0.69	11.35	8.27	0.25	2.23	11.84	5.27	0.92
BP007	25	61.97	0.72	11.71	8.67	0.26	2.06	8.39	5.45	0.77
BP007	26	62.4	0.71	11.59	8.64	0.27	1.87	8.29	5.46	0.77
BP005	27	56.41	0.74	12.24	8.5	0.28	2.42	14.67	4.5	0.24
BP005	28	60.48	0.74	11.85	9.06	0.2	1.79	10.09	5.13	0.66
BP005	29	57.39	0.75	12.56	9.18	0.25	2.11	12.6	4.89	0.27
BP005	30	57.86	0.73	12.22	8.33	0.31	1.64	13.71	4.73	0.48
BP005	31	57.27	0.74	12.5	8.91	0.23	2.24	12.86	4.91	0.34
BP005	32	55.09	0.74	12.25	8.94	0.27	2.37	15.58	4.5	0.26
BP005	33	56.65	0.74	12.72	9.15	0.21	2.15	13.36	4.68	0.35
BP005	34	54.28	0.74	12.54	8.67	0.24	1.93	16.48	4.67	0.46
BP005	35	53.91	0.74	12.47	8.73	0.25	1.86	16.82	4.77	0.45
BP005	36	58.03	0.74	12.46	8.78	0.25	2.17	12.02	4.97	0.59
BP005	37	60.7	0.74	11.78	9.3	0.28	1.7	9.93	5.02	0.56
BP005	38	60.2	0.73	12.17	8.9	0.26	2.02	10.14	5.03	0.53
BP005	39	62	0.72	11.76	8.77	0.26	1.88	9.05	5.04	0.52
BP005	40	62.82	0.72	11.7	8.77	0.26	2.15	7.88	5.18	0.51
BP005	41	61.69	0.73	12.02	8.89	0.26	1.87	8.81	5.22	0.5
BP005	42	63.68	0.7	11.47	8.72	0.26	2	7.77	4.91	0.49
BP008	43	59.19	0.75	12.23	9.61	0.28	2.25	10.65	4.84	0.2
BP008	44	57.6	0.75	12.52	9.33	0.28	2.18	12.3	4.86	0.19
BP008	45	53.53	0.74	12.81	9.58	0.26	2.27	15.78	4.86	0.17
BP008	46	53.11	0.73	12.6	9.38	0.27	2.28	16.64	4.8	0.19
BP008	47	55.68	0.75	12.55	9.41	0.27	2.21	13.79	5.06	0.26
BP008	48	51.48	0.71	11.93	7.89	0.24	2.46	18.06	6	1.24
BP008	49	50.32	0.7	12.18	7.67	0.24	2.84	18.79	5.89	1.37
BP008	50	57.59	0.72	12.2	8.43	0.25	1.98	12.61	5.3	0.92
BP008	51	64.12	0.73	11.8	8.86	0.27	1.76	6.51	5.25	0.71
BP008	52	58.75	0.72	11.98	8.49	0.25	2.05	11.17	5.68	0.93
BP008	53	61.08	0.72	12	8.67	0.27	1.74	9.19	5.51	0.83
BP008	54	61.29	0.73	12.03	8.55	0.27	1.75	9.03	5.55	0.8
BP008	55	61.15	0.73	11.99	8.66	0.27	1.54	9.29	5.53	0.84

Table 7.4: Main elements in volume %.

Section	Sample	S	V	Cr	Co	Ni	Cu	Zn	As	Rb	Sr
BP006	1	1387	133	224	42	123	78	163	28	190	1023
BP006	2	1413	120	221	41	115	87	174	22	181	1199
BP006	3	3293	97	191	30	114	128	215	28	156	1855
BP006	4	1949	102	215	39	117	83	162	19	177	1224
BP006	5	1636	112	216	39	120	64	138	19	180	963
BP006	6	1826	94	220	39	116	67	139	19	177	961
BP006	7	2425	85	202	35	120	69	160	18	165	1079
BP006	8	996	121	250	48	119	67	130	29	217	556
BP006	9	852	137	241	44	118	90	159	22	198	580
BP006	10	786	137	240	46	115	71	148	23	203	544
BP006	11	926	128	237	45	122	70	147	23	198	593
BP006	12	812	124	231	44	117	71	144	23	198	530
BP006	13	793	124	222	42	116	68	141	20	200	512
BP006	14	798	139	234	44	115	79	148	24	199	510
BP007	15	1141	141	240	46	119	63	117	28	201	589
BP007	16	999	121	240	45	120	63	116	43	196	615
BP007	17	995	140	241	47	130	76	124	38	198	676
BP007	18	894	124	262	48	123	72	120	34	199	667
BP007	19	806	128	244	44	117	67	115	34	204	584
BP007	20	743	158	251	46	126	68	123	62	205	616
BP007	21	795	132	242	47	121	120	172	22	206	683
BP007	22	1154	112	214	38	110	88	183	22	186	890
BP007	23	1288	75	202	36	105	84	194	24	178	1064
BP007	24	1026	102	221	41	118	78	174	22	192	770
BP007	25	913	134	226	42	115	82	172	22	197	607
BP007	26	1065	132	225	45	127	75	170	22	198	605
BP005	27	2180	122	217	40	114	53	99	34	172	712
BP005	28	1388	131	234	44	121	82	160	26	190	793
BP005	29	1398	131	234	46	128	60	121	32	195	694
BP005	30	1371	107	235	41	126	64	119	28	178	719
BP005	31	1016	115	230	47	118	66	127	36	192	654
BP005	32	948	138	222	47	116	62	113	52	185	657
BP005	33	806	148	226	46	123	63	114	39	193	662
BP005	34	844	119	230	42	121	70	126	34	182	700
BP005	35	827	121	225	42	121	59	123	24	191	667
BP005	36	829	122	228	42	115	74	145	20	191	592
BP005	37	762	122	243	49	123	110	185	22	206	570
BP005	38	789	124	238	42	123	70	149	20	197	558
BP005	39	762	116	242	45	113	76	147	22	201	533
BP005	40	796	127	244	45	116	75	145	24	195	503
BP005	41	810	143	229	44	118	96	156	24	197	519
BP005	42	863	115	247	45	122	73	144	24	202	518
BP008	43	995	139	261	49	125	61	124	36	202	611
BP008	44	929	132	242	46	123	60	115	30	200	637
BP008	45	1154	139	245	46	126	59	113	29	200	701
BP008	46	984	134	234	46	138	72	119	41	197	689
BP008	47	864	159	243	46	127	59	119	49	207	639
BP008	48	1569	113	203	40	121	79	177	24	178	1078
BP008	49	1450	95	193	36	115	83	189	22	177	1125
BP008	50	999	105	221	44	123	78	173	20	192	793
BP008	51	801	143	230	44	118	78	169	20	201	568
BP008	52	1043	121	226	44	121	82	180	24	195	757
BP008	53	926	120	245	42	120	76	172	22	201	656
BP008	54	1033	122	227	44	115	81	172	20	199	637
BP008	55	895	134	227	44	126	79	177	20	199	658

Table 7.5: Trace elements in volume ppm.

Section	Sample	Y	Zr	Nb	Mo	Sn	Sb	Ba	Ce	Pb	Th	U
BP006	1	49	200	22	8	2	0	1047	59	82	13	0
BP006	2	46	200	20	7	2	0	989	55	64	11	0
BP006	3	38	229	18	4	2	0	1100	51	19	9	0
BP006	4	47	208	20	6	2	0	932	55	50	11	0
BP006	5	49	198	22	7	2	0	1067	57	69	12	0
BP006	6	47	185	19	5	2	0	865	56	58	11	0
BP006	7	42	184	20	3	2	0	891	50	42	10	0
BP006	8	53	166	23	7	2	0	1031	61	102	17	0
BP006	9	50	162	23	6	2	0	1053	59	107	15	2
BP006	10	50	165	24	7	2	0	1195	59	108	15	0
BP006	11	51	162	21	7	2	0	1030	56	96	14	0
BP006	12	50	163	22	6	2	0	1207	58	93	14	0
BP006	13	50	165	23	7	2	0	1208	56	113	16	0
BP006	14	54	167	21	7	2	0	1278	59	96	14	0
BP007	15	53	177	20	14	2	0	909	59	106	15	0
BP007	16	53	171	25	18	2	0	935	62	105	14	0
BP007	17	52	163	23	20	2	0	1086	69	120	16	0
BP007	18	53	164	23	13	2	0	1138	58	117	15	0
BP007	19	53	164	22	10	2	0	1006	59	95	14	0
BP007	20	51	164	20	7	2	0	943	63	123	16	6
BP007	21	50	171	22	5	2	0	1013	59	80	14	0
BP007	22	41	168	21	7	2	0	1094	54	64	11	0
BP007	23	40	173	17	5	2	0	822	47	54	11	0
BP007	24	46	170	21	5	2	0	977	52	61	12	0
BP007	25	52	160	22	5	2	0	1220	55	97	13	0
BP007	26	50	156	21	7	2	0	1361	56	108	15	0
BP005	27	52	205	23	15	2	0	1026	63	76	12	0
BP005	28	52	188	21	10	2	0	974	61	91	15	0
BP005	29	53	175	20	7	2	0	1012	61	101	14	0
BP005	30	53	206	23	13	2	0	947	59	60	13	0
BP005	31	52	174	24	10	2	0	1017	57	85	14	0
BP005	32	52	173	21	5	2	0	1072	59	65	13	0
BP005	33	53	168	20	7	2	0	1054	60	90	15	0
BP005	34	48	182	23	5	2	0	949	58	70	11	0
BP005	35	48	172	21	5	2	0	885	57	92	14	0
BP005	36	47	164	22	5	2	0	1304	57	96	14	0
BP005	37	52	165	22	7	2	0	1082	61	119	16	0
BP005	38	54	160	24	5	2	0	1250	58	80	11	0
BP005	39	52	166	21	7	2	0	1048	58	87	13	0
BP005	40	52	161	23	5	2	0	1103	59	92	14	0
BP005	41	54	165	24	5	2	0	1207	58	86	14	0
BP005	42	50	167	23	8	2	0	1099	57	77	14	0
BP008	43	55	175	22	15	2	0	967	61	101	14	0
BP008	44	53	168	22	15	2	0	1160	61	90	15	0
BP008	45	51	155	20	17	2	0	1235	61	115	15	0
BP008	46	51	158	20	14	2	0	828	54	84	14	0
BP008	47	47	160	24	7	2	0	1077	58	105	16	0
BP008	48	44	179	21	2	2	0	1159	52	43	10	0
BP008	49	39	179	21	2	2	0	957	49	37	10	0
BP008	50	50	173	21	5	2	0	1020	55	64	13	0
BP008	51	51	167	20	10	2	0	1324	57	102	15	0
BP008	52	48	166	22	7	2	0	1130	56	75	13	0
BP008	53	49	167	21	5	2	0	1085	54	91	14	0
BP008	54	45	167	19	10	2	0	1238	56	107	15	0
BP008	55	47	163	22	2	2	0	1091	56	96	14	0

Table 7.6: Trace elements in volume ppm (continued).

		$m$ in g	$R_{LF}$	$\chi_{LF}$ in $m^3/kg$	$R_{HF}$	$\chi_{HF}$ in $m^3/kg$	$\chi_{FD}$ in %	$h$ in cm	$V$ in $cm^3$	$\kappa_{LF}$ (dimensionless)	$M_{LF}$ (mA/m)
BP006	1	8.138	48.9	60.1	46.6	57.2	4.77	1.85	7.03	85.5	63.9
BP006	2	7.550	48.6	64.4	46.2	61.2	4.94	1.80	6.84	94.1	70.3
BP006	3	6.515	79.0	121.2	72.4	111.1	8.30	1.90	7.22	167.9	125.4
BP006	4	7.801	52.8	67.6	49.9	64.0	5.43	1.90	7.22	93.7	70.0
BP006	5	8.605	51.4	59.7	49.0	57.0	4.60	2.00	7.60	78.6	58.7
BP006	6	7.986	52.4	65.6	49.6	62.1	5.38	1.90	7.22	90.9	67.9
BP006	7	7.085	51.8	73.1	48.5	68.5	6.31	1.80	6.84	106.9	79.8
BP006	8	9.092	58.5	64.3	55.2	60.7	5.53	1.90	7.22	89.1	66.5
BP006	9	7.906	69.0	87.3	64.2	81.2	6.98	1.70	6.46	135.2	101.0
BP006	10	8.540	73.2	85.8	68.3	80.0	6.74	1.85	7.03	122.0	91.1
BP006	11	9.068	77.7	85.7	72.6	80.1	6.48	1.95	7.41	115.6	86.4
BP006	12	7.667	70.8	92.3	65.7	85.7	7.16	1.70	6.46	142.9	106.8
BP006	13	8.244	75.0	91.0	70.0	84.9	6.73	1.85	7.03	129.4	96.7
BP006	14	8.144	73.7	90.4	68.6	84.2	6.88	1.85	7.03	128.7	96.1
BP007	15	9.175	35.9	39.1	35.3	38.5	1.72	2.00	7.60	51.5	38.5
BP007	16	9.139	32.2	35.2	31.6	34.6	1.66	2.00	7.60	46.3	34.6
BP007	17	8.764	30.1	34.3	29.5	33.6	2.16	1.90	7.22	47.6	35.5
BP007	18	9.253	33.6	36.3	32.7	35.3	2.58	2.00	7.60	47.7	35.6
BP007	19	9.307	36.7	39.4	35.8	38.4	2.54	2.00	7.60	51.9	38.8
BP007	20	9.417	43.3	45.9	41.8	44.3	3.47	2.00	7.60	60.4	45.2
BP007	21	8.829	56.6	64.0	53.1	60.2	6.07	1.95	7.41	86.5	64.6
BP007	22	7.554	75.1	99.4	68.2	90.3	9.19	1.90	7.22	137.7	102.9
BP007	23	7.595	79.1	104.2	71.4	94.1	9.73	1.90	7.22	144.3	107.8
BP007	24	8.509	83.6	98.2	76.4	89.8	8.57	2.05	7.79	126.1	94.2
BP007	25	8.800	79.7	90.5	73.3	83.2	8.05	2.10	7.98	113.5	84.8
BP007	26	8.546	77.0	90.1	70.9	83.0	7.86	2.15	8.17	110.3	82.4
BP005	27	8.867	51.4	57.9	50.4	56.9	1.82	1.85	7.03	82.4	61.6
BP005	28	6.957	61.2	88.0	57.0	81.9	6.86	1.60	6.08	144.7	108.1
BP005	29	7.977	40.8	51.2	39.2	49.2	3.88	1.80	6.84	74.8	55.9
BP005	30	7.408	40.9	55.2	39.2	52.9	4.12	1.60	6.08	90.8	67.8
BP005	31	7.911	48.2	60.9	46.0	58.2	4.56	1.80	6.84	89.1	66.6
BP005	32	7.573	42.0	55.5	40.7	53.7	3.17	1.70	6.46	85.9	64.2
BP005	33	7.967	50.5	63.4	48.6	61.0	3.80	1.80	6.84	92.7	69.2
BP005	34	7.189	50.7	70.5	48.2	67.0	5.00	1.55	5.89	119.8	89.5
BP005	35	7.772	54.1	69.7	51.3	65.9	5.33	1.70	6.46	107.8	80.6
BP005	36	8.465	73.9	87.3	69.0	81.5	6.61	1.85	7.03	124.2	92.8
BP005	37	8.808	81.3	92.3	75.8	86.1	6.74	1.90	7.22	127.9	95.5
BP005	38	8.379	72.5	86.5	67.8	80.9	6.48	1.80	6.84	126.5	94.5
BP005	39	8.224	74.3	90.3	69.1	84.1	6.93	1.80	6.84	132.1	98.7
BP005	40	8.437	76.8	91.1	71.6	84.8	6.83	1.95	7.41	122.9	91.8
BP005	41	8.597	78.4	91.2	73.0	84.9	6.89	1.90	7.22	126.3	94.4
BP005	42	8.554	78.5	91.7	73.2	85.6	6.67	2.00	7.60	120.7	90.2
BP008	43	7.873	34.3	43.5	33.4	42.4	2.48	1.80	6.84	63.6	47.5
BP008	44	8.113	33.0	40.7	32.3	39.8	2.27	1.75	6.65	61.2	45.7
BP008	45	7.724	28.6	37.0	27.7	35.9	2.98	1.80	6.84	54.1	40.4
BP008	46	8.386	31.0	36.9	30.2	36.1	2.37	1.85	7.03	52.5	39.2
BP008	47	8.347	32.9	39.4	32.2	38.5	2.23	1.80	6.84	57.6	43.0
BP008	48	6.550	62.9	96.1	57.9	88.4	7.97	1.65	6.27	153.2	114.5
BP008	49	5.975	62.0	103.7	56.3	94.2	9.22	1.70	6.46	160.6	120.0
BP008	50	7.279	59.9	82.3	55.5	76.3	7.29	1.80	6.84	120.3	89.9
BP008	51	7.517	75.5	100.5	69.3	92.2	8.25	1.70	6.46	155.5	116.2
BP008	52	7.094	101.1	142.5	92.4	130.2	8.62	1.75	6.65	214.3	160.1
BP008	53	7.388	70.8	95.8	65.1	88.0	8.06	1.75	6.65	144.0	107.6
BP008	54	7.720	73.4	95.1	67.5	87.4	8.06	1.80	6.84	139.1	103.9
BP008	55	7.835	74.3	94.9	68.5	87.5	7.78	1.90	7.22	131.4	98.2

Table 7.7: Results of the susceptibility measurements.

## Chapter 8

# Conclusion and Perspectives

Magnetometer prospecting, along with archaeomagnetic dating, is the flagship of magnetic methods in archaeology and has become an integral research tool for the study of archaeological sites, the analysis of archaeological material and the characterisation of archaeological objects. Magnetometer prospecting is the mapping of the magnetic field at a survey area at a fixed height to the ground surface in a fine spatial resolution. It does not rely on the injection or the induction of an artificial signal into the ground but on the registration of the magnetic fields induced by the Earth's magnetic field and the magnetic fields of the potential features. It is essentially based on the magnetisation contrast between archaeological features and the surrounding material. Magnetometer prospecting has triumphed in recent decades since 1958 in the large-scale investigation of archaeological sites, and to identify areas of particular interest to archaeologists for subsequent excavation, but above all to gain unprecedented insights into the organisation of ancient settlements. Therefore, research must not come to a standstill in this area and has to ascertain the further potential lurking in the results of magnetometer prospecting. Magnetometer prospecting in archaeology faces different challenges and questions than its relatives in geology and resource research. This is why a separate community has formed where researchers with different backgrounds, including geophysics and archaeology, work hand in hand. This thesis contributes to a better understanding the different parameters that influence magnetic anomalies and how this translates into prospecting results and vice versa.

The different operating principles of the various magnetometers used in magnetometer prospecting are categorised as scalar or vector magnetometers, depending on which element of the anomalous magnetic field they measure. Advantages and disadvantages are known and different for each instrument, as are the physical quantities measured and, therefore, their visual results. This is irrelevant when there is only one type of magnetometer used at a site, but it is crucial if different ones are applied on adjacent areas, either during one campaign to save time or if the work of another group is continued. Hooked by the idea that vector gradiometers are intrinsic high-pass filters, instead of deriving a pseudo-gradient for the total field magnetometer by calculating the upward continuation of the magnetic field map for 65 cm and subtracting then the original data set, I suggest an alternative method to merge the data sets of vector gradiometers and total-field magnetometers to visually uniform magnetometers. Firstly, an image high-pass filter ( $R=10$ ) is applied to the total-field data. The vector gradiometer data set is multiplied by a factor of two based on comparing the standard deviations of both data sets. This compensates for the missing signal strengths for measuring only one magnetic field component by the vector

gradiometer. Eventually, this provides visually uniform magnetograms, as the case studies for Fara and Gumbati show, which greatly simplifies the interpretation of such surveyed areas, as traces and features can be tracked across segments surveyed by different devices. In my case, this approach is more time-efficient and convenient than the previously known method. This approach works for Earth's magnetic field inclinations of around  $60^\circ$ . It is to be expected that the multiplication factor depends on the inclination. With decreasing inclination, closer to the magnetic equator, the vertical vector gradiometer will register a lower signal than the total field of the buried features as the vertical component of the anomaly decreases with decreasing inclination. I show in my case study of Yeha and Melazo at a geomagnetic inclination of  $15^\circ$  that the additional application of a high-pass filter on the total field data can replace prospecting in a gradient set-up, saving considerable and even provides two data sets, i.e. total-field data and high-pass filtered data similar to a vertical (pseudo-)gradient. Although applying a high-pass filter originates from the same idea, which is filtering large-wave scale contributory, the idea of wavelength filtering in archaeological prospecting is still virgin ground and more used to pretty up images for interpreting than qualitative evaluation of magnetograms—something which should definitely be further investigated.

The registered anomaly of a buried body depends on source-specific parameters such as the dimensions and burial depth of the body, as well as the magnetisation contrast to the surroundings. These primarily influence the intensity of the anomaly, but the pattern of anomaly in the magnetogram is mainly dominated by the type of pole and the direction of magnetisation. Whether a body has a monopole or dipole anomaly is mostly due to its shape. The effect of a strong remanence in the body is a neglected topic, but understanding its effect holds great potential for gaining more information from a magnetogram. For a simple body such as a spherical dipole, I showed that the anomaly pattern directly mimics the direction of the total magnetisation. If the Königsberger ratio is high, i.e. the remanence dominates the total magnetisation, the anomaly pattern directly reflects the remanence. I have proven that the strong remanence of volcanic rocks at the Artanish burial site explains their different anomaly patterns and similar patterns at other sites. Suppose the interpreter is unaware that a body with positive magnetisation contrast can cause many different anomaly patterns. In that case, this can lead to misinterpretation of features in the magnetogram, especially concerning the building material. As it turned out, the anomaly pattern can be a helpful tool for distinguishing features that have acquired and remained in situ, such as hearths and pits, from objects having a random magnetisation direction on the surface of the Ethiopian Ethio-Sabaeen sites Yeha and Melazo. I see great potential in pursuing the work with reading or obtaining the direction of remanence from a magnetogram. Actual archaeomagnetic dating might be difficult in most cases as an accurate reading depends, e.g. on a known or ideal shape of the body and a homogeneous magnetisation. This is not always the case for hearths, which will be the primary target for such investigations. I recommend a project to study a furnace or hearth identified in the magnetogram, excavate it, analyse it for its induced and remanent magnetic contributions, and then produce synthetic magnetograms for comparison with the actual magnetogram. This gives an idea of the reliability of the estimates that can be made from the magnetogram. In an archaeological context, mapping the kiln or hearth direction of remanence in combination with conventional survey data can indicate different phases of occupation in different areas.

The anomaly pattern observed in magnetometer prospecting also depends on the direction of the Earth's magnetic field immersing the survey site. Since the interpretation of magnetograms is primarily based on visual identification of features, I provide synthetic magnetograms for all declinations and inclinations in  $15^\circ$  steps. These are accompanied by sections crossing the location of the body to understand the signal behaviour and peak ratios for different inclinations. I show that the influence of declination on dipole anomalies can easily be avoided by aligning the grid to magnetic North or simply rotating the magnetogram to magnetic North during data processing. Although there are signal drops off for non-zero declinations, the change in value is negligible since, in particular, the contrast to the reference value is still high enough to detect features in the magnetogram. The effect of the Earth's inclination is not as easily avertible. The anomaly pattern and peak ratios change significantly with the inclination, which even inverts for negative inclinations. The inclination can also affect the detectability of features. I show that linear features running in a north-south are difficult to distinguish at inclinations of around  $15^\circ$ . I can only limitedly recommend applying methods which suppress the effect of the Earth's magnetic field, such as RTP or analytic signal mapping, as valuable source-specific information, such as the direction of the magnetisation, is lost. In this thesis, I have intensively studied the effect of inclination on spherical dipoles for total field magnetograms. However, there is little or no information in the literature on archaeological prospecting about how inclination affects vector gradiometers or different scalar magnetometer setups and anomalies which cannot be approximated as spherical dipoles.

The case study of Fara is an example of how important it is to protect archaeological sites from looting. The resulting loss of information is manifold. Finds that could provide new and important insights into Mesopotamian culture as well as the history of the site are missing, and they may now never be revealed. At the same time, the methods of areal prospecting that could be used on the site, namely aerial photography and magnetometer prospecting, suffer greatly from the topographical changes caused by the looting mounds. This affects magnetometer prospecting in that the looting mounds make areas inaccessible with the devices or render the data around them useless because they cause strong anomalies. Radar prospecting can already be excluded from the list of applicable methods because the clayey and loose sand causes too much scattering to get adequate results. Only the methods of archaeological prospecting have the potential to provide an overview of the outline and the functioning of an entire site. This understanding is gone when areas are exposed to this level of looting, and retrievable knowledge will be irrevocably lost. At the same time, Fara's prospecting results demonstrate the potential of these methods to provide new discoveries from sites that have already been excavated. A hundred-year-old question was answered with a measurement that took only a few days: Fara had, indeed, a city wall, and the part we discovered on the east of the mound was a casemate. I can thus confirm Walter Andrae's concern that the excavation trenches did not reach far enough east to unearth the city wall. With my findings, I can also better identify the structure that was excavated during the 1902/1903 campaign. It is not part of a fortification, as Andrae had assumed due to the lack of other finds, but the quay of one of the city's harbours. In addition, the magnetometer survey provided new insights into the canal system running through the city and its settlement structure. When there are maps or drawings of the earlier excavation for the areas we have prospected, they show an astonishing correlation with the magnetometer prospecting results, especially regarding baked brick walls - an indication of their good preservation. The investigation of the site continued in autumn 2022, including magnetometer prospecting, and one can be curious about what new results they will bring to light. Perhaps in a future campaign, drill cores

taken around the city wall will provide information on whether this area is covered with additional alluvial sediments than the other parts or whether water-logging has partially dissolved the iron oxide minerals and reduced their susceptibility. Perhaps in a future campaign, drill cores at the area of the city wall will answer if it is covered with more alluvial sediments than the other parts or water-logging dissolved partly the iron oxide minerals and decreased their magnetic susceptibility.

The case study of the two Ethio-Sabaen sites of Yeha and Melazo shows that magnetometer prospecting can elicit information even at complex sites that represent an amalgamation of soil, environmental, geological, archaeological and modern features. This presupposes an immersion in the conditions of a site to categorise each feature accordingly and identify those that are important for the archaeological investigation of the site. Yeha and Melazo are still inhabited today, which left traces not only of the last millennia but also of the recent use of the areas. The bedrock geology and stones on the surface, metal parts on houses, the infrastructure, and the cultivation of the fields generate anomalies that might be mistaken for archaeological features or, in the worst case, hide archaeological traces. Only through detailed dissecting of the magnetograms and comparing the anomalies to my field notes, ortho-photos, and literature were I able to relate anomalies to field boundaries, formations of the volcanic rocks in the underground, modern features, and rocks on the surface. I anticipate this detailed breakdown of the identified anomalies will help other researchers at similarly complex sites and sites on an isocline of  $15^\circ$  to classify their anomalies. Eventually, I could identify wall remains, fireplaces, pits and the continuation of the monumental building found in Melazo. Although magnetometer prospecting is challenging at both sites, it is a reliable method for suggesting areas for new settlements where the upper meters of the soil do not contain remains to be preserved.

The case study of Gumbati evolved from a search for an Achaemenid palace with magnetometer prospecting into decoding a magnetic ghost feature. The complex of Gumbati was discovered in the mid-1990s, but recreating the site's true location was near on impossible because of the inaccurate determination of geographical coordination, which was usual for the time, and the heavy cultivation of the fields. As it turned out later, the results of our magnetometer prospecting also covered the old excavation trenches, but they did not show any correlations with anomalies found in the magnetogram. Based on the magnetometer prospection results in the previous year, trenches were laid out in 2019. Strangely, no features were found during the excavation, which could explain the anomalies visible in the magnetogram. I arranged for soil samples to be taken from vertical profiles from the excavation trenches. Their chemistry was analysed by pXRF measurements and complimented by my susceptibility measurements. It turned out that the magnetic susceptibility differs considerably between the two profiles, showing a significant enhancement for the lower topsoil and plough horizon. First forward simulations of the magnetic field of the magnetisation contrast reveal that this difference in susceptibility can cause the positive anomaly detected in the magnetogram. The magnetic susceptibility correlates with phosphorus and calcium, showing a similar increase for the lower topsoil and plough horizon. Both oxides of the elements are associated with the use of fertilisers and are residues of the field's fertilisation. This would explain the anomalies' linearity and parallelism to the field's plough furrows. Further rock magnetic measurements might disclose if this hypothesis is correct. So far, residues of fertiliser seems to be a plausible explanation of the detected features. Further investigations, unfortunately, are complicated since there are disputes with the owner of the field.

In conclusion, all the case studies in this thesis offer new insights into the archaeology of the sites but also show that it takes a basic understanding of magnetism to understand the anomalies of magnetometer prospecting. Simulations, synthetic magnetograms and susceptibility analysis extended this understanding.



# Acknowledgements

First and foremost, I would like to express my deepest gratitude to my supervisor, Prof. Jörg Fassbinder, for giving me this unique opportunity to work in the field of archaeological prospection and providing me with the freedom to set the focus of my thesis according to my interests and abilities. This endeavour would not have been possible without his support, guidance, expertise, composure, and unwavering confidence in my abilities. Sincere thanks for allowing me to participate in the numerous field trips, conferences, meetings and training schools and for pushing me out of my comfort zone in small increments to let me grow from the experiences I have gained and thus become the scientist and person I am now.

I also would like to thank all the co-authors who supported my drafts of the articles with fruitful discussions and insightful comments. I would like to extend my thanks to all colleagues, partners, and staff for facilitating and financing our field trips and research and helping with the fieldwork. I owe them a great debt of gratitude, as this thesis would not have been possible otherwise. I gratefully acknowledge the financial support of the Deutsche Forschungsgemeinschaft during the first three years.

I would like to thank the Ludwig-Maximilians-Universität for an excellent education over the last ten years, particularly the Department of Earth and Environmental Sciences, for hosting me, providing the necessary infrastructure and maintaining an outstanding research facility. I am also thankful to Prof. Gilder for letting me access the LMU laboratory for rock and palaeomagnetism, but of greater importance to me, our sparring matches, our discussions and his continuous, critical and extensive input on magnetism and science.

Special thanks to Dr. habil. Florian Lhuillier, although he never really bore any responsibility in my dissertation project, always found time to answer questions, give honest insights and offer a helping hand. I am also grateful for being allowed to give the Geomagnetism lecture exercises the last years and thus gain valuable teaching experience. Thanks for bringing me along to a palaeomagnetism field trip and asking for my company to maintain the VFTB or laboratory facilities so that I could broaden my professional horizon.

Many thanks to Marion Scheiblecker for initiating me into magnetometer prospecting and data analysis in Fara, for her archaeological perspective on our results, her helpful insights, and her tireless engagement from that day on. I would like to thank Mandana Parsi, my fellow researcher during the PhD phase, for her scientific and emotional support over the last few years. I am very grateful that I joined paths with her, that we became friends, that we grew so much as persons and scientists in this time, and most of all, that she never lost faith in me. The work on the soil samples of the Gumbati campaign would not have been possible without Michaela Schauer's patience, motivation, curiosity, and commitment. Special thanks for performing and evaluating the pXRF and for the overall

contribution of the Gumbati chapter of this thesis.

I am grateful to all my colleagues, mates, and lunch partners for the inspiring discussions over the last few years. Without them, this time would not have been so memorable. Thanks to Mathias Huth, who taught me not only how to play the piano in his lessons but also a lot about life, patience and the joy of learning. Without him, I would never have become the person I am now. Finally, I thank my family and friends for their patience and understanding over the past months. My sincere thanks go to my beloved husband for his unconditional love, his emotional and financial support, our scientific discussions and most of all, for being the joy of my life and making every day truly unique.

# References

- Adamia, S., Zakariadze, G., Chkhotua, T., Sadradze, N., Tsereteli, N., Chabukiani, A., & Gventsadze, A. (2011). Geology of the Caucasus: a review. *Turkish Journal of Earth Sciences*, 20(5), 489–544.
- Aitken, M. J. (1958). Magnetic prospecting. *Scientific methods in medieval archaeology*, 423–434.
- Aitken, M. J. (1974). *Physics and archaeology*. Oxford: Clarendon Press.
- Alken, P., Thébault, E., Beggan, C. D., Amit, H., Aubert, J., Baerenzung, J., ... others (2021). International geomagnetic reference field: the thirteenth generation. *Earth, Planets and Space*, 73(1), 1–25.
- Allred, J. C. (1964). A fluxgate gradiometer for archaeological surveying. *Archaeometry*, 7(1), 14–19.
- Almamori, H. O. (2014). The Early Dynastic Monumental Buildings at Umm al-Aqarib. *Iraq*, 76, 149–187.
- Andrae, W. (1902a). Aus einem Berichte W. Andrae's über seine Exkursion von Fara nach den südbabylonischen Ruinenstätten (Tell Īd, Jöcha und Hamām). *Mitteilungen der Deutschen Orient-Gesellschaft*, 16, 16–24.
- Andrae, W. (1902b). Die Umgebung von Fara und Abu Hatab (Fara, Bismāja, Abu Hatab, Hētime, Dschidr und Jubā'i). *Mitteilungen der Deutschen Orient-Gesellschaft*, 16, 24–30.
- Andrae, W. (1903). Ausgrabungen in Fara und Abu Hatab. Bericht über die Zeit vom 15. August 1902 bis 10. Januar 1903. *Mitteilungen der Deutschen Orient-Gesellschaft*, 17, 4–35.
- Asăndulesei, A., et al. (2011). Geophysical prospecting techniques used in archaeology. Magnetometry. *Studia antiqua et archaeologica*, 17(1), 5–17.

- Aspinall, A., Gaffney, C., & Schmidt, A. (2009). *Magnetometry for archaeologists* (Vol. 2). Rowman Altamira.
- Baniamerian, J., Liu, S., Hu, X., Fedi, M., Chauhan, M. S., & Abbas, M. A. (2020). Separation of magnetic anomalies into induced and remanent magnetization contributions. *Geophysical Prospecting*, 68(7), 2320–2342.
- Becker, H. (1997). Hochauflösende Magnetik am Beispiel der archäologischen Prospektion. *Umweltgeophysik, Ernst, Berlin*, 59, 70.
- Becker, H. (1999). Duo-and quadro-sensor configuration for high speed/high resolution magnetic prospecting with caesium magnetometer. *ICOMOS-Hefte des Deutschen Nationalkomitees*, 33, 100–105.
- Becker, H., & Fassbinder, J. W. E. (1999). In Search for Piramesses-the Lost Capital of Ramesses II. in the Nile Delta (Egypt) by Caesium Magnetometry. *ICOMOS-Hefte des Deutschen Nationalkomitees*, 33, 146–150.
- Becker, H., & Fassbinder, J. W. E. (2001). Uruk-City of Gilgamesh (Iraq). First tests in 2001 for magnetic prospecting. *Monuments and Sites*, 6, 93–97.
- Belshé, J. C. (1957). Recent magnetic investigations at Cambridge University. *Advances in Physics*, 6(22), 192–193.
- Bender, F. (1985). Angewandte Geowissenschaften: Methoden der Angewandten Geophysik und Mathematische Verfahren in den Geowissenschaften. *Band, 2*, 766.
- Benoist, A., Gajda, I., Schiettecatte, J., Albukaai, D., Alkhatib-Alkontar, R., BLOND, N., ... Gorea, M. (2020, September). *French-Ethiopian Archaeological Mission in Eastern Tigray (Ethiopia). Report on the 2020 season. The Region of Wolwalo.* (Research Report). CNRS ; Université Lyon 2 ; Université de Strasbourg. Retrieved from <https://halshs.archives-ouvertes.fr/halshs-02954201>
- Bevan, B. W. (1994). The magnetic anomaly of a brick foundation. *Archaeological Prospection*, 1(2), 93–104.
- Bevan, B. W. (1995). Magnetic surveys and lightning. *Near-Surface Views (newsletter of the Near Surface Geophysics section of the Society of Exploration Geophysics)*, 7–8.
- Bevan, B. W. (2009). Archaeological Dating from Magnetic Maps: Some Failures. *Journal of Environmental & Engineering Geophysics*, 14(3), 129–144.
- Bevan, B. W. (2010). Directions of magnetization. In *Making History Interactive: Com-*

- puter Applications and Quantitative Methods in Archaeology (CAA); Proceedings of the 37th International Conference, Williamsburg, Virginia, United States of America, March 22–26, 2010.*
- Bevan, B. W. (2016). Forward magnetic models: creation and calculation. *Geosight: Weems, VA, USA.*
- Bevan, B. W., & Smekalova, T. (1996). Magnetization directions of iron slag at Snorup. *Manuscript Report for Olfert Voss, National Museum: Copenhagen.*
- Bevan, B. W., Smekalova, T. N., Cucarzi, M., & Conti, P. (2001). Magnetization directions of iron slag in Denmark. *Filtering, Optimisation and Modelling of Geophysical Data in Archaeological Prospecting*, 9–25.
- Blakely, R. J. (1996). *Potential theory in gravity and magnetic applications.* Cambridge university press. (ISBN: 0521575478)
- Bobokhyan, A., & Kunze, R. (2021). Ushkiani-Project: Preliminary archaeological investigations in the Lake Sevan Region/Armenia. *Præhistorische Zeitschrift*, 96(2), 500–510.
- Bondar, K. M., Fassbinder, J. W., Didenko, S. V., & Hahn, S. E. (2022). Rock magnetic study of grave infill as a key to understanding magnetic anomalies on burial ground. *Archaeological Prospection*, 29(1), 139–156.
- Breiner, S., et al. (1973). *Applications manual for portable magnetometers* (Vol. 395). Geometrics Sunnyvale, California.
- Breuning-Madsen, H., Holst, M. K., & Rasmussen, M. (2001). The chemical environment in a burial mound shortly after construction — an archaeological-pedological experiment. *Journal of Archaeological Science*, 28(7), 691–697.
- Brückner, H., & Engel, M. (2020). Noah’s Flood—Probing an Ancient Narrative Using Geoscience. In J. Herget & A. Fontana (Eds.), *Palaeohydrology: Traces, Tracks and Trails of Extreme Events* (pp. 135–151). Cham: Springer International Publishing. doi: 10.1007/978-3-030-23315-0\_7
- Burks, J., Viberg, A., & Bevan, B. W. (2015). Lightning strikes in archaeological magnetometry data. A case study from the High Bank Works site, Ohio, USA. *Arctic*, 61(4), 407–425.
- Butler, R. F. (1992). *Paleomagnetism: Magnetic domains to geologic terranes, Electronic edition.* Blackwell Scientific Publications Boston. (ISBN: 086542070X)

- Chulliat, A., Brown, W., Alken, P., Beggan, C., Nair, M., Cox, G., ... Panizza, M. (2020). The US/UK world magnetic model for 2020-2025.
- Clark, D. A. (2014). Methods for determining remanent and total magnetisations of magnetic sources—a review. *Exploration Geophysics*, 45(4), 271–304.
- Clark, D. A., & Emerson, D. W. (1991). Notes on rock magnetization characteristics in applied geophysical studies. *Exploration Geophysics*, 22(3), 547–555.
- Creekmore, A. (2010). The structure of Upper Mesopotamian cities: Insight from fluxgate gradiometer survey at Kazane Höyük, southeastern Turkey. *Archaeological Prospection*, 17(2), 73-88. doi: <https://doi.org/10.1002/arp.375>
- Darras, L., & Vallet, R. (2021). Magnetic signatures of urban structures: Case study from larsa (iraq, 6th–1st millennium bc). *Revue d'archéométrie*, 45, 1. doi: <https://doi.org/10.4000/archeosciences.8378>
- Dearing, J., Lees, J., & White, C. (1995). Mineral magnetic properties of acid gleyed soils under oak and Corsican Pine. *Geoderma*, 68(4), 309–319.
- de Barros, A., Bongiolo, S., de Souza, J., Ferreira, F. J. F., & de Castro, L. G. (2013). Grav mag prism: A matlab/octave program to generate gravity and magnetic anomalies due to rectangular prismatic bodies. *Brazilian Journal of Geophysics*, 31(3), 347–363.
- Demtröder, W. (2004). *Experimentalphysik* (Vol. 2). Springer.
- Dugast, F., & Gajda, I. (2011, May). *Report on fieldwork - First investigation on the site of Wakarida (March 21st - April 2nd 2011)* (Research Report). French-Ethiopian project of archaeological and epigraphic investigations in Tigray region, Ethiopia - Pre-Aksumite and Aksumite period (8th c. BC-AD 7th c.). Retrieved from <https://halshs.archives-ouvertes.fr/halshs-00662850>
- Du Mesnil du Buisson, R. (1934). *La technique des fouilles archéologiques: les principes généraux*. Geuthner.
- Dunlop, D. J., & Özdemir, Ö. (2001). *Rock magnetism: fundamentals and frontiers* (No. 3). Cambridge university press. (ISBN: 052100098X)
- Eshetae, M. A., Hailu, B. T., & Demissew, S. (2021). Spatial characterization and distribution modelling of *ensete ventricosum* (wild and cultivated) in ethiopia. *Geocarto International*, 36(1), 60-75. Retrieved from <https://doi.org/10.1080/10106049.2019.1588392> doi: 10.1080/10106049.2019.1588392

- Evans, M. E., & Heller, F. (2003). *Environmental magnetism: principles and applications of enviromagnetics*. Elsevier.
- Fassbinder, J. W. E. (2009). *Geophysikalische Prospektionsmethoden–Chancen für das archäologische Erbe*. na.
- Fassbinder, J. W. E. (2015). Seeing beneath the farmland, steppe and desert soil: magnetic prospecting and soil magnetism. *Journal of Archaeological Science*, 56, 85-95. doi: <https://doi.org/10.1016/j.jas.2015.02.023>
- Fassbinder, J. W. E. (2017). Magnetometry for archaeology. *Encyclopedia of geoarchaeology*, 499–514.
- Fassbinder, J. W. E., & Becker, H. (2003). Magnetometerprospektion des großen Kurgans 1 von Bajkara, Kasachstan. *Archaeologie in Eurasien*, 16, 131-136.
- Fassbinder, J. W. E., Becker, H., & van Ess, M. (2005). Prospections magnétiques à Uruk (Warka): La cité du roi Gilgamesh (Irak). *Les Dossiers d'archéologie (Dijon)*(308), 20–25.
- Fassbinder, J. W. E., & Gorka, T. H. (2009). Beneath the desert soil–archaeological prospecting with a caesium magnetometer. In *New technologies for archaeology* (pp. 49–69). Springer.
- Fassbinder, J. W. E., & Gorka, T. H. (2011). Magnetometry near to the geomagnetic Equator. In *Archaeological prospection: 9th international conference on archaeological prospection* (pp. 45–48).
- Fassbinder, J. W. E., Hahn, S. E., Parsi, M., Becker, F., Wolf, M., Gagošidze, I., & Kaniuth, K. (2021). Persian Residences in the Southern Caucasus: Latest Discoveries in the Periphery of the Achaemenid Empire. *Revue d'archéométrie*, 45, 1.
- Fazeli Nashli, H., & Schmidt, A. (2006). Tepe Ghabristan: Geophysical Survey Report. *The International Journal of Humanities*, 13(3).
- Furtwängler, A. E., & Knauß, F. (1996). Gumbati: Archäologische Expedition in Kachetien 1995. 2. Vorbericht. *Eurasia antiqua*, 2, 363–381.
- Furtwängler, A. E., Knauß, F., & Egold, A. (1995). Gumbati: Archäologische Expedition in Kachetien 1994. 1. Vorbericht. *Eurasia antiqua*, 1, 177–211.
- Gagoshidze, I., Knauß, F., & Babaev, I. (2007). An Achaemenid «Palace» at Qarajamirli (Azerbaijan) Preliminary Report on the Excavations in 2006. *Ancient Civilizations*

- from Scythia to Siberia*, 13(1-2), 31–45.
- Gamkrelidze, I., Okrostsvaridze, A., Koiava, K., & Maisadze, F. (2021). *Geotourism potential of Georgia, the Caucasus*. Springer.
- Gerlach, I. (2017a). Horn von Afrika, Äthiopien/Eritrea: Migrationsprozesse am nördlichen Horn von Afrika im frühen 1. Jahrtausend v. Chr. *e-Forschungsberichte*, 29–31.
- Gerlach, I. (2017b). Neue Forschungen zur äthio-sabäischen Kultur. In S. Wenig & B. Vogt (Eds.), *In kaiserlichem Auftrag: Die Deutsche Aksum-Expedition 1906 unter Enno Littmann Band 3: Ethnographische, kirchenhistorische und archäologisch-historische Untersuchungen, Forschungen zur Archäologie außereuropäischer Kulturen* (p. 355–390). Wiesbaden: Reichert Verlag.
- Gerovska, D., & Araúzo-Bravo, M. J. (2006, 09). Calculation of magnitude magnetic transforms with high centricity and low dependence on the magnetization vector direction. *Geophysics*, 71(5), I21-I30. Retrieved from <https://doi.org/10.1190/1.2335516> doi: 10.1190/1.2335516
- Getaneh, A., Haile, T., & Sernicola, L. (2018). Three-dimensional modelling of a pre-Aksumite settlement at the archaeological site of Seglamen, Aksum, northern Ethiopia using integrated geophysical techniques. *Archaeological Prospection*, 25(3), 231–241.
- Ghazaryan, H. (2013). Soils of Armenia. *Soil Resources of Mediterranean and Caucasus Countries*, 3.
- Górka, T. (2009). *Methodical research and further development of caesium magnetometry for the investigation of geoglyphs of palpa/nasca, southern peru* (Unpublished doctoral dissertation). Ludwig Maximilians University, Munich (Germany).
- Gröger, S. (2005). Laser-pumped cesium magnetometers for the PSI-nEDM experiment.
- Hahn, S., & Fassbinder, J. W. E. (2021). The Effect of Remanence in Magnetometer Prospection. *Revue d'archéométrie*, 45, 1.
- Hanesch, M., & Scholger, R. (2005, 04). The influence of soil type on the magnetic susceptibility measured throughout soil profiles. *Geophysical Journal International*, 161(1), 50–56. doi: 10.1111/j.1365-246X.2005.02577.x
- Heinrich, E., & Andrae, W. (1931). Fara, Deutschen Orient-Gesellschaft in Fara und Abu Hatab 1902/03. Berlin.

- Helfert, M. (2013). Die portable energiedispersive Röntgenfluoreszenzanalyse (P-ED-RFA)–Studie zu methodischen und analytischen Grundlagen ihrer Anwendung in der archäologischen Keramikforschung. *Naturwissenschaftliche Analysen vor und Frühgeschichtlicher Keramik III: Methoden, Anwendungsbereiche, Auswertungsmöglichkeiten*.
- Herbich, T. (2015). Magnetic prospecting in archaeological research: a historical outline. *Archaeologia Polona*, 53, 21–68.
- Herbich, T., & Zych, I. (2003). Archaeological geophysics in Egypt: the Polish contribution. *Archaeologia Polona*, 41, 13–55.
- Hesse, A. (2000). Count Robert du Mesnil du Buisson (1895–1986), a French precursor in geophysical survey for archaeology. *Archaeological Prospection*, 7(1), 43–49.
- Hesse, A., Barba, L., Link, K., & Ortiz, A. (1997). A magnetic and electrical study of archaeological structures at Loma Alta, Michoacan, Mexico. *Archaeological Prospection*, 4(2), 53–67.
- Hummel, A. W. (1963, 01). Science and Civilisation in China. Volume IV, Physics and Physical Technology. Part 1, Physics. By Joseph Needham et al. (New York: Cambridge University Press. 1962. Pp. xxxiv, 434. *The American Historical Review*, 68(2), 463–464. doi: 10.1086/ahr/68.2.463
- Hus, J., Ech-Chakrouni, S., & Jordanova, D. (2002). Origin of magnetic fabric in bricks: its implications in archaeomagnetism. *Physics and Chemistry of the Earth, Parts A/B/C*, 27(25–31), 1319–1331.
- Hus, J., Ech-Chakrouni, S., Jordanova, D., & Geeraerts, R. (2003). Archaeomagnetic investigation of two mediaeval brick constructions in north Belgium and the magnetic anisotropy of bricks. *Geoarchaeology: An International Journal*, 18(2), 225–253.
- Japp, S. (2019). Yeha, Äthiopien. Archäologische Untersuchungen auf dem Kirchenvorplatz von Yeha. Die Arbeiten der Jahre 2013 bis 2018. *e-Forschungsberichte*, 14–18.
- Japp, S., Gerlach, I., Hitgen, H., & Schnelle, M. (2011). Yeha and Hawelti: cultural contacts between Saba' and D'MT' New research by the German Archaeological Institute in Ethiopia. In *Proceedings of the seminar for arabian studies* (pp. 145–160).
- Javakhishvili, A., Maruashvili, L., Gobejishvili, R., & Tielidze, L. (2019). Morphological Division of the Landscape of Georgia. In *Geomorphology of georgia* (pp. 91–98). Springer.

- Jones, F. (2007). *Magnetic Surveys*. [https://www.eoas.ubc.ca/ubcgif/iag/methods/meth\\_3/](https://www.eoas.ubc.ca/ubcgif/iag/methods/meth_3/).
- Jones, G., & Maki, D. L. (2005). Lightning-induced magnetic anomalies on archaeological sites. *Archaeological Prospection*, 12(3), 191–197.
- Jordanova, N. (2016). *Soil magnetism: Applications in pedology, environmental science and agriculture*. Academic press.
- Kaniuth, K. (2022). Gumbati and Saaklemo (2018-2020). In A. Otto & K. Kaniuth (Eds.), *50 Jahre Vorderasiatische Archäologie in München* (pp. 359–366).
- Kazmin, V. (1972). *Geological map of ethiopia 1:2000000*. Geological Survey of Ethiopia, Ministry of Mines, Energy and Water Resources, Addis Ababa.
- Kharazyan, E., Sargsyan, H., & Hayastan, B. N. (2005). *Geological map of Republic of Armenia*. Ministry of Nature.
- Knauß, F. (2000). Der Palast von Gumbati und die Rolle der Achaimeniden im transkaukasischen Iberien. *Archäologische Mitteilungen aus Iran und Turan*, 32, 119–130.
- Koenigsberger, J. (1932). Über remanenten Magnetismus von Gesteinen. *Beilr. Geophys.*, 35, 204–216.
- Koldewey, R. (1902a). Acht Briefe Dr. Koldewey's (teilweise im Auszug) (Babylon, Fara und Abu Hatab). *Mitteilungen der Deutschen Orient-Gesellschaft*, 15, 6–24.
- Koldewey, R. (1902b). Auszug aus fünf Briefen Dr. Koldewey's (Babylon, Fara und Abu Hatab). *Mitteilungen der Deutschen Orient-Gesellschaft*, 16, 8–15.
- Kunze, R., Bobokhyan, A., Meliksetian, K., Pernicka, E., & Wolf, D. (2011). Archäologische Untersuchungen zur Umgebung der Goldgruben in Armenien mit Schwerpunkt Sotk, Provinz Gegharkunik. *Archäologie in Armenien, Landesmuseum für Vorgeschichte, Halle*, 1–7.
- Kunze, R., Bobokhyan, A., Pernicka, E., Meliksetian, K., von Ruzan Mkrtchyan, M. B., & zur Paläoanthropologie, H. S. (2013). Projekt Ushkiani. Untersuchungen der Kulturlandschaft um das Prähistorische Goldrevier von Sotk. *Veröffentlichungen des Landesamtes für Denkmalpflege und Archäologie Sachsen-Anhalt*, 49–92.
- Kushnareva, K. K., & Kušnareva, K. C. (1997). *The southern Caucasus in prehistory: stages of cultural and socioeconomic development from the eighth to the second millennium BC* (Vol. 99). UPenn Museum of Archaeology.

- Kvamme, K. L., et al. (2006). Magnetometry: Nature's gift to archaeology. *Remote sensing in archaeology: An explicitly North American perspective*, 205–233.
- Lambers, L., Fassbinder, J. W. E., Campbell, S., & Hauser, S. (2019). Ancient Charax Spasinou (Iraq)—Interpreting a multi-phase city based on magnetometer survey data. In *New global perspectives on archaeological prospection: 13th international conference on archaeological prospection, 28 august–1 september 2019, sligo-ireland* (p. 201).
- Lanza, R., & Meloni, A. (2006). *The Earth's Magnetic Field*. Springer.
- Leclant, J. (1959). Haoulti-Melazo (1955-1956). In *Annales d'ethiopie* (Vol. 3, pp. 43–82).
- Lévêque, F. (2020). Geomagnetic survey. In *Methods in historical ecology* (pp. 53–60). Routledge.
- Lhuillier, F., & Gilder, S. A. (2019). Palaeomagnetism and geochronology of Oligocene and Miocene volcanic sections from Ethiopia: geomagnetic variability in the Afro-Arabian region over the past 30 Ma. *Geophysical Journal International*, 216(2), 1466–1481.
- Linford, N., Linford, P., Martin, L., & Payne, A. (2007). Recent results from the English Heritage caesium magnetometer system in comparison with recent fluxgate gradiometers. *Archaeological Prospection*, 14(3), 151–166.
- Linford, N. T. (2003). *The application of environmental magnetism to archaeological prospection* (Unpublished doctoral dissertation). University of London, University College London (United Kingdom).
- Lowrie, W., & Fichtner, A. (2020). *Fundamentals of geophysics*. Cambridge university press. (ISBN: 978-0-511-35447-2)
- Maki, D. (2005). Lightning strikes and prehistoric ovens: determining the source of magnetic anomalies using techniques of environmental magnetism. *Geoarchaeology: An International Journal*, 20(5), 449–459.
- Manoli, S. (2014). *Fluxgate Magnetometer for Archaeological Prospecting. Adaptation, Installation, Set-up and comparative measurements with Caesium Magnetometer on Archaeological sites in Bavaria*. (Unpublished master's thesis). Ludwig-Maximilians-Universität München, Department of Earth and Environmental Sciences, Geophysics.
- Martin, H. P. (1983). Settlement patterns at Shuruppak. *Iraq*, 45(1), 24–31.

- Martin, H. P. (1988). *Fara: A Reconstruction Of The Ancient Mesopotamian City of Shuruppak*.
- McClellan, R. G., & Kean, W. (1993). Contributions of wood ash magnetism to archaeomagnetic properties of fire pits and hearths. *Earth and Planetary Science Letters*, *119*(3), 387–394.
- Michels, J. W. (2005). Changing settlement patterns in the Aksum-Yeha region of Ethiopia: 700 BC-AD 850. *BAR International Series*, *1446*.
- Militzer, H., & Weber, F. (2013). *Angewandte Geophysik: Band 1: Gravimetrie und Magnetik*. Springer-Verlag.
- Millaire, J.-F., & Eastaugh, E. (2011). Ancient urban morphology in the Virú Valley, Peru: Remote sensing work at the Gallinazo Group (100 B.C.–A.D. 700). *Journal of Field Archaeology*, *36*(4), 289–297. doi: 10.1179/009346911X13200731373908
- Morozova, G. S. (2005). A review of Holocene avulsions of the Tigris and Euphrates rivers and possible effects on the evolution of civilizations in lower Mesopotamia. *Geoarchaeology*, *20*(4), 401–423. doi: <https://doi.org/10.1002/gea.20057>
- Murthy, I. V. R. (1974). Analysis of total field anomalies of magnetised spherical ore deposits. *Geoexploration*, *12*(1), 41–50.
- NCEI Geomagnetic Modeling Team and British Geological Survey. (2019). World magnetic model 2020. *NOAA National Centers for Environmental Information*. doi: <https://doi.org/10.25921/11v3-da71>
- Nöldeke, A. (1903). Die Rückkehr unserer Expedition aus Fara. *Mitteilungen der Deutschen Orient-Gesellschaft*, *17*, 35–44.
- O'Reilly, W. (2012). *Rock and mineral magnetism*. Springer Science & Business Media.
- Ostner, S., Fassbinder, J., Parsi, M., Gerlach, I., & Japp, S. (2019). Magnetic prospection close to the magnetic equator: Case studies in the Tigray plateau of Aksum and Yeha, Ethiopia. *13th Int. Conf. on Archaeological Prospection*, *13*, 180–183. doi: 10.32028/9781789693072
- Otto, A., & Einwag, B. (2020). The Survey at Fara - Šuruppak 2016–2018. In A. Otto, M. Herles, K. Kaniuth, L. Korn, & A. Heidenreich (Eds.), *Proceedings of the 11th International Congress on the Archaeology of the Ancient Near East* (Vol. 2, p. 293–306). Wiesbaden.

- Otto, A., Einwag, B., Al-Hussainy, A., Jawdat, J., Fink, C., & Maaß, H. (2018). Destruction and Looting of Archaeological Sites between Fara/Šuruppak and Išān Bahriyāt/Isin Damage Assessment during the Fara Regional Survey Project FAR-SUP. *Sumer*, 64, 35–48.
- Parkinson, W. A., Yerkes, R. W., Gyucha, A., Sarris, A., Morris, M., & Salisbury, R. B. (2010). Early copper age settlements in the Körös region of the Great Hungarian Plain. *Journal of Field Archaeology*, 35(2), 164–183.
- Parsi, M., Hahn, S., & Fassbinder, J. (2021). Illuminating Traces of an Achaemenids Paradise in the south Caucasus by Electrical Resistivity Tomography. In *Agu fall meeting abstracts* (Vol. 2021, pp. GP51A–02).
- Parzinger, H. (2017). Burial mounds of Scythian elites in the Eurasian steppe: New discoveries. *Journal of the British Academy*, 5, 331–355.
- Petrovskỳ, E., Remeš, J., Kapička, A., Podrázskỳ, V., Grison, H., & Boruvka, L. (2018). Magnetic mapping of distribution of wood ash used for fertilization of forest soil. *Science of the Total Environment*, 626, 228–234.
- Phillipson, D. W. (2012). *Foundations of an African Civilisation: Aksum & the Northern Horn, 1000 BC-1300 AD*. Boydell & Brewer Ltd.
- Pickartz, N., Rabbel, W., Rassmann, K., Müller-Scheeßel, N., Furholt, M., Müller, J., ... Dreibrodt, S. (2020). What over 100 drillings tell us: a new method for determining the Koenigsberger ratio of soils from magnetic mapping and susceptibility logging. *Archaeological Prospection*, 27(4), 393–414.
- Pignatelli, A., Nicolosi, I., Carluccio, R., Chiappini, M., & Von Frese, R. (2011). Graphical interactive generation of gravity and magnetic fields. *Computers & geosciences*, 37(4), 567–572.
- Primdahl, F. (1979, apr). The fluxgate magnetometer. *Journal of Physics E: Scientific Instruments*, 12(4), 241. Retrieved from <https://dx.doi.org/10.1088/0022-3735/12/4/001> doi: 10.1088/0022-3735/12/4/001
- Rajagopalan, S. (2003). Analytic Signal vs. Reduction to Pole: Solutions for Low Magnetic Latitudes. *Exploration Geophysics*, 34(4), 257-262. Retrieved from <https://doi.org/10.1071/EG03257> doi: 10.1071/EG03257
- Ralph, E. K. (1964). Comparison of a proton and a rubidium magnetometer for archaeological prospecting. *Archaeometry*, 7(1), 20–27.

- Rao, D. B., & Babu, N. R. (1991). A rapid method for three-dimensional modeling of magnetic anomalies. *Geophysics*, 56(11), 1729–1737.
- Rice, P. M. (2015). *Pottery analysis: a sourcebook*. University of Chicago press. (ISBN: 9780226711188)
- Robin, C. J., & de Maigret, A. (1998). Le grand temple de Yéha (Tigray, Éthiopie), après la première campagne de fouilles de la mission française (1998). *Comptes rendus des séances de l'Académie des inscriptions et belles-lettres*, 142(3), 737–798.
- Save, S., Kovacik, J., Demarly-Cresp, F., Issenmann, R., Poirier, S., Sedlbauer, S., & Teyssonneyre, Y. (2020). Large-scale geochemical survey by pxf spectrometry of archaeological settlements and features: new perspectives on the method. *Archaeological Prospection*, 27(3), 203–218.
- Scheiblecker, M. (2021). Can Magnetic Directions of Kilns Help Us Distinguish Settlement Phases? *Revue d'archéométrie*, 45, 1.
- Schmidt, A. (2007). *Encyclopedia of Geomagnetism and Paleomagnetism* (D. Gubbins & E. Herrero-Bervera, Eds.). Springer Berlin/Heidelberg, Germany.
- Schmidt, A. (2008). Electrical and magnetic methods in archaeological prospection. In *Seeing the unseen. geophysics and landscape archaeology* (pp. 93–108). CRC Press.
- Schmidt, A., Coningham, R., & Gunawardhana, P. (2009). At the equator: making sense of magnetometer data. *ArcheoSciences. Revue d'archéométrie*(33 (suppl.)), 345–347.
- Schmidt, A., Dabas, M., & Sarris, A. (2020). Dreaming of perfect data: Characterizing noise in archaeo-geophysical measurements. *Geosciences*, 10(10), 382.
- Schmidt, A., Linford, P., Linford, N., David, A., Gaffney, C. F., Sarris, A., & Fassbinder, J. W. E. (2015). *Each guidelines for the use of geophysics in archaeology: Questions to ask and points to consider*.
- Schnelle, M. (2011). Towards a Reconstruction of the Great Temple of Yeha (Ethiopia). *A. Sedov (Hg.), New Research in Archaeology and Epigraphy of South Arabia and its Neighbors, Proceedings of the Rencontres Sabéennes*, 15, 387–415.
- Schnelle, M. (2014). Monumentalbauten des 1. Jahrtausends v. Chr. in Yeha (Äthiopien) und Vergleichsbauten in Südarabien: Architektur als Spiegelbild von Kulturtransfer. *Zeitschrift für Orient-Archäologie*, 7, 368–391.

- Schnelle, M. (2017). Yeha, Äthiopien: Die Restaurierungsarbeiten am Monumentalbau Grat Be'al Gebri. *e-Forschungsberichte*, 7–12.
- Schnelle, M. (2019). Timber-frame Architecture on Both Sides of the Red Sea from the Early First Millennium BCE: Recent Investigations of the German Archaeological Institute in South Arabia and Northern Ethiopia. In A. Manzo, C. Zazzaro, & D. Jocyce de Falco (Eds.), *Stories of globalisation: The red sea and the persian gulf from late prehistory to early modernity, selected papers of red sea project vii* (pp. 95–118). Brill.
- Schnelle, M. (2021). Observations on architectural features from the early 1st millennium BC in South Arabia and East Africa. In C. Darles, L. Khalidi, & M. Arbach (Eds.), *Contacts between south arabia and the horn of africa, from the bronze age to islam. in honor of rémy audouin* (pp. 145–158). Rencontres Sabéennes 21, Toulouse: Presses universitaires du midi.
- Schnepp, E., Pucher, R., Reinders, J., Hambach, U., Soffel, H., & Hedley, I. (2004). A German catalogue of archaeomagnetic data. *Geophysical Journal International*, 157(1), 64–78.
- Scollar, I. (1969). Some techniques for the evaluation of archaeological magnetometer surveys. *World archaeology*, 1(1), 77–89.
- Sharma, P. V. (1966). Rapid computation of magnetic anomalies and demagnetization effects caused by bodies of arbitrary shape. *Pure and Applied Geophysics*, 64(1), 89–109.
- Simon, F.-X., Koziol, A., & Thiesson, J. (2012). Investigating magnetic ghosts on an Early Middle Age settlement: Comparison of data from stripped and non-stripped areas. *Archaeological Prospection*, 19(3), 191–200.
- Smellie, D. W. (1956). Elementary approximations in aeromagnetic interpretation. *Geophysics*, 21(4), 1021–1040. doi: 10.1190/1.1438294
- Soffel, H. C. (1991). *Paläomagnetismus und Archäomagnetismus*. Springer. (ISBN: 978-3-642-76547-6) doi: 10.1007/978-3-642-76547-6\_3
- Tauxe, L. (2010). *Essentials of paleomagnetism*. University of California Press. (ISBN: 0520260317)
- Tema, E. (2009). Estimate of the magnetic anisotropy effect on the archaeomagnetic inclination of ancient bricks. *Physics of the Earth and Planetary Interiors*, 176(3–4), 213–223.

- Thompson, R., & Oldfield, F. (1986). *Environmental Magnetism*. Allen and Unwin. (ISBN: 978-94-011-8038-2)
- Tielidze, L., Gobejishvili, R., & Javakhishvili, A. (2019). Eastern Greater Caucasus. In *Geomorphology of georgia* (pp. 157–187). Springer.
- Tielidze, L., Gobejishvili, R., Tsereteli, D., Maruashvili, L., & Kumladze, R. (2019). Eastern Georgia (Iveria) Intermountain Plain. In *Geomorphology of georgia* (pp. 205–223). Springer.
- Tielidze, L., Gobejishvili, R., Tutberidze, B., Maruashvili, L., Astakhov, N., & Wheate, R. (2019). Long-term geomorphic history of Georgia. In *Geomorphology of georgia* (pp. 3–14). Springer.
- Tite, M. (1966). Magnetic prospecting near to the geomagnetic equator. *Archaeometry*, 9(1), 24.
- Tite, M., & Mullins, C. (2007, 08). Enhancement of the Magnetic Susceptibility of Soil on Archaeological Sites. *Archaeometry*, 13, 209 - 219. doi: 10.1111/j.1475-4754.1971.tb00043.x
- van Ess, M., Becker, H., Fassbinder, J. W. E., Kiefl, R., Lingenfelder, I., Schreier, G., & Zevenbergen, A. (2006). *Detection of looting activities at archaeological sites in Iraq using Ikonos imagery*. Herbert Wichmann Verlag.
- von der Osten-Woldenburg, H. (1992). Naturwissenschaften und Archäologische Denkmalpflege (4). Die Geophysik am Landesdenkmalamt im Aufbau. *Denkmalpflege in Baden-Württemberg-Nachrichtenblatt der Landesdenkmalpflege*, 21(1), 25–33.
- Von Frese, R. R. B., & Noble, V. E. (1984). Magnetometry for archaeological exploration of historical sites. *Historical Archaeology*, 18(2), 38–53.
- Williams-Thorpe, O., Jones, M. C., Tindle, A. G., & Thorpe, R. S. (1996). Magnetic susceptibility variations at Mons Claudianus and in Roman columns: a method of provenancing to within a single quarry. *Archaeometry*, 38(1), 15–41.
- Wolf, D., & Kunze, R. (2013). Gegharkunik–Neue Quellen für altes Gold aus Südkaukasien. In *Metalle der macht–frühes gold und silber/metals of power–early gold and silver/6th archaeological conference of central germany* (pp. 111–140).
- Wunderlich, T., Kahn, R., Nowaczyk, N. R., Pickartz, N., Schulte-Kortnack, D., Hofmann, R., & Rabbel, W. (2022). On-site non-destructive determination of the remanent magnetization of archaeological finds using field magnetometers. *Archaeological*

*Prospection*, 29(2), 205–227.

Wynn, J. C. (1986). A review of geophysical methods used in archaeology. *Geoarchaeology*, 1(3), 245–257.

